THÈSE

En vue de l'obtention du

DOCTORAT DE L'UNIVERSITÉ DE TOULOUSE

Délivré par : *l'Université Toulouse 3 Paul Sabatier (UT3 Paul Sabatier)*

Présentée et soutenue le *25/11/2016* **par :**

Audrey Iranzo

Electrosynthèse assistée par ultrasons de nanoparticules de fer à valence zéro : étude de la croissance de dépôts et de leur dispersion par ondes acoustiques

---

JURY

Paul KENIS	Professeur des Universités (University of Illinois)	Rapporteur
Emmanuel MAISONHAUTE	Professeur des Universités (U. Pierre et Marie Curie)	Rapporteur
Béatrice BISCANS	Directrice de recherche CNRS (U. de Toulouse)	Présidente du jury
Rosaria FERRIGNO	Professeur des Universités (U. Claude Bernard Lyon 1)	Membre du Jury
Marc VERELST	Professeur des Universités (U. de Toulouse)	Invité
Fabien CHAUVET	Maître de Conférences (U. de Toulouse)	Directeur de thèse
Théo TZEDAKIS	Professeur des Universités (U. de Toulouse)	Directeur de thèse

---

École doctorale et spécialité :
Mécanique, Energétique, Génie civil, Procédés (MEGeP)
Unité de Recherche :
Laboratoire de Génie Chimique (UMR CNRS 5503)
Directeur(s) de Thèse :
Théo TZEDAKIS et *Fabien CHAUVET*
Rapporteurs :
Paul KENIS et *Emmanuel MAISONHAUTE*

Remerciements

C'est sur ces premiers mots que débute ce manuscrit et que s'achève pour moi ces trois années de thèse, passées au Laboratoire de Génie Chimique de l'Université Paul Sabatier. Je tiens donc, pour commencer, à remercier tous les membres du personnel du laboratoire pour leur accueil et pour avoir, tous, de près ou de loin, fait partie de ces trois années.

Je tiens aussi à exprimer ma gratitude à tous les membres du jury (venant de très près ou de très loin) de s'être déplacé jusqu'à Toulouse pour participer à l'évaluation de ce travail de recherche. Toute ma gratitude à Paul Kenis et Emmanuel Maisonhaute pour leurs rôles de rapporteurs, merci pour votre temps et merci d'avoir contribué à l'amélioration de ce manuscrit par vos remarques. Merci également à Béatrice Biscans d'avoir accepté la présidence de ce jury.

Je voudrais ensuite dire toute ma gratitude à mes deux encadrants Fabien Chauvet et Théo Tzedakis. Fabien, merci pour tout le temps que tu m'as accordé, merci pour ton aide au quotidien et pour toutes les idées que tu as amenées à ce projet. Théo, merci de m'avoir poussé à exprimer et à défendre mes idées, merci aussi de m'avoir incité à prendre du recul sur mon travail et à voir plus loin que la thèse. De manière générale, merci à tous les deux de m'avoir poussé à faire plus, à faire mieux jusqu'au tout dernier jour! Bien que ce fût parfois éreintant, c'est aussi ce qui m'a permis de m'améliorer sous divers aspects. Vous avez, de mon point de vue, formé un duo d'encadrants complémentaires aussi bien scientifiquement qu'humainement, mêlant perfectionnisme et bonne humeur et je garderai un souvenir amusé de nos réunions souvent aussi animées qu'interminables.

Je remercie également Stéphane Le Blond du Plouy et Laurent Weingarten du Centre de microcaractérisation Raimond Castaing ainsi que Marie-Line de Solan-Bethmale

du LGC, pour les analyses MEB et MET réalisées durant ma thèse. Merci de manière générale à tout le personnel technique du laboratoire qui nous apporte leur aide et expertise au quotidien.

D'autre part, ces années de thèse ont aussi été pour moi l'occasion d'expérimenter le rôle d'enseignant. Je tiens donc à remercier tous les enseignants qui m'ont accordé et/ou avec qui j'ai partagé ces heures de TP-TD. Merci plus particulièrement à David Evrard, les nombreuses séances de TP, le jury des M1 (etc...), resteront un super souvenir.

Je pense aussi à tous mes collègues doctorants (anciens, nouveaux) que j'ai pu côtoyer durant ces trois années. Un grand merci à tous les doctorants, post-doctorants, stagiaires qui se sont succédés dans le bureau 186 et qui ont égayé mes journées. Je pense à Dancheng, Sylvain, Sandra, Inès, Pohere, Assane, à mon stagiaire Minghui (merci pour ton travail !), Chams (ravie d'avoir partagé cette période de transition entre ancienne et nouvelle génération) et tous ceux que j'ai oubliés. J'ai une pensée particulière pour ceux qui ont cohabité le plus longtemps à mes côtés. Yingying, merci pour ton sourire et ta sérénité à toute épreuve. Guillaume, aussi bruyant que Yingying fut discrète, merci pour ton humour (et merci pour Mike Brant...). Melissa, tu as amené ta joie de vivre, merci d'avoir été autant à l'écoute, tu as été un vrai soutien pour moi. J'espère être dans les parages quand tu termineras ta thèse pour te rendre la pareille.

Un immense merci à tous mes amis : Pierre, Melissa, Seb, Lydie, JC, Sylvain, Sandra, Sandy, Laura, Laurie, Bédou, Loïc, Nicolas, Fanny. Vous avez rythmé ces trois années (et toutes les autres, passées et à venir j'espère !) à coup de soirées, cinés, bar à tapas, badminton, voyage au bout du monde.

Enfin, j'en viens à mon essentiel. Merci à ma famille, à mes parents, de m'encourager, de croire en moi plus que moi-même parfois. Merci à toi, Jesús, de ne pas t'être enfui durant la période de rédaction. Merci d'avoir supporté mes doutes, mon stress, ma folie. Merci d'avoir adapté ton quotidien au mien, ces derniers mois, de t'être levé tôt quand je me levais tôt, couché tard quand je bossais tard, merci de t'être occupé de moi et de ne pas m'avoir laissé mourir de faim devant mon écran d'ordinateur. En bref, merci de rendre mon quotidien plus tendre et facile, plus drôle et vivant depuis que tu es là.

Abstract

This study concerns the coupling of the ultrasounds with the electrodeposition process for the synthesis of zero-valent iron nanoparticles; it is structured in two sections. The first focuses on the material of the electrode substrate used for the iron electrodeposition and aims to determine its influence on both the deposit growth and its dispersion by ultrasonication. The interfacial and the adhesion energies of the deposit on the substrate are controlled by both the surface energy and the roughness of the substrate, therefore a particular focus is put on the influence of these two properties. Two materials of different surface energies (gold and vitreous carbon), as well as various roughnesses, are tested. The affinity of the gold and vitreous substrates with the metallic iron deposit is correlated with the energy required for its formation. The voltamperometric studies reveal, indeed, that a higher overpotential is necessary to produce the iron deposit on the vitreous carbon substrate than on the gold substrate. This difference impacts the deposit morphology (on the gold substrate the iron deposit forms a thin and continuous layer whereas, a 3D growth is favored on the vitreous carbon substrate) but also the deposit adhesion. Indeed, experiments performed to study the effect of ultrasound on the iron electrodeposit, reveal its progressive and complete dispersion for the vitreous carbon case while no dispersion (no removal of the deposit from the electrode) is obtained with the gold substrate. Finally, results show that the substrate roughness is also a control parameter for the deposit adhesion and thus for its dispersion by ultrasonication. To sum up, this first part of the study has enabled to determine the optimal parameters (ultrasounds power and duration, roughness and surface energy of the substrate) for a fast and complete dispersion.

The second section of the present study deals with the synthesis of iron nanoparticles; to this end, the electrodeposition of branched deposits has been investigated in

a Hele-Shaw cell integrating a vibrating element (piezoelectric diaphragm), expected to allow both the deposit formation and its fragmentation. Experiments reveal that the hydrogen bubbles, formed by the co-reduction of free protons during the iron electrodeposition, strongly influence the fragmentation process. Using high frequencies and high amplitudes vibrations, the bubbles oscillate with surface deformations, inducing interface velocity sufficiently high (≈ 4 m/s) to allow the fragmentation of the deposit into particles of sizes ranging between 1 μm and 100 nm. These particles have a high specific surface due to their dendritic morphology. The understanding and the optimization of the synthesis in the vibrating Hele-Shaw cell, coupled with the possibility to apply a flow of iron precursor solution, and an in-situ magnetic separation allow the proposal of a new electrochemical synthesis of micro/nanoparticles in microchannels.

Contents

Introduction

For the last 50 years, research has shown significant interest in the nanomaterials which, thus, have been developed for a wide array of novel technologies: medical, cosmetic, energy, electronic, environmental. The interest of nanoparticles lies in their small size. In general, a particle (assumed as spherical) is considered as a nanoparticle if its diameter is ranging between 1 and 100 nm; 2D structures like fiber or tube are considered as nanostructures if one of their dimensions is lower than 100 nm. By decreasing the size of a particle, its specific surface area, and consequently the proportion of atoms located at its surface, increase. This results in an enhancement of the particles ability to interact, adsorb, react with other atoms [1]. Thus, nanoparticles show unique properties in various field such as: catalytic, chemical, magnetic, optical, electronic [2].

Industrial production of nanomaterials saw its origins in the twentieth century, since then, the market of nanoparticles is in constant expansion. By 2016, the global consumption of nanocomposites should reach 333043 metric tons which represent a value of $2.4 billion. Titanium dioxide nanoparticles, for example, are manufactured worldwide in large quantities for both industrial and consumers products. They can find application as additives in the food, cosmetic, sunscreen, building sectors, but also they are used for the production of rubber compounds. Besides, metal oxides nanoparticles also attract considerable interest. For example, iron oxide nanoparticles have been investigated for their magnetic properties in the medical field, for MRI or cancer treatment. However, zero-valent iron nanoparticles (nZVI) have proven more efficient due to better magnetic properties than iron oxides. In addition nZVI are increasingly investigated in the treatment of contaminated water and soil [2] [1] [3] due to their reductive properties. Indeed, due to both the low standard potential of iron ($E^0 = -0.44V$) and the high specific surface of nanoparticles, nZVI show a high reactivity. Also their small

size allows their injection and dispersion in contaminated subsurface [1]. Thus nZVI has been proven effective for the treatment of a wide range of pollutants such as heavy metals or chlorinated organic compounds.

Generally, nanoparticles can be synthesized through two approaches: top-down or bottom-up. Based on this two global approaches, various physical or chemical syntheses have been explored to produce nZVI (ball milling, thermal reduction of iron salt, iron salt wet-chemical reduction). Among the wet chemical syntheses, the production of nZVI by reduction of iron salt by borohydride salt is a method commonly employed at the laboratory scale.

$$2\,FeCl_3 + 6\,NaBH_4 + 18\,H_2O \longrightarrow 2\,Fe^0 + 6\,B(OH)_3 + 6\,NaCl + 21\,H_2$$

Nevertheless, the scaling up of this synthesis, to produce large quantities, requires specific security conditions, first, because of the risk of gaseous hydrogen production and secondly due to toxicity, corrosiveness, and flammability of the borohydride reductant.

The direct electrochemical nZVI synthesis appears to be a promising alternative for an economical and safe production process, particularly on a large scale; the reducing reagent is replaced by the electron and, under controlled conditions, hydrogen production is avoided. Also, the reaction rate and the electrodeposited particles size can be controlled by the current applied. Nevertheless, metallic iron, produced at the cathodic surface, must be removed from the electrode and dispersed in the liquid at the required size. Various works involve the dispersion of electrodeposited iron by ultrasounds, simultaneously or sequentially with iron-precursors reduction, allowing the renewal of the cathode surface. These techniques combining electrochemical and ultrasonication processes are known as sonoelectrochemical syntheses and consist of producing electrochemically iron deposits and to disperse it from the substrate by ultrasonication (see Figure 1). The effects induced by ultrasound waves are attributed to the generation of cavitation bubbles which, during their violent collapses, create strong enough fluid motion to remove solid deposits from the electrode surface. Even if, various authors propose parametric studies to optimize and control the size of the obtained nanoparticles, the electrodeposit growth and the mechanism of its dispersion are not yet well

understood.

This thesis expects to provide a better understanding of the whole sonoelectrochemical process, by investigating each phase of the synthesis: the electrodeposition and the deposit dispersion. The first objective is to analyze the iron salt reduction as well as the influencing parameters affecting the deposit electrodeposition and its morphology (electrolyte composition, pH, concentration, substrate material and roughness). Then the focus is put on the effect of ultrasonication on the obtained electrodeposit and the parameters controlling the deposit dispersion are discussed (iron salt, work of adhesion of the deposit on the substrate, size of the electrodeposited iron particles, ultrasounds power).

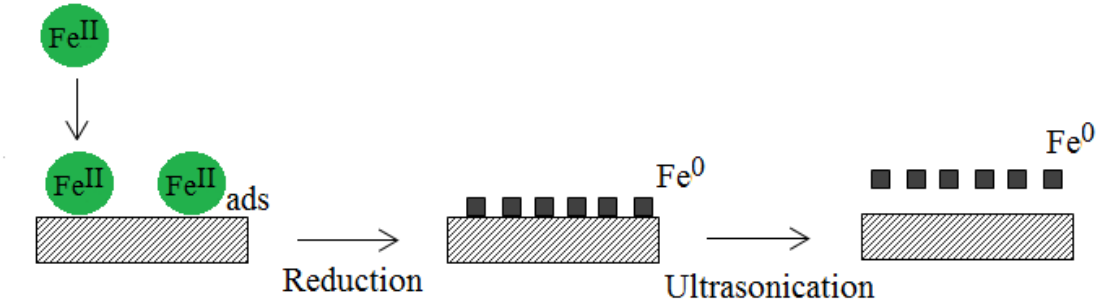

Figure 1: Schematic representation of the first procedure investigated: dispersion by ultrasound of electrodeposited iron particles.

In a second part of the thesis, a new approach for the synthesis of nZVI is investigated. It combines the iron electrodeposition with acoustic vibrations and thus, can be classified as acoustofluidic synthesis. It consists of exploiting the high aspect ratio of a microchannel (Hele-Shaw cell) to achieve the growth and the fragmentation of ramified electrodeposits in a confined space and under controlled conditions (see Figure 2). The technique is expected to enable:

- to reach high conversion rates of the iron precursor due to the high surface to volume ratio of the microcell,
- the set up of a multistep synthesis combining the production of iron, the fragmentation and the rinsing of the deposit, before collecting the particles.

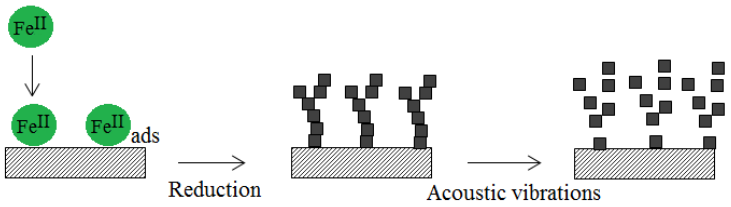

Figure 2: Schematic representation of the second procedure investigated: fragmentation assisted by acoustic waves of ramified iron branches.

To present the context for this study and allow the understanding of the sonoelectrochemical synthesis, Chapter 1 provides the state of the art of this technique as well as the theoretical background required to comprehend both the metal electrodeposition and the dispersion by ultrasonication processes. Chapter 2 deals with the electrodeposition of iron. The Fe^{II} reduction is studied and the parameters influencing the electrodeposit growth and its morphology are discussed (iron salt, pH, concentration, substrate). A particular focus is put on the influence of the substrate surface energy and roughness. Chapter 3 describes the dispersion process of the electrodeposits obtained for various operating conditions: iron salts, substrates, quantity and size of the electrodeposited iron particles. The efficiency of the deposit dispersion process is correlated with the work of adhesion of iron on the substrates, enabling the investigation of the substrate effect. Chapter 4 deals with the acoustofluidic synthesis of iron particles in a Hele-Shaw cell. The electrodeposition of ramified iron deposit is studied, and the influence of both the current and iron salt concentration on the iron growth is highlighted. Then the fragmentation of the iron deposit under acoustic vibration is analyzed, and the behavior of the bubbles trapped into the microchannel is discussed. A parametric study is carried out to optimize the efficiency of the deposit fragmentation.

1 Bibliographic study

This chapter presents the state of the art of the sonoelectrochemical synthesis of zero valent iron nanoparticle (nZVI)s. After a brief, a presentation of both the nZVI properties as well as the current synthesis routes, the focus is put on the sonoelectrochemical synthesis, particularly on the different procedures and experimental devices used.

The sonoelectrochemical synthesis consisting of the coupling between metallic electrodeposition and ultrasonication processes, the theoretical knowledge about both fields is required for the understanding of the whole process. Thus, the second section of this chapter presents the theoretical concepts reported by the bibliographic research on the electrochemical nucleation and growth of the metal deposit. The last section focuses on the deposit dispersion/fragmentation induced by acoustic waves propagation. The effects of the ultrasonication and their impact on both the electrochemical process and on the electrodeposit dispersion are discussed.

1.1 Iron nanoparticles

Iron is a very abundant material in the earth's crust; in its metallic form, it has catalytic, chemical (as a reducing agent, $E^0_{Fe^{2+}/Fe} = -0.44$ V/SHE [1]) and magnetic properties. At the nanoscale, these properties are truly enhanced due to the large surface to volume ratio, S/V [3]. Concerning the use of nZVI for their magnetic properties, iron oxide nanoparticles were somewhat preferred to nZVI because of their easier synthesis, however, even if the high reactivity of nZVI leads to difficulties in their handling, their performances for magnetic and also catalytic and chemical applications are more interesting than that of iron oxide [1] [4]. That is why, for the past 15 years, research has shown an increasing interest for nZVI and their application for both environmental remediation and medical treatment (contrast agent for MRI [4] [5] [6], cancer treatment by hyperthermia [7] [6]).

1.1.1 nZVI structure

Before starting to describe the various properties and application of the nZVI, let's begin with a short presentation of the nZVI structure. This step is necessary because the

[1] Standard hydrogen electrode

specific properties of the zero-valent iron nanoparticles are directly related to their structure (see Figure 1.1) and composition, therefore their characterization is essential for the understanding of their chemical and magnetic activity.

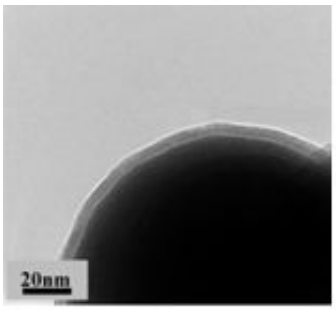

Figure 1.1: core-shell structure of the nZVI [8]

Because of their chemical reactivity the nZVI are practically always covered by a core-shell structure (see Figure 1.1) constituted of an iron oxide or hydroxide layer surrounding the iron core [9]. Generally speaking, this oxide layer presents a mixed of $Fe^{(II)}$ and $Fe^{(III)}$ oxides phase, and the $Fe^{(III)}$ oxide phase predominates at the nanoparticle surface [2]. However, the composition of the oxide shell depends both on the synthesis method employed to produce the nZVI and on the environmental conditions. For example, nanoparticles produced by vapor-phase deposition contain a shell consisting of $\gamma-Fe_2O_3$ and Fe_3O_4 whereas nZVI produced by the reduction of goethite (FeO(OH)) and hematite (Fe_2O_3) particles using dihydrogen, only present a Fe_3O_4 shell. For nZVI prepared by aqueous reduction, the oxide shell is mainly constituted of FeO(OH) due to its hydration [10]. Indeed, in aqueous solution, iron reacts with water to form a layer of hydroxide [11]:

$$Fe(s) + 2H_2O \rightarrow FeOOH + \frac{3}{2}H_2 \tag{1.1}$$

In this particular example, the thickness of the oxide/hydroxide layer has been estimated to be around 2-4 nm [8] [12]. However, it is not possible to determine an exact thickness since the oxide shell thickens as the iron oxidation progresses. Indeed, Wang et al. observe that the shell thickness had roughly double after being exposed during one month to the atmosphere (85 % humidity). These examples show that spontaneous

corrosion (air, acids...) of nZVI occurs, but its rate can be controlled depending on the conditions, and last but not the least, the Fe^0 core stays accessible during the growth of the oxide layer because of its porous nature.

Let's focus now on the application of the nZVI as reducing agent for the contaminants remediation and medical treatments. The impact of the core-shell structure, composition, and shell thickness on the efficiency of the nZVI is also developed.

1.1.2 Applications of the nZVI

Contaminants removal and degradation by nZVI

The main application of nZVI is undoubtedly the removal of contaminants from groundwater and wastewater. Since the 1990s, the zero-valent iron material was employed in the form of granular ZVI for groundwater treatment in permeable reactive barrier (PRBs) systems [2]. This technique consists of a ZVI powders wall through which groundwater flows to be decontaminated. However, the efficiency of this technique decreases with time due to the deposition of iron oxidation products and biofilm growth. The use of ZVI for pollutants removal has been extended by the development of nanoscale ZVI. Indeed, their nanometric scale allows:

- a direct injection of the nZVI which will disperse by convection only into the contaminated area (contaminated soils),
- a higher reactivity than ZVI thanks to a high surface to volume ratio (see Figure 1.2).

The number of studies focusing on the reductive properties of nZVI, to degrade various kinds of pollutants (in less toxic or non-toxic species), continuously increases. However, the reduction reaction is not the only mechanism enabling to degrade the contaminants; other pathways have to be taken into account. Indeed, as explained in the previous section, the nZVI are covered by iron oxide (in a core-shell structure) which can also have a beneficial effect in the pollutant degradation. The zero valent iron core acts as an electron donor, and the oxide layer can [2]:

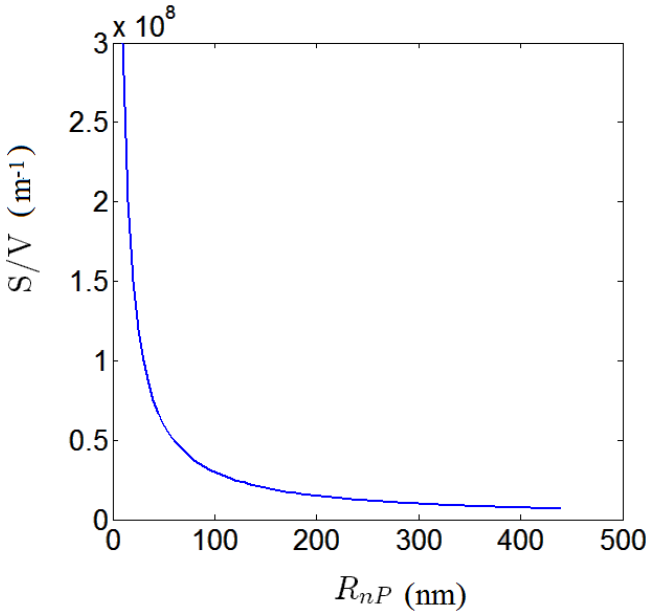

Figure 1.2: Surface to volume ratio of a spherical nanoparticle as a function of its radius.

- enable the electron transfer either by direct transfer through the defects and pinholes or thanks to the semiconducting nature of the oxide layer,
- act as a protective barrier to avoid rapid oxidation of the Fe^0 (by H^+, O_2 and H_2O),
- facilitate the adsorption of various contaminants and provides coordinative sites.

Thus, through the combined properties of iron and iron oxide, the nZVI enable various removal mechanisms of pollutants, like reduction, adsorption, and precipitation. W. Yan et al. [13] proposed the reaction mechanisms for four different metallic contaminants (see Figure 1.3).

Hg^{II} : The reduction of Hg^{II} is achieved by a reduction transformation. Indeed, because $E^0_{Fe^{II}/Fe} = -0.44$ V/SHE $< E^0_{Fe^{II}/Fe^{III}} = +0.77$ V/SHE $< E^0_{Hg^{II}/Hg} = +0.86$ V/ESH, the reduction of Hg^{II} should be spontaneous, Equation 1.2. However, the metallic liquid Hg^0 formed, spreads on the nZVI surface and decrease the nZVI reductive behavior.

$$Hg^{II} + Fe^0 \rightarrow Hg^0 + Fe^{II} \tag{1.2}$$

$$Hg^{II} + Fe^{II} \rightarrow Hg^{0} + Fe^{III} \tag{1.3}$$

Ni^{II} : Ni^{II} is first adsorbed on the oxide shell of the nZVI and then reduced ($E^{0}_{Ni^{II}/Ni} = -0.25$ V/SHE) by the zero valent iron Equation 1.4.

$$Ni^{II}_{ads} + Fe^{0} \rightarrow Ni^{0} + Fe^{II} \tag{1.4}$$

H_2S : The H_2S can be reduced by nZVI via two different pathways. H_2S can react directly with the zero valent iron (Equation 1.5) to forms FeS; or can also react with the oxyhydroxide shell (FeOOH) of the nZVI (Equation 1.6) and forms FeS and FeS_2

$$H_2S + Fe^{0} \rightarrow FeS + H_2(g) \tag{1.5}$$

$$2FeOOH + 3H_2S \leftrightarrow FeS + FeS_2 + 4H_2O \tag{1.6}$$

Other reaction mechanisms for Cr(VI) and Zn^{II} removal, by reduction-precipitation for the first one and adsorption-precipitation for the second, are proposed by these authors (see [10] for more information); all of these reaction pathways reveal the high reactivity of nZVI and explains why the nZVI enable to degrade a large variety of pollutants. Concerning the organic compounds, the most treated contaminants by nZVI during the last decade are the trichloroethylene (TCE), phenol and nitrobenzene [14] but many other pollutants such as nitrate ions, for example, are concerned (see Table 1.1).

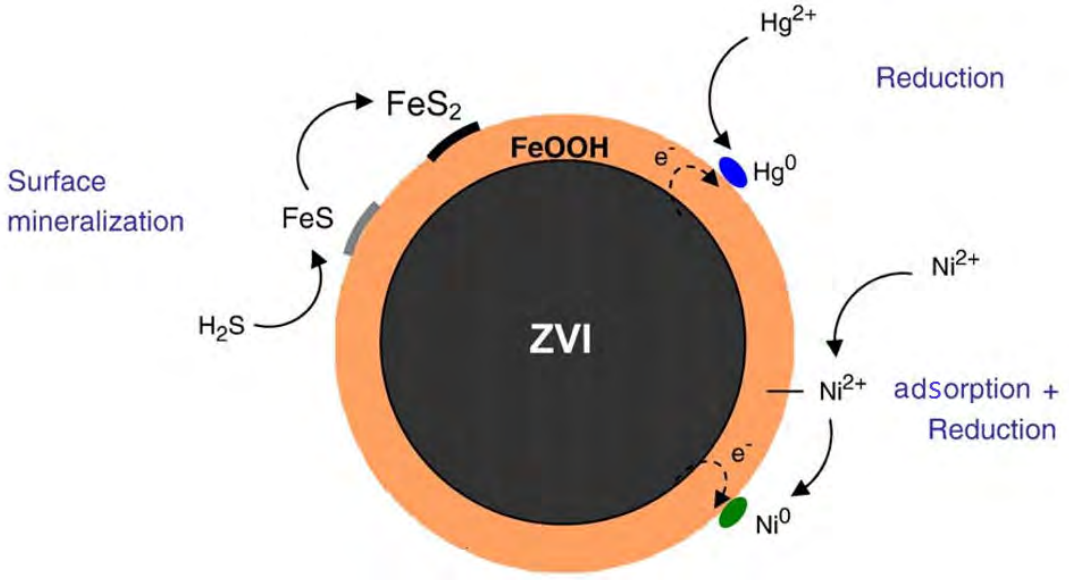

Figure 1.3: Different reaction pathways for contaminants removal by nZVI (extracted from [13]).

Heavy metals	Cr(VI) Hg(II) Cu(II) Ni(II) Pb(II) Zn(II)	[14] [13] [1] [1] [13] [1] [13]
Halogenated hydrocarbons	Trichloroethylene (TCE) Trichloroethylene (PCE) Polychlorinated Biphenyls (PCBs) 1,1,1-trichloro-2,2-bis(4-chlorophenyl)ethane (DDT)	[15] [16] [17] [18]
Nitroaromatic compounds	Nitrobenzene	[14]
Dyes	Methyl orange dye Methylene blue dye	[14] [14]
Other contaminants	Phenol Perchlorate Nitrate Uranium	[14] [13] [14] [19]

Table 1.1: Non exhaustive list of contaminant degraded by nZVI

However, the nZVI efficiency for decontamination can vary over time because of changes in their composition. Indeed, exposed to aerated water or air, nZVI are likely to develop a maghemite or hematite oxide layer, which presents a more passivating character than a Fe_3O_4-like shell [10]. Therefore the corrosion of nZVI particles implies a modification of the core-shell composition which impacts their properties and their efficiency to remove contaminants. That is why the conditioning of the nZVI is important to maintain their efficiency.

V. Smuleac et al. [20] study the dechlorination of TCE and highlighted the aging of the nZVI. Using aqueous borohydride as reductant, authors reduce Fe^{II} into PAA/PVDF[2] membranes and synthesize nZVI immobilized within these membranes. The as prepared nZVI membranes are stored in water. TCE is dechlorinated by cutting into small pieces the PAA/PVDF membranes containing the immobilized nZVI, and then immersing the pieces in a 20 mL TCE solution (30 mg/L) during 24 h. Then samples are collected at different times to analyze the evolution of the TCE concentration.

Authors observe an exponential decrease of TCE with time. Furthermore, the degradation rate increases linearly with the nZVI quantity. They propose a pseudo first kinetics order $\frac{dC}{dt} = k_{obs} \times C$ and express the apparent kinetics constant as follows:

$$k_{obs} = k_{SA} S_{spe} \rho_m \tag{1.7}$$

Where C is the concentration of TCE, k_{obs} the observed constant rate (h^{-1}), k_{SA} the surface normalized rate constant, S_{spe} (m^2/g) the surface rate area and ρ_m the nanoparticles loading (g/L).

Results allow determining an observed constant rate of 0.03 h^{-1}, and a surface normalized rate constant of 0.005 $L.m^{-2}.h^{-1}$.

The authors observe that the initially black membrane turns to orange after 5 h dechlorination reaction, highlighting a rapid corrosion of the particles. To demonstrate the impact of the nZVI aging on their efficiency, several dechlorination experiments are proceeded with the same nZVI membrane which is stored in water and tested periodically during 3 months. Results reveal a loss of the nZVI membrane activity for TCE

[2]PAA: Polyacrylic acid, PVDF: polyvinylidene

degradation above 80 % after 4 cycles[3] (see blue diamonds of Figure 1.4).

Different capping agents can be used to protect nZVI from corrosion, like PAA (polyacrylic acid), PSS (polystyrene Sulfonate), carboxymethyl cellulose (CMC) [10]. They enable to limit iron oxidation but also nZVI aggregation. Instead of borohydride as Fe^{II} reductant, V. Smuleac et al. use tea extract, which both acts as reducing and capping agent. They compare the efficiency of nZVI prepared with tea extract (pink squares in Figure 1.4) with the results mentioned above (blue diamonds of Figure 1.4) for nZVI prepared following the classical borohydride reaction. For the tea extract case, the loss of activity after 4 cycles is below 20 %. This highlights a real improvement in nZVI stability allowed by tea extract.

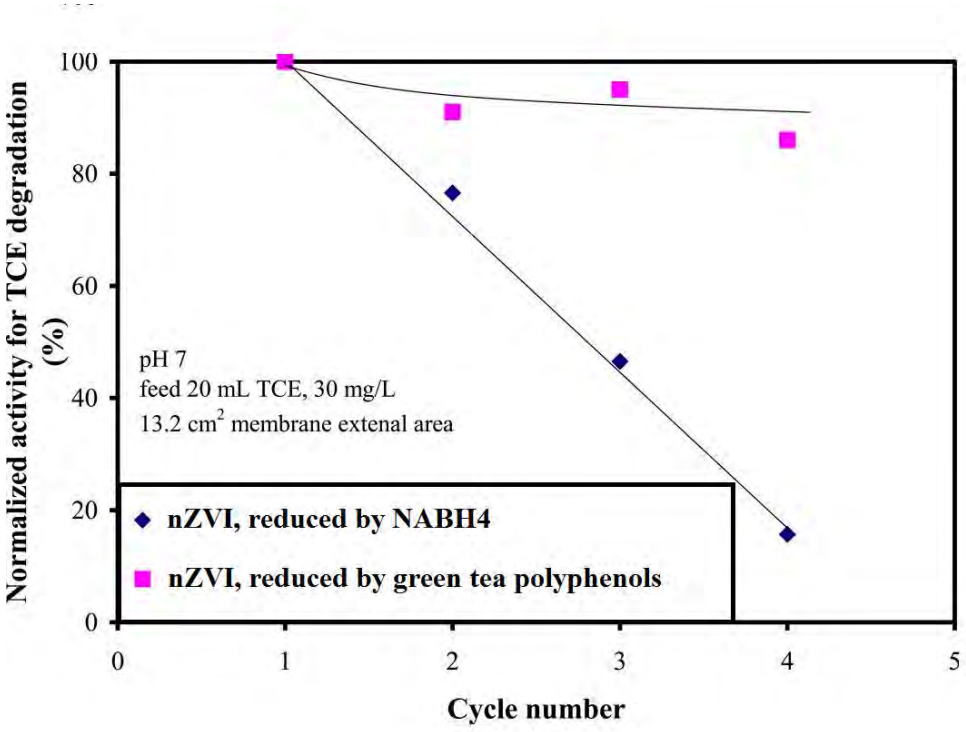

Figure 1.4: Normalized nZVI activity for TCE degradation [20]

[3]One cycle represents one experiment of TCE dechlorination (duration = 24h).

nZVI for medical applications

Zero-valent iron nanoparticles are also of great interest for a medical field such as magnetic cell separation, hyperthermia treatment of cancer and contrast enhancement for MRI. Their use for hyperthermia is based on the fact that when nZVI are subjected to an alternating magnetic field, the resulting hysteresis losses provide heat than can damage and kill cancer cells with, theoretically, a minimal injury to normal cells. Concerning the application of nZVI for MRI, the principle is based on the fact that the nanostructure of the particles reduces the relaxation times of the surrounding water molecules. The shorter is the relaxation times, the greater the MRI contrast is.

Currently, magnetic nanoparticles such as magnetite and maghemite (Fe_3O_4 and $\alpha-Fe_2O_3$, respectively), have been used for biomedical applications but their use is limited by their magnetic properties. Indeed, nZVI have a higher saturation magnetization than iron oxide nanoparticles (see Figure 1.5) and thus interact more with the applied magnetic field. This induces that the relaxation time of water molecules is further reduced using nZVI than using iron oxide nanoparticles.

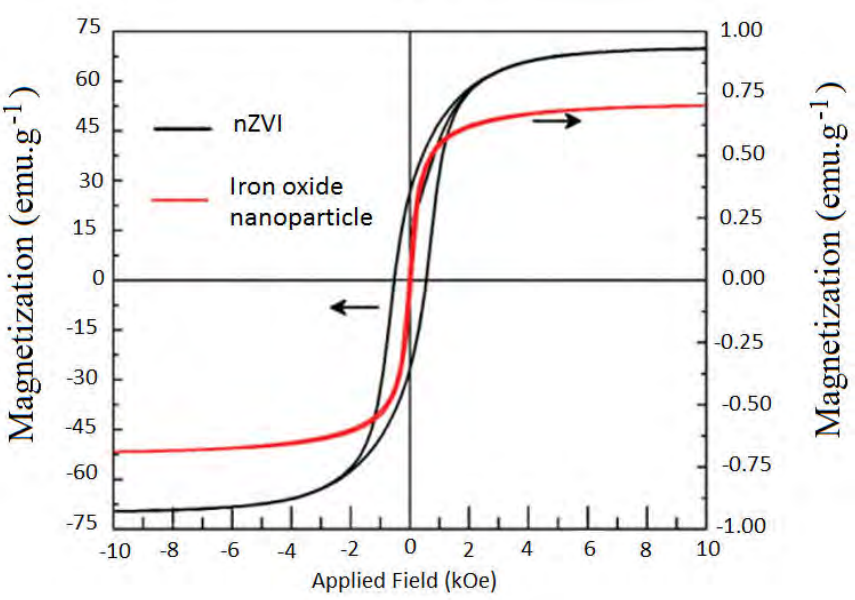

Figure 1.5: Magnetization ($emu.g^{-1}$) curves as a function of the applied field (kOe) for iron and iron oxide nanoparticles (extracted from [4]).

Concerning the hyperthermia application, the difference in magnetization induces that for an nZVI, a lower excitation frequency is needed to reach the desired temperature. This is advantageous for biological application since the applied frequency has to be lower than 1.2 MHz, the safe biological frequency limit. Figure 1.6 (extracted from [4]) shows that with a magnetic field of 500 kHz and 4 Oe [4], the heat provided by nZVI is suitable for hyperthermia treatments, whereas a much higher frequency is needed to reach the same temperatures for the iron oxide nanoparticles.

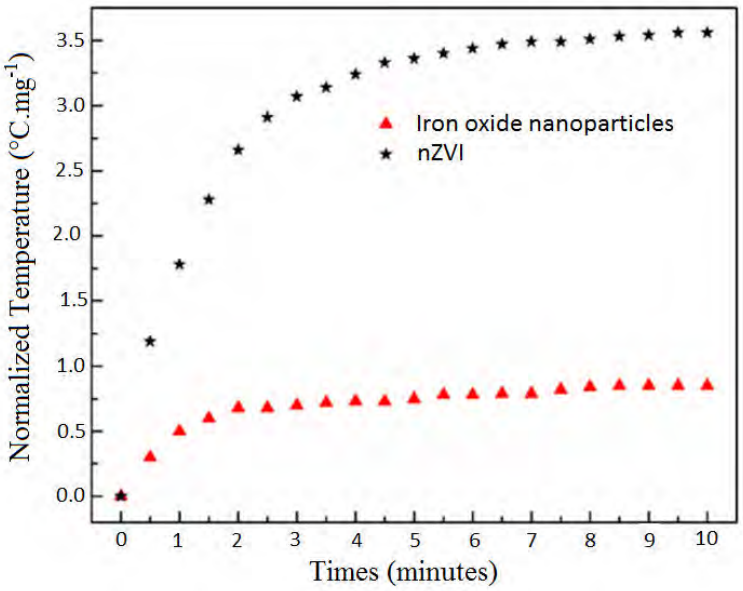

Figure 1.6: Normalized temperature for iron and iron oxide nanoparticles submitted to an alternating magnetic field (500 MHz, 4 Oe) (extracted from [4]). Temperature measurements are normalized per unit mass for comparison.

1.1.3 Zero-valent iron nanoparticles syntheses

Main syntheses routes

Techniques enabling the synthesis of iron nanoparticles can be classified in two global categories depending on whether it employs a "bottom-up" or a "top down" approach [2]. In bottom-up synthesis, atoms clusters or even molecules are used as building

[4] Oersted is the unit used to measured the magnetic field: 1 Oe= $\frac{10^3}{4\pi}$ A.m^{-1}

blocks which are self-assembled to produce the nanostructures. For the top down approach, the process is reversed, and nanoparticles are produced by the chemical or physical break-up of a large size material (micrometric particles for example). Within these two major categories, many different techniques exist; a brief presentation and classification of some of these techniques are proposed here.

Among the top down approaches, high energy ball milling is one of the most representative techniques [3]; this is a mechanical method which has the advantage of being easy to scale up and economical, but it provides polydisperse nanoparticles with an irregular shape. Regarding bottom-up approaches, various synthesis ways exist; among them the gas-phase syntheses (which differ from each other by the technique used to vaporize the solid material or the precursor), the thermal reduction of iron salts or oxides and finally the syntheses by aqueous reduction of iron salts. Table 1.2 gives a non-exhaustive classification of these syntheses methods.

Top down /Bottom up	General Category	Synthesis technique	Brief description
Top down	Mechanical [21]	High energy ball-milling	Micrometric particles of the starting material are introduced in a vibratory mill which by a shaking and rotation motion enables their grinding.
Bottom up	Vapour phase [22]	Inert gas condensation	This gas-phase method employs a solid precursor which is vaporised into an inert gas leading to the growth of metal clusters; the vapor is then mixed with a cold gas to reduce the temperature.
		Pulse laser ablation	A pulse laser ablates targets that contain the desired element and thus enables to produce a plume (jet of vapor) of the material.
		Spark discharge generation	An electrode made of the desired metal in the presence of an inert gas is submitted to a high voltage. When the breakdown voltage is reached, the arc formed across the electrodes leads to the evaporation of a small amount of metal. This is followed by a rapid cooling which leads to the formation of nanoparticles.
		Ion sputtering	Vaporization is managed by bombarding the surface of the desired material with a high-velocity beam of inert gas ions.
		Chemical vapour condensation	A chemical precursor in a carrier gas is brought into a hot-wall reactor to induce gas-phase reactions and procude nanoparticles.
	Thermal reduction [1]	Carbothermal reduction of iron (II) or (III)	The thermal decomposition of carbon-based materials is used to produce the following gases H_2, CO_2 and CO, which act as reducing agents enabling the reduction of iron oxide nanoparticles or of aqueous Fe(II) or Fe(III) into Fe^0.
	Aqueous reduction	Reduction by $NaBH_4$ [2]	The method consists of reducing iron (II) or (III) (usually chloride or sulphate) to zero-valent iron using sodium borohydride.
		Reduction by $NaBH_4$ in microemulsion [3]	The reduction is carried out inside the reversed micelles of a water-oil emulsion which act as nanoreactors.
		Reduction by polyphenolic plant extract [20]	Green syntheses have been proposed, replacing $NaBH_4$ by polyphenolic plant extract (green tea, coffee) which can both reduces Fe(II) into zero-valent iron and acts as a capping agent.
		Electrolysis [1]	Fe(II) or Fe(III) is reduced electrochemically by applying a direct current between two electrodes diving in a Fe(II) salt solution and a method to dispersed the iron nanoparticles formed at the cathode.

Table 1.2: Main synthesis routes for the production of nZVI.

Aqueous reduction of an iron salt

Next part focuses on aqueous syntheses which constitute the main objective of this study.

- *Reduction by $NaBH_4$*

The reduction of iron salt by sodium borohydride is the most common method employed for the synthesis of nZVI at the laboratory scale due to its simplicity. The synthesis is typically performed at ambient temperature [23] and under stirring, by adding an excess of sodium borohydride aqueous solution into a ferric chloride solution. The reaction 1.8 occurs [24]:

$$2\,FeCl_3 + 6\,NaBH_4 + 18\,H_2O \longrightarrow 2\,Fe^0 + 6\,B(OH)_3 + 6\,NaCl + 21\,H_2 \qquad (1.8)$$

As mentioned above, iron ions reduction by $NaBH_4$ can also proceed in a Water/Oil microemulsion which consists of nanosized water droplets stabilized by a surfactant and dispersed in a continuous oil phase. This technique leads to nanometer-sized nanoparticles with narrow size distribution and uniform morphology [24].

Despite the simplicity of the reduction by $NaBH_4$ methods, scaling-up, to produce large quantities of nZVI, requires expensive reagents and specific security conditions because of the gaseous hydrogen production [2].

- *Sonoelectrolysis*

This technique combines the electrolysis for the formation of the iron deposit with ultrasounds to dispersed it into fine particles. The major advantage of this technique is that it enables a good control of the electrodeposited nanoparticles size and morphology by adjusting the operating parameters (current density and duration of the electrolysis) and bath composition (iron salt and supported electrolyte).

A typical synthesis consists of applying a direct current between two electrodes immersed in the iron salt solution so as, the Fe^{II} is directly reduced at the cathode according the following reaction:

$$Fe^{(II)} + 2e^- \longrightarrow Fe^0(s) \tag{1.9}$$

The zero valent iron electrodeposited on the cathode, requires specific conditions to be dispersed in the bulk solution. Ultrasonication is the commonly used technique to remove the electrodeposit from the substrate or to fragment it, so as the whole synthesis can be classified as sonoelectrochemical synthesis.

Two different operating modes can be used to combine electrodeposition and ultrasonication. The first one consists in applying a current and ultrasounds simultaneously. In this case, there is a competition between electrodeposit growth and its dispersion, depending on both the applied current and the ultrasounds power [25].

Another method, called pulsed sonoelectrochemical technique, is proposed by some authors: the electrodeposit growth and the dispersion by ultrasonication are driven sequentially, in a succession of current and ultrasound pulses (see an example in Figure 1.7 [26]. The general principle is that a "massive" nucleation is generated by a high-intensity current pulse and directly followed by an ultrasound pulse, which enables the removal of the metallic nuclei. This technique allows a better control of the nanoparticles sizes by the current pulse parameters: pulsation duration and current density. Indeed, a short pulse enables to limit the growth of the nuclei and therefore to provide small nanoparticles sizes, while a high current density provides a high nucleation rate. The ultrasound intensity pulse also has an influence on the nanoparticles size; indeed, if the nuclei freshly electrodeposited are not removed by the first ultrasound pulse, they can continue to grow during the following current pulse and became bigger. A high ultrasound intensity enables to remove all the nuclei by a single pulse, the following current pulse is therefore executed on a renewed electrode surface [27]. This allows reproducible growth/dispersion cycles and thus a narrow distribution of particle sizes.

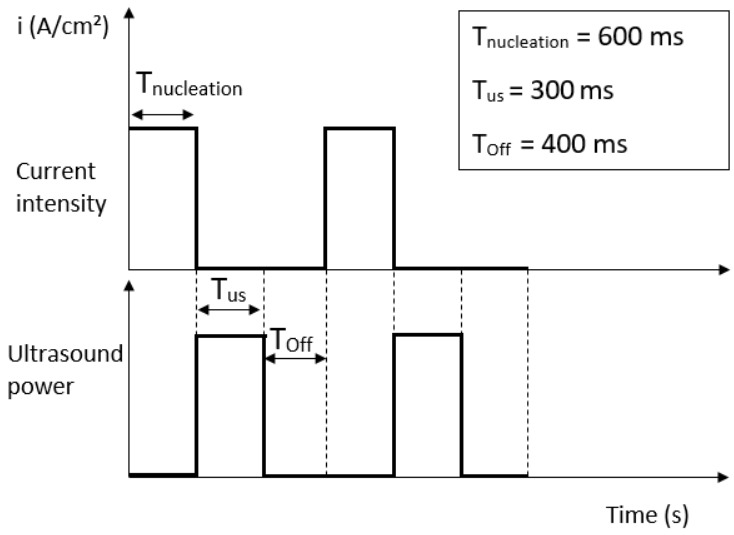

Figure 1.7: Sequence of ultrasonic and current pulses. Experimental values of $T_{nucleation}$, T_{US} and T_{Off} are extracted from [26].

1.1.4 State of the art and principle of sonoelectrochemical devices

The sonoelectrochemical techniques have been increasingly employed in the last decade but the first application of ultrasound to the electrochemistry field, dates to the 1930s [28]. Since then, ultrasounds have been used in electrochemical applications like electroplating, electropolymerisation, and also, activation of electrodes by ultrasonic pretreatment [28].

Different sonoelectrochemical processes are proposed in the bibliography, some of them are briefly presented. Generally, the sonoelectrochemical devices fell into two major categories: 1) the ultrasonic baths 2) the ultrasonic horns [29].

- *Ultrasound bath*

For the first category, a conventional electrochemical cell is immersed in an ultrasonic bath containing water. This is a simple method, but the intensity of the ultrasound waves inside the electrochemical cell is lower than that produced by an ultrasonic horn, directly immersed into the electrochemical cell. An ultrasonic bath consists of several transducers positioned along the bath walls. Therefore the ultrasound field is not homogeneous. To keep a constant ultrasonic intensity during experiments, special care

must be taken with the cell positioning into the bath [29], the electrochemical cell has to be placed into a fixed position. In their sonovoltammetric studies, Walton et al. [30] examine the effect of the location of the cell into the ultrasonic bath to benefit of the maximum ultrasonic intensity, before starting experiments. Despite this drawback, several authors use the ultrasonic bath successfully as ultrasonic source [30] [31]: Chen et al. [31] synthesize iron nanoparticles from iron (III) salt precursor using a simple two-electrodes reactor immersed into a 20 kHz ultrasonic bath. The electrodeposition is achieved by applying a current of 17 mA/cm^2 between the two platinum electrodes, simultaneously with ultrasonication. After an optimization of the surfactant concentration (0.2 g/L CPC[5]) iron nanoparticles of 1-20 nm are observed.

- *Ultrasonic horn*

Generally, an ultrasonic horn tip is placed in front of the cathode, to generate ultrasonic waves close to the cathodic surface. This technique provides higher ultrasound intensity but leads to an increase of the temperature inside the electrochemical cell, and this may cause changes in electrodeposit growth. Moreover, the horn tip (generally made of titanium alloy) can be subjected to erosion during ultrasonication, causing a contamination of the cell solution [29]. Despite these drawbacks, this technique is employed in many sonoelectrochemical studies for its efficiency. Compton et al. present a typical apparatus, which consists of a classical three-electrodes cell in which an ultrasonic horn is introduced, in front of the cathode [32]. A more sophisticated system, proposed by Khachatryan et al. [33], combines two different sources of ultrasound: the ultrasonic horn dived into the cell and oriented to the electrodes (Figure 1.8), and also the cathode which acts both as a second ultrasonic source and as a source of current for iron(II) reduction. This configuration was used to study three different operating modes:

1. the cathode is vibrating with a frequency of 200 kHz and a power density of 1.5 W/cm^2.

2. the ultrasonic horn is activated with a frequency of 20 kHz and a power density of 50 W/cm^2.

[5]CPC: cetylpyridinium chloride

3. the two vibrating sources are activated simultaneously with the same frequencies and power densities as before in 1 and 2.

Note that, for each case, ultrasonication is activated continuously during the electrolysis. The average size of the obtained iron nanoparticles for these three modes are respectively: 29, 18, and 7 nm.

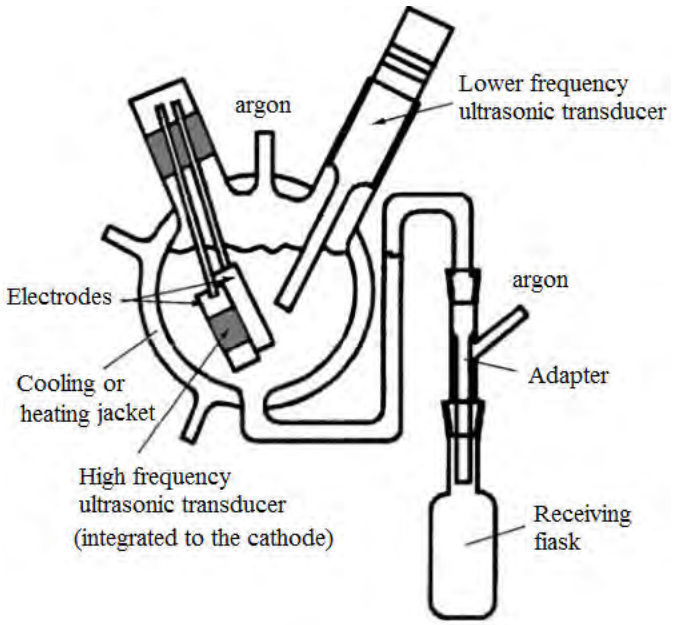

Figure 1.8: Apparatus with two sources of ultrasound proposed by Khachatryan [33]

The bibliography reveals another arrangement widely employed: the ultrasonic titanium horn (referred as sonotrode), is also used as the working electrode. This device is used by J. Delplancke et al. [26] (see Figure 1.9) to prepare magnetic nanopowder. With this operating mode, the ultrasonication and the electrodeposition are not achieved simultaneously, but separately from one another, in a succession of current and ultrasonic pulses, as it was explained in Section 1.1.3.

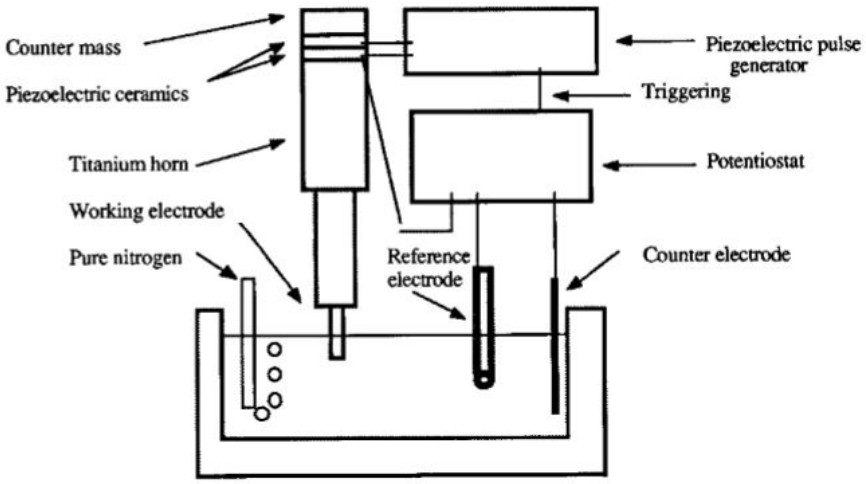

Figure 1.9: Apparatus for sonoelectrochemical pulse synthesis with a sonotrode [26]

To sum up, there are many ways to achieve the sonoelectrochemical synthesis:

- by coupling or not the electrodeposition and dispersion steps,
- using an ultrasonic bath, an ultrasonic horn or a sonotrode

Through these different sonoelectrochemical syntheses, many authors propose parametric studies to optimize the production of nanoparticles [34]. However, the understanding of both the metal electrodeposit growth and dispersion, as well as how these two steps are combined, need further studies. To allow a better understanding of the sonoelectrochemical synthesis, the focus is put in this thesis on two different procedures which are investigated separately:

- the removal by ultrasounds of iron electrodeposit,
- the fragmentation of branched electrodeposits (long growth duration) by acoustic vibrations.

While the first one has recently been a growing focus of metallic nanoparticles research, the second one is a new way for metallic nanoparticles synthesis that we propose to explore in this thesis. Both procedures are detailed below.

- *First procedure: dispersion by ultrasound of electrodeposited iron particles*

This procedure is similar to the typical sonoelectrosyntheses presented above: the electrodeposit consisting of small nuclei is directly removed from the electrode surface to the liquid phase by ultrasonication (either by ultrasonic bath or by ultrasonic horn, either sequentially or simultaneously with the electrodeposition) (see Figure 1.10).

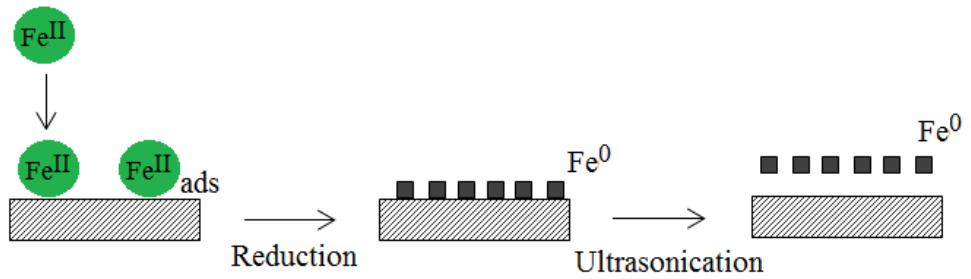

Figure 1.10: Mechanisms for iron deposit dispersion

- *Second procedure: acoustofluidic synthesis*

A new technique has been developed in this thesis (Figure 1.11), employing an acoustofluidic process which combines the electrodeposition of branched iron in a Hele-Shaw cell [6], its fragmentation under the effect of acoustic vibrations. Unlike the first procedure, the idea is to fragment larger iron structures (longer growth duration) instead of removing the electrodeposited particle. Thus, the interest of this new technique is based on several aspects:

- the adhesion between the deposit and the substrate has no effects, neither on the electrodeposition process, nor on the deposit fragmentation, contrary to the sono-electrochemical synthesis,
- the metallic ramified branches, exhibiting high porosity, are easily breakable
- the use of the Hele-Shaw cell, which exhibits a high surface to volume ratio enables to obtain higher particles concentrations (than the sonoelectrochemical method).

[6] A Hele-Shaw cell is a thin gap cell with a high aspect ratio (thickness « lateral dimensions).

- The Hele-Shaw cell configuration enables to produce, to rinse, and to fragment the particles, keeping the produced suspension inside the electrolytic compartment, before collecting the particles.

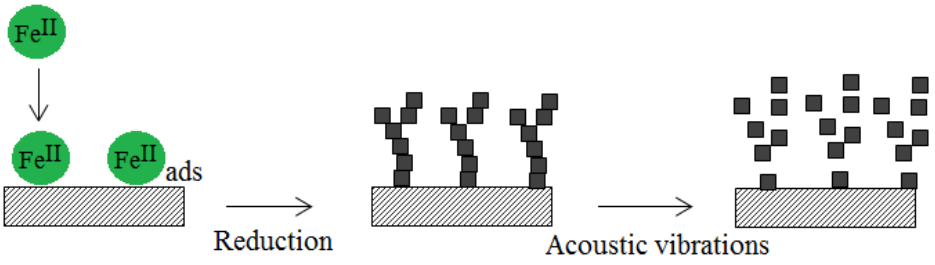

Figure 1.11: Schematic representation of the fragmentation of ramified iron electrodeposits under acoustic vibrations.

Despite their differences, both procedures couple the growth of the iron electrodeposit with its dispersion (its removal from the electrode for the first procedure or its fragmentation for the second) by the action of an acoustic field. Therefore to understand and control these two phases, the theoretical knowledge required is developed in the following sections.

The second section of this chapter focuses on the metal electrodeposition process, by developing the thermodynamical and kinetics aspects of:

- a typical electrochemical reaction,
- the metal nucleation and growth process.

This section also focuses on the particular case of the metal electrodeposition in a Hele-Shaw cell, which concerns specifically the second procedure (Figure 1.11).

Then the last section of this chapter develops the effect induced by the propagation of an acoustic field in aqueous solutions, in the case of:

- ultrasonication on the electrochemical process,
- acoustic vibrations in the microfluidic devices.

1.2 Electrodepostion of metallic deposits

1.2.1 Theory of the electrodeposition and influencing parameters

This section focusing on the formation of metallic electrodeposits, expects to provide the theoretical knowledge required to understand the different processes involved:

- the metallic ions reduction
- the nucleation and growth of a metallic deposit.

The metallic electrodeposition involves the reduction of a metallic ion M^{z+} at an electronic conducting substrate in an electrolytic solution. Therefore, before presenting the case of metal electrodeposition, some theoretical concepts about the global process of a typical heterogeneous reaction (Equation 2.14) are presented.

Thermodynamic and kinetics aspects of an electrochemical reaction

A typical electrochemical reaction can be expressed as follows:

$$Ox + n_g e^- \rightleftharpoons Red \tag{1.10}$$

With n_g, the global electrons exchanged number.

First, it is necessary to consider thermodynamic aspects which enable to predict whether the electrochemical reaction is possible or not. Each Red/Ox system is characterized by an equilibrium potential known as Nernst potential:

$$E_{Ox/Red} = E^0_{Ox/Red} + \frac{RT}{n_g F} ln \left(\frac{a^{electrode}_{Ox}}{a^{electrode}_{Red}} \right) \tag{1.11}$$

with $E_{Ox/Red}$ the Nernst potential, $E^0_{Ox/Red}$ the standard potential of the Ox/Red system, $a^{electrode}_{Ox}$ and $a^{electrode}_{Red}$, the interfacial activities of the oxidant and reductant respectively.

The externally applied potential, E, determines the direction of the reaction 1.10, the oxidant can be reduced if $E < E_{Ox/Red}$. Thus, the overpotential $\eta = E - E_{Ox/Red}$ has to

be below zero for the reduction to take place.

Now let's focus on the kinetics aspects, to understand how the reaction rate evolves with the applied overpotential. The reaction rate r, is proportional to the current flowing through the electrochemical cell:

$$r = \frac{I}{n_g F S} = k_c.C_{ox}^{\alpha} - k_a.C_{Red}^{\beta} \tag{1.12}$$

S being the surface area of the electrode.

That is why the current I is used to characterize the reaction rate for the rest of the discussion.

A global heterogeneous reduction is composed of different steps leading to the conversion of the dissolved oxidant into its reduced form:

- mass transfer of the electroactive species from the bulk to the electrode by diffusion, migration, and convection,
- adsorption of the reactant,
- electron transfer from the cathode to the reactant
- mass transfer of the remaining species to the bulk.

The slowest step of the reaction dictates the global reaction rate. Therefore different regimes exist, and it is necessary to understand how the current evolves as a function of the applied η for each of these regimes. A good way to represent these regimes is to analyze a typical voltamperometric curve (I-E curve) obtained at the steady state.

The steady-state voltammetry on a rotating disk electrode consists in applying a linear potential sweep to the working electrode and to monitor and analyze the evolution of the resulting current. The rotation of the working electrode generates a convective mass transfer of reactants and enables a continuous supply to the electrode. This convective mass transfer maintains all species concentration constant beyond a distance δ from the electrode, which corresponds to the thickness of the diffusion layer. A typical voltammogram (I-E curve) obtained by the reaction of dissolved species on an RDE, exhibits a sigmoïd shape (see Fig. 1.12) and can be divided into three different zones:

1. The electron transfer controlled region
2. The mixed controlled region
3. The diffusion controlled region

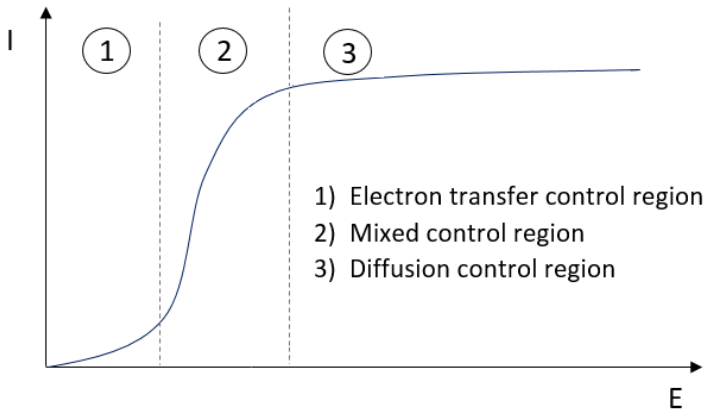

Figure 1.12: Sketch of the sigmoïd shape on a typical voltammogram

The electron transfer controlled region (region 1, Figure 1.12) occurs for low overpotentials η; to increase the reaction rate, the electrode requires more energy. The mass transfer does not limit the overall rate and the concentrations of the electroactive species at the electrode surface are close to their concentrations in the bulk. In this case, the current can be modeled by the Butler-Volmer law, which expresses the current versus the applied potential [35] [36].

$$I = n_g F S \left[k_a^0 C_{Red}^{el} \exp\left(\frac{\alpha n_l F E}{RT}\right) - k_c^0 C_{ox}^{el} \exp\left(-\frac{\beta n_l F E}{RT}\right) \right] \tag{1.13}$$

With:

- k_a^0 and k_c^0 the intrinsic heterogeneous rate constants for oxidation and reduction respectively
- α and β the electronic transfer coefficients for anodic and cathodic processes respectively

- C_{Red}^{el} and C_{ox}^{el} the interfacial concentrations of the red/ox species
- n_g, the global electrons exchanged number
- n_l, the electron exchanged number at the limiting step

A more useful form of the Butler-Volmer law is given below:

$$I = I^0 \left[\frac{C_{Red}^{el}}{C_{Red}^{bulk}} \exp\left(\frac{\alpha n_l F (E - E_{i=0})}{RT} \right) - \frac{C_{Ox}^{el}}{C_{Ox}^{bulk}} \exp\left(-\frac{\beta n_l F (E - E_{i=0})}{RT} \right) \right] \tag{1.14}$$

Where:

- k^0, the intrinsic heterogeneous electronic transfer constant of the electrochemical system ox/red
- $C^{bulk} = C_{Red}^{bulk} = C_{Ox}^{bulk}$
- $E_{i=0}$, the zero current potential
- I^0, the exchange current defined as:

$$I^0 = n_g F S k_c^0 \left(C_{Ox}^{bulk} \right)^{\alpha} = n_g F S k_a^0 \left(C_{Red}^{bulk} \right)^{\beta} = n_g F S k^0 C_{bulk}, \tag{1.15}$$

if $C_{Ox}^{bulk} = C_{Red}^{bulk}$ and, $\alpha = \beta = 1$.

The diffusion control region (region 3) corresponds to a pure mass transfer limitation (fast electronic transfer). At the interface, the electroactive species concentration is considered to be zero. Thus, there is a concentration gradient and the maximal current I_{lim} is reached. Simple film model assumes a linear variation of the concentration in this diffusion layer (thickness = δ) and enable to obtain the following simplified expression of the limiting current:

$$I_{lim} = +\frac{n_g F S D C_{Red}^{bulk}}{\delta} = -\frac{n_g F S D C_{Ox}^{bulk}}{\delta} \tag{1.16}$$

Van Caraman and Cochran solve the Navier Stokes equation in the case of a rotating disk electrode and get the fluid velocity profile. Levich solves the mass balance at

the steady-state (convection flux + diffusion flux = 0) and provides the expression of the current versus the applied potential, which enables to obtain the expression of the cathodic limiting current:

$$I_{lim} = -0.62 n_g F S D_{Ox}^{2/3} \nu^{-1/6} C_{Ox}^{bulk} \omega^{0.5} \tag{1.17}$$

with ω the angular velocity of the RDE, ν the kinematics viscosity and D_{Ox} the diffusion coefficient of the oxidant.

Finally, the mixed control region (region 2) corresponds to a transition zone between the electron transfer and the mass transfer limitations. In this region, the current is expressed by the following equation:

$$I = I^0 \left[\frac{I_{lim_a} - I}{I_{lim_a}} \exp\left(\frac{-\alpha n_l F (E - E_{i=0})}{RT} \right) - \frac{I_{lim_c} - I}{I_{lim_c}} \exp\left(\frac{-\beta n_l F (E - E_{i=0})}{RT} \right) \right] \tag{1.18}$$

Thermodynamic and kinetics aspects of nucleation

The electrochemical deposition of a metal follows several steps:

- mass transfer of the metal ions from the bulk to the electrode by diffusion, migration and convection,
- adsorption of the reactant,
- electron transfer to the reactant,
- nucleation and crystal growth of the metallic bulk phase.

Let's focus on the nucleation and growth phases, which are critical steps of the electrodeposition process. The nucleation starts with the birth of small clusters of metal atoms leading to the formation of a new metallic crystal. The generation of a cluster of N metal atoms is associated with changes in the Gibbs energy of the system, $\Delta G(N)$, which corresponds to the energy required for the formation of the cluster. This energy is associated to both the transfer of metallic ions from the solution to the electrode

under the influence of the overpotential, as well as, to the energy $\Phi(N)$ needed for the formation of the new interfaces: cluster/solution and cluster/substrate. Therefore, the energy of formation of a cluster, $\Delta G(N)$, consists of two components:

$$\Delta G(N) = -Nze|\eta| + \Phi(N) \tag{1.19}$$

With N the size of a cluster (number of atoms), z the charge number, e the elementary charge and η the overpotential. The second term $\Phi(N)$ can be expressed as follow [37]:

$$\Phi(N) = \sum_{i \neq j^*} \gamma_i S_i + S_{j^*}(\sigma_j - W) \tag{1.20}$$

With γ_i and S_i the surface energies and the surface areas of the cluster faces, i. j^* corresponds to the contact face between the cluster and the substrate, which is parallel to the crystal face j. Thus γ_j and S_{j^*} are the surface energy of the face j and the surface area of the contact face j^* respectively. W is the work of adhesion.

It can be noticed that both terms of Equation 1.19 are a function of the size, N, of the cluster. The first term is proportional to N and makes the metal deposition possible (negative term), while the second is positive and proportional to the surface of the new cluster. The representation of $\Delta G(N)$ as a function of N is presented Figure 1.13. For small clusters, the second term $\Phi(N)$ of the Equation 1.19, which is proportional to $N^{2/3}$, dominates. For larger clusters, the first term of Equation 1.19 becomes higher and the slope of $\Delta G(N)$ function becomes negative. Thus the crystal begins to grow spontaneously. The transition between small cluster and large cluster is defined by a critical size, N_{crit} at which the function $\Delta G(N)$ reaches its maximum value $\frac{d\Delta G(N)}{dN} = 0$: ΔG_{crit}. This critical size is characterized by the equal probability for growth and dissolution of the cluster. Therefore, if by an energy fluctuation a crystal of size $N > N_{crit}$ is formed, the crystal can begin to grow spontaneously. These critical values N_{crit} and ΔG_{crit} can be expressed as follows [37]:

$$N_{crit} = 8BV_m^2\gamma^3/27(ze|\eta|)^3 \tag{1.21}$$

and:

$$\Delta G_{crit} = N_{crit} z e |\eta| / 2 \tag{1.22}$$

where:

- B is a constant related to the cluster geometry, $B = S^3/V^2$ (S and V the surface area and volume of the cluster)
- γ, the average surface energy
- V_m is the volume occupied by one atom of the cluster, $V = V_m \times N$

The critical size and energy to reach for the formation of a cluster depend on the overvoltage (Equations 1.21, 1.22), on the surface energy and also on the geometry of the cluster.

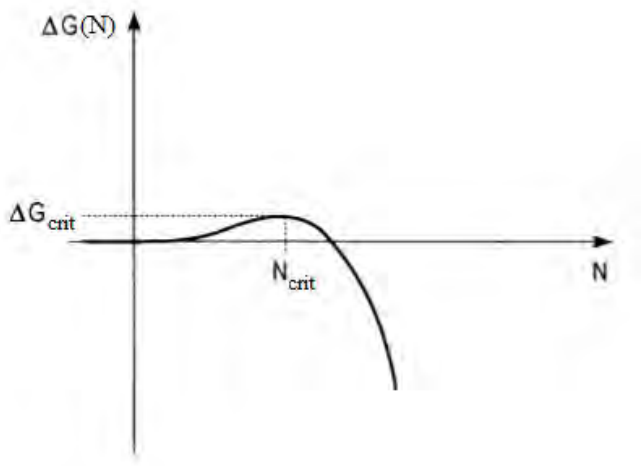

Figure 1.13: Gibbs energy as a function of the cluster size (N) [38]

Excluding the kinetics aspects, the description of the deposition process at nearly thermodynamic equilibrium is a good starting point for the understanding of both the whole electrodeposition process and the morphology of the obtained deposits. The electrodeposition of a metal M on a foreign substrate T ($M \neq T$) can be described by three different mechanisms (see Figure 1.14) [37]. The parameters determining the mecha-

nism of growth are the binding energy between the metal adatoms M_{ads} and the substrate T, as well as the crystallographic misfit[7] between the metal and the substrate [37] [38]:

1. For the first case, the binding energy between the adatoms of metal, and the metal itself $\psi(M_{ads}/M)$ is higher than the binding energy between adatoms of metal and atoms of the substrate T $\psi(M_{ads}/T)$. Then, the metal does not spread on the substrate and a 3D metallic bulk phase consisting of islands (crystallites) is formed. In this case, the metallic growth follows the "Volmer-Weber" mode.

For the second case and third cases, the binding energy between the adatoms of the metal, and the metal itself $\psi(M_{ads}/Me)$ is lower than that between the adatoms of the metal and the substrate T, $\psi(M_{ads}/T)$. These two cases differ from one another by the crystallographic misfit.

2. If the crystallographic misfit between the electrodeposited metal and the substrate is negligible, the metal spreads on the substrate, and the deposition follows a layer by layer mode, also called the "Frank-van der Merwe" mode.

3. If there is an important crystallographic misfit between the metal and the substrate, the deposit growth follows the Stranski-Krastanow mechanism, meaning that a first 2D layer of metallic adatom is formed, on top of which, metallic crystallites will grow. This growth mode is an intermediate case between the "Volmer-Weber" and the "Frank-van der Merwe" modes.

This highlights the importance of the substrate in the metal electrodeposition process and its influence on the deposit morphology.

[7] Valid for the electrodeposition of metal on a substrate presenting a crystalline structure.

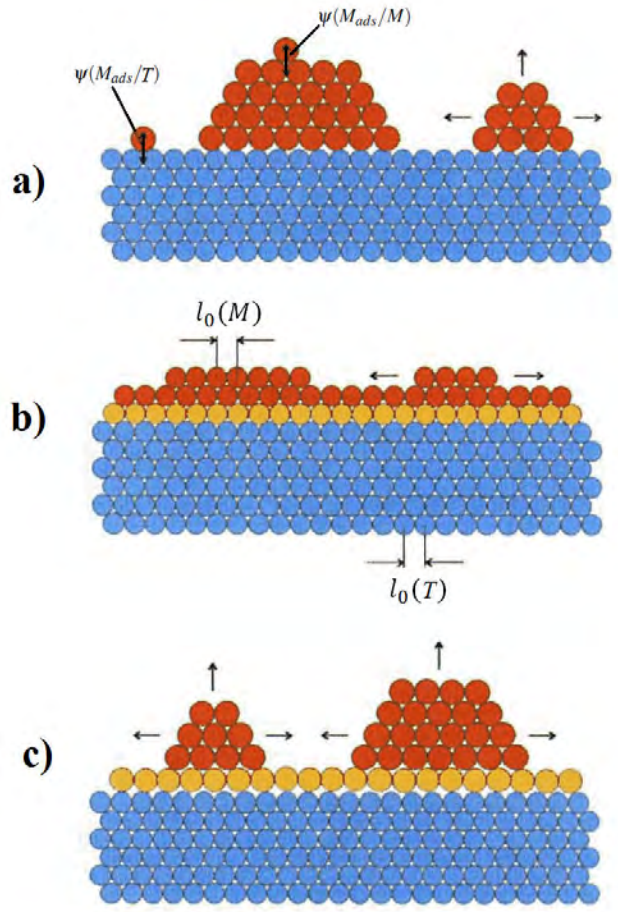

Figure 1.14: Schematic representation of the three different growth models of the deposition of a metal on a foreign substrate, T: a) Volmer-Weber mode b) Frank-van der Merwe mode c) Stranski-Krastanow. The classification was made as a function of the binding energy $\psi(M_{ads}/T)$ and $\psi(M_{ads}/T)$ and of the crystallographic misfit characterized by the interatomic distances l_0 (adapted from [37]).

Only thermodynamical aspects were considered above to describe the electrodeposition process. Let's consider now, the kinetics aspect of nucleation process and more precisely the description of the growth of nuclei. Usually, the formation of a new metallic phase by electrodeposition is studied by applying a constant potential (a constant η) and analyzing the current transient (chronoamperometry) without solution stirring. Under such conditions, the nuclei growth is limited by diffusion. A theoretical model, the Scharifker model [39], enables to simulate the evolution of the recorded current as

a function of time, a rapid description of this model is proposed below.

Just after the polarization of the electrodes (constant E applied) allowing the nucleation, metallic nuclei appears randomly on its surface, either following an instantaneous mode or a progressive mode [8]. The analysis here is restricted to the instantaneous mode. Then, immediately following t=0 s, N nuclei appear on the electrode surface.

The recorded electric current is proportional to the electroactive surface (the nuclei surfaces) and also, varies with time (no stirring of the solution). Thus two effects have to be considered:

- first, the growth of the nuclei induces an increase of the electroactive surface and consequently an increase of the current,
- then, the thickness of the diffusion layer increases with time inducing a decrease of the current for a long time (Cottrell effect)

The Sharifker model takes into account these two effects. The total current is assumed to follow the Cottrell equation:

$$I(t) = \frac{zF\sqrt{D}C^{\infty}}{\sqrt{\pi t}} \times S(t) \tag{1.23}$$

where $S(t)$ is the electroactive surface varying with time (growth of the nuclei).

Each nucleus is considered as an hemispherical particle surrounded by an hemispherical diffusion layer (see Figure 1.15) of which the external radius R(t) is given by:

$$R(t) = \sqrt{kDt} \tag{1.24}$$

where k is a parameter equal to $\sqrt{\frac{8\pi C^{\infty}M}{\rho}}$ [39]. The surface, S' crossed by the current streamlines to reach the surface of one nuclei is defined as:

$$S'(t) = \pi R(t)^2 = \pi kDt \tag{1.25}$$

[8] The instantaneous nucleation corresponds to the process where all the nuclei are formed simultaneously at the beginning of the chronoamperometric measurement while for the progressive mode, the nuclei are continuously formed during the crystal growth.

At short times, the electroactive surface S can be writtens $S = NS'(t) = N\pi kDt$. During their growth, the diffusion zones overlap, thus, S is no longer equal to $NS'(t)$. A relation (Avrami theorem [39]), allows the estimation of the actual surface, S, taking into account the overlap of the diffusion zones:

$$S(t) = S_0 \left(1 - exp\left(-\frac{N}{S_0}\pi kDt\right)\right), \tag{1.26}$$

where S_0 is the surface area of the electrode. Therefore, for instantaneous nucleation the transient current can be modeled with the following expression:

$$I(t) = \frac{zD\sqrt{D}C^{\infty}}{\sqrt{\pi t}} S_0 \left(1 - exp\left(-\frac{N}{S_0}\pi kDt\right)\right) \tag{1.27}$$

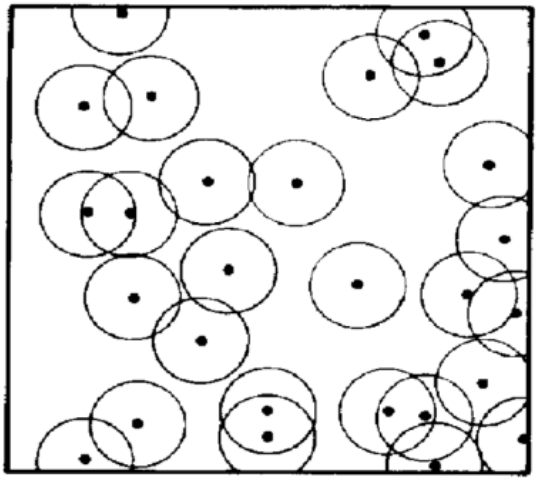

Figure 1.15: Representation of nuclei as hemispherical growing centers randomly distributed on the electrode and growing under spherical diffusion.

A typical potentiostatic transient, obtained experimentally, is shown in Figure 1.16 [38]. Three different sections, corresponding to the different stages of the nucleation process, can be observed in the current time curve:

- The first section (1), very short, corresponds to the double layer charging current (capacitive current).
- The rise in current (2) is observed due to the growth of each independent nucleus or due to an increase in the number of nuclei which induce an increase of the

electroactive surface. During this stage, the nuclei develop diffusion zones around themselves (3).

- The diffusion zones overlap, changing the hemispherical mass transfer to a linear mass transfer. Thus, the current decreases (4) and reaches the evolution described by a linear diffusion model (Cottrell).

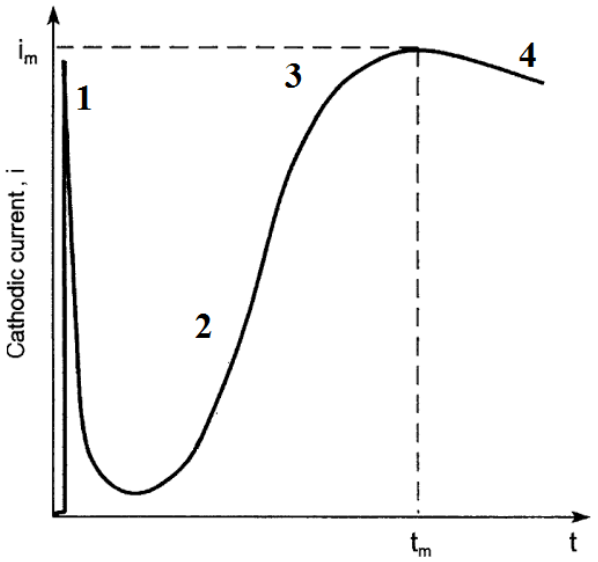

Figure 1.16: Temporal evolution of the cathodic current during nucleation under a constant applied potential [38]

Parameters influencing the electrodeposition

The control of the electrodeposition requires the optimization of many parameters having an influence on the deposit appearance and its morphology; their effects are developed in this section.

The first influencing parameter is the power (voltage or current) supplied to the cathode. Indeed, the overpotential (for a chronoamperometry) or the current (for a galvanostatic electrolysis) strongly influence the deposit growth and particularly the critical nucleus size (see Equation 1.19). Increasing the overpotential leads to a reduction in the critical nucleus size. Therefore a larger number of nuclei is created. Grujic et al. provide

in their study [40] AFM pictures of copper electrodeposited obtained at three different potentials and highlight that, the overpotential increase generates a higher population density and smaller nuclei (see Figure 1.17). A.M. Rachid et al. [41] also demonstrate that increasing the current density, during a galvanostatic electrolysis, leads to decrease the size of the nuclei. The first influencing parameter is the power (voltage or current) supplied to the cathode. Indeed, the overpotential (for a chronoamperometry) or the current (for a galvanostatic electrolysis) strongly influence the deposit growth and particularly the critical nucleus size (see Equation 1.19). Increasing the overpotential leads to a reduction in the critical nucleus size. Therefore a larger number of nuclei is created. Grujic et al. provide in their study [40] AFM pictures of copper electrodeposited obtained at three different potentials and highlight that, the overpotential increase generates a higher population density and smaller nuclei (see Figure 1.17). A.M. Rachid et al. [41] also demonstrate that increasing the current density, during a galvanostatic electrolysis, leads to decrease the size of the nuclei.

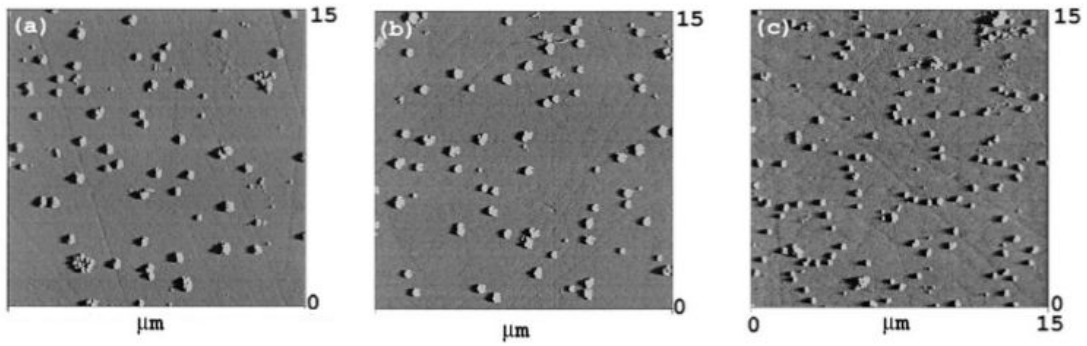

Figure 1.17: AFM pictures of copper nuclei for three different potential of electrodeposition: a) E = -300 mV, b) E = -400 mV, c) -500 mV, in a 0.01M $CuSO_4$ solution. [40]

Other factors related to the solution composition, like the metallic ions concentration, the pH and the electrolyte, also affect the number and size of the nuclei. Grujic et al. [40] study the copper nucleation, at three different concentrations of the copper precursor, and highlight that increasing the concentration generates an increase of the nuclei size and a decrease in the nuclei population density. For low concentrations, at the beginning of the electrodeposition, a low number of copper atoms are generated, and they are dispersed at the cathode surface. Then, increasing the electrolysis duration,

enables the copper atoms to group together to minimize the surface energy; due to the large distance to travel, they only group together with the nearest atoms. Thus a large number of small nuclei is formed. At high concentration, the close proximity between metallic atoms induces the formation of large nucleus. The electrolyte composition also affects the nuclei shape [42]. Finally, the decrease in the pH could cause the hydrogen production rate to increase and by the way impacts the iron nucleation. Grujic et al. [43] show that a narrow sizes distribution of the nuclei (ranging between 50-75 nm) is obtained for a pH of 2, due to the shielding of the electrode by hydrogen bubbles, while at pH=5, the nuclei size lies in the range 50-150 nm (see Figure 1.18 extracted from [43]).

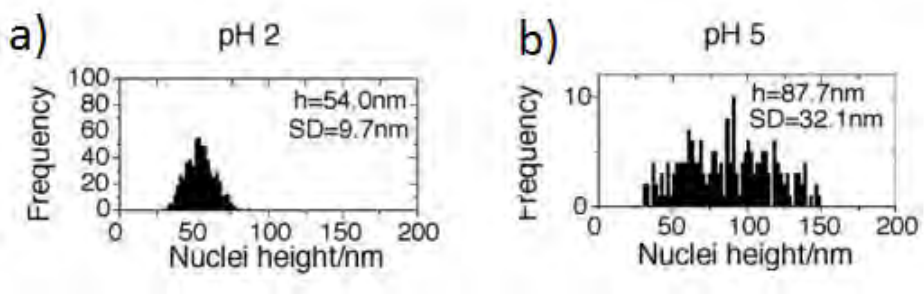

Figure 1.18: Size distribution of iron nuclei electrodeposited using a constant potential E=-1150 mV, in 0.1 M $FeSO_4$ a) pH=2, b) pH=5.

1.2.2 Electrodeposition in a thin layer cell

This section aims to present the Hele-Shaw cell and to explain the mechanisms leading to the electrodeposit growth as well as the morphology of the obtained deposits (metallic ramified branches).

The different stages of the deposit growth

The typical setup employed for an electrodeposition experiment in a Hele-Shaw cell, described in Fig. 1.19, is constituted by two electrodes, sandwiched by two glass slides, which determine the thickness of the electrolytic compartment. The electrolytic solution fills the gap left free between the two electrodes. Generally, no supporting electrolyte

is used contrary to the classical electrodeposition processes, and the solution is kept stagnant.

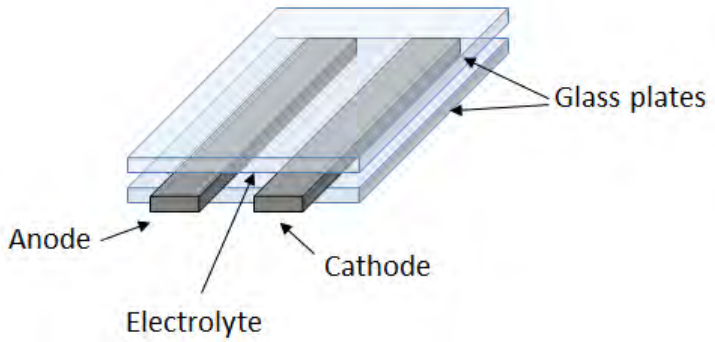

Figure 1.19: Picture of a Hele-Shaw cell

The applied current enables the reduction of the metallic ions at the cathode surface and subsequently to the formation of a ramified deposit, which grows across the thin layer cell. The obtained deposits are quasi 2D, and the glass walls enable to monitor the growth by direct visualization. The anode is made of the same metal than the deposit (sacrificial anode), to limit the formation of foreign species such as O_2 bubbles generated by H_2O oxidation. The electrodeposition process takes place in three steps: the depletion, the destabilization and the growth phase [44], and the evolution of the cell voltage, at constant applied current, enables to identify these different phases (a, b, c in Figure 1.20) [44].

- Depletion phase

When the current is applied to the Hele-Shaw cell, the metal ions concentration decreases at the cathode interface and simultaneously increases at the anode. During this depletion phase and until the cathodic interfacial concentration reaches zero, the voltage measured between the two electrodes stays almost constant, (see region a, Figure 1.20). Simultaneously, the induced concentration gradient generates density gradients, which may result in the formation of convective rolls. The use of very thin cell ($50\mu m$ thick) enables to avoid this effect. Thus, only diffusion and migration govern the cations mass transfer.

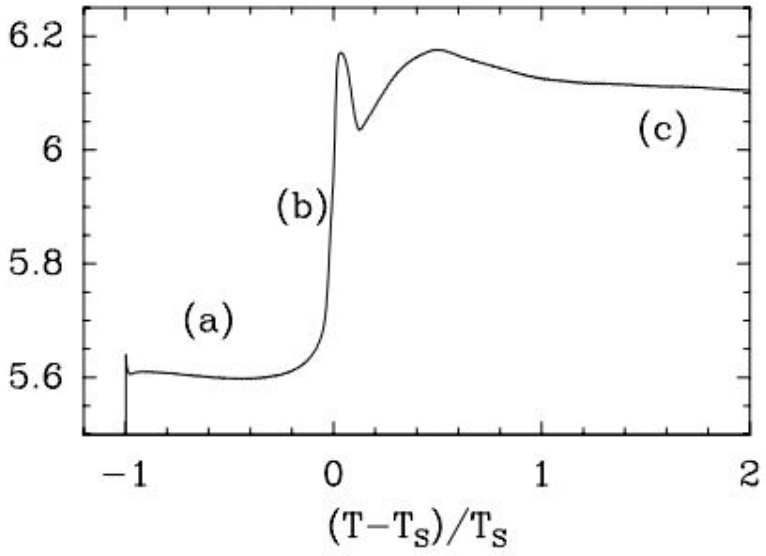

Figure 1.20: Dimensionless time dependance of the cell voltage during the deposit growth [44]

- Destabilization phase

After the cathodic depletion phase, the interfacial concentration of metallic ions tends toward zero and the voltage between the two electrodes increases (region b of the curve Figure 1.20). The time required to reach this phase is known as the Sand time. To ensure the current flow through the cell two options are possible:

1. The cathode interface becomes unstable, and a ramified and porous deposit starts growing through the cell. In fact, the deposit front has to advance across the cell to reach zones concentrated in metal ions.

2. A second electrochemical reduction occurs ($H^+ \rightarrow H_2$).

The bibliography suggests various explanations for the ramification of the cathode interface. The Chazalviel model [45] describes that the cathodic depletion leads to the disrupt of the electroneutrality (to avoid the divergence of the electric field), implying the formation of a "space-charge" depleted in anions along the cathode. The model predicts that the deposit will grow at the same velocity than the anions migration, to avoid

the growth of this space charge. Thus a highly porous deposit has to be formed. According to Sundström et al. [46], the cathode interface becomes unstable as soon as the current is applied and this does not depend on the interfacial concentration. They perform a linear stability analysis of the growing front, assuming the electroneutrality and taking into account the electrode kinetics. They show that the front is always unstable, but this destabilization increases rapidly when the concentration reaches zero. Finally, this diffusion model predicts the same grow velocity than the Chazalviel's model.

- Growth phase

After the ramification, the deposit grows and crosses the cell toward the anode inducing a linear decrease of the voltage because of the decrease of the electrolyte resistance (electrodes get closer) (see the phase c of Figure 1.20).

Morphology of the electrodeposits obtained in Hele-Shaw cell

The obtained ramified deposit exhibits different kind of morphologies, depending on the applied current and on the metallic ion concentration. Many of these morphologies (see Figure 1.21) have been described by Grier et al. [47] [48] and Sawada et al. [49]. These morphologies fall into three classes:

- the branched and disorderly fractal morphology (DLA),
- the dense branching morphology (DBM),
- the ordered dendritic morphology.

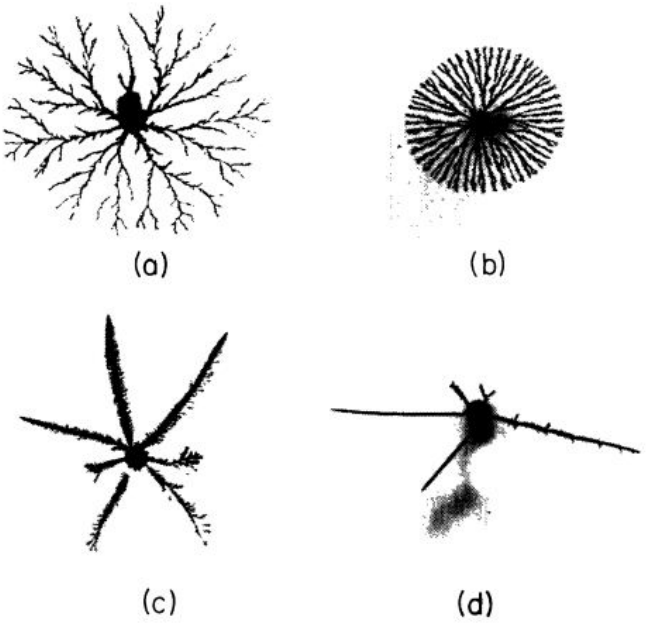

Figure 1.21: Various morphologies obtained in thin layer cell (extracted from [47]): a) DLA, b) Radial dense branching (DBM), c) dendritic, d) needle crystal in the extreme dendritic limit

The branched and fractal deposits are commonly known as DLA-like deposits, due to their similarity with aggregates obtained numerically by the diffusion limited aggregation model [50].

The principle of the DLA model can be described as follows:

- a first particle is generated and acts as a seed for the growth of the aggregate,
- a second particles is generated far away from the seed particle (from a distance Ld [9]) and walks randomly (by Brownian motion),
- when this random walker reaches one of the lattice sites adjacent to the seed particle it stops.

After a succession of 10^5 iterations of this process, a DLA aggregate is obtained (see Figure 1.22). This model corresponds to the limiting case of 1) a purely limited growth,

[9] Ld is the diffusion length defined as the ratio between the diffusion coefficient and v_g the deposit growth velocity

and 2) an extremely slow growth: $v_g \to 0$ and hence $Ld \to \infty$. This morphology has been obtained experimentally using the electrodeposition of Zn [51].

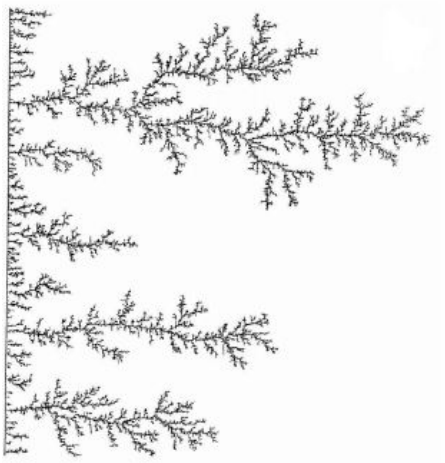

Figure 1.22: Picture extracted from [44] of a DLA aggregate obtained in linear geometry by numeric DLA model.

The DBM-like consists of a large number of thin branches which fill space uniformly in the thin cell. Another particularity of this type of morphology is that when they grow, the fine branches of the deposit advance within a smooth, stable envelope [48] [49]. The deposit forms a flat (or circular for radial deposits) front, advancing at a constant velocity [44] (see Figure 1.21, b).

According to Grier et al. [47], the deposit morphology can vary from a fractal to a DBM growth by varying the applied potential (or current) and the precursor concentration (Figure 1.23). It is generally recognized that the deposits have a DLA morphology for low growth velocity and a dense branching morphology for high growth velocity [44] [47] [52]. Some authors suggest that this transition is induced by phenomena of electroconvection [53] [54].

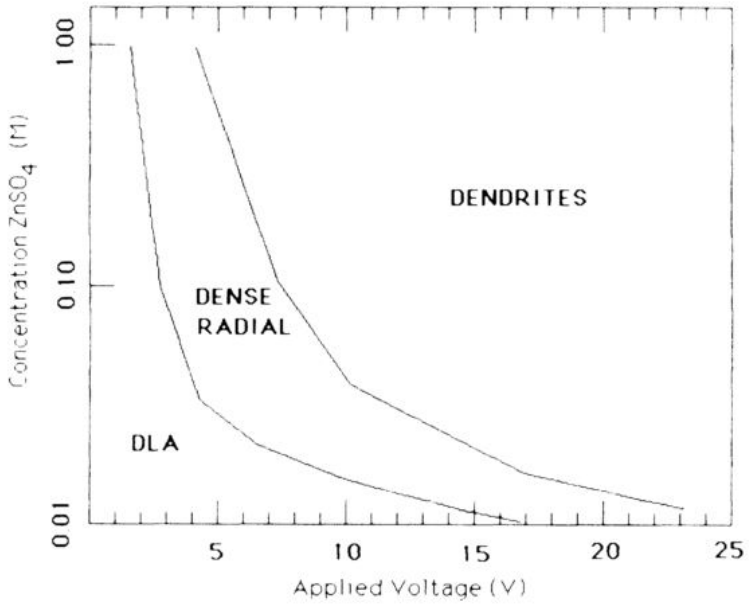

Figure 1.23: Predominance chart (extracted from [48]) of the different morphology classes as a function of the voltage and the concentration of the precursor.

Fleury et al. have observed the presence of electroconvection vortices at the tip of the iron branches [53]. They suggest that, at low growth velocity, these electroconvective vortices induce the splitting of the tip (see Figure 1.24), causing the ramification of the deposit. At high growth velocity, the magnitude of the vortices increases and thus the nip of the funnel becomes thinner. Therefore, the splitting of the branches is limited by the thinning of the nip. Indeed, when a splitting of a branch occurs, the two tips formed at the top of the branch cannot be feed equally by the fluid flow. One of the branches remains in the concentrated zone and continues to grow, while the second one is pushed in the depleted zone and stop growing. Therefore, the electroconvective vortices induce the ramifaction of the branches at low current densities, favoring the DLA morphology, whereas at high current densities, the increase of the electroconvection effects hinders the branching and leads to a DBM-like deposit.

Conversely, Wang et al. [54] claim that the DBM-like deposit is obtained in the absence of electroconvection.

To get a better understanding of the transition between the DLA and DBM deposits,

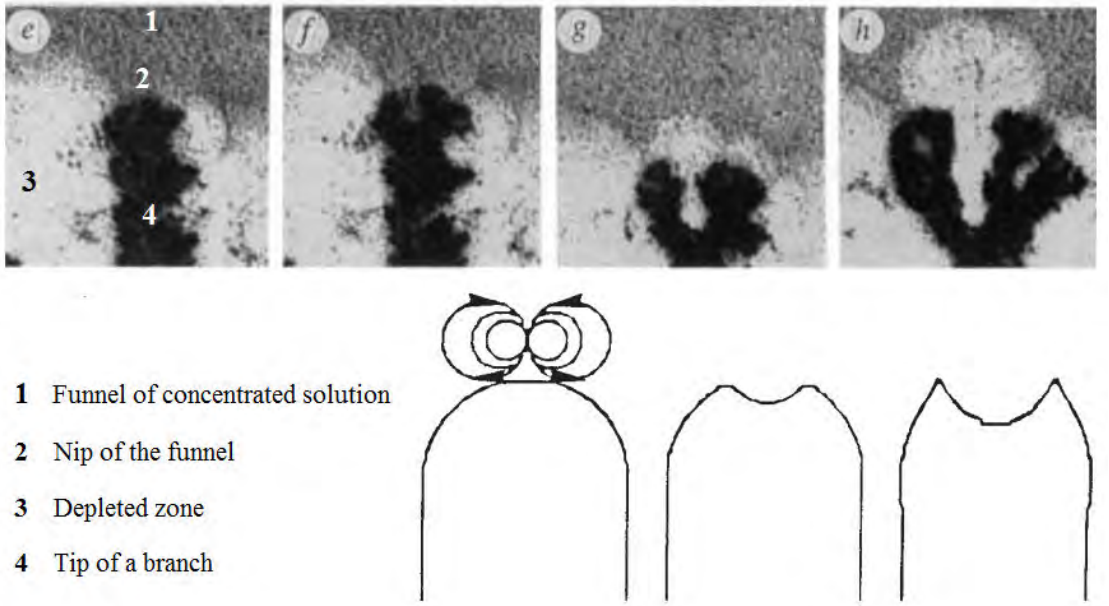

Figure 1.24: Pictures and schematic representation of the splitting of a branch induced by the electroconvective vortices.

several authors propose variants of the DLA model, that would lead to a DBM deposit. The variant proposed by Smith et al. [55] and Brower et al. [56] is described as a Finite Diffusion Length model (FDL), beginning as the DLA model described previously, and assuming that the random walkers are released at a finite distance Ld of the aggregate. Smith et al. [55] apply this modified DLA model for a planar geometry instead of a radial geometry, which means that the planar surface acts as the substrate for the aggregates growth, instead of a seed particles as it was said previously. Smith et al. [55] showed that by decreasing the diffusion length Ld, the deposit becomes denser and loses its fractal property. Furthermore, the obtained deposits are similar to a DBM deposit obtained experimentally. To conclude, the transition from DLA to DBM could also be explained considering only a finite value of Ld.

Finally, the dendritic morphology is described as having a needlelike crystal shape [47] or snowflakes [48] when the growth is radial (see Figure 1.25). The main difference between the dendritic morphology and the DLA and DBM-like deposit is that the deposit shows preferred axes of growth whose orientation is determined by crystalline

anisotropy [49]. This morphology is generally observed at high overvoltages/current and high concentrations (see Figure 1.23).

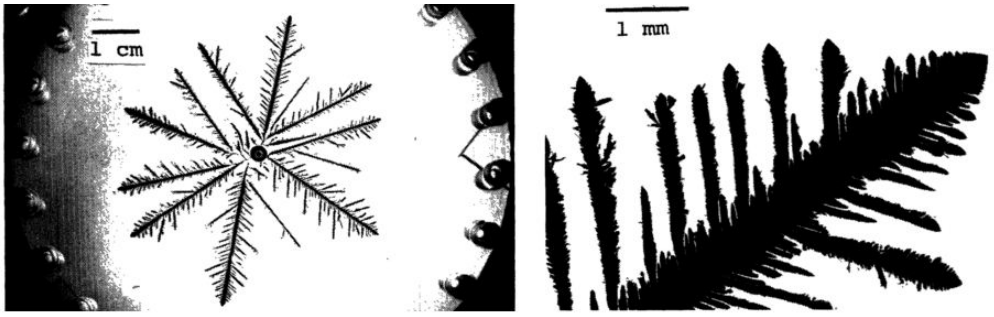

Figure 1.25: Picture (extracted from [49]) of a zinc dendritic deposit obtained with a 0.03M $ZnSO_4$ and ΔV = 6V.

Contrary to most of the studies, which present a large-scale approach to understand the deposit growth in a thin layer, Fleury [57] puts the emphasis on the nucleation and the deposit growth on a microscopic scale. Thus, he tries to correlate the deposit growth velocity with the internal structure of the metal deposits. To this end, he first highlights, in [57], the granular texture of the electrodeposits by presenting copper deposit (see Figure 1.26) which consists of small grains between 10 and 1000 nm. He proposes then, an oscillatory model for the nucleation based on Chazalviel's theory. As explained above, according to Chazalviel, when a constant current flow through the cell, the metal ion concentration decreases along the cathode surface and goes to zero, which induces high local field. Fleury assumes that a critical surface field E* is necessary to generate the formation of a new grain. Furthermore, under constant current, the grain grows at a constant rate, which means that its diameter increases with time as $t^{1/3}$: the radial growth speed of the grain decreases as its surface increases[10]. When the growth speed of the grain becomes slower than the migration velocity of the anion, a space charge region is formed in the vicinity of the grain surface and thus, the potential rises (in absolute value). When the critical surface field is reached, a new grain is created and grows with a velocity higher than the migration velocity of the anion. Thus, the growing grain invades the space charge region, which inhibits new nucleation events.

[10]For simplicity, in a first approximation, the grains are assumed to be spherical.

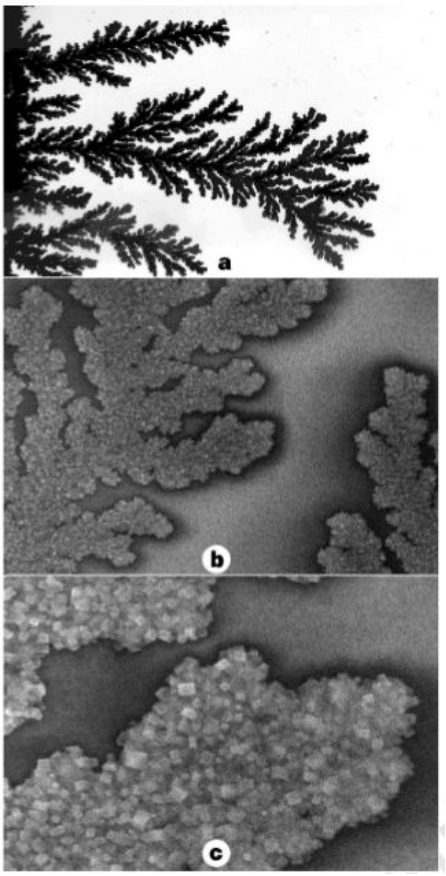

Figure 1.26: Internal grain structure of a DLA-like copper deposit. Magnifications a) $\times$ 45, b) $\times$ 1780, c) $\times$ 7580 [57]

This oscillatory model is based on the competition between the nucleus growth speed and the migration velocity of the anions, both depending on the current applied to the system. According to Fleury, the grain appears smaller for high current density (high growth speed). Therefore, this model enables to explain the branch microstructure currently observed, but also highlights that the small-scale structure is also affected by the local deposit growth speed.

Growth speed for a DBM deposit

As it was described previously, the dense branching aggregate consists of a densely ramified deposit, which fills the cell uniformly. All branches are growing at the same

speed and thus, the DBM-like deposit is bounded by a flat front which crosses the cell with a constant rate. The model proposed by Léger et al. [44] to describe this stationary growth is presented below, and corresponds to the use of a binary electrolyte[11] (without supporting electrolyte). υ_+ and υ_- are the stoichiometric coefficients of the salt used; the salt concentration is:

$$C = \frac{C_+}{\upsilon_+} = \frac{C_-}{\upsilon_-} \tag{1.28}$$

C_+ and C_- being the concentrations of cations and anions respectively.

As mentioned above, diffusion and migration control the mass transfer in a Hele-Shaw cell (thickness < 50 μm), therefore, the mass conservation equation for the cation and the anion can be written as follows (assuming diluted solutions):

$$\frac{\partial C_+}{\partial t} = z_+ u_+ F \vec{\nabla} \cdot (C_+ \vec{\nabla} \Phi) + D_+ \Delta C_+ \tag{1.29}$$

$$\frac{\partial C_-}{\partial t} = z_- u_- F \vec{\nabla} \cdot (C_- \vec{\nabla} \Phi) + D_- \Delta C_- \tag{1.30}$$

where z_+, z_- are the charge numbers (valence) of the cations and anions respectively, u_+ and u_- their mobilities[12] ($\frac{cm^2.mol}{J.s}$), D_+ and D_- their molecular diffusion coefficients, and Φ represents the electrical potential (V).

Assuming the electroneutrality in the whole cell:

$$z_+ C_+ = -z_- C_- \tag{1.31}$$

C_+ and C_- can be replaced by C in Equation 1.29:

$$\frac{\partial C}{\partial t} = z_+ u_+ F \vec{\nabla} \cdot (C \vec{\nabla} \Phi) + D_+ \Delta C \tag{1.32}$$

$$\frac{\partial C}{\partial t} = z_- u_- F \vec{\nabla} \cdot (C \vec{\nabla} \Phi) + D_- \Delta C \tag{1.33}$$

The subtraction of Equations 1.32 and 1.33 enables to deduce the relationship be-

[11] A binary electrolyte is an electrolyte that contains only one solvent and one salt.

[12] The mobility u_i of the ion i is related to its diffusion coefficient by the Nernst-Einstein equation $u_i = \frac{D_i}{RT}$.

tween ΔC and $\vec{\nabla}\cdot(C\,\vec{\nabla}\,\Phi)$:

$$F\,\vec{\nabla}\cdot(C\,\vec{\nabla}\,\Phi) = -\frac{(D_+ - D_-)\Delta C}{z_+u_+ - z_-u_-} \tag{1.34}$$

By combining Equation 1.34 and 1.32, $\vec{\nabla}\,\Phi$ can be eliminated:

$$\frac{\partial C}{\partial t} = \frac{z_+u_+D_- - z_+u_+D_+}{z_+u_+ - z_-u_-}\Delta C + D_+\Delta C \tag{1.35}$$

Therefore it can be concluded that:

$$\frac{\partial C}{\partial t} = \bar{D}\Delta C \tag{1.36}$$

$\bar{D}$ is the apparent diffusion coefficient of the binary electrolyte; it represents a compromise between the molecular diffusion coefficients of the anion and the cation [58] and is expressed as follows:

$$\bar{D} = \frac{z_+u_+D_- - z_-u_-D_+}{z_+u_+ - z_-u_-} \tag{1.37}$$

Equation 1.36 shows that the mass transfer problem in the electrolyte solution could be simplified as a diffusion problem.

As already said above, for a DBM deposit, the growth front is flat and move forward at a constant velocity, v_g (for galvanostatic conditions). Then, as represented in Figure 1.27, the 2D transfer problem could be reduced to a 1D transfer problem.

$$\frac{\partial C}{\partial t} = \bar{D}\frac{\partial^2 C}{\partial x^2} \quad for \;\; x \geq x_f(t) \tag{1.38}$$

Using the coordinate system relative to the growth front $x' = x - x_f(t)$ (the concentration corresponding to this system can be written $C'(x') = C(x,t)$) and using the fact that $v_g = \frac{dx_f}{dt}$ is constant, leads to:

$$\frac{\partial C}{\partial t} = \frac{\partial C'(x'(x,t))}{\partial t} = \frac{dC'}{dx'} \times (-v_g). \tag{1.39}$$

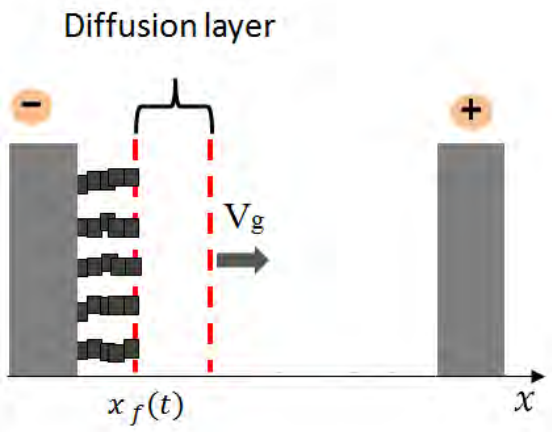

Figure 1.27: Schematic representation of a DBM deposit growth

Using this last result in Equation 1.38 leads to a 1D advection diffusion equation:

$$-v_g \frac{dC'}{dx'} = \bar{D} \frac{d^2C'}{dx'^2}, \quad for \;\; x' \geq 0 \tag{1.40}$$

which could be easily solved using the following boundary conditions:

$$C'(x' = 0) = C_0 \tag{1.41}$$

$$C'(x' \to \infty) = C^{\infty}. \tag{1.42}$$

The concentration profile is given by:

$$\frac{C'(x') - C_0}{C^{\infty} - C_0} = 1 - exp\left(-\frac{x'}{Ld}\right) \tag{1.43}$$

where, as said previously $Ld = \frac{\bar{D}}{v_g}$.

This expression can be written in terms of C(x,t):

$$\frac{C(x,t) - C_0}{C^{\infty} - C_0} = 1 - exp\left(\frac{x_f - x}{Ld}\right). \tag{1.44}$$

At the front location, the flux of anions is equal to 0:

$$-z_- u_- F \upsilon_- C \left.\frac{\partial \Phi}{\partial x}\right|_{x_f} - D_- \upsilon_- \left.\frac{\partial C}{\partial x}\right|_{x_f} = 0, \tag{1.45}$$

whereas the flux of cations depends on the applied current density i (i=I/S):

$$-z_+ u_+ F \upsilon_+ C \left.\frac{\partial \Phi}{\partial x}\right|_{x_f} - D_+ \upsilon_+ \left.\frac{\partial C}{\partial x}\right|_{x_f} = \frac{i}{z_+ F}. \tag{1.46}$$

Combining these two equations leads to:

$$\frac{i}{z_+ \upsilon_+ F} = -\frac{D}{1-t_+} \left.\frac{\partial C}{\partial x}\right|_{x_f} \tag{1.47}$$

where $\left.\frac{\partial C}{\partial x}\right|_{x_f} = \frac{C^\infty}{Ld}$ (from Equation 1.44) and t_+ is the transference number of the cation obtained for a binary electrolyte:

$$t_+ = \frac{z_+ u_+}{z_+ u_+ - z_- u_-} \tag{1.48}$$

Using Equation 1.43 (concentration profile), the concentration gradient at the front location $\left.\frac{\partial C}{\partial x'}\right|_0 = \frac{C^\infty - C^0}{Ld}$ and setting $C_0 = 0$, the following expression is obtained for v_g:

$$v_g = -i \frac{1-t_+}{\upsilon_+ F z_+ C^\infty} \tag{1.49}$$

This equation enabling to predict the growth speed of a DBM deposit has been verified experimentally in various studies [59] [60].

1.3 Dispersion of the iron electrodeposit by acoustic waves

This section expects to study the phenomena generated by the acoustic waves propagation in an aqueous solution enabling the deposits removal or fragmentation.

1.3.1 Physical aspects of phenomena induced by the ultrasounds propagation

Ultrasounds refer to sound waves transmitted at a frequency greater than the limit of human hearing, typically, higherthan 20 kHz. The propagation of ultrasounds in aqueous media generates various effects, the two prominent ones are the acoustic streaming and the cavitation.

Acoustic cavitation

The acoustic cavitation is defined as the growth and collapse of bubble nuclei, under the action of an ultrasonic field passing through a liquid media. The growth of a bubble nuclei starts if the pressure, applied by the acoustic field, is lower than the critical tensile strength [13], which depends on the liquid and on the concentration of dissolved gas [61]. The origin of the bubbles nuclei is still not well understood (microbubbles trapped into the defects of the solid surfaces, microbubbles population stabilized by traces of organics adsorbed on the liquid/gas interface) [61].

During ultrasonication, the sound waves pass through the liquid and induce a succession of compression and rarefaction cycles. When a microbubble is submitted to a rarefaction phase, in comparison with the average hydrostatic pressure, its volume increases, leading to the creation of cavities which are bubbles containing a small quantity of gas or solvent vapor [62]. Bubble volume decreases during the compression phase and increases during the rarefaction (see Figure 1.28). However, during the successive cycles (compression/rarefaction) the bubble volume increases due to a phenomenon known as rectified diffusion[14] [62] [28] [61]. Then, the growing bubble can reach a critical size (resonance size) leading to its collapse.

[13] The critical tensile strength corresponds to the pressure required to apply to rupture the liquid either by the growth of a vapor bubble (if no dissolved gas is present) or by the growth of bubble consisting of vapor and gas being initially dissolved in the liquid.

[14] This is because the gas diffusion across the bubble wall depends on the bubble surface. During the compression phase, the gas pressure in the bubble is high, and gas diffuse from the bubble surface to the liquid. During the rarefaction phase, the pressure in the bubble is low, and the gas dissolved in the liquid diffuse inside the bubble. The bubble surface being lower during the compression phase than during the rarefaction phase; this means that the gas transfer does not balance during both phases.

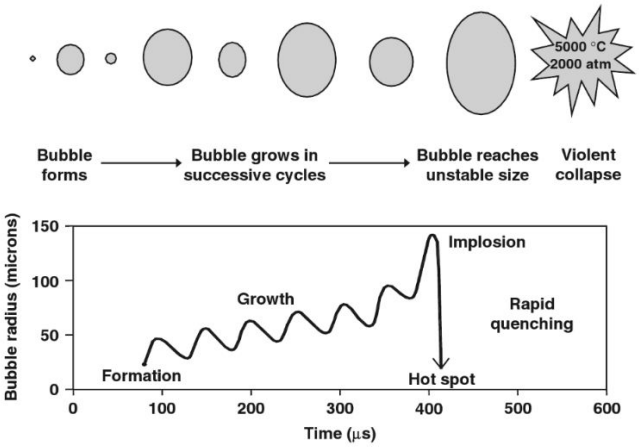

Figure 1.28: Compression and rarefaction phases of a liquid submitted to ultrasounds, leading to the bubble collapse [63]

Several effects are generated by acoustic cavitation like turbulence, microjet, shock waves or microstreaming [64]. The collapse of cavitation bubbles releases enough energy to enable the removal of particles from the substrate provided that cavitation takes place in the vicinity of the electrode.

Acoustic streaming

In addition to the effects generated by acoustic cavitation, the propagation of ultrasound through a liquid induces a steady flow in the fluid due to the absorption of the ultrasonic field [64]. This phenomenon is known as acoustic streaming and is responsible of the enhancement of the mass transfer. The acoustic streaming velocity increases by increasing the frequency and the power of ultrasound, and decreases by increasing the kinematic viscosity.

These different effects of ultrasonic propagation (turbulence, microjet, shock waves, and acoustic streaming) lead to an increase of the mass transfer to the electrode. The mass transfer enhancement induced by acoustic streaming is weak, in comparison with other effects, but this increase occurs even if there is no cavitation in the vicinity of the electrode surface [64]. Conversely, turbulence, microjets, and shock waves, resulting from cavitation, induce more violent fluid motions. The most efficient action to remove a particle from a surface is the microjet which appears when cavitation occurs nearby

the surface [64] (see Figure 1.29). Indeed, when a bubble collapse in the vicinity of a surface, the compression is not symmetric, the bubble deforms, and the collapse of the bubble leads to a violent microjet of liquid projected at high speed onto the surface. This microjet can reach the surface with a velocity of 200 m/s, enabling the removal of electrodeposited particles [64] [65].

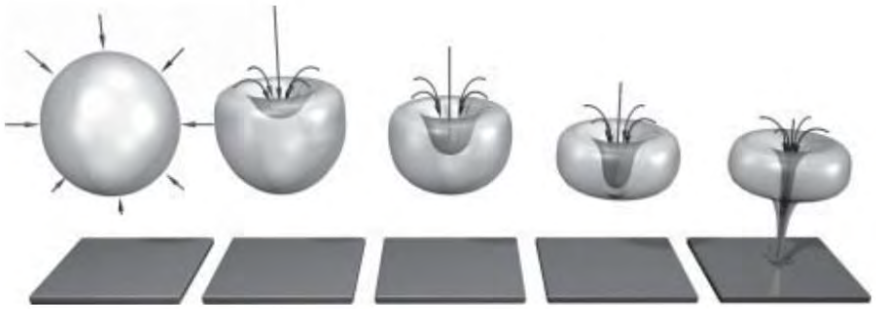

Figure 1.29: Schematic representation extracted from [66] of a microjet formation by cavitation bubble collapse.

1.3.2 Influence of ultrasounds on the electrochemical process

Let's focus now on the two major effects of ultrasound on the electrodeposition process, which are the enhancement of mass transfer and the removal of electrodeposited particles.

Mass transfer enhancement

To highlight the enhancement of mass transfer induced by ultrasonication, J. Klima [64] applied ultrasounds during voltammetrics measurement and compare the obtained voltammograms with the one performed by steady-state voltammetry with a rotating disk electrode (RDE) (technique presented in Section 1.2.1).

The author compares the voltammograms of methyl viologen ($C_{14}H_{14}Cl_2N_2$) reduction (see Figure 1.30) obtained on a platinum RDE (80 RPS) without ultrasound b), with the one obtained on a platinum foil with ultrasounds a). Both voltammograms present two waves exhibiting limit currents characteristic of mass transfer limited process. The limiting current measured for both waves (see Figure 1.12 Section 1.2.1) is about three

times higher with ultrasonication than the one obtained with an RDE at 80 RPS (under silent conditions). As explained in Section 1.2.1, the limiting current is inversely proportional to the diffusion layer thickness δ (see Equation 1.16). Therefore, the enhancement of the mass transfer induced by ultrasonication leads to a decrease of δ and thus, to the increase of the limiting current. For the case presented in [64], it means that the diffusion layer is three times thinner with ultrasonication than without using a RDE angular velocity of 80 RPS.

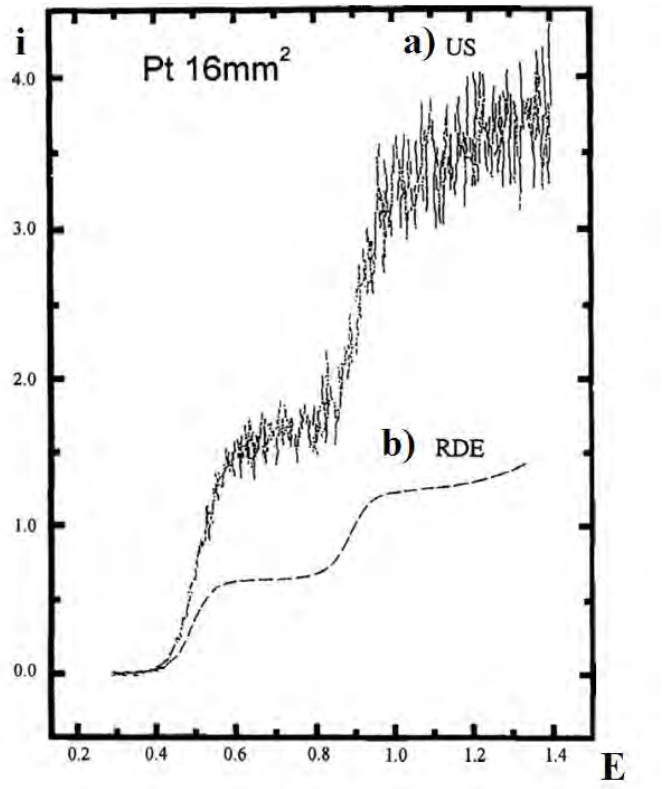

Figure 1.30: Voltammograms (adapted from [64]) of 0.5 mM methylviologen in acetonitrile with: a) a platinum foil electrode under ultrasonication, b) a platinum RDE at 80 RPS with no ultrasound. Scan rate = 0.1 V/s

Particle removal

The second effect of ultrasound is the removal of particles from a surface. The objective of this section is to give a better understanding of the electrodeposited particles removal mechanisms, to identify the parameters affecting their dispersion from an elec-

trode submitted to ultrasonication. The most efficient effect of ultrasound for particles removal is known to be the action of microjet, induced by the collapse of cavitation bubbles. Indeed, as mentioned before, the fluid velocity reached in a microjet, can be estimated to be about 200 m/s [64] [65]. According to Gale [67] the acoustic streaming does not have a direct effect on particle detachment but enables to take away the detached particles from the surface. To give a most detailed analysis of the removal mechanism, it is necessary to identify the forces acting on the particles subjected to a fluid flow (see Figure 3.13); first, the focus is put on the particle adhesion force to the surface.

The adhesion force of a spherical particle on a surface T could be estimated considering Van der Waals attraction [65] [68]; in the case of a spherical particle adhering on a smooth surface this adhesion force F_A can be expressed as follows [69]:

$$F_A = \frac{A_{part/T/L} R_p}{6.d_0^2} \tag{1.50}$$

where: $A_{part/T/L}$, is the Hamaker constant for the particle/surface system in a liquid L; R_p the radius of the particle, and d_0 is the separation distance between the particle and the substrate.

On another hand, the forces acting for the particles removal are [65]:

- the shear force (N/m^2) $\sigma = \mu dv/dy$, μ is the dynamic viscosity, v is the fluid velocity and y, the coordinate perpendicular to the surface T,
- the lift force $F_L = 6.46 R_p^2 v(\eta \rho dv/dy)^{1/2}$ where R_p is the particle radius, and ρ is the liquid specific gravity,
- the drag force $F_D = 6\pi\eta R_p v$.

Maisonhaute et al. [65] admit that for small particles, the shear force causes the stronger force. Therefore, the removal of the particles from the surface is controlled by the ratio χ, between the shear force and the adhesion force:

$$\chi = \frac{\mu(dv/dy)R_p^2}{\frac{A_{part/T/L}R_p}{6d_0^2}} = \frac{6d_0^2\mu(dv/dy)R_p}{A_{part/T/L}} \tag{1.51}$$

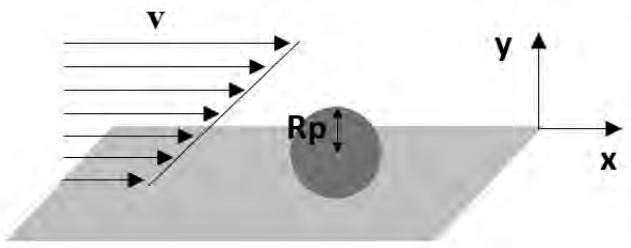

Figure 1.31: Spherical particle adhering on a smooth surface and subjected to a shear flow

Considering the work of adhesion between two flat solids interacting across a liquid layer, $W = \frac{A}{12\pi {d_0}^2}$ J/m^2, the last equation could be rewritten:

$$\chi = \frac{1}{2\pi} \frac{\mu \frac{dv}{dy} R_p}{W} \tag{1.52}$$

Increasing this removal coefficient χ, enables an easier removal of the particle from the surface. The expression of χ allows the identification of important parameters for the particles removal:

- the work of adhesion of the particle material on the electrode material, which depends on both materials,
- the shear stress close to the electrode surface $\mu \frac{dv}{dy}$ which depends on the hydrodynamics ,
- the size of the particle; for small particles the shear stress needed to remove them has to be increased.

1.3.3 Electrodeposit fragmentation in a Hele-Shaw cell

In the previous paragraph, dealing with the effects induced by ultrasonication, it has been seen that the dispersion process is mainly induced by bubble cavitation inside the cell volume. In a Hele-Shaw cell, the characteristic dimensions are so small that it is difficult to reach the cavitation threshold. Indeed, cavitation (and also acoustic streaming) appears with the propagation of the acoustic wave in the liquid. The wave propagates if the wavelength, λ, is lower than the dimensions of the system. Furthermore, cavitation

appears using "Power ultrasounds" which the frequency f, is around 20 kHz; the corresponding wavelength in water ($c = 1497$ m/s), $\lambda = c/f$, is around 7.5 cm. This quite high length is generally higher than the typical sizes of a Hele-Shaw cell, length ≈ 5 cm, width ≈ 1 cm, and depth ≈ 50 μm (as the sizes of the Hele-Shaw cell used in this work). Therefore, no cavitation is expected to appear in a Hele-Shaw cell subjected to a "Power ultrasounds" signal.

To overcome this situation, several authors have integrated bubbles in microfluidics devices to exploit their oscillations when they are subjected to an acoustic signal; that is why several studies propose to use the bubble based acoustic streaming [70] [71] [72]. The principle of this technique is to use an air bubble as acoustic actuator inside the microdevice. Indeed, when a bubble is subjected to an acoustic field, its surface acts as a vibrating interface which induces an acoustic streaming in the vicinity of the particle [72].

The typical set-up, for bubble based acoustic streaming in microfluidic device, consists of connecting a PZT diaphragm to a mixing chamber filled with two liquids, usually deionized water and fluorescent dye water, inside which a bubble or several bubbles have been trapped. Bibliography reports several configurations of this device which differ from each other by 1) the method involved to trap the bubble, 2) the PZT position and 3) the mixing chamber configuration. A short description of these devices is proposed below.

Ahmed et al. [71] use a classical Y-microchannel cell to introduce the two liquids in a side-by-side laminar flow. To trap a bubble, a "horse-shoe" shaped microstructure is created inside the microchannel (Figure 1.32). The aperture of the "horseshoe" is oriented backward the liquids flow, so as when the liquids filled the microchannel, a bubble is formed inside the horseshoe due to surface tension. In this configuration, the PZT is bonded adjacent to the microfluidic device on the same plastic plate and activated at a frequency of 70 kHz and a voltage of 8 Vpp.

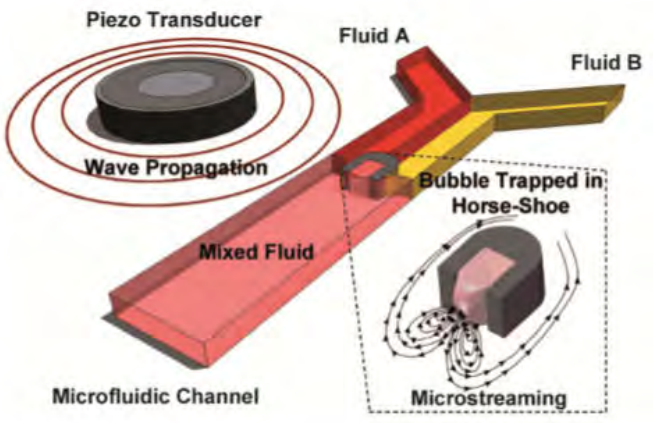

Figure 1.32: Microfluidic device (one channel), using the oscillations of a bubble trapped inside the horse-shoe structure [71].

Another example of micromixer, proposed by Liu et al. [72] consists of a circular chamber (Figure 1.33); the half of this chamber is filled with DI water, and the rest with red dye water. The chamber is made of polycarbonate plate which presents cavities on its surface to create air pockets. Thus, the number and the size of the bubble trapped in the mixing chamber can be adjusted. The PZT diaphragm is positioned under the circular chamber and employed at a frequency of 2kHz with a voltage of 5Vpp.

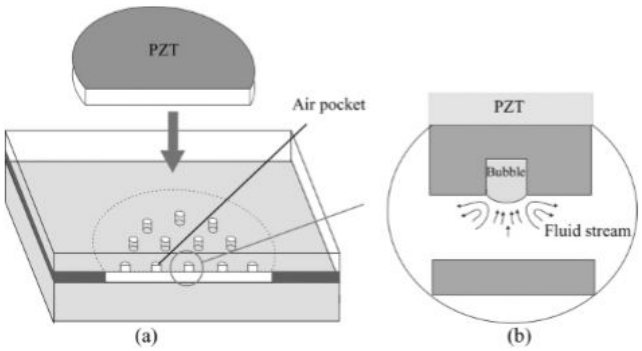

Figure 1.33: Microfluidic channel device and bubble trapped inside cavities [72]

Wang et al. [70] propose a more complex experimental set-up: a circular mixing chamber is connected to an exponentially expanded nozzle. A Y-Channel is used to introduce into the mixing chamber DI water, and fluorescent dye water, in a side-by-side laminar flow. The PZT is located under the mixing chamber and employed for a

range of frequency from 0.5 to 10 kHz with a voltage of 5 Vpp. The particularity of this device is that no bubble is trapped in the micromixer before the chamber is filled. The bubble is generated inside the chamber by "cavitation" for frequencies ranging from 1 to 5kHz. The authors suppose that cavitation threshold can be reached , due to the specific shape of the microchamber which present a decreasing cross section of the channel; the high liquid velocity obtained would lead to a very large pressure drop allowing to locally reach the critical tensile strength.

Even if some differences are noted between these experimentals set-up, the observations resulting from the experiments are quite similar: all authors agree on the need to have a bubble in the microchamber to induce a significant mixing enhancement. Wang et al. [70] observe that for frequencies lower than 1 kHz, no bubble is generated and thus no mixing enhancement is observed. This confirms that, in the absence of a bubble, the acoustic wavelength is too small for the acoustic field to contribute to the mixing.

All these studies agree with the fact that when the PZT is activated, the bubble strongly interacts with the acoustic field and generates churning motions which allow efficient mixing enhancement. Wang et al. [70] calculate the mixing efficiency based on the fluorescence intensity of a mixture of two liquids, and observe a mixing efficiency as high as 90% for a frequency of 1.5 kHz. Ahmed et al. also obtain an efficient mixing of the two liquids and evaluate the time required for a complete mixing at approximately 7 ms. The different studies also highlight the importance of the frequency of the acoustic field. Indeed, the acoustic streaming of the bubble is most efficient when the bubble is excited at its resonance frequency which is proportional to $1/R_0$ (R_0 being the bubble radius). Liu et al. [72] also investigated the effect of other acoustic parameters on the mixing and highlight, on the one hand, that a square sound wave provides faster mixing than a sinusoidal acoustic wave, and on the other hand, they also proved that increasing the voltage amplitude leads to decrease the mixing time. Thus, with a 10 Vpp and 5 kHz square acoustic wave, a complete mixing was obtained after 35 s instead of 1.75 minutes for a 5 Vpp and 5 kHz sinusoidal acoustic wave.

According to these studies, the acoustic streaming pattern generated by the excited bubble presents recirculation flow pattern, like rotating vortices (see Figure 1.34) ; Liu et al. [72] describe this streaming motion as a "tornado" pattern. The shear stress, in-

duced by this acoustic streaming, can be considered as a promising way to fragment iron dendrites produced during the electrodeposition step.

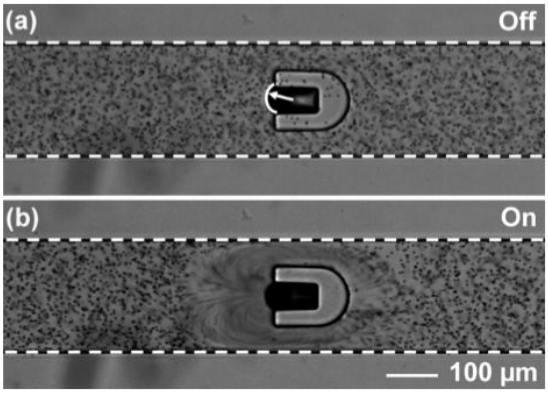

Figure 1.34: Acoustic streaming flow pattern [71]

Therefore, the last objectives of this thesis (Chapter IV) will be first to achieve a ramified iron deposit growth inside a Hele-Shaw cell and, in a second time, to optimize the acoustic field parameters, in order to introduce strong enough shear stress to break the ramified deposit into fine iron particles.

1.4 Conclusion

This chapter presents, in a first instance, the interest of the zero valent iron nanoparticles by a presentation of the most interesting nZVI properties and their main applications:

- environmental remediation
- medical field

Then, the different synthesis routes are presented, and the focus is put on the sonoelectrochemical synthesis which, in comparison with others techniques, present the advantages of requiring basic equipment, cheap reagents, and consists of a fast economic and safe synthesis route. Indeed, it only requires an iron salt solution, conductive substrates, a power supply and an ultrasonic device to disperse the electrodeposit.

The sonoelectrochemical synthesis of nZVI couples two different processes detailed in this chapter: the electrochemical formation of iron deposits and the deposit dispersion by ultrasonication. Even if the sonoelectrosynthesis has been increasingly investigated during the last decades, the understanding of both the metal electrodeposit growth and the mechanism of electrodeposit dispersion, as well as how these two steps are combined appears not so clear yet. Also, even if the bibliography proposes various studies of the sonoelectrochemical synthesis to optimize the influencing parameters, few considerations have been given to the influence of the substrate on the sonoelectrochemical process. It has been shown in this chapter that the substrate can play a role in both the deposit nucleation (Section 1.2.1) and the deposit removal processes, through its surface energy (Equation 1.19) and its influence on the deposit adhesion (Section 1.3.2).

Therefore, one of the objectives of this study is to provide a better understanding of the sonoelectrochemical process by:

- studying the simultaneous coupling of the electrochemical process with the ultrasonication for different iron salt solutions and substrates,
- investigating the influence of the electrodeposited particles size on the efficiency of the dispersion process,
- analyzing the influence of the electrodeposited particles adhesion on the dispersion efficiency, via the investigation of the role of the electrode material.

A new approach for the nZVI synthesis is also investigated, it consists of exploring the possibility of exploiting the microstructure of ramified branches by their fragmentation in a Hele-Shaw cell. This acoustofluidic synthesis constitutes a new approach for the synthesis of nZVI, and to the best of our knowledge, no similar study has been proposed. Therefore, to carry out the electrodeposit fragmentation in a Hele-Shaw cell, this study is based on the state of the art of microdevices used for mixing enhancement (Section 1.3.3).

2 Study of iron electrodeposition process and influence of the substrate

2.1 Objectives

The sonoelectrochemical synthesis of iron nanoparticles is the combination of two different processes, the metallic electrodeposition and its dispersion by ultrasounds. Therefore, the understanding of the laws and parameters, governing both steps of the synthesis, is necessary.

Various parameters have been investigated to control the whole synthesis process. For example, the influence of the ultrasound intensity, the temperature, or the duration of the electrodeposition and ultrasonication steps (when both steps are achieved sequentially), have been studied [34]. However, little consideration has been given to the choice of the electrode used as a substrate for the metallic electrodeposition.

In response to this lack, the objective of this chapter is to provide a better understanding of the influence of the electrode substrate, on the iron electrodeposition step. To that end, the focus is put on two properties of the substrate:

- the surface energy, dictated by choice of the material,
- the roughness.

As a first step, this chapter provides a preliminary study of the $Fe^{(II)}/Fe$ system, necessary to understand and control the iron electrodeposition process. This will be achieved by a voltammetric study with a rotating disk electrode (RDE), which allows to choose the optimum operating parameters for iron electrodeposition such as the reduction potential of iron ions, or the pH of the solution for examples.

Then, a detailed description of both the voltammetric curves and the obtained iron deposit morphologies, will allow highlighting the effect of the substrate on the electrodeposition process. These results will be related to the surface energies of the different material used as the substrate, to understand its influence on the deposit/substrate interface properties. At the same time, the influence of the substrate roughness will also be discussed.

Finally, the conclusions drawn from the voltammetric study about the influence of the substrate will be compared to results obtained with another electrodeposition technique, the galvanostatic electrolysis, to confirm or invalidate our statements.

2.2 Materials and methods

2.2.1 Experimental set-up

Experimental device

A detailed presentation of the experimental device is presented Figure 2.1 .

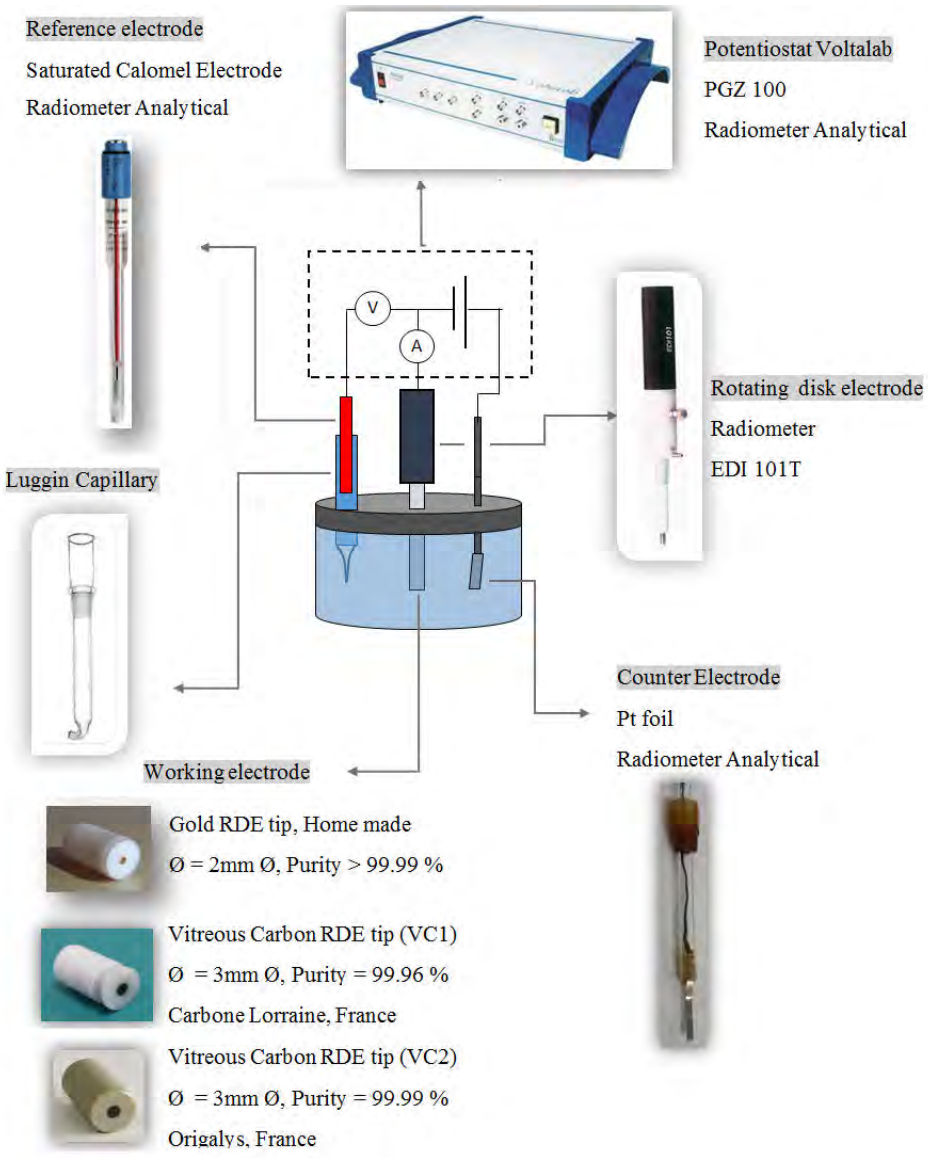

Figure 2.1: Pictures and schematic representation of the experimental device used.

Preparation of the solutions

All solutions are prepared using ultrapure water (18.2 MΩ.cm) and are deaerated with argon (1 bar), before each experiment, during at least 15 minutes.

Solutions containing iron(II) are prepared by dissolving Normapur solid $FeCl_2$ supplied by Sigma-Aldrich in a 0.1 M KCl supporting electrolyte. In the same manner, $(NH_4)_2Fe(SO_4)_2$ solution (Mohr's salt) is supplied by Sigma-Aldrich and dissolved in a 0.05 M K_2SO_4 solution (see Table 2.1 for an overview of the chemical products used).

The pH of the iron salt solutions is adjusted to 4.0, by the addition of hydrochloric acid or sulphuric acid. The choice of this pH will be explained later, in the experimental section.

Chemical products		Purity (%)
Iron Chloride (II)	$FeCl_2 \cdot 4H_2O$	≥ 99.0
Mohr's salt	$(NH_4)_2Fe(SO_4)_2 \cdot 6H_2O$	≥ 99.0
Potassium Chloride	KCl	≥ 99.0
Potassium Sulfate	K_2SO_4	≥ 99.0

Table 2.1: Chemical products and their purity

Preparation of the electrodes surfaces

Electrodes are polished using alumina aqueous suspension of 9, 5, 1 and 0.3 μm on a rotating pad. The electrodes are sonicated for 5 minutes in a 50:50 ethanol/water mixture between each polishing and, 5 minutes more in ultrapure water to remove the remaining alumina particles. For studying the influence of the substrate roughness, the VC2 electrode is polished with paper grid P1200 and P800.

2.2.2 Characterization of the electrode surfaces

The vitreous carbon electrodes show slight differences in their chemical compositions: VC1 contains 0.04 % ash, 50 ppm sulfur and bore traces, VC2 contains 0.0042 % ash and 13.5 ppm metal traces (data provided by suppliers).

Determination of the electrodes surface energy

Three different electrodes are employed (Au, VC1, VC2, see the experimental device Figure 2.1) to study the effect of their substrate material on the iron electrodeposit morphology. The value of the surface energy of each substrate material is determined experimentally using the Owens-Wendt "one liquid" method [73]. This technique enables to determine the dispersive γ^D_{elect} and polar γ^P_{elect} components (Equation 2.1) of the surface energy γ_{elect} of a solid (the electrode here) from contact angle measurements. To that end, contact angles, formed by liquids on the studied surface, are measured using a series of liquids of known surface energy components (dispersive, γ^D_L and polar, γ^P_L see equation 2.2). A representation of the measurement is proposed Figure 2.2.

$$\gamma_{elect} = \gamma^P_{elect} + \gamma^D_{elect} \tag{2.1}$$

$$\gamma_L = \gamma^P_L + \gamma^D_L \tag{2.2}$$

Where: γ_{elect} and γ_L are the surface energy of the electrode and of the liquid respectively, γ^P_S and γ^P_L their polar component, γ^D_S and γ^D_L their dispersive components.

The liquids employed for this measurement and their surface energy components are presented in Table 2.2.

	Surface energy (mN/m)		
Liquid	γ_L	γ^d_L	γ^P_L
Decane	23.4	23.4	0.0
Dimethylsulfoxide	44.0	36.0	8.0
Glycerol	63.4	37.0	26.4
Water	72.8	21.8	51.0

Table 2.2: Surface energy, dispersive and polar components, of the four liquids used for contact angle measurements.

According to Owens and Wendt [73], the interfacial energy $\gamma_{elect/L}$ is considered as the sum of surface energy of the individual phases (γ_{elect} and γ_L), reduced by the

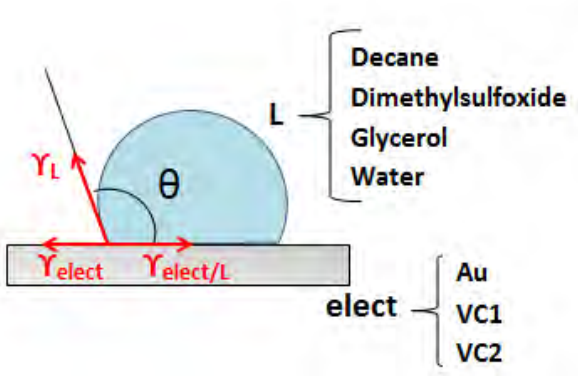

Figure 2.2: Schematic representation of the contact angle measurement for the determination of the electrodes surface energies

geometric mean values of the dispersive and polar contribution:

$$\gamma_{elect/L} = \gamma_{elect} + \gamma_L - 2\sqrt{\gamma^D_{elect}\gamma^D_L} - 2\sqrt{\gamma^P_{elect}\gamma^P_L} \tag{2.3}$$

The interfacial energy $\gamma_{elect/L}$ can also be expressed by Young's equation:

$$\gamma_{elect/L} = \gamma_{elect} - \gamma_L \cos\theta \tag{2.4}$$

By combining equation 2.3 and equation 2.4, the following expression is obtained:

$$\gamma_L(1+\cos\theta) = 2\sqrt{\gamma^D_{elect}\gamma^D_L} + 2\sqrt{\gamma^P_{elect}\gamma^P_L} \tag{2.5}$$

With θ, the contact angle formed by the liquid on the solid surface.

This equation can also be written:

$$\frac{\gamma_L(1+\cos\theta)}{2\sqrt{\gamma^D_L}} = \sqrt{\gamma^P_{elect}}\sqrt{\frac{\gamma^P_L}{\gamma^D_L}} + \sqrt{\gamma^D_{elect}} \tag{2.6}$$

Therefore, by plotting $\frac{\gamma_L(1+\cos\theta)}{2\sqrt{\gamma^D_L}}$ versus $\sqrt{\frac{\gamma^P_L}{\gamma^D_L}}$, the slope and the intercept of the linear regression are respectively $\sqrt{\gamma^P_{elect}}$ and $\sqrt{\gamma^D_{elect}}$, enabling to determine the surface energy of the electrode from Equation 2.1.

Contact angles are measured with four different liquids: ultrapure water, glycerol, dimethylsulfoxide and decane (of known surface energy, presented in table 2.2). Liquid droplets of $\approx 2\mu$L are formed in ambient conditions with a GBX Digidrop goniometer DGD fast 60. The results obtained are shown in Figure 2.3 and the resulting surface energy values are indicated in Table 2.3.

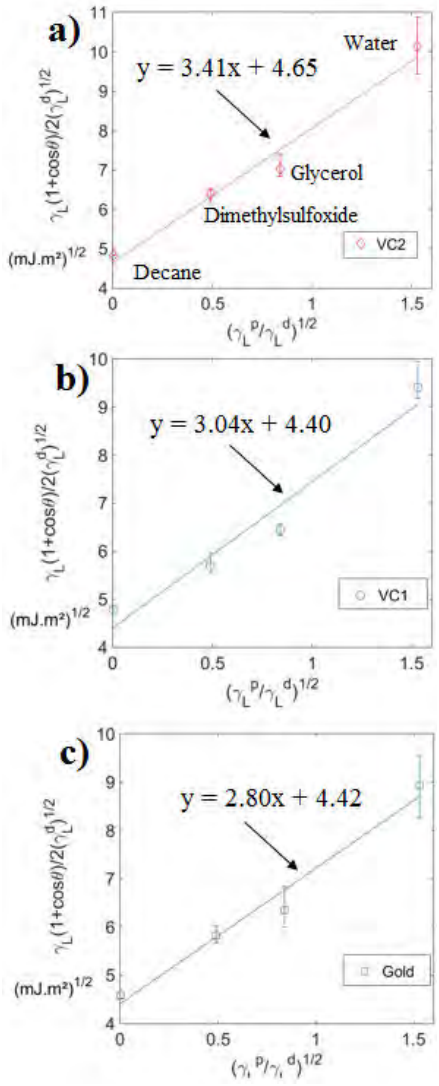

Figure 2.3: Evolution of $\frac{\gamma_L(1+\cos\theta)}{2\sqrt{\gamma_L^D}}$ as a function of $\sqrt{\frac{\gamma_L^P}{\gamma_L^D}}$ for three different electrodes material a) VC2 and b) VC1 and c) Gold surface, obtained from the contact angle measurement of ultrapure water, glycerol, dimethylsulfoxide and decane, and analyzed according to the Owens-Wendt method.

	γ_d (mJ/m^2)	γ_p (mJ/m^2)	γ_{elect} (mJ/m^2)
VC2	21 ± 1	13 ± 3	34 ± 3
VC1	19 ± 1	10 ± 2	29 ± 2
Gold	19 ± 1	8 ± 2	27 ± 2

Table 2.3: Measured surface energies of VC1 and VC2 electrodes; γ_P and γ_P are respectively the polar and dispersive component of the total surface energy γ_{elec}

Measurement of the electrodes roughness

The surface roughness of the two vitreous carbon electrodes, VC1 and VC2, polished with 0.3 μm alumina suspension, are visualized by an optical microscope (Zeiss Axiolab) and surface profiles are measured by an interferometric surface profiler (Zygo 3D). This apparatus operates with light interferences generated by reflections on the examined surface. The distance between the fringes allows determining the local height. The obtained pictures and roughness profiles are presented in Figure 2.4. It can be seen in this figure that both electrodes show regular stripes on their surface, which are due to the polishing. The VC1 surface appears to be not as smooth as the VC2 surface. Indeed, small holes, with diameters in the range of 1-10 μm, are visible on the VC1 surface. In addition to surface profiles, the interferometric surface profiler provides information on the surface roughness like the arithmetic roughness *Ra*. This value is the most commonly used parameter to characterize a surface roughness and is expressed by the equation 2.7.

$$Ra = \frac{1}{S}\int_S |y(x,z)|dS \tag{2.7}$$

With y(x) the local height, and *S* the surface of the sample.

The *Ra* obtained for the VC1, and VC2 surfaces polished with the finest alumina suspension (0.3 μm) are respectively 35 nm and 8 nm ($\pm$ 3 nm).

Additionally, the VC2 electrode is polished with paper grid P1200 and P800. The VC2P1200 and VC2P800 roughness are measured in the same manner as previously. The obtained picture and roughness profile are presented in Figure 2.5.

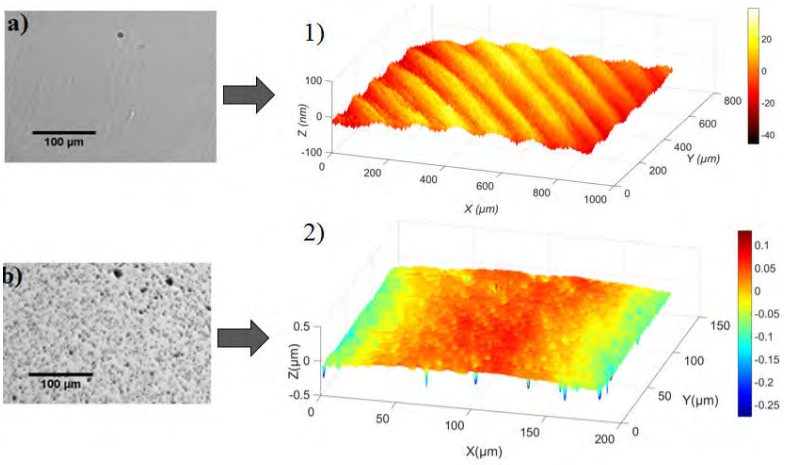

Figure 2.4: Optical images and surface profiles of the polished (alumina suspension 0.3 μm) vitreous carbon electrodes ; for VC2: a) optical image and 1) surface profile; for VC1: b) optical image and 2) surface profile.

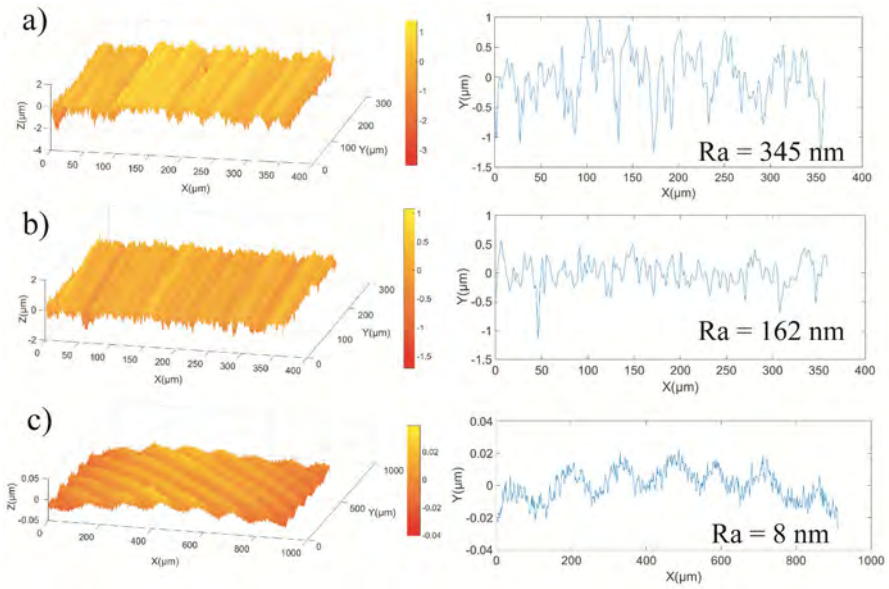

Figure 2.5: Surface profiles of the VC2 electrode obtained by an optical surface profiler (Zygo 3D) and their one-dimensional profiles (perpendicular to the stripes), a) VC2 P800, b) VC2 P1200, VC2 0.3μm.

An overview of the obtained surface roughnesses is presented in table 2.4. These measurements will serve as a basis for the discussion about the influence of the roughness on the iron electrodeposition.

Electrode	Ra (nm)
VC1 0.3 μm	35 ± 3
VC2 0.3 μm	8 ± 3
VC2 P1200	162 ± 3
VC2 P800	345 ± 3

Table 2.4: Electrode surface properties: surface roughness

2.2.3 Characterization of the deposit morphology

Morphology of iron electrodeposits is observed by scanning electron microscopy (SEM) with an MEB FEG JEOL JSM 7100F TTLS or an MEB FEG JEOL JSM 780 0F Prime-EDS. Before observations, the sample is rinsed with ultrapure water (to avoid electrolyte crystallization) and dried under ambient conditions. The whole sample surface is coated with a nanometric layer of gold by vapor deposition, to avoid electrons beam deviation (due to the presence of insulating material surrounding the disk electrode) if it is necessary. An electric connection between electrodes and the SEM support is ensured by a brass stud adapted to the electrode.

2.2.4 Electrochemical methods

Voltammetry

In the present study, steady-state voltammetry experiments (see Section 1.2.1 Chapter I, for the voltammetry theory) are achieved by varying the potential from the zero current potential, $E_{i=0}$ to the cathodic potentials to induce the iron ions reduction, until E reaches a set value, $E_{reverse}$. Then, the potential is swept in the opposite direction, to study the behavior of the modified electrode and also to examine the oxidation of the freshly deposed iron (see Figure 2.6). At the end of the cyclic voltammograms, the iron deposit is totally reoxydized. The choice of the potential $E_{reverse}$ will be developed in the experimental section. The cyclic voltammograms are recorded under an angular velocity of the RDE of 1000 RPM.

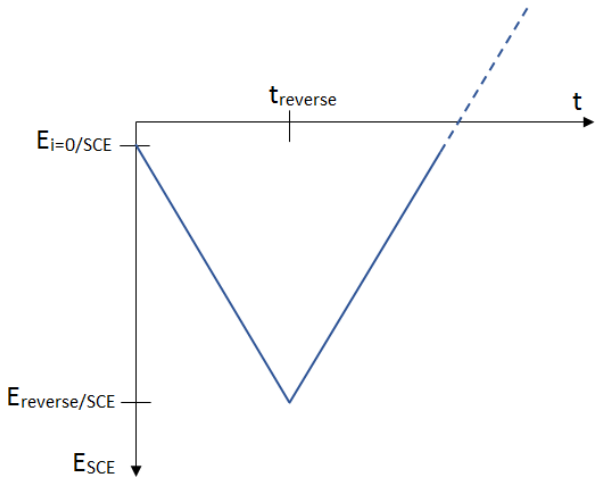

Figure 2.6: Cyclic potential sweep

Galvanostatic electrolyses on an RDE

The procedure followed for the galvanostatic electrolysis is detailed below:

- Before each galvanostatic electrolysis, three cyclic voltammograms are achieved to check the repeatability of the electrocatalytic properties of the electrode.
- Then, a pretreatment step, which consists of applying an anodic potential, is achieved to recover the initial state of the electrode (possible traces of iron remained on the surface after the first step are oxidized). It enables a better reproducibility.
- The galvanostatic electrolysis is carried out with a constant current $I = 90\% I_{lim}$ to avoid secondary reactions to occur.
- As a final step, the iron produced is oxidized by linear voltammetry starting from the open circuit potential ($E_{i=0}$), OCP, obtained after iron formation to 0 V/SCE, so as to remove the deposit and recover the initially bare surface of the working electrode. Note that this new OCP corresponds to the Nernst potential of the $Fe^{(II)}$/Fe, all the involved species are present at the electrode.

The angular velocity is maintained at 1000 RPM during the whole procedure.

Determination of the amount of iron deposited

The iron quantity produced at the cathode can be determined from the charge Q_{Fe} passed through the electrochemical cell during the iron ion reduction (forward and backward scans) thanks to the Faraday's law:

$$Q_{Fe} = nFn_{iron} \tag{2.8}$$

And Q could also be expressed as follows:

$$Q_{Fe} = y_F \times \int_0^t I(t)dt \tag{2.9}$$

Where: n_{iron} is the iron quantity produced, t the duration of the electrolysis, and n the number of electrons exchanged (here n=2), and with y_f, the percentage of the applied current allotted to the iron ions reduction. The Voltamaster 4 software enables the numerical integration of the $I = f(t)$.

When a constant current is applied:

$$Q = I.t \tag{2.10}$$

Thus the iron quantity produced is:

$$n_{iron} = \frac{I \times t \times y_f}{nF} \tag{2.11}$$

2.3 Study of electrochemical behavior of the $Fe^{(II)}$/Fe system, in different electrolytes, and choice of operating conditions for iron electrodeposition

2.3.1 Study of the redox system $Fe^{(II)}$/Fe

The electrochemical behavior of $Fe^{(II)}$ salts used ($FeCl_2$ and Mohr's salt) is examined by voltammetry, in presence of two supporting electrolytes, on a gold RDE electrode

($\omega = 1000$ RPM). Voltamperometric curves are shown in Figure 2.7. In both media (chloride and sulfate) the scan starts at the OCP (-0.2 V/SCE), shifts toward the cathodic potentials until $E_{reverse} = -1.30$ V/SCE and then it is reversed until 0 V/SCE.

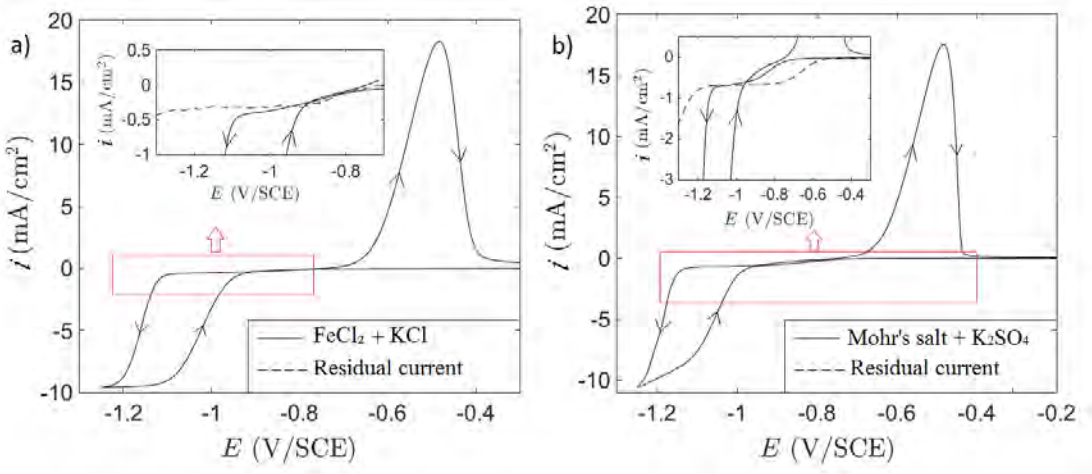

Figure 2.7: Cyclic voltammetry scans (steady-state conditions) obtained on a RDE for the gold material, υ = 20 mV/s, T = 25 °C, ω = 1000 RPM. a): In a 0.01 M $FeCl_2$ solution + KCl 0.1 M, b): in 0.01 M Mohr's salt solution + 0.05 M K_2SO_4. Inset:zoom of the curves including the residual current curves (dashed lines). All solution pH are adjusted to 4.0.

During the forward scan, a first reduction reaction is highlighted, by a slight increase in the current density (absolute value) and the formation of a diffusion-limited wave starting at ≈ -0.7 V/SCE for $FeCl_2$ and Mohr'salt is observed. An enlarged view of this signal is presented in the inset of each graph (Figure 2.7, a) for $FeCl_2$, and Figure 2.7, b) for Mohr's salt media). Voltamperometric curves of the residual currents obtained with the supporting electrolyte alone, without $Fe^{(II)}$ (KCl or K_2SO_4 with a pH adjusted to pH=4.0) are also presented in the inset (dotted lines); they reveal a signal exhibiting a diffusion-limited wave. This signal is attributed to the reduction of the free proton at pH=4.0 (see equation 2.12). This is confirmed by the Figure 2.8 which shows that by changing the pH value, the diffusion-limited wave varies in a similar way with or without the presence of iron ions. By varying the pH from 4.0 to 3.0, the diffusion-limited wave obtained with both the $FeCl_2$ solution and the KCl solution, is multiplied by 10; i (≈ -0.3 mA/cm^2 $\longrightarrow \approx -3$ mA/cm^2). The limiting current being proportional to the electroactive species concentration, this increase is consistent with the increase of

the H^+ concentration from 10^{-4} to 10^{-3} mol/L.

$$H^+ + e^- \rightarrow 1/2H_2 \tag{2.12}$$

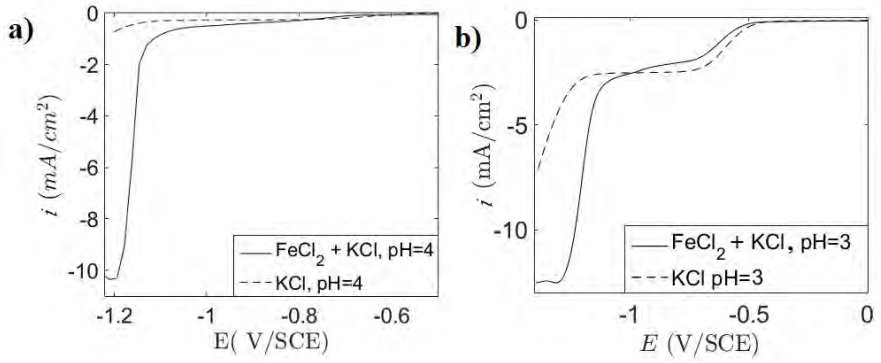

Figure 2.8: Voltammetric scans (solid lines) obtained with an RDE $\omega = 1000$ RPM, $\upsilon = 200$ mV/s, on a gold electrode in a 0.01 M $FeCl_2$ solution with pH fixed to 4.0 in a) and to 3.0 in b), and their residual current (dotted line): a) 0.1 M KCl at pH=4 and b) 0.1M KCl at pH=3.

Comparison of the limiting currents obtained in KCl (0.34 mA/cm^2) and in K_2SO_4 (0.65 mA/cm^2) leads to a ratio of 2, attributed to the di-acid nature of H_2SO_4 compared to the mono-acid nature of HCl (see Figure 2.7). Indeed, a solution of sulfuric acid and K_2SO_4 at pH=4.0 contains the following species: H^+, HSO_4^-, SO_4^{2-} and K^+, so after the consumption of the free H^+, HSO_4^- dissociates and supplies additional H^+ which could be reduced. This leads, for the sulfate system, to an apparent H^+ concentration two times higher than the one for the chloride system, and explains the ratio of the limiting current observed. Values for limiting current density of H^+ reduction, i_{lim}, can be estimated using the Levich's equation 1.17. Calculations leads to $i_{lim} = 0.33$ mA/cm^2 (the values for D, C_{H^+}, and ν are respectively 9.3×10^{-9} m^2/s [74], 10^{-4} M, and 10^{-6} m^2/s) which is consistent with the measured value of i_{lim} for the chloride system (0.34 mA/cm^2 , $C_{H+} = 10^{-4}$ M).

Concerning the more cathodic potentials of the forward scans in Figure 2.7, a) and b), an additional signal is observed between -1.1 and -1.3 V/SCE, it is attributed to the $Fe^{(II)}$ reduction (Equation 2.13) on the initially bare electrodes. It clearly indicates a slow red/ox system: $E_{i=0.1\text{mA/cm}^2} - E_{i=0} \approx -0.9$ V. The corresponding electrochemical

reaction is:

$$Fe^{(II)} + 2e^{-} \rightarrow Fe^{0} \tag{2.13}$$

During the forward scan, the gold electrode is partially covered by zero valent iron, so once the reverse potential is reached, the substrate tends to act as an iron electrode. Indeed with the potential scan rate used, the cathodic curve obtained during the return scan (-1.4 to -0.4 V/SCE), exhibits a resolute diffusion-limited wave, corresponding to the $Fe^{(II)}$ reduction on the native iron surface. The reduction of $Fe^{(II)}$ on the Fe^{0} deposit appears to be less irreversible compared to the reduction on the gold electrode ($E_{i=0} - E_{i=0.1\mathrm{mA/cm^2}}$ decreases by 150 mV). The limiting current of the $Fe^{(II)}$ reduction measured experimentally (see Figure 2.9) increases linearly with the square root of the angular velocity ($\omega^{0.5}$). The slope of the linear regression (according to the Levich's equation), enables to determine the diffusion coefficient of the $Fe^{(II)}$ species: 8.6×10^{-6} $\mathrm{cm^2/s}$ ($T = 20\ ^{\circ}\mathrm{C} \pm 5\ ^{\circ}\mathrm{C}$), a value higher but consistent with the diffusion coefficient of $Fe^{(II)}$ at infinite dilution found in [75]: 5.82×10^{-6} $\mathrm{cm^2/s}$ for $T = 18\ ^{\circ}\mathrm{C}$ and 7.19×10^{-6} for $T = 25\ ^{\circ}\mathrm{C}$.

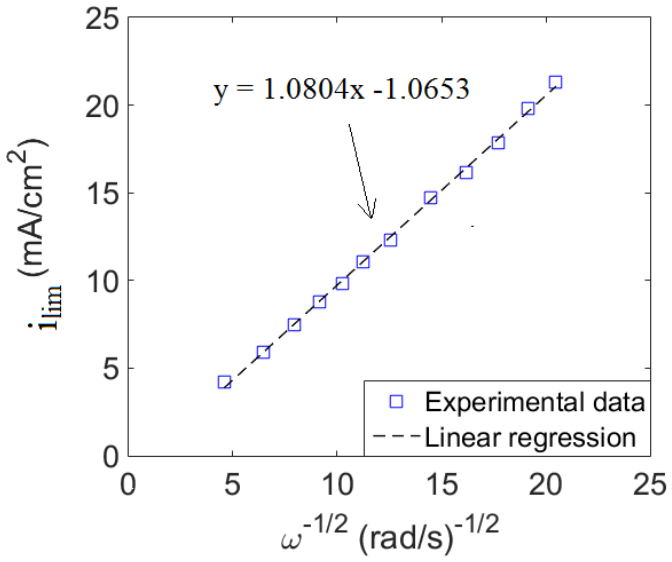

Figure 2.9: Evolution of limiting current for the $Fe^{(II)}$ reduction against the square root of the angular velocity of a RDE (Gold electrode). Squares represent experimental data obtained in a 0.01 M $FeCl_2$ at ambient temperature (20 μC ± 5 μC), the solid line is the linear regression of the experimental curve.

It can be noticed that for Mohr's salt solutions (Fig. 2.7 b), the diffusion-limited wave is not well defined due to the co-reduction of free protons on electrodeposited iron followed by water reduction. This distinction between chloride and sulfate systems for iron electrodeposition has already been observed by Grujicic and Pesic [43].

For the backward scans, the cathodic current is canceled at the equilibrium potential which lie in the range [≈ -0.8 to ≈ -0.75 V/SCE] for both media. These potentials are consistent with the Fe^{2+}/Fe Nernst's law $E = -0.44 - 0.25 + 0.03 \times (log(10^{-2}/1)) = -0.74V/SCE$.

The anodic curve obtained during the backward scan for potentials higher than -0.8 V/SCE (Figure 2.7 a and b), exhibits a peak attributed to the iron electrodeposit oxidation, for both media (chloride and sulfate).

$$Fe^0 \rightarrow Fe^{(II)} + 2e^- \tag{2.14}$$

The sharp decrease in current clearly indicates the complete oxidation of the electrodeposit and the regeneration of the initially bare surface of the working electrode (gold). This is the end of one complete cycle of the operated experiments.

2.3.2 Effect of the pH on the $Fe^{(II)}$ reduction and the deposit corrosion

The analysis of the obtained voltammograms is achieved and presented below, to help the selection the optimum operating parameters allowing to get a zero valent iron deposit zero valent. The co-reduction of the free proton during iron electrodeposition that has been demonstrated above, already enables to consider the pH as a crucial parameter for the electrodeposition of iron. The lower the pH, the more the cathodic charge devoted to the H^+ reduction will be large, simultaneously, the Faradaic yield of the $Fe^{(II)}$ reduction decreases.

Moreover, the pH decrease induces a corrosion reaction 2.15 which is an important aspect to consider.

$$Fe + 2H^+ \rightarrow Fe^{2+} + H_2 \tag{2.15}$$

The rate of this corrosion is evaluated for different pH values in $FeCl_2$ solutions. To that

end, a first electrodeposition step is proceeded by linear voltammetry on a rotating gold electrode, in deaerated 0.01 M $FeCl_2$ solution. The electrode is depolarized during a certain time t, and an anodic scan is carried out to electrooxidize the residual iron deposit not corroded chemically. A rotation speed of 1000 RPM is applied during the different steps of the procedure. The comparison of the cathodic and anodic charge enables to estimate the quantity of iron lost by corrosion, $n_{Fe(lost)}$ during the depolarization step thanks to the following equation:

$$n_{Fe(lost)} = \frac{Qc_{Fe} - Qa_{Fe}}{2F} = \frac{Qc_{total} - Qc_{H^+} - Qa_{Fe}}{2F} \tag{2.16}$$

With:

- Qc_{Fe} and Qa_{Fe}, the cathodic and anodic charge for the iron production and oxidation respectively
- Qc_{H^+}, the cathodic charge of hydrogen reduction [1]
- Qc_{total}, the total cathodic charge

Figure 2.10 presents the calculated $n_{Fe(lost)}$ as a function of the depolarized time of the electrode, for experiments achieved at various pH; each point is a mean of at least two experiments. The linear curves obtained suggest an iron corrosion with a chemical kinetic order for Fe^0 of zero. This implies first, that the surface of the iron deposit in contact with the solution remains constant during the corrosion process (the iron deposit is consumed layer by layer). It also means that the corrosion reaction is not limited by the H^+ mass transfer; the electrode is indeed continuously supplied in H^+ by the rotation of the RDE $\omega = 1000$ RPM. Consequently a simplified expression of the chemical rate reaction (reaction 2.15) can be proposed:

$$\frac{dn_{Fe(lost)}}{dt} = r_{corr} = Cst \tag{2.17}$$

This constant, Cst depends on the H^+ concentration, and the activity of the zero valent iron:

[1] Qc_{H^+} is estimated by multiplying the limiting current of H^+ by the duration of the cathodic scan.

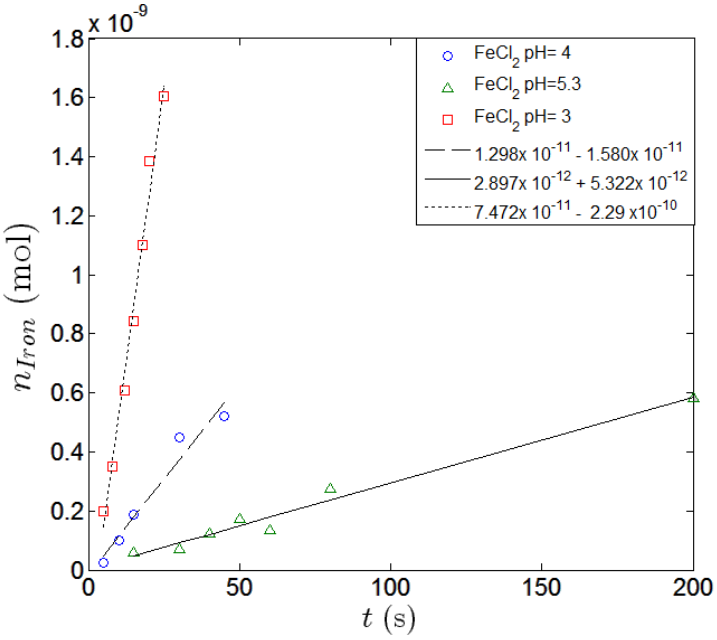

Figure 2.10: Measurement of the loss of the iron electrodeposit by corrosion as a function of time in a 0.01 M $FeCl_2$ using three different pH: 3.0, 4.0, and 5.3. $\omega = 1000$ RPM

pH	r_{corr} (mol/s)
3.0	$7.5 \times 10^{-11} \pm 2 \times 10^{-13}$
4.0	$1.3 \times 10^{-11} \pm 4 \times 10^{-13}$
5.3	$2.9 \times 10^{-12} \pm 5 \times 10^{-13}$

Table 2.5: Corrosion rate estimated experimentally for different pH of the $FeCl_2$ solution

$$\frac{dn_{Fe(lost)}}{dt} = r_{corr} = k a_{Fe}^{\alpha} C_{H^+}^{\beta} (f(\omega)) \tag{2.18}$$

So:

$$r_{corr} = k' C_{H^+}^{\beta} \tag{2.19}$$

To sum up, the corrosion rate obtained experimentally and indicated in Table 2.5 enables to estimate the coefficient β (see Figure 2.11):

$$\ln(r_{corr}) = \ln(k') + \beta \ln(C_{H^+}) \tag{2.20}$$

Therefore r_{corr} can be expressed:

$$r_{corr}(\text{mol/s}) = k' \times C_{H^+}^{1.63}(\text{mol/L}) \tag{2.21}$$

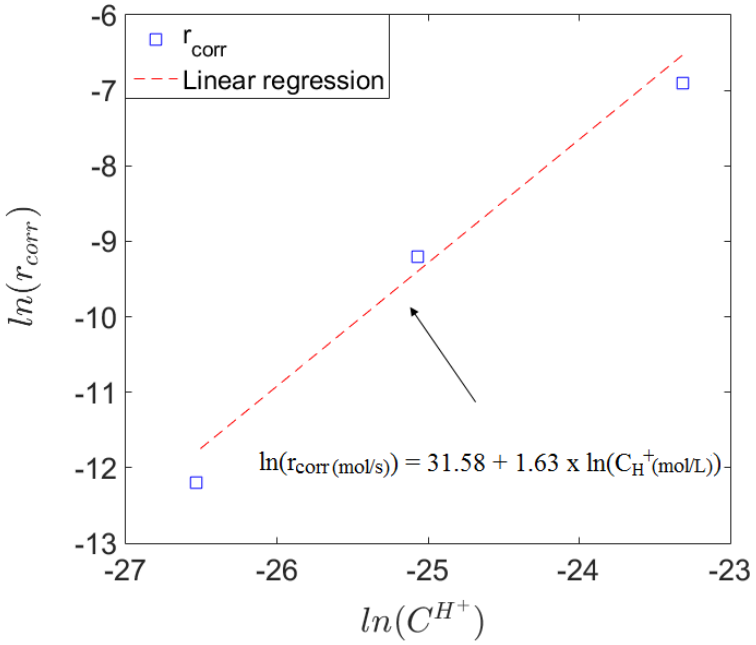

Figure 2.11: Evolution of $ln(r_{corr})$ as a function of $ln(C_{H^+})$; results extracted from table 2.5

These experimental estimations of the corrosion rate have to be taken into account for the rest of our experiments, to know if the corrosion can be neglected in regards to the duration of the experiment and the iron quantity deposed. For example for pH = 4.0, an electrode depolarization of 15 s, induces a loss of iron of corresponding to approximately 40 μC when $\omega = 1000$ RPM. A higher pH would reduce the corrosion rate. Indeed, for a pH value of 5.0, the corrosion rate is around 26 times lower than for pH=3.0 and around four times lower than for pH=4.0. However, results show that an increase of the pH also has a negative impact on the iron formation. Changing the pH from 4.0 (natural pH of a 0.01 M $FeCl_2$) to 4.9 affects the shape of the cyclic voltammograms (see Figure 2.12). The cyclic voltammogram, obtained in a solution of pH=4.9, exhibits three oxidation peaks (low resolution) during the backward scan for potentials higher than -0.8 V/SCE; they probably correspond to the oxidation of iron oxides or

hydroxides.

Grujic et al. [43] obtained similar results in sulfate and chloride media for a pH equal to 5.0 in a 0.005 M Fe^{2+} solution. They described "wavy and ill-defined" anodic peaks attributed to the presence of iron hydroxide species forming a passivation layer. This also explains why the iron seems to be hardly oxidized (slow decrease of the anodic peak which cancels at ≈ 0 V, instead of -0.4 V in Figure 2.7).

In conclusion, $pH < 3.0$ would cause an increase in the corrosion rate and a loss of the faradaic yield, while a $pH > 5.0$, even though it is advantageous for the corrosion, could induce the formation of iron hydroxide that disturbs the measurements. In the rest of the study the natural pH of the $FeCl_2$ solution (pH=4.0) will be use. However, as it has been mentioned, for this pH value, the corrosion rate is not negligible (a loss of iron corresponding to 40 μC, in 15 s, for $\omega = 1000$ RPM) and will be taken into account in our calculations.

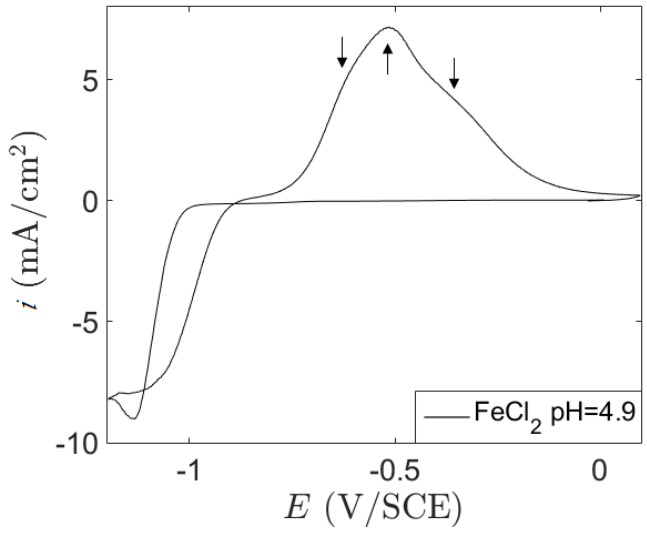

Figure 2.12: Cyclic voltamperometric scan obtained on a gold RDE $\omega = 1000$ RPM, $\upsilon = 200$ mV/s, in a 0.01 M $FeCl_2$ solution at pH=4.9; KCl 0.1M; N_2=1 bar.

Another important parameter for the formation of an iron electrodeposit is the applied current or potential (see Chapter 1.2.2). A too high overpotential ($\eta < 0$) is not appropriate because the possible water reduction and the basification of the solution in the vicinity of the interface induce the formation of iron hydroxides (see Figure

2.13). Indeed, Figure 2.13 shows voltamperometric scans obtained for cathodic potentials $E_{reverse}$ equal to -1.2 and -1.3 V/SCE. The resulting graph shows that by changing the limit cathodic potential the composition of the deposit changes. Indeed, several oxidation peaks are observed during the anodic scan highlighting once again the presence of iron hydroxides. For each electrodeposition method (voltammetric, galvanostatic) the potential or the constant current must be selected to avoid the reduction of the solvent.

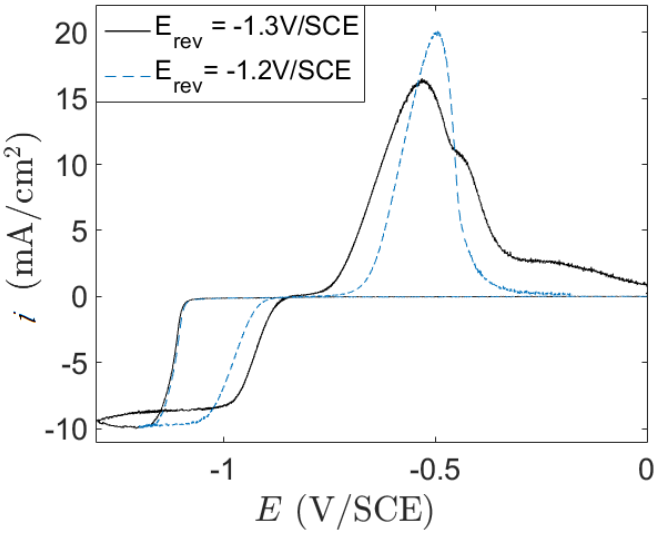

Figure 2.13: Cyclic voltamperometric scans recorded on a gold RDE for two different reverse cathodic potentials: $E_{rev} = -1.3$ V/SCE (solid line) and $E_{rev} = -1.2$ V/SCE dotted line. $\omega =$ 1000 RPM; $\upsilon = 20$ mV/s, in 0.01M $FeCl_2$ at pH = 4.0.

2.4 Influence of the substrate characteristics on the iron electrodeposition

This section presents voltammetric studies, expecting to highlight the influence of the electrode material on the iron electrodeposition, and its morphology. Thus different electrode materials are used:

- a gold electrode,
- a vitreous carbon VC1 showing irregularities on its surface,

- another vitreous carbon VC2 showing a smooth surface.

The substrates characteristics (surface energy and roughness) have been detailed in section 2.2.2 and serve as a basis for the following discussion. The influence of the substrate on the electrodeposition process is evaluated by both the analysis of the cyclic voltammograms and the study of the electrodeposit morphology. Iron electrodeposits obtained on the three substrates and for both chloride and sulfate media, are observed by SEM at the end of the cathodic cycle (Figures 2.14 and 2.15).

2.4.1 Study of the $Fe^{(II)}$ reduction by cyclic voltammetry, in two different electrolytes

Analysis of the voltammograms provides information on the influence of substrate on the iron electrodeposition: as mentioned before, the effects of both the substrate material and its roughness are investigated. The curves indicated in Figure 2.14 and 2.15, show that the overpotentials η required for iron reduction on the initially bare gold electrode (the first forward scan) η_{Au} are systematically lower than those of the vitreous carbons 1 and 2 ($\eta_{VC1} \approx \eta_{VC2}$)for both media used. Indeed, in chloride medium for the forward scan (Figure 2.14), the half wave potential $E_{1/2}$ of the $Fe^{(II)}$ reduction is around -1.17 V/SCE on the gold electrode and around -1.24 V/SCE on the both vitreous carbon substrates. The same observation can be done in sulfate medium (Figure 2.15) since the $E_{1/2}$ is around -1.18 V on the gold electrode and around -1.26 V/SCE and -1.3 V/SCE on the VC2 and VC1 substrate respectively ($E_{Fe^{2+}/Fe} = -0.74$ V/SCE). These observations lead us to conclude that a lower energy (lower cell voltage) is required to create and increase the Fe/Au interface than the Fe/VC interface.

The electrolyte also seems to have an effect on the limiting current value. Indeed, in sulfate medium, similar magnitudes of the pseudo limiting current are measured for gold and VC electrodes (cathodic backward scans in Figure 2.15), corresponding to the reduction of $Fe^{(II)}$ on the substrate covered by the iron electrodeposit). Conversely, in chloride medium (Figure 2.14) the limiting current density is higher on the gold electrode than on the vitreous carbon substrates. This difference in the limiting current value will be discussed afterward (section 2.4.3), some information about the iron morphology

(section 2.4.2) are necessary for its understanding.

Concerning the effect of the substrate roughness, the difference between VC1 (Ra = 35 nm) and VC2 (Ra = 8 nm) does not seem to influence the electrodeposition, since the cyclic scans on VC1 and VC2 are almost identical on both chloride and sulfate media.

2.4.2 Influence of the substrate characteristics (surface energy and roughness) on the iron morphology

The morphology of the electrodeposited iron on the three substrates and in the different media is analyzed by SEM (pictures 1 to 3 of Figure 2.14 and Figure 2.15) to evaluate the influence of the substrate.

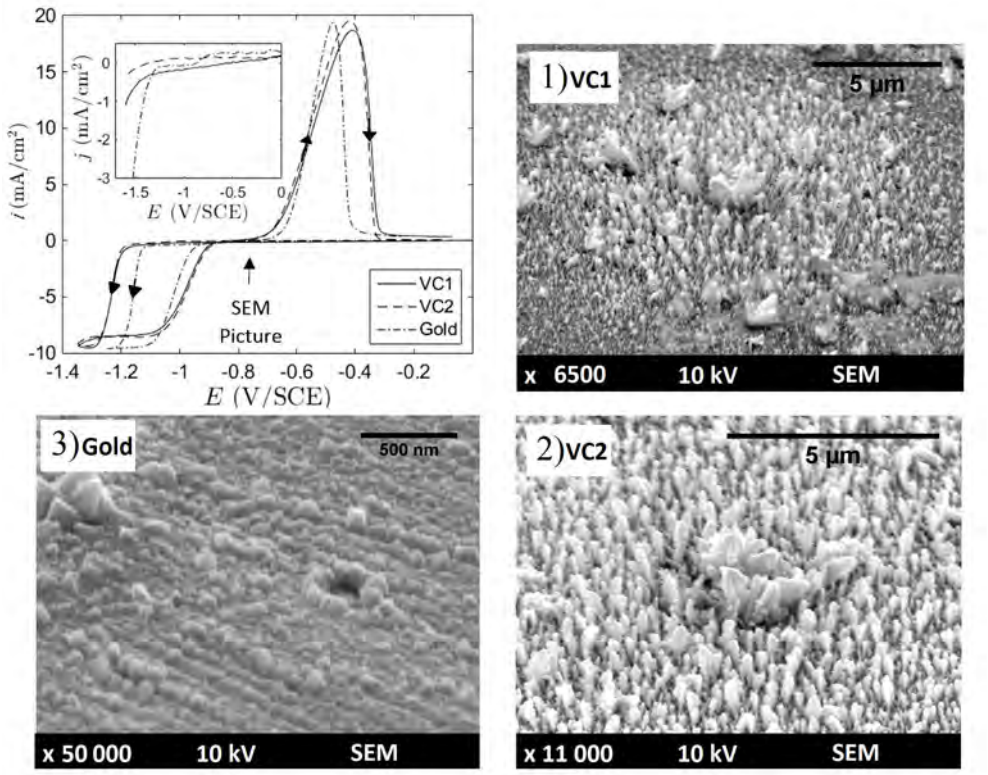

Figure 2.14: Cyclic voltammetric scans obtained in chloride medium and the corresponding SEM pictures. Curves (forward and backward) obtained on a RDE for: VC1, VC2, and gold. Inset: Residual currents (forward curve). SEM pictures with a 40Â° tilt angle (taken at the end of the cathodic cycle): 1) to 3) iron electrodeposited on respectively VC1, VC2 and gold electrodes.

In chloride medium, a clear morphological difference can be noticed between iron electrodeposits obtained on vitreous carbon and gold electrodes (Figure 2.14, pictures 1-3). Indeed, on the gold electrode (picture 3), the SEM image reveals iron electrodeposit as a compact layer that covers well the electrode surface. This layer consists of cubic structures sized in the range of a few hundred nanometers. Conversely, on the VC substrates (pictures 1) and 2)) iron electrodeposits consist of micrometric dendritic structures with heights not exceeding 1 μm.

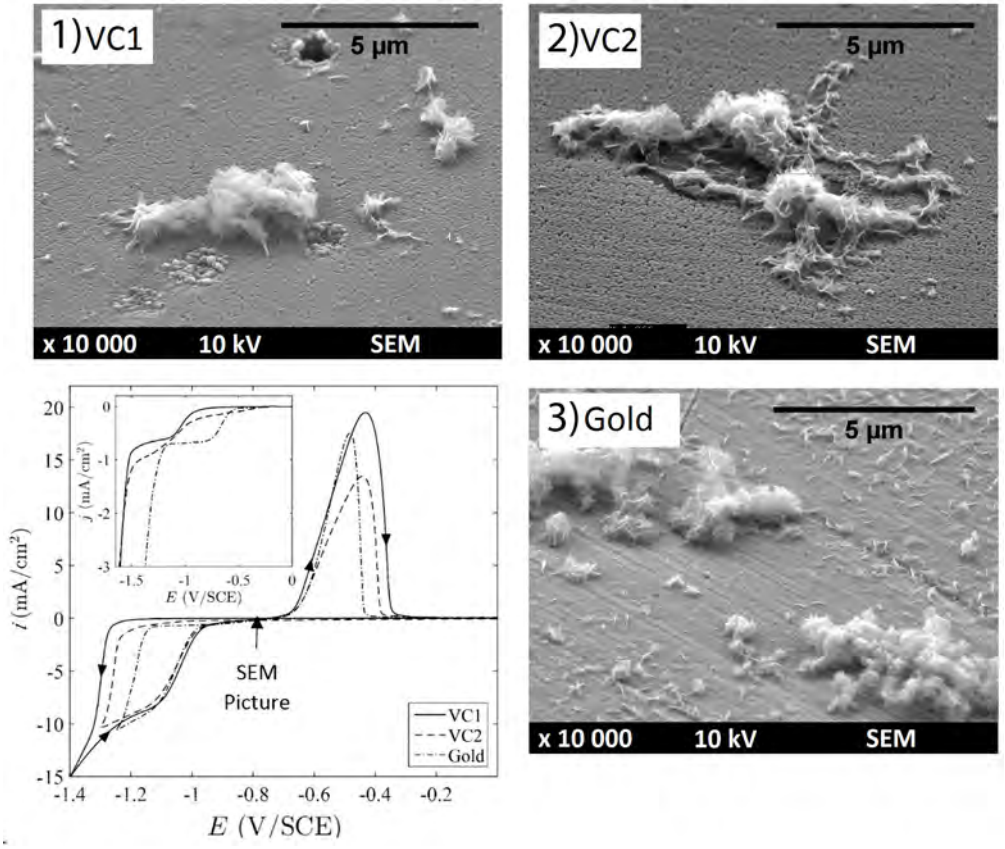

Figure 2.15: Cyclic voltammetry scans obtained in Mohr's salt and the corresponding SEM pictures. Curves (forward and backward) obtained on an RDE for: VC1, VC2, gold. Insets: Residual currents (forward curve). SEM pictures (taken at the end of the cathodic cycle): 1) to 3) iron electrodeposited on respectively VC1, VC2 and gold electrodes.

In the sulfate medium, iron electrodeposited on gold (Figure 2.15, picture 3) and VC substrates (Figure 2.15, pictures 1-2) presents quite similar morphologies: a thin layer of iron covers the surface (verified by Energy Dispersive X-Ray Spectroscopy) with

iron micrometric structures on it. However, a more detailed analysis of this thin layer of iron (Figure 2.16) shows that on the gold electrode, the deposit forms a continuous layer which offers a total coverage of the substrate (Figure 2.16 a)). Conversely, on the VC2 substrate (Figure 2.16 b)), some holes are visible in the iron layer revealing the substrate; the thin layer of iron is not as continuous as on the gold electrode.

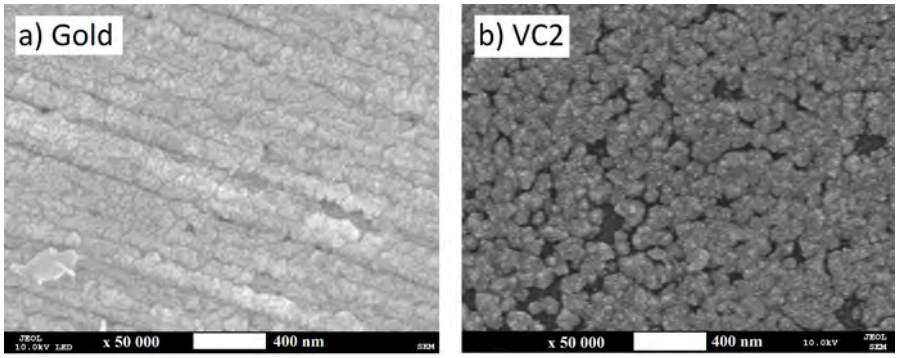

Figure 2.16: SEM pictures of iron electrodeposits, formed at the end of the cathodic part of the voltamperometric scan (starting at 0.2 V/SCE, reversed at -1.3 V/SCE, stopped at -0.8 V/SCE) using Mohr's salt solution, for the gold electrode a) and for the VC2 electrode b) respectively.

Iron spreads better on gold than on VC during its electrodeposition for both media used (the influence of the iron salt solution on iron deposit morphology will be discussed afterward). These observations show that the electrodeposited iron has more affinity with gold than with vitreous carbon electrodes. This is in agreement with the analysis of the cyclic voltammetric scans (Section 2.4.1) which has revealed that a higher energy is required to create the iron/VC interface than to create the iron/gold interface.

It has to be noticed that no difference is observed between electrodeposits on VC1 and VC2, which also confirms that the difference in roughness between these two electrodes does not affect the iron electrodeposition (neither the energy required for the iron formation nor its morphology). This is consistent with the similar shape of the cyclic voltamperogram obtained for VC1 and VC2 (Figures 2.14 and 2.15).

These results highlight the influence of the substrate on both the energy required for the iron electrodeposition and its morphology. The affinity of the iron deposit for the substrate material appears to be the key parameter.

Determination of the interfacial energy of the deposit/substrate interface

This affinity can be characterized by the interfacial energy of the deposit/substrate interface, $\gamma_{Fe/elect}$. The interfacial energies for the gold and the vitreous carbon substrates are estimated using the following theoretical development. The first step consists of estimating the work of adhesion of iron on the electrode, considering only the Van der Waals interactions and following the theory developed in [69]. Regarding the Van der Waals interactions potential profile (see Figure 2.17) for iron interacting with electrode across the liquid phase, the work of adhesion corresponds to the lowest value of this profile, it is found for a separation distance, ${d_0}^2$. The work of adhesion can then be estimated by the summation of molecular interaction between all the atoms of one medium, with all the atoms of the other medium; this leads, for two planar media, to the following equation 2.23:

$$W_{Fe/elec} = \frac{A_{elec/L/Fe}}{(12\pi d_0)^2} \tag{2.22}$$

where $A_{elect/L/Fe}$ is the Hamaker constant for iron and electrode interacting across the liquid (L). $A_{elect/L/Fe}$ is computed thanks to the following equation [69]:

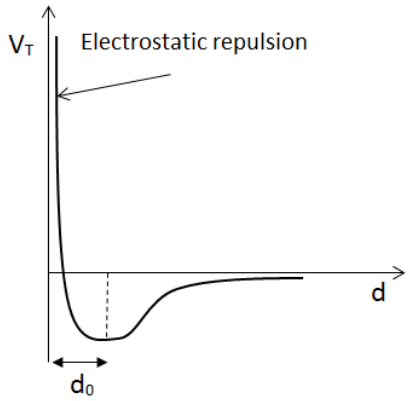

Figure 2.17: Van der Waals interactions potential, d_0 represents the separation distance between both interacting media (iron and substrate).

[2]The value d_0 to use in this equation is not known and gave rise to many questions. However, surface and adhesion energies estimated for various compounds with a value $d_0 = 0.165$ nm, yields values in good agreement with those measured [69].

$$A_{elect/L/Fe} = (\sqrt{A_{elect}} - \sqrt{A_L})(\sqrt{A_{Fe}} - \sqrt{A_L}) \tag{2.23}$$

Where A_{elect}, A_L and A_{Fe} are the computed Hamaker constants from the Lifshitz theory of respectively electrode material, water and iron; the following Hamaker constants values are used: $A_{Au} = 45.3 \times 10^{-20}$ J [76], $A_L = 3.7 \times 10^{-20}$ J (Hamaker constant of water, [69]) and $A_{Fe} = 26.0 \times 10^{-20}$ J [77]. The value of A_{VC} can be estimated using the measured surface energy of the VC electrodes, $\gamma_{VC} = 31.5$ mJ/m^2 (averaged value of surface energies measured for VC1 and VC2, see Table 2.3), via the following calculation.

From Dupré's equation [3]:

$$W_{VC/VC} = \gamma_{VC} + \gamma_{VC} - \gamma_{VC/VC} = 2\gamma_{VC} \tag{2.24}$$

The equation 2.22 can be applied for the VC/VC case [4]:

$$W_{VC/VC} = \frac{A_{VC}}{12\pi d_0^2} \tag{2.25}$$

Therefore, from Equation 2.25 and 2.24:

$$A_{VC} = 24\pi d_0^2 \gamma_{VC} \tag{2.26}$$

Finally, the combination of Equations 2.22 and 2.23, leads to the work of adhesion of iron on each electrode material: $W_{Fe/Au} = 149$ mJ/m^2 and $W_{Fe/VC} = 19$ mJ/m^2. These estimations of the work of adhesion will be further exploited in Chapter III; here they are used as the first step for the interfacial energies determination.

On the basis of these values of the work of adhesion, interfacial energies $\gamma_{Fe/elect}$ can be estimated. Indeed, the work of adhesion can be expressed as a function of the interfacial energies involved in the system using the Dupré's equation:

$$W_{Fe/elect} = \gamma_{Fe/L} + \gamma_{elec/L} - \gamma_{Fe/elec} \tag{2.27}$$

[3] $\gamma_{VC/VC}$ =0 mJ/m^2
[4] $A_{VC} = A_{VC/VC}$

Where $\gamma_{Fe/L}$, $\gamma_{elec/L}$ and $\gamma_{Fe/elec}$ are the interfacial energies of respectively the iron/liquid (the liquid, L is the electrolytic solution), of the electrode/liquid and iron /electrode interfaces.

$W_{Fe/elect}$ corresponds to the energy per unit area required to separate the iron surface from the electrode surface in the electrolytic solution. Using Equation 2.27, $\gamma_{Fe/VC}$ - $\gamma_{Fe/Au}$ can be expressed as:

$$\gamma_{Fe/VC} - \gamma_{Fe/Au} = \gamma_{VC/L} - \gamma_{Au/L} + W_{Fe/Au} - W_{Fe/VC} \tag{2.28}$$

Girifalco and Good [78] have shown that interfacial energies can be approximately computed as a function of the surface energies by:

$$\gamma_{a/b} = \gamma_a + \gamma_b - 2\phi_{a/b}\sqrt{\gamma_a \gamma_b} \tag{2.29}$$

Where $\gamma_{a/b}$ is the interfacial energy between phase a and phase b, γ_a and γ_b are the surface energies of respectively phase a and b, $\phi_{a/b}$ is an adjustment parameter which depends on interactions between a and b.

The relation 2.29 is applied for the VC electrode and for the gold electrode interfaces:

$$\gamma_{VC/L} = \gamma_{VC} + \gamma_L - 2\phi_{VC/L}\sqrt{\gamma_{VC}\gamma_L} \tag{2.30}$$

$$\gamma_{Au/L} = \gamma_{Au} + \gamma_L - 2\phi_{Au/L}\sqrt{\gamma_{Au}\gamma_L} \tag{2.31}$$

γ_L is taken as the pure water surface energy, 73 $\mathrm{mJ/m^2}$ at 20 μC (i.e. neglecting salts content). As previously, the value 31.5 $\mathrm{mJ/m^2}$ is chosen for γ_{VC}. For the gold surface energy, the value of γ_{Au}, determined by contact angle measurement in section 2.2.2, is also used: $\gamma_{Au} = 27$ $\mathrm{mJ/m^2}$ (measured at ± 2 $\mathrm{mJ/m^2}$). The adjustment parameters $\phi_{Au/L}$ and $\phi_{VC/L}$ are generally close to 1. Indeed, according to the experiments of Girifalco and Good [78], carried out with a lot of material combinations (including mercury as metal), the adjustment parameter lies in the range [0.31, 1.17].

Using extreme values (0.31 and 1.17), interfacial energies $\gamma_{VC/L}$ and $\gamma_{Au/L}$ are estimated as being within the wide range [75 mJ/m^2 ; 0 $\mathrm{mJ/m^2}$] and [73 $\mathrm{mJ/m^2}$; 0

mJ/m^2] respectively (restricting to positive values). Finally, applying equation 2.29, $\gamma_{Fe/VC} - \gamma_{Fe/Au}$ lies in the range of positive values [204 mJ/m^2 ; 57 mJ/m^2] meaning that $\gamma_{Fe/VC} > \gamma_{Fe/Au}$.

Thus, this theoretical development confirms our previous observations on the deposit morphology, since it highlights that more energy is needed to create the iron/VC interface than the iron/gold interface ($\gamma_{Fe/VC} > \gamma_{Fe/Au}$). It is also consistent with the overpotential needed for $Fe^{(II)}$ reduction: $\eta_{Fe/VC} > \eta_{Fe/Au}$.

Furthermore, these results can also be correlated to the electrodeposition theory (exposed in section 1.2.1), which considers that the initial stage of metal deposition depends on the affinity between the deposit and the substrate, and more precisely to the binding energy and the crystallographic misfit between the two materials. This theory is only valid for metal electrodeposition on another foreign metal. Therefore, it cannot be applied to the vitreous carbon case, since it is not a metal and does not have a crystallographic structure contrary to iron and gold. Regarding the internal structure of the vitreous carbon (see Figure 2.18), it can be justified to say that the misfit between the crystallographic structure of the iron deposit and the structure of vitreous carbon is important. This misfit can explain the higher energy required to create the iron/VC interface and the less regular deposit obtained on VC in comparison with the gold substrate case (Figure 2.14 and Figure 2.16).

Regarding the iron electrodeposition on gold (thin iron layer, see Figure 2.14 picture 3 and Figure 2.15 picture 3), the deposit mechanism followed does not seem to be the Volmer-Weber mode, which leads to a 3D island growth, but rather the Frank-van der Merwe or the Stranski-Krastanov models (see Chapter I) revealing a good affinity between iron and gold.

To conclude, these results have highlighted the influence of the substrate on the iron electrodeposition, particularly on its morphology but also on the energy required for its formation. The key parameter seems to be the substrate material and not the substrate roughness. As mentioned above, no significant effect of the roughness has been revealed. Therefore, it can be concluded that the substrate material and more precisely the interfacial energy of the deposit/substrate material is a control parameter for the iron electrodeposition.

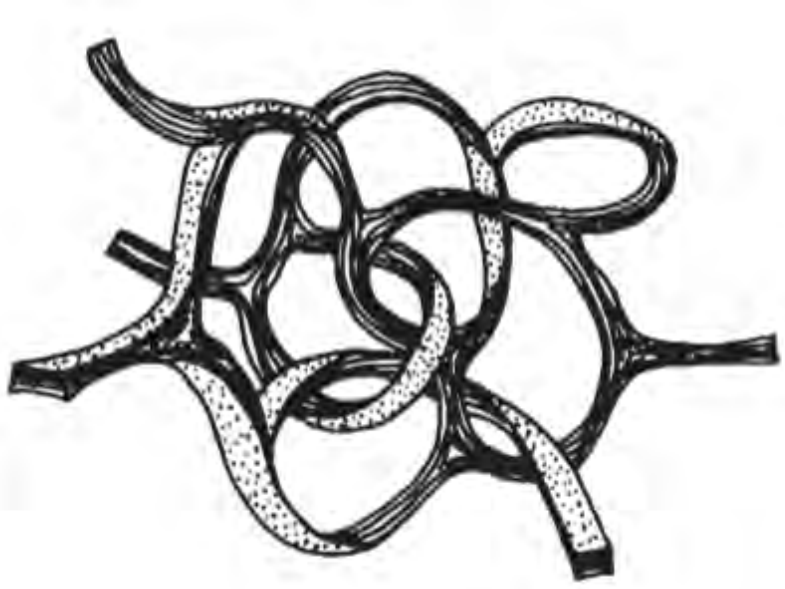

Figure 2.18: Structural model proposed by [79] for the network of ribbon stacks in glassy carbon

However, this interfacial energy value only drives the first stage of iron electrodeposition. Others factors, such as the iron salt, impact the growth of the deposit afterward. Indeed, for the VC substrates, the morphology obtained in sulfate medium is really different from the one obtained in chloride medium (Figure 2.15, picture 1-2 and Figure 2.14 picture 1-2). The effect of the composition of the electrolytic solution, on the deposit morphology, have already been observed and investigated by different authors [42] [80]. Trompette et al. [42] show that the morphology of iron deposit changes from cubic to round shape as a function of the nature of the supporting electrolyte. These observations can be correlated to the Wulff's law, which predicts that the crystal shape depends on the growth rates of the different crystallographic faces. The presence of some ions in the solution can modify the morphology of a crystal, by the preferential adsorption of these ions on specific crystal faces. This induces the reduction of the growth of the crystal faces affected, leading to a modification of the crystal shape. This phenomenon can explain the difference of morphology observed between iron electrodeposited in sulfate and chloride media on the same substrate. Therefore, the electrodeposit morphology is dictated both by the electrode material and the electrolyte

composition.

2.4.3 Influence of the electrodeposit morphology on the cyclic voltammetric scan

Identification of the different morphologies obtained on each substrate, in both chloride and sulfate media, enables now to have a better understanding of the differences observed (in section 2.4.1) between the voltammetric scans. It has been mentioned before (section 2.4.1), that the limiting current in chloride medium is higher on the gold than on the VC electrodes (Figure 2.14). The great difference in iron morphology observed for gold and VC electrodes, can explain this slight but systematic difference of limiting current value, measured for both substrates (cathodic backward scan).

As previously mentioned, on the gold electrode, the SEM image reveals a quasi-total coverage of the electrode surface by a thin iron layer (90 nm). Therefore, the electroactive surface area for the gold can be considered as the geometrical surface area (see a schematic representation of the electrodeposits in Figure 2.19 a) for gold and b) for VC). On the VC electrodes (Figure 2.14, pictures 2 and 3) iron electrodeposits consist of relatively small dendrites of which heights (< 1 μm) are lower than the thickness of the diffusion layer δ, deduced from the Levich Law ($\delta = 1.61 D^{1/3} \nu^{1/6} \omega^{-1/2} \approx 14$ μm). Therefore, the diffusion layer can still be considered as linear (no deformation of the diffusion layer induced by the deposit morphology). However, the deposit being constituted of dendrites, the electroactive surface area may be limited to the sum of surface areas of the growing dendrites tops (projected surface area), which is lower than the geometrical surface area of the electrode (see Figure 2.19 b). Thus, the difference of limiting currents observed between the gold and the VC substrate, for the $Fe^{(II)}$ reduction in chloride medium can perhaps, be simply explained by a reduced electroactive surface area associated with iron dendritic growth on the VC electrodes, while on the gold electrode, a fine iron layer is formed.

In sulfate medium, similar magnitudes of the pseudo limiting current are measured for gold and VC electrodes (cathodic backward scans, Figure 2.15), corresponding to the reduction of $Fe^{(II)}$ on the substrate covered by the iron electrodeposit). This is consistent with the similar iron morphology observed on the different substrates in Mohr's salt

medium (Figure 2.15, pictures $1-3$).

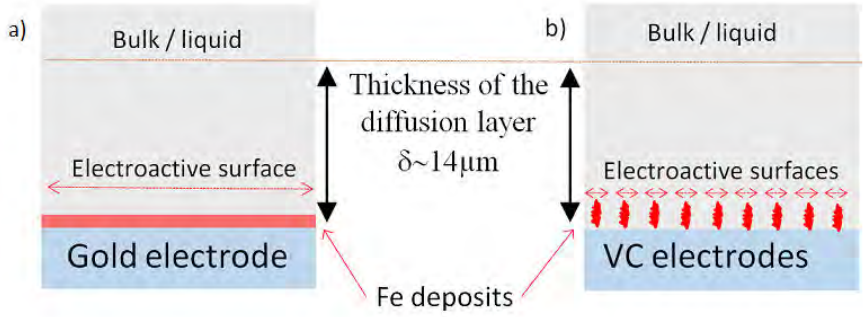

Figure 2.19: Schematic representation of the iron electrodeposit morphologies obtained in chloride medium and the corresponding electroactive surface. a): on the gold electrode, b): on the VC1 and VC2 electrodes

In addition to the observations made about the limiting current, differences also appear between gold and VC electrodes, on the backward cathodic curves ($Fe^{(II)}$ reduction on electrodeposited iron). While the curves obtained overlap in sulfate medium (Figure 2.15), they do not in chloride medium (Figure 2.14). Indeed, the backward curves for VC1 and VC2 in chloride medium (Figure 2.14), overlap and exhibit lower overpotential (activation area starting at ≈ -0.9 to ≈ -1.05 V/SCE in comparison to the backward curve obtained using the gold electrode (higher overpotential, activation area starting at ≈ -0.95 to ≈ -1.15 V/SCE). The iron electrodeposits morphology (Figure 2.14, SEM pictures 1-3) could explain the surprising lower overvoltage observed on VC electrodes; indeed, the iron electrodeposit on the gold electrode (picture 3 in Figure 2.14) is more uniform but consists of a really thin layer ($thickness = 80$ nm), while iron electrodeposited on VC electrodes (pictures 1 and 2 in Figure 2.14) presents micrometric dendrites of ≈ 1 μm. Therefore, the thickness of the iron deposit seems to be the cause of the difference observed in the cyclic scans.

To check this theory, a higher quantity of iron on the gold electrode will be produced. To that end, the potential scan rates are decreased ($20 \longrightarrow 8 \longrightarrow 2$ mV/s) in order to increase the cathodic charge passing through the electrochemical cell ($5.7 \longrightarrow 14.7 \longrightarrow 62.7$ mC), leading to a higher quantity of iron electrodeposited. The results are shown in Figure 2.20. The SEM pictures (Figure 2.20 b and c) of iron deposit produced on the

gold substrate during a cathodic scan, show that increasing the amount of iron deposit leads to a change in its structure.

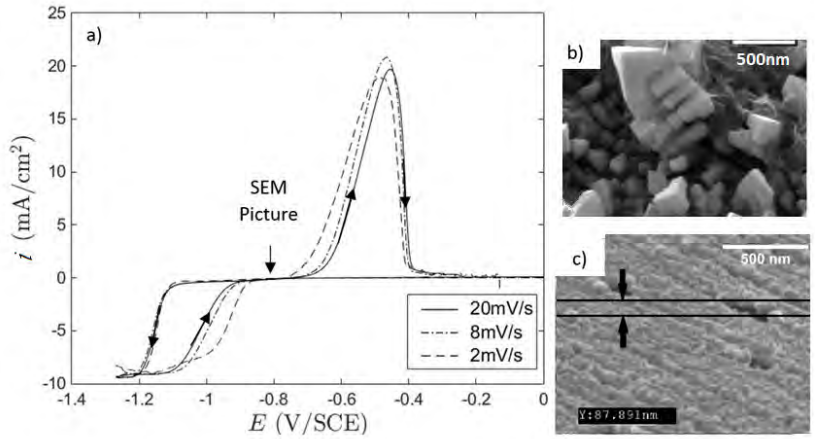

Figure 2.20: a) Potential scan rate dependence of the voltamperometric curves (forward and backward) obtained on a rotating gold disk electrode, immersed in the $FeCl_2$ solution. SEM pictures of iron electrodeposit obtained on gold after a cathodic cycle (starting at 0.2 V/SCE) reversed at -1.25 V/SCE, and stopped at -0.8 V/SCE at b) 8 mV/s and c) 20 mV/s.

As previously mentioned, iron deposits produced for a scan rate of 20 mV/s on gold, during the cathodic scan, spread on the electrode surface as a thin layer. The SEM picture (Figure 2.20c) reveals that for a scan rate of 20 mV/s, the thickness of the deposit is about 80 nm which is closed to the equivalent compact layer thickness:

$$e = (M_{Fe} \int Idt)/(2F\rho_{Fe}S_{disk}) = 67nm \tag{2.32}$$

With M_{Fe} and ρ_{Fe} respectively the molar mass and density of iron.

This confirms the spreading of iron and a 2D growth of the deposit on the gold electrode. A 3D growth of the deposit is obtained only when a larger quantity of iron is deposited (Figure 2.20b), e.g for low scan rates 8 mV/s and 2 mV/s. Indeed, decreasing the scan rate from 20 mV/s to 8 mV/s leads to a change from a homogeneous and ultrathin deposit (Figure 2.20c) to a micrometric and dendritic deposit [5]. The $I = f(E)$

[5]Iron spreads on the gold surface and once the surface is totally covered, deposit starts to growth following a 3D growth mode and dendritic morphology appears. As mentioned, this dendritic structure may be favored by the chloride medium, as it is the case for the electrodeposition on vitreous carbon.

curves obtained for the three scan rates (Figure 2.20a) are similar to those indicated in Figure 2.14; the forward cathodic scans exhibit a diffusion-limited plateau at -1.2 V/SCE for which the magnitude of the limiting current is not affected by the potential scan rate. This means that the system operates in a steady-state for the three curves; the limitation of the current is due to the mass transfer which remains constant under a constant agitation applied. Concerning the backward cathodic scan, the curves show that, decreasing the potential scan rate ($20 \longrightarrow 8 \longrightarrow 2$ mV/s) causes the half-wave potential of the $Fe^{(II)}$ reduction on native iron, to shift to the anodic values ($-1.014 \longrightarrow -0.992 \longrightarrow -0.938$ V/SCE).

This confirms the assumption that the shape of the cathodic curves is dictated by the structure of iron deposited and therefore by the quantity of iron produced: the greater the quantity produced, the more reversible the system becomes. This fact suggests that a certain quantity of iron is required for the deposit to behave as a "bulk iron" electrode. It can be thought that the electrodeposit obtained at 20 mV/s is so thin (80 nm) that its electrocatalytic properties are affected by the electronic collector (gold), and the $Fe^{(II)}$ reduction appears as a slower system; for slower scan rates bigger iron structures are formed (dendrites) and can act as a "bulk iron" electrode.

This effect is not observed on VC electrodes because, even at 20 mV/s, the corresponding iron electrodeposits consists of micrometric iron dendrites, which behave as massive iron form (Figure 2.14, SEM pictures 1 and 3).

2.5 Iron electrodeposited by galvanostatic electrolysis

The study of the iron electrodeposits obtained by cyclic voltammetry has enabled to highlight the influence of the substrate on both, the energy required for its formation and its morphology. It also appeared that the main control parameter is, in fact, the substrate material. Indeed, the difference in the roughnesses of the VC substrates (VC1 and VC2, see Figure 2.4) does not induce significant effects on the iron electrodeposition (neither on the cyclic scans nor the iron morphology). To confirm the statements obtained by cyclic voltammetry, iron galvanostatic electrodeposition is performed, and the effect of both the electrode material and the electrode roughness are examined.

SEM pictures of iron electrodeposited in chloride medium, during 30 s [6] at a constant current of 90% I_{lim} on the gold , VC1 and VC2 substrates are presented in Figure 2.21.

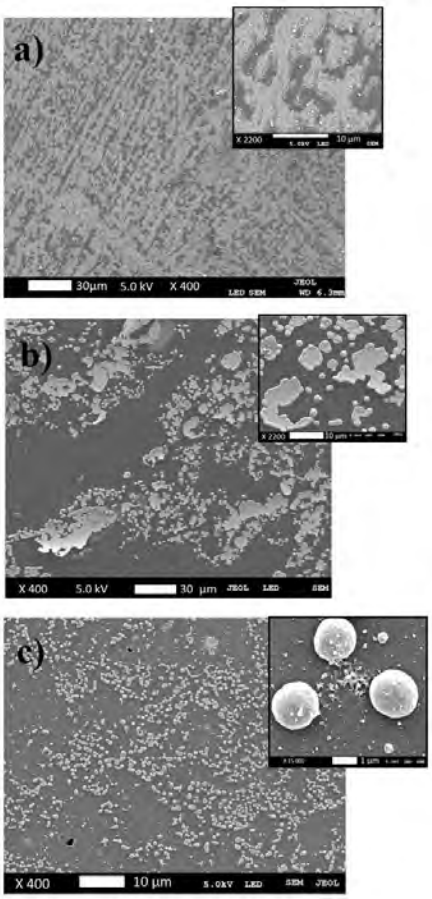

Figure 2.21: Iron electrodeposited under constant current I=90% I_{lim} in 0.01 M $FeCl_2$, during 30s, with a rotating speed of 1000 RPM on a) a gold, b) VC2 and c) VC1 substrates.

As for cyclic voltammetry, iron electrodeposited on the gold electrode under constant current electrolysis consists of a thin film which offers a relatively uniform coverage of the electrode Figure 2.21 a). By contrast, the electrodeposit on the VC substrates consists of spherical and micrometric iron particles, isolated form one another (Figure 2.21 b) c)). It can be noticed that on the VC2 substrates, some iron particles

[6] The duration of the electrolysis Δt is chosen in order to obtain an equivalent iron-compact layer of 85 nm for each electrode.

seems to have coalesced forming bigger plates Figure 2.21 b). Therefore these results are consistent with the conclusion of the cyclic voltammetric study: the iron deposit tends to spread in a thin 2D layer on the gold electrode, whereas on the VC substrates a 3D growth is favored. Results confirm that the interfacial energy $\gamma_{Fe/elect}$ controls the growth mode of the iron deposit (2D or 3D mode).

Besides, even if the tendency is almost the same in voltammetry and galvanostatic electrodeposition, the morphologies of the deposits, obtained with these two methods, differ from one another on the VC substrates: iron electrodeposits have a dendritic structure with cyclic voltammetry, whereas round shape particles are observed under galvanostatic electrolysis. This difference in the morphology of the electrodeposited iron could be attributed to the electrodeposition mode and the cathodic current applied: with voltammetry, electrodeposition is conducted under continuous evolution of the applied voltage and the resulting current continuously increases to its limiting value, while galvanostatic electrolysis is carried out with a current close (90 %) to the limiting current. As often observed in galvanostatic electrodeposition, electrodeposit tends to be dendritic/powdery when the applied current is equal to, or higher than the limiting current [81] [82]. Even when the applied current is just below the limiting current, a "less rough" and "less dendritic" electrodeposit morphology could be obtained [83] [82].

On another hand, some iron plates seem to be partially detached from the VC2 electrode, probably with the effect of the electrode rotation; this can be related to the low values of the adhesion work estimated in the previous section: $W_{Fe/VC} < W_{Fe/Au}$. However, it can be noticed that this observation is only valid for the VC2 substrate; no detachment of the deposit is observed on VC1. Both substrates (VC1 and VC2) presenting surface energies quite similar, this difference between the two deposits may be attributed to the electrode roughness (Ra = 35 nm for VC1 and Ra = 8 nm for VC2). To confirm this assumption, iron electrodeposits are produced on the VC2 P1200 and VC2 P800 electrodes (VC2 electrode polished with paper grid P1200 and P800, section 2.2.2) which show arithmetic roughnesses of 162 nm and 345 nm respectively.

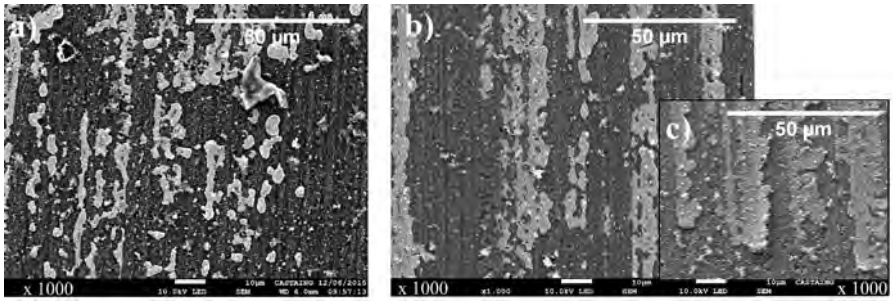

Figure 2.22: SEM images of the galvanostatic electrodeposits produced on VC2 polished with a) P1200 and b) P800 paper grids. c) SEM image with 40 ° tilt angle of the iron electrodeposit on VC2 P800.

Deposits obtained on these rough surfaces (Figure 2.22) can be compared with deposits obtained on a smooth VC2 electrode (polished with 0.3 mm alumina suspension, Figure 2.21 b) where iron is deposited randomly, forming rounded particles and micrometric plates/flakes (Figure 2.21 b)). On the rough surfaces (VC2 P800 and VC2 P1200), micrometric plates are also observed, but they grow along the stripes, following the topography of the substrates (Figure 2.22). Furthermore, SEM pictures, taken with 40 ° tilt, show that iron preferentially grows at the bottom of the stripes (Figure 2.22 c)). This behavior does not correlate with the classical phenomenology of galvanostatic electrodeposition on rough substrates. When the thickness of the diffusion layer ($\approx 14\ \mu$m here) is greater than the height of the stripes (2 μm here, macroprofile), metal should be preferentially deposited at the top of the stripes [83]. This observation can not be explained at this time. However, linear voltammetry conducted on these three surfaces reveals that the greater the roughness, the lower the overpotential of initial $Fe^{(II)}$ reduction is (Figure 2.23). By analogy with the analysis undertaken in section 2.4.2, this fact suggests that polishing stripes offer an area where $\gamma_{Fe/VC}$ is lowered, facilitating iron deposition. $\gamma_{Fe/VC}$ should, therefore, be lower at the bottom of the stripes than at the top, leading to an improved adhesion of these "anchored" deposits.

To conclude, the iron deposit morphologies obtained under galvanostatic electrolysis confirm the conclusion established in the cyclic voltammetric study. The interfacial energy of the deposit/electrode interface induces preferentially a 2D growth on the gold substrate and a 3D growth on VC substrate. Concerning the influence of the roughness, even if no difference of morphology between iron deposited on VC1 and VC2 is

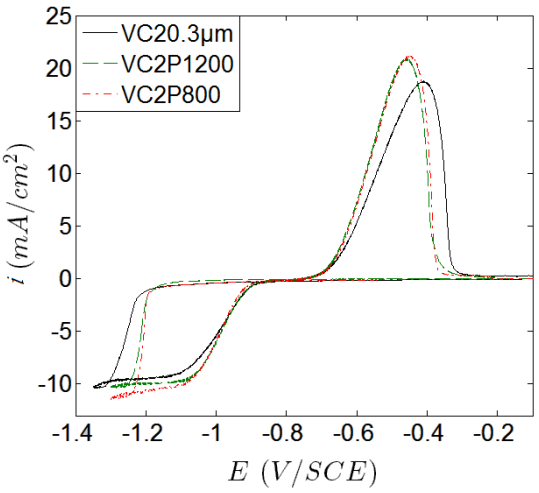

Figure 2.23: Influence of the substrate roughness on cyclic voltamperometric scans. The cyclic voltammetry is performed in a 0.01 M $FeCl_2$ solution, $\upsilon = 20$ mV/s, $\omega = 1000$ RPM, on VC20.3μm, VC2P1200 and VC2P800.

observed by the cyclic voltammetric study, the iron deposited by galvanostatic electrolysis highlights that the roughness can have an influence on the adhesion of the deposit; surface defects could act as anchorage points.

2.6 Conclusion

This chapter, focusing is on influence of the electrode substrate on the the iron electrodeposition, provides a better understanding of the laws and parameters governing this process.

As a first step, a preliminary analysis is conducted to study the $Fe^{(II)}$/Fe system and to define the main influencing parameters for the formation of the iron deposit. To that end, steady-state voltammetry is performed on a gold electrode by varying the pH of the solution and the reverse potential of the scans.

This analysis enables to demonstrate that the proton H^+ reduces before, or simultaneously to the $Fe^{(II)}$ reduction. The pH of the solution is a parameter to consider for the iron electrodeposition because of a pH$<$ 2.0 induces both the decrease of the Faradaic yield as well as the corrosion of the deposit. Higher pH (pH$>$ 5.0) appears to

be more advantageous, but the voltammetric study reveals the formation of iron hydroxides. Therefore, the study was carried out with the natural pH of the $FeCl_2$ solution (pH = 4.0). The voltammetric study also highlights the importance of choosing the appropriate potential for ion electrodeposition. Indeed, a too cathodic potential induces also the formation of hydroxides.

The influence of the different substrate materials (gold, and vitreous carbon) at various roughnesses (VC1, VC2, VC2 P1200, VC2 P800) are tested, and a detailed analysis of the cyclic voltammetry scans enables to highlight that the energy required to create the iron/VC interface, is higher than this for the iron/gold interface. Simultaneously, the analysis of the deposits morphology obtained (during the cathodic part of the cyclic voltammetry scans) confirms the previous observation, showing that the iron deposit tends to spread in a continuous 2D layer on the gold substrate, while a 3D growth is favored on the VC substrates. This confirms a better affinity between iron and gold than between iron and vitreous carbon.

These results are correlated with estimations of the interfacial energy of the deposit/substrate interface for both substrates (gold and VC) which are determined from surface energies measurements. The results of these calculations show that $\gamma_{Fe/VC} - \gamma_{Fe/Au}$ lies in the range of positive values [204 mJ/m^2 ; 57 mJ/m^2] meaning that: $\gamma_{Fe/VC} > \gamma_{Fe/Au}$.

Concerning the substrate roughness, the slight difference observed between both VC substrates (Ra is about 35 nm for VC1 and 8 nm for VC2) does not have a significant effect on iron electrodeposition. In fact, higher roughnesses values are necessary to observe the influence of the substrate roughness. Indeed, electrodeposition by galvanostatic electrolysis on the VC2, VC2 P1200, VC2 P800 substrates show that the iron electrodeposit tends to grow along the stripes, because the polishing creates stripes which offer areas exhibiting lower $\gamma_{Fe/VC}$, favoring the iron deposition.

To conclude, this chapter enables to demonstrate the influence of the substrate on both the energy required for the formation of an iron electrodeposit and its morphology. The substrate material, through its effect on the interfacial energy of the deposit/substrate interface, appears to be the most influencing parameter.

3 Dispersion of iron electrodeposit by ultrasonication: influence of the substrate

3.1 Objectives

The sonoelectrochemical synthesis of metallic particles is the combination of two different processes: the metallic electrodeposition and the deposit dispersion by ultrasounds; both steps can be carried out simultaneously or sequentially. This chapter focuses on the second step of the sonoelectrochemical synthesis, the deposit dispersion by ultrasonication, and expect to define and optimize the influencing parameters, specifically, the two substrate properties (surface energy and roughness). The obtained results will be correlated with the iron electrodeposit morphology as well as with the work of adhesion values studied in Chapter II.

First, the iron electrodeposition by cyclic voltammetry is performed under ultrasonication, and experiments are carried out using three different substrates.

Then, the electrodeposition and dispersion phases are performed separately. The iron electrodeposits are produced by galvanostatic electrolysis under silent conditions and the dispersion by ultrasound of the obtained deposits is discussed.

In addition to the influence of the substrate, the effect of the electrodeposited particles size on the dispersion process is also investigated, with the aim of determining the size of the smallest particle removable by the ultrasonic device employed.

3.2 Material and methods

3.2.1 Experimental device

The experimental device consists of the electrochemical cell presented in chapter II which is immersed into an ultrasonic bath. Special care is always taken to put the cell in the same place so as to generate the same ultrasound intensity into the cell. A schematic representation is proposed in the Figure 3.1

3.2.2 Electrodes involved and their physical properties

The electrodes used in this chapter, and their preparation, are the same as the ones employed in the previous chapter (section 2.2.1 and 2.2.2).

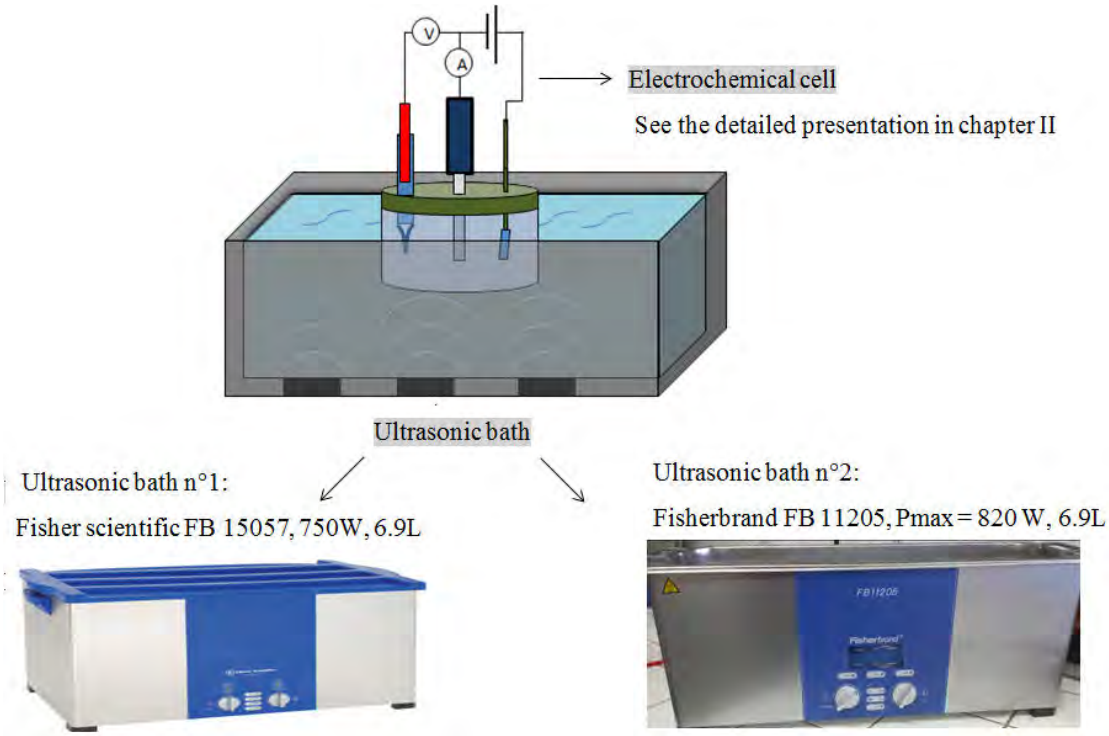

Figure 3.1: Three electrodes electrochemical cell immersed into an ultrasound bath (two types of baths are used)

Electrode materials surfaces energies

From the obtained values of the electrodes surface energy, the theoretical development presented in section 2.2.2 has enabled to estimate the work of adhesion of the deposit/substrate interfaces. These values serve as a basis for the discussion proposed in this chapter. Therefore a summary table 3.1 is proposed.

	Surface energy	Adhesion work
Electrode	γ_{elect} mJ/m^2	$W_{Fe/elect}$ (mJ)
Gold	27 ± 3	148
VC1	29 ± 2	16
VC2	34 ± 2	22
Average value for VC	31.5 ± 2	19

Table 3.1: The used electrode materials (from Chapter II: Surface energy and adhesion work values.

The theoretical development (section 2.2.2) has also enabled to compare the interfacial energies of the deposit/substrate interfaces obtained with gold and VC substrates, it has been concluded that the difference $\gamma_{Fe/VC} - \gamma_{Fe/Au}$ lies in the range of positive values [204 mJ/m^2 ; 57 mJ/m^2] meaning that a higher energy is required to create the Fe/VC interface.

Electrodes surfaces roughness

The influence of the substrate roughness on the electrodeposit dispersion is also discussed in this chapter. Therefore a summary table 3.2 of the roughness values measured for the different VC substrates in Chapter II section 2.2.2 is reminded.

Electrode	Ra (nm)
VC1 0.3 μm	35 $\pm$3
VC2 0.3 μm	8$\pm$3
VC2 P1200	162 $\pm$3
VC2 P800	345 $\pm$3

Table 3.2: Roughness values of the electrodes used (from Chapter II)

3.2.3 Electrochemical techniques coupled with ultrasonication

Cyclic voltammetry

Cyclic voltammetry at the steady state, coupled with ultrasonication, is used here to plot the I/E curves on the gold, VC1 and VC2 substrates polished with a 0.3 μm alumina suspension, in both chloride and sulfate media. The ultrasonication is activated during the cyclic scan measurement, e.g., the electrodeposition.

Procedure

Typical experiment consists of the following steps:

1. Three cyclic scans are carried out under silent conditions, to check repeatability of the voltammogram of the electrode.

2. Cyclic voltamperometry is performed with a continuous stirred solution ($\omega =$ 1000 RPM potential scan rate = 20 mV/s), under ultrasonication or under silent

conditions (for a reference scan measurement). Forward scan starts from the open circuit potential (OCP $\approx +0.2$ V/SCE and goes to the cathodic direction (to -1250 mV/SCE for the gold electrode and to -1360 mV/SCE for the VC electrodes), then the scan is reversed to potentials of around 0 V/SCE.

Evaluation of the deposit dispersion

The integration of both the cathodic wave (forward and backward) and the anodic peak of each cyclic scan, achieved with and without ultrasounds, enables determining the ratio of the cathodic and anodic charges Qc/Qa. The total cathodic charge Qc corresponds both to the Fe^{II} and the H^+ reduction (see Chapter II section 2.3.1) while the anodic charge Qa only corresponds to the oxidation of the iron freshly produced and remained on the electrode surface. Without ultrasounds, the ratio Qc/Qa is expected to be slightly higher than 1.0. With ultrasounds, if a portion of the iron deposit has been removed from the electrode during the process, the resulting ratio Qc/Qa increases and can reach infinite. Thus, the comparison of the obtained Qc/Qa values allows discussing the effect of ultrasounds.

Galvanostatic electrolyses

The electrodeposition and ultrasonication steps are carried out separately:

- first, the iron is electrodeposited by galvanostatic electrolysis under silent conditions,
- then, ultrasonication is activated.

Procedure

The experiments are achieved in both chloride and sulfate media.Typical experiment consists of the following steps:

1. Before each galvanostatic electrodeposition, three cyclic voltammograms are achieved to both check the repeatability of the voltammogram and to determine the limiting current value.
2. Then, a pretreatment step consisting of applying a potential $E = 0$ mV/SCE during 20 s is achieved, it expects to remove possible traces of iron remained on the

surface and to regenerate the surface of the bare electrode. It enables a better reproductivity.

3. The galvanostatic electrolysis is carried out under stirring ($\omega = 1000$ RPM) with a current $I = 90\%I_{lim}$ in order to have a fast conversion of the Fe^{II} into Fe and, at the same time, to avoid a secondary reaction to occur (formation of hydroxides see Chapter II section 2.3.2). The duration of the electrolysis Δt is chosen in order to obtain an equivalent iron-compact layer of 85 nm (see Equation 3.4) which corresponds, for example, to a cathodic charge of ≈ 16.5 mC for the VC substrates (Φ = 3 mm).

4. Once the iron is electrodeposited, the depolarized working electrode is immediately subjected to ultrasonication for a specific duration. During this step, the rotation of the working electrode is maintained.

5. To evaluate the effect of ultrasonication on the deposit dispersion, an anodic scan is immediately carried out after the ultrasonication phase (from the measured OCP to +0.2 V/SCE at 20 mV/s, with $\omega = 1000$ RPM) and without ultrasound).

Evaluation of the deposit dispersion

The integration of the anodic peak obtained during the step $n°5$ of the procedure leads to the anodic charge Qa, corresponding to the oxidation of the iron electrodeposit, remained on the electrode after the ultrasonication (step $n°4$).

The corrosion rate of the iron electrodeposit immersed in an iron salt solution at pH=4 has been estimated, in chapter II section 2.3.1 to 1.3×10^{-11} mol/s. The quantity of Fe^0 oxidized by the corrosion in 60 s is around 7.8×10^{-10} mol, which corresponds to a charge of 0.15 mC and represents a loss of $\approx 1\%$ of the total cathodic charge. To separate the effect of the corrosion from the effect of ultrasonication (step $n°4$), the Qa value is compared to a reference value Qa_{ref}, obtained using the same conditions (same procedure followed) except that the step $n°4$ is achieved without activation of ultrasound. Thus, only the effect of ultrasonication is considered.

Chronoamperometric electrolysis

The last section of this chapter is dedicated to the study of the influence of the electrodeposited particles size on the deposit dispersion. The chronoamperometric electrolysis without stirring is employed, because it enables a good control of the deposit growth. Indeed, as explained in Chapter I (section 1.2.1), the current-time curve obtained during a chronoamperometric electrolysis can be divided into three different zones corresponding to different phases of the growth:

- The double layer charge
- The growth of each single nucleus
- The overlap of the nuclei diffusion zone

The electrolysis is interrupted during the second part of the current-time curve to allow the formation of iron particles, while avoiding their overlapping. Therefore by analyzing the obtained current-time curve, this technique allows the control of the nuclei growth.

The same kind of procedure as for the galvanostatic electrolysis presented above is carried out here, the expected aim is to form a smaller quantity of iron electrodeposits.

Procedure

- Steps 1 2, 4, and 5 are identical to the three described above.

This technique differs to the previous one by step 3:

- A constant potential (corresponding to ≈ 90 % of the limiting current observed on the cyclic voltammogram achieved with $\omega = 1000$ RPM) is applied without stirring of the solution. The electrolysis time is fixed to apply a certain cathodic charge; two electrolyses are carried out with a cathodic charge of 50 and 25 μC.

Evaluation of the deposit dispersion

The same procedure as for the galvanostatic method is employed to evaluate the dispersion of the iron electrodeposit, and the Qa/Qa_{ref} value is determined for different durations of the ultrasonication (from 0 to 60 s).

3.3 Iron electrodeposition by cyclic scan voltammetry under ultrasonication

The effect of ultrasound on the iron electrodeposition process is studied by cyclic voltammetry achieved under ultrasonication. The cyclic voltammograms are carried out in chloride and sulfate media, on the three electrodes (Gold, VC1 and VC2), and compared with the ones obtained under silent conditions (see Figure 3.2. Solid lines represent the cyclic scan under ultrasonication, dashed lines the one achieved under silent conditions). The objectives of this analysis are first, to investigate the effects of ultrasounds on the electrochemical process and then, to estimate the influence of the substrate on the deposit dispersion.

3.3.1 Effect of ultrasound on mass transfer during iron electrodeposit growth

Several effects of ultrasonication on the cyclic voltamperometric scans can be observed on the Figure 3.2. The first one to be discussed here is the increase of the mass transfer and consequently of the limiting current value. Indeed, the current-potential curves obtained under ultrasonication (Figure 3.2) exhibit higher Fe^{II} reduction limiting currents (obtained during the backward scan) than those obtained under silent conditions (except the current-potential curves in Figure 3.2c which will be discussed below). These observations are in line with results of Klima [64] and Walton et al. [30] among others, already discussed in the bibliographic chapter. Indeed, as mentioned in Chapter I, section 1.3.2 Klima [64] obtains under sonication (and without rotation of the RDE) a current-potential curve similar to those obtained under steady-state voltammetry performed under stirring (see Figure 1.30). The author claims a limiting current three times higher than those obtained with an RDE (80 RPS). This increase in the mass transfer arises because ultrasounds induce cavitation bubbles and acoustic streaming, causing additional convection near the electrode and then increasing the mass transfer flux of the electroactive species. Current fluctuations observed (Figure 1.30 and mentioned in [30] [64]), are visible in the voltamperometric scans, especially on the diffusion lim-

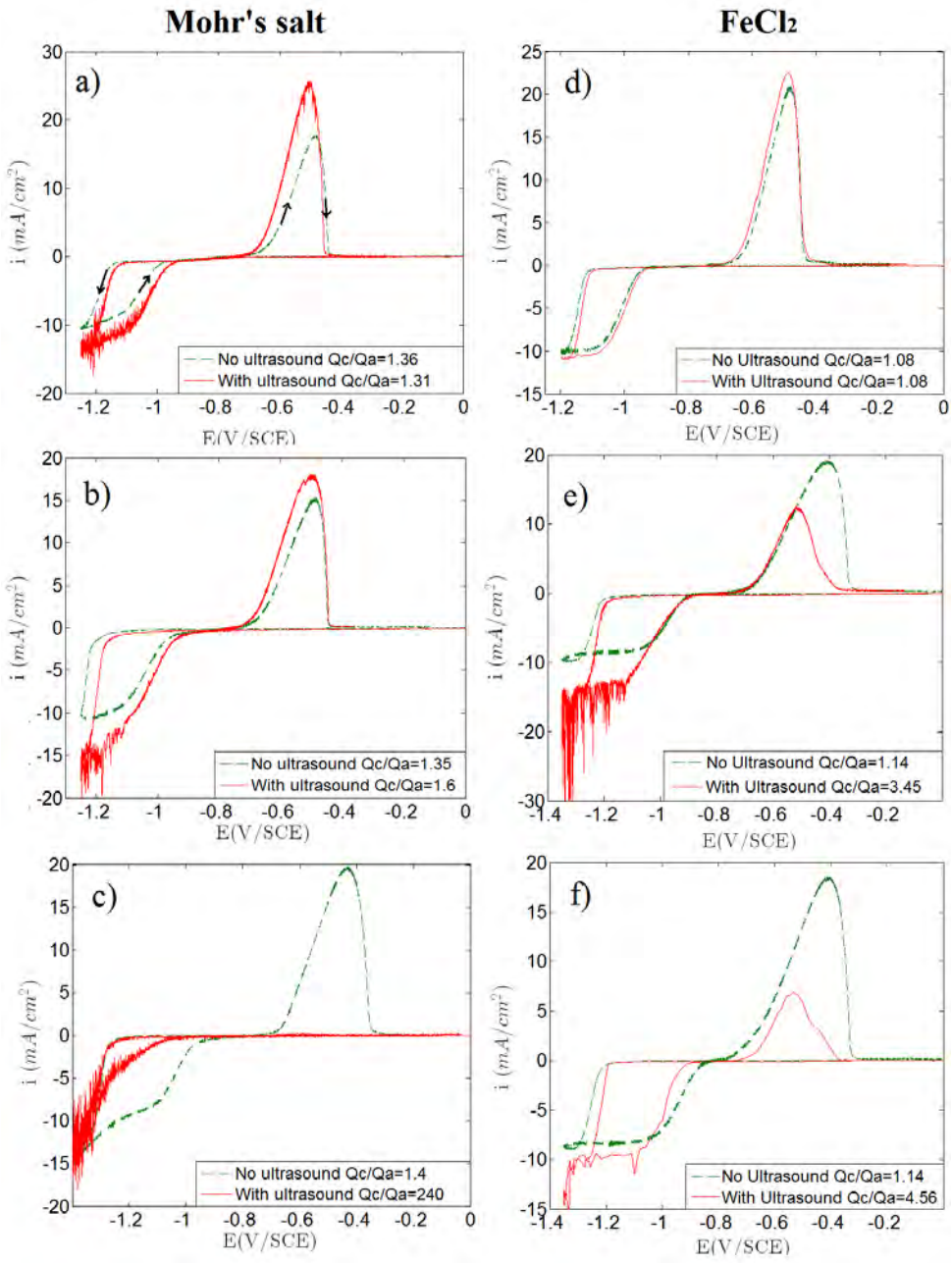

Figure 3.2: Cyclic voltammetric scans (forward and backward, see arrows in a)) obtained on a rotating disk electrode $\omega = 1000$ RPM, for three different materials: gold (a) and d)), VC1 (b) and e)) and VC2 (c) and f)). Curves in a), b) and c) obtained with Mohr's salt solution; curves in d), e) and f) obtained with $FeCl_2$ solution. Dashed lines: silent conditions, solid lines: ultrasound activated. The ratio, Qc/Qa is indicated in the graph. Ultrasonic bath 1, P=750 W.

ited plateau of Fe^{II} reduction (see Figure 3.2 a, b, e and f). They are attributed to successive collapses of the cavitation bubbles. It can be noticed that no fluctuation is observed in the activation zones of the voltammograms, confirming that ultrasounds affect the electrochemical processes mainly via mass transfer enhancement. The electronic transfer kinetics appears to be slightly affected [30] [25].

It can be noticed that the increase in the limiting current of Fe^{II} reduction on the gold electrode in chloride medium, when ultrasounds are activated (Figure 3.2 d), is low (relative increase of 7%), compared to the other ones corresponding to the curves in Figure 3.2 a, b, e and f (relative increase from 15 to 60%). On the basis of electrodeposited iron morphology (observed by SEM imaging Chapter II, pictures 1-3 of Figure 2.14 2.15), it appears that the electrodeposit obtained on the gold electrode in chloride medium and under silent conditions (Chapter II, Figure 2.14, pictures 3) is the only one to grow as a thin film. For all other Fe^{II} salts and electrode material combinations, electrodeposited iron presents micrometric dendrites reaching about 1 μm height in chloride medium (Chapter II, Figure 2.14, pictures 1 and 2) or micrometric structures in Mohr's salt medium (Chapter II, Figure 2.15, pictures 1-3). To explain this difference, different assumptions can be made.

First, one can think that changing the deposit morphology affect the quantity of cavitation bubble created by the ultrasonication. Indeed, as mentioned before, the bubbles nuclei (origin of the cavitation bubbles) can be microbubbles trapped into the defects of the solid surface. Thus, one can think that more bubbles nuclei (and so more cavitation bubbles) are obtained for rough deposits. Finally, a higher quantity of cavitation bubble will lead to an increase in the mass transfer.

Another assumption can be made, indeed, one can think that submitting the solution to ultrasounds causes an increase in the limiting current associated with the decrease in diffusion layer thickness [84]. Consequently, the increase of the iron growth induced can leads to taller dendrites than the one obtained without ultrasounds (heights > 1 μm). If the dendrites reach a height similar to the thickness of the diffusion layer, this can induce an increase of the electroactive surface area leading to a higher current magnitude (see the schematic representation in Figure 3.3 a2) and b2)). For electrodeposits growth as "a film," the electroactive surface area remains equal to the geometrical surface area of

the electrode and the current augmentations is only due to the enhancement of mass transfer by ultrasounds (Figure 3.3 a1) and b1)). This analysis provides an explanation for the observed differences in the limiting current increases with ultrasounds, between the thin film growth mode and the dendritic growth mode.

To conclude, the main effect of the ultrasounds on the electrochemical process is the enhancement of the mass transfer induced by the successive cavitation events in the vicinity of the electrode surface. The increase of the mass transfer induces the decrease of the diffusion layer and thus the increase of the limiting current.

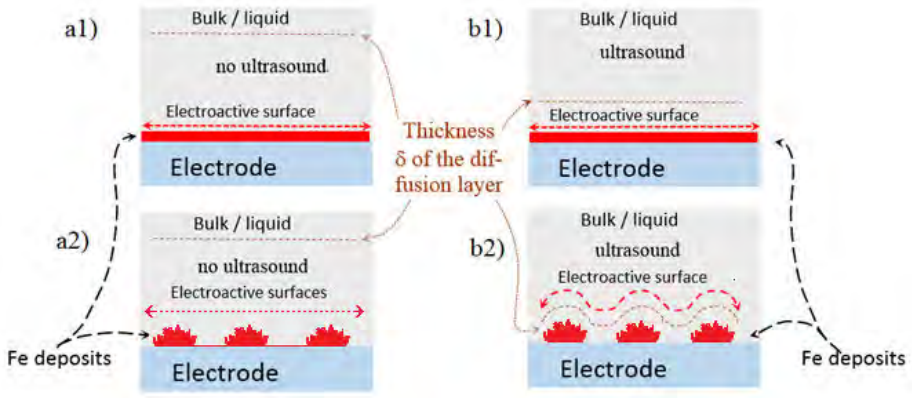

Figure 3.3: Schematic representations of diffusion layer configurations for the two main types of iron electrodeposit morphology encountered, a1)-b)1: thin film without and with ultrasounds, a2)-b2):

3.3.2 Effect of ultrasounds on iron electrodeposits dispersion

The second effect highlighted by the cyclic voltamperometric scan is the loss of iron electrodeposit revealed by the Qc/Qa ratio (see Figure 3.2). The value of the ratio Qc/Qa, higher than 1 in all cases, are used below as criterion to discuss the competitive effects of adhesion and ultrasounds on the iron electrodeposits dispersion from the electrode.

In absence of ultrasonication, Qc/Qa obtained in $FeCl_2$ (≈ 1.10) is lower than those obtained in Mohr's salt (≈ 1.35), because of the co-reduction of H^+ during the Fe^{II} reduction. Note that the charge allotted to H^+ reduction represents, in chloride medium

9 % of the total cathodic charge Qc passed, and 13 % in sulfate medium (I_{lim} is about -0.34 mA/cm^2 in $FeCl_2$ and about -0.65 mA/cm^2 in Mohr's salt medium, see Chapter II section 2.3.1).

Concerning the adhesion/dispersion of the iron electrodeposit on the gold electrode (Figure 3.2 a and d), the effect of the ultrasounds appears minor in both $FeCl_2$ and Mohr's salt media. Indeed, comparison of the ratio Qc/Qa (see legends in Figure 3.2 a and d) with ultrasonication (1.31 in Mohr's salt; 1.08 in $FeCl_2$) and without (1.36 in Mohr's salt; 1.08 in $FeCl_2$) shows very similar values, demonstrating that all the iron electrodeposited during Fe^{II} reduction, remains on the gold surface and oxidizes totally during the backward anodic scan. Conversely, for VC electrodes (see Figure 3.2 b, c, e and f), iron electrodeposits dispersion is observed in every case, Qc/Qa obtained with ultrasound is at least equal to 1.6, and it is always higher than Qc/Qa values obtained under silent conditions (Figure 3.2 b, c, e, and f). These experiments show that the substrate material as an important influence on the dispersion process.

Iron electrodeposit appears to adhere much more on the gold electrode surface than on the VC electrodes surfaces, because of the high adhesion energy between both materials; the solid deposit requires higher ultrasonication power to be removed and dispersed in the liquid. These results are in agreement with the work of adhesion determined in Chapter II (section 2.4.2),

- For iron on gold, $W_{Fe/Au} = 149$ mJ/m^2
- For iron on VC, $W_{Fe/VC} = 19$ mJ/m^2

and clearly demonstrate the importance of the deposit/substrate interface on the deposit dispersion by ultrasonication. Decreasing the surface energy of the substrate enables to minimize the work of adhesion of the deposit (Equation 2.22 2.23 2.26) inducing the enhancement of its dispersion. Similar observations were made by Hyde et al. [25] for cyclic voltammetry performed under ultrasonication for the deposition of different metals (zinc, cobalt, lead, mercury) on a vitreous carbon electrode: the resulting Qa/Qc ratio appears to decrease as the ultrasound intensity increases, highlighting a loss of metal. Authors also show that the deposit dispersion highly depends on the metal electrodeposited: lead and mercury can be dispersed by ultrasound, whereas no

significant loss in zinc and cobalt are obtained. The theoretical development presented Chap II (section 2.4.2) is applied to the metals studied in [25] to check conclusions deduced above. Thus, using Equation 2.22, 2.23, and 2.26, the work of adhesion of the Zn/VC, Co/VC, Pb/VC and Hg/VC interfaces are estimated from the surface energy values obtained from the bibliography [85] and presented in Table 3.3.

	γ_{metal} (mJ/m^2)	$W_{metal/VC}$ (mJ/m^2)
Zn	990	67
Co	2200	105
Pb	540	47
Hg	580	49

Table 3.3: Work of adhesion of Zn, Co, Pb and Hg on a VC substrate estimated from surface energy values (extracted from [85]) using Equation 2.22 2.23 2.26.

The results of these calculations show that the work of adhesion of lead and mercury are the lowest. This is consistent with results presented in Figure 3.4 by [25] which show that only lead and mercury are dispersed by ultrasonication. The fast dispersion of the mercury, in comparison with lead, occurs because mercury is a liquid forming drops and its contact area with the substrate is thus reduced. The non-dispersion of zinc and cobalt is explained by their higher work of adhesion with the VC substrate (67 and 105 mJ/m^2 respectively). However, even if the work of adhesion of zinc is lower than the one of cobalt, results of [25] show a better adherence of zinc under ultrasonication (Figure 3.4) and this could be due to the morphology of the obtained deposit.

In addition to the influence observed between both substrate materials (gold and VC), differences of dispersion efficiency also appear between the two VC substrates (VC1 and VC2). Concerning the VC1 electrode (Figure 3.2 b and e), results reveal that a portion of the iron deposit is dispersed during the cyclic voltammetry. In the Mohr's salt solution, Qc/Qa reaches 1.6 with ultrasound, and the main part of the iron deposit (62.5%) remains on the VC1 electrode surface. Note that the anodic peak (and thus the anodic charge), when ultrasounds are activated, is higher than the one obtained under silent conditions. As discussed in the studies of M. Hyde et al. [25] and S. Floate et al. [86], this is due to the competition between the removal of iron deposit (which induces the decrease of the anodic charge) and the enhancement of mass transfer (induced by

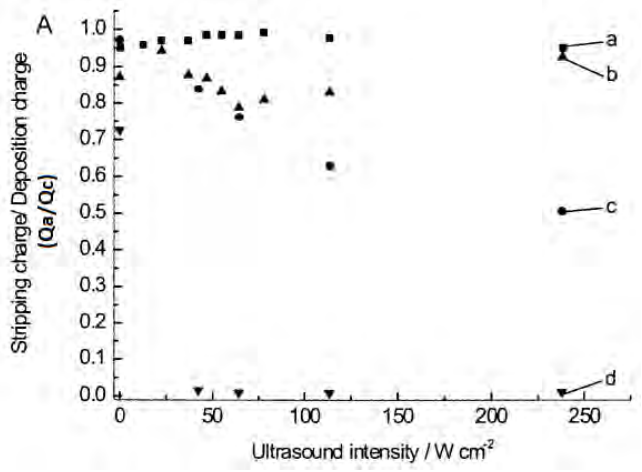

Figure 3.4: Ratio of the anodic charge to the deposition charge obtained for various metals, during cyclic scan voltammetry started by the reduction of the corresponding ion on a VC substrate (extracted from [25]). (a) zinc, (b) cobalt, (c) lead, (d) mercury. Metallic solutions used are 1 M $ZnBr_2$, 0.4 M $CoSO_4$, 1 M $Pb(NO_3)_2$, 50 mM $Hg(NO_3)_2$ respectively.

ultrasound, and leading to larger quantity of iron formed on the electrode in comparison to the silent conditions case). In $FeCl_2$, ultrasonication appears to be more efficient, Qc/Qa reaches 3.45. Nevertheless, ultrasonication effect on iron deposit dispersion appears less efficient on VC1 than on VC2 (see Figure 3.2 b, c, e, and f).

Indeed, VC2 electrode leads to the most interesting results (Figure 3.2 c and f) particularly with Mohr's salt solutions (Figure 3.2 c). The anodic peak corresponding to the oxidation of the remaining iron, electrodeposited during the cathodic scan, is missing, indicating that all the iron has been removed from the electrode surface and Qc/Qa reaches 240 (instead 1.4 without ultrasound). Also, the backward cathodic scan (Figure 3.2 c) tends to overlap the cathodic forward scan, meaning that Fe^{II} reduction takes place on an almost clean/bare VC2 surface, where iron electrodeposits are continuously removed thanks to ultrasounds. Iron electrodeposits adhesion on the VC2 electrode surface is very weak, and they are dispersed easily during their formation. The removal of the deposit from the electrode under ultrasonication is also observed with $FeCl_2$ on VC2 (Figure 3.2 f), Qc/Qa reaches 4.56 under ultrasonication. However the effect is less pronounced than in Mohr's salt.

In their study, M. E. Hyde et al. [25] also obtain loss in the metallic deposit; how-

ever, conversely to the present study (Figure 3.2 c), no overlapping of both the cathodic backward and forward scans are observed on their cyclic voltammograms (see Figure 3.5 extracted from [25]). The analysis of their cyclic scans indicates primarily that no loss of metal deposit is observed for zinc and cobalt (Figure 3.5 A and B) confirming what has been said before. Besides, for the lead and mercury cases, decrease (or disappearing) of the anodic peak is obtained, but the cathodic forward and backward scans do not overlap, indicating that a portion of the metal still remain on the electrode during the cathodic backward scan (even for higher ultrasound intensity).

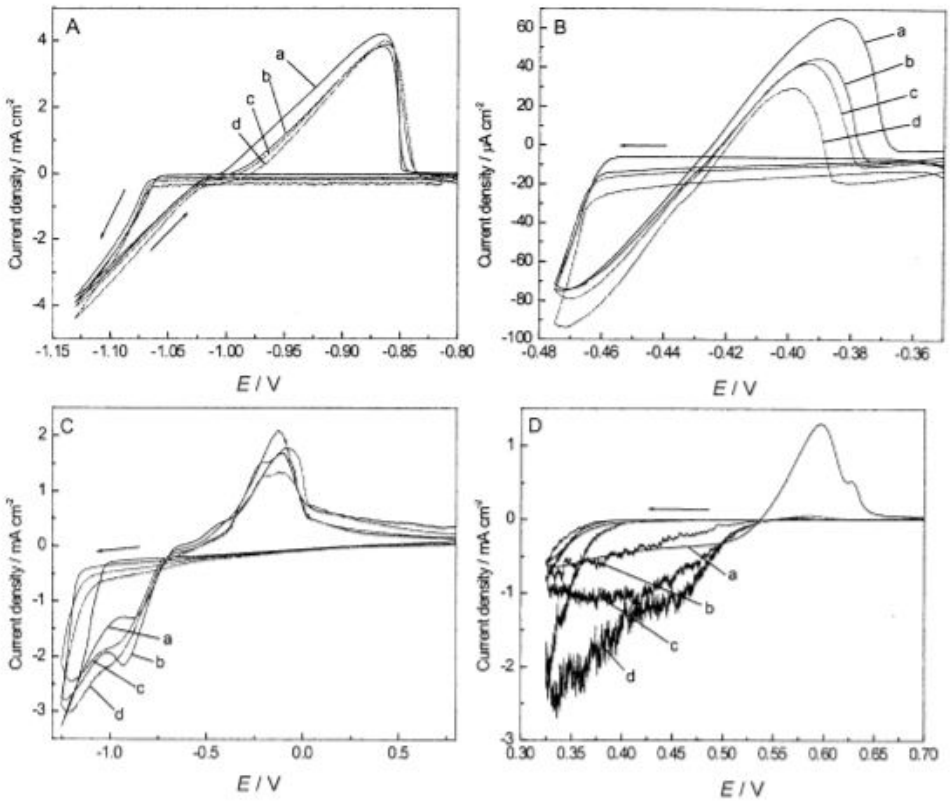

Figure 3.5: Cyclic voltamperometric scans (extracted from [25]) obtained under sonication and silent consitions for various metal systems on a VC substrate. (A) Zinc, scan rate 50 mV/s, (a) silent, (b) 37 W.cm^2, c) 64 W.cm^2, (d) 238 W.cm^2. (B) Lead, 10 mV/s, (a) silent, (b) 42 W.cm^2, (c) 64 W.cm^2, (d) 238 W.cm^2. (C) Cobalt, 100 mV/s, (a) silent, (b) 37 W.cm^2, (c) 78 W.cm^2, (d) 238 W.cm^2. (D) Mercury, 20 mV/s, (a) silent, (b) 42 W.cm^2, (c) 64 W.cm^2, (d) 238 W.cm^2. Metallic solutions used are 1 M $ZnBr_2$, 0.4 M $CoSO$84, 1 M $Pb(NO_3)_2$, 50 mM $Hg(NO_3)_2$.

The overlap of the cathodic forward and backward scans, obtained in the present

study, shows that it is possible to drive the electrodeposition of iron simultaneously with its total dispersion. This continuous dispersion of the iron deposit enable to limit its growth and thus can lead to the continuous synthesis of fine iron particles.

Furthermore, because of the continuous removal of the electrodeposit (Figure 3.2 c), the cathodic charge is lower than that passed in the other cases, leading to a lower synthesis rate (only valid for deposition under variable applied potential). As discussed, in [25] and [86], the competitive effect of metal deposition and its dispersion could be adjusted by the control of the Fe^{II} concentration, the applied current and the ultrasound intensity.

To sum up, main differences in the dispersion of iron electrodeposited on gold and VC electrodes, are due to the work of adhesion of the iron on the used substrates. However, differences can also be observed between apparently similar VC electrodes: VC1 and VC2. Dispersion by ultrasonication is more efficient on VC2 than on VC1, suggesting that iron adheres lesser on VC2 than on VC1. However, the surface energy values for VC1 and VC2 are very similar $\gamma_{VC1} \approx \gamma_{VC2}$ (see Table 3.1), consequently, another parameter is responsible for this observed difference, for example, the roughness of the substrate. VC2 has a smooth surface with an arithmetic roughness $Ra = 8$ nm, whereas VC1 shows a porous structure with a $Ra = 35$ nm the material and method. Even if the roughness does not appear to have a significant influence on the iron electrodeposit morphology on VC1 and VC2 electrodes (see Chapter II), it affects its adhesion. Therefore, the influence of this parameter will be further discussed in the following section.

To conclude, the voltammetric study performed under ultrasonication demonstrates the importance of the substrate material; choosing the unappropriated substrate could make the deposit dispersion impossible. Thus, it has been proven that decreasing the surface energy of the substrate, enables to minimize the work of adhesion of the deposit and thus, induces the enhancement of its dispersion. The roughness of the substrate also seems to influence the dispersion, but further analysis is needed to confirm that (see the following section). The voltammetric study does not enable the control of the iron quantity electrodeposited, due to the competition between the enhancement of mass transfer and the removal of the deposit (as explained previously). That is why the study of the iron deposit dispersion, and its influencing parameters, will be carried out in the

following section, by separating the electrodeposition and the ultrasonication phases.

3.3.3 Dispersion by ultrasound of iron electrodeposited by galvanostatic electrolysis under silent conditions

As indicated in the last section, the iron deposit on the gold electrode is not removed by ultrasounds. For this reason, this section focuses on the vitreous carbon electrodes only. The first objective of this section is to investigate the influence of the substrate roughness on the deposit dispersion. To that end, iron electrodeposits are produced by galvanostatic electrolysis under silent conditions, on VC1 and VC2 substrates, for the two iron salt solutions ($FeCl_2$ and Mohr's salt). The influence of the ultrasonication on the resulting electrodeposits is then discussed.

The method employed to estimate the loss of iron induced by ultrasound has been described in the material and method section. The resulting Qa/Qa_{ref} value representing the proportion of iron remained on the substrate in comparison with silent conditions experiments, is plotted for VC1 and VC2 substrates in both $FeCl_2$ and Mohr's salt precursor (see Figure 3.6). Points on each curve correspond to the average values Qa/Qa_{ref} measured for at least three experiments; error bars correspond to standard deviations.

Ultrasound action for two VC substrates and two salt precursors

The effect of the substrate (VC1 and VC2) on the iron dispersion, for both $FeCl_2$ and Mohr's salt precursors are examined and all the obtained curves (Figure 3.6) exhibit a decrease of the ratio Qa/Qa_{ref} as a function of t_{US}(except curve b). For all experiments, an ultrasonication duration of 60 s allows the removal of most ($\approx$ 90 %) of the iron deposit, and disperses it into the liquid. The standard deviation of the ratio Qa/Qa_{ref} has been determined in both media and with both substrates. The low reproducibility, obtained for short ultrasonication times, is improved for longer durations. In addition, the Qa/Qa_{ref} evolution highlights that the quantity of the iron deposit remaining on the substrate decreases progressively with t_{US} (except curve b); this is particularly visible for the VC1 electrode where exponential decreases are observed (Figure 3.6 a and c). For the VC2 electrode, the dispersion is too fast for both iron salt; the iron deposit is

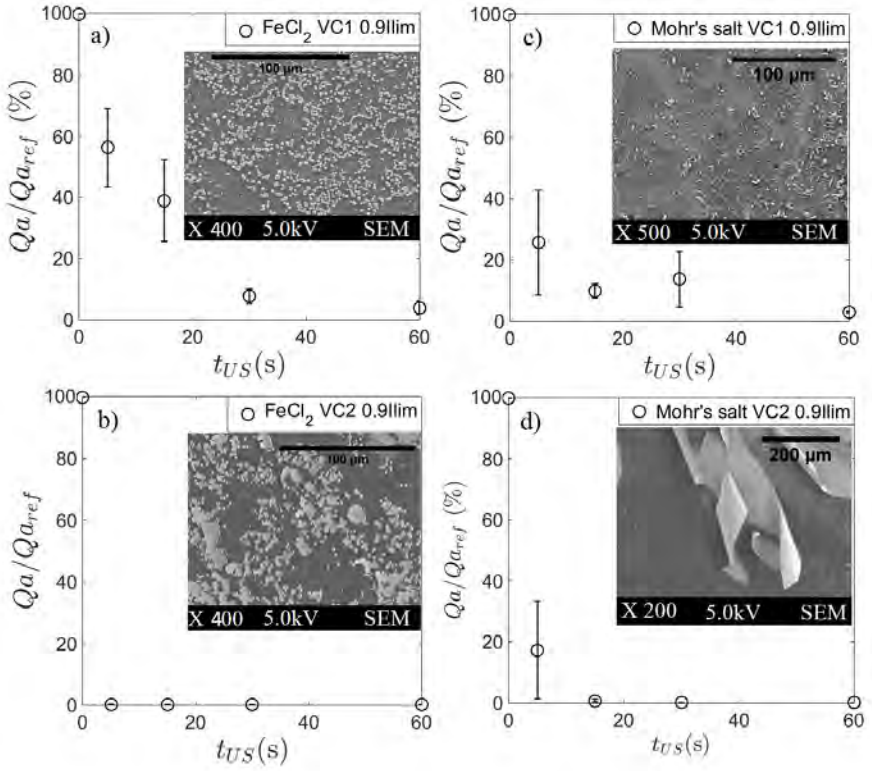

Figure 3.6: Dimensionless iron quantity Qa/Qa_{ref} remaining on the electrode as a function of the ultrasonication duration (t_{US}). Experiments a) VC1 and b) VC2 were achieved in the $FeCl_2$ solution. Experiments c) VC1 and d) VC2 were achieved in the Mohr's salt solution. Points correspond to the average values Qa/Qa_{ref} measured for at least three experiments; error bars correspond to standard deviations. Insets: SEM images of the electrodeposits just after the electrolysis (not exposed to ultrasonication)

totally dispersed after 15 s (and even after 5 s in $FeCl_2$). In this case, it can be thought that the progressive decrease of Qa/Qa_{ref} could be observed for shorter ultrasonication durations ($t_{US} < 5s$)) (Figure 3.6 b)).

The progressive removal of iron from the VC1 electrode can be explained by the operated mode of ultrasonic dispersion. Indeed, constant power ultrasound produces a constant rate of cavitation bubbles, per unit of volume in the liquid. However, only the collapses of cavitation bubbles in the vicinity of the iron deposit surface, can cause its dispersion. The flux of removed particles should then be proportional to the quantity of iron deposit presents on the electrode surface. Thus, decreasing the iron quantity at the

surface, reduces the removed particles flux, as observed experimentally (see schematic representation Figure 3.7). A simple first order kinetics model can be built to quantify this behavior:

$$\frac{d}{dt}\left[\frac{Qa}{Qa_{ref}}\right] = -s\frac{Qa}{Qa_{ref}} \tag{3.1}$$

s represents the dispersion rate constant (s^{-1}) that depends on 1) the ultrasound power, 2) the adhesion energy $E_{adh} = W_{Fe/VC} \times S_{Fe/VC}$ ($S_{Fe/VC}$ is the surface area of the iron/VC interface) and 3) the size of the electrodeposited iron particles. Equation 3.1 leads to the exponential decrease: $Qa/Qa_{ref}(t_{US}) = exp(-s.t_{US})$.

The plots of $\ln\left(Qa/Qa_{ref}\right)$ versus t_{US}, using data from Figure 3.6 a and c show (in Figure 3.8) that the removal of the iron deposit from the VC1 fits acceptably the first order kinetics model described above, even if a certain dispersion around the linear regression is observed. Nevertheless, it should be pointed out that this very simple model captures the overall dynamic of the phenomenon. It can be noticed that the dispersion rate constants, determined for both iron salts using the VC1 substrate (Figure 3.8) are quite similar (0.0608 s^{-1} in $FeCl_2$ and 0.0661 s^{-1} in Mohr's salt). This suggests that the iron salt does not influence significantly the deposit dispersion. The influencing parameter appears to be, once again, the substrate. As mentioned above, even if the exponential decrease of the Qa/Qa_{ref} ratio could not be easily measured (too fast) for the VC2 substrate, one can expect that the same behavior is obtained for short ultrasonication duration ($t_{US} < 5s$)) and the corresponding dispersion rate constant must be higher than those obtained for the VC1 substrate.

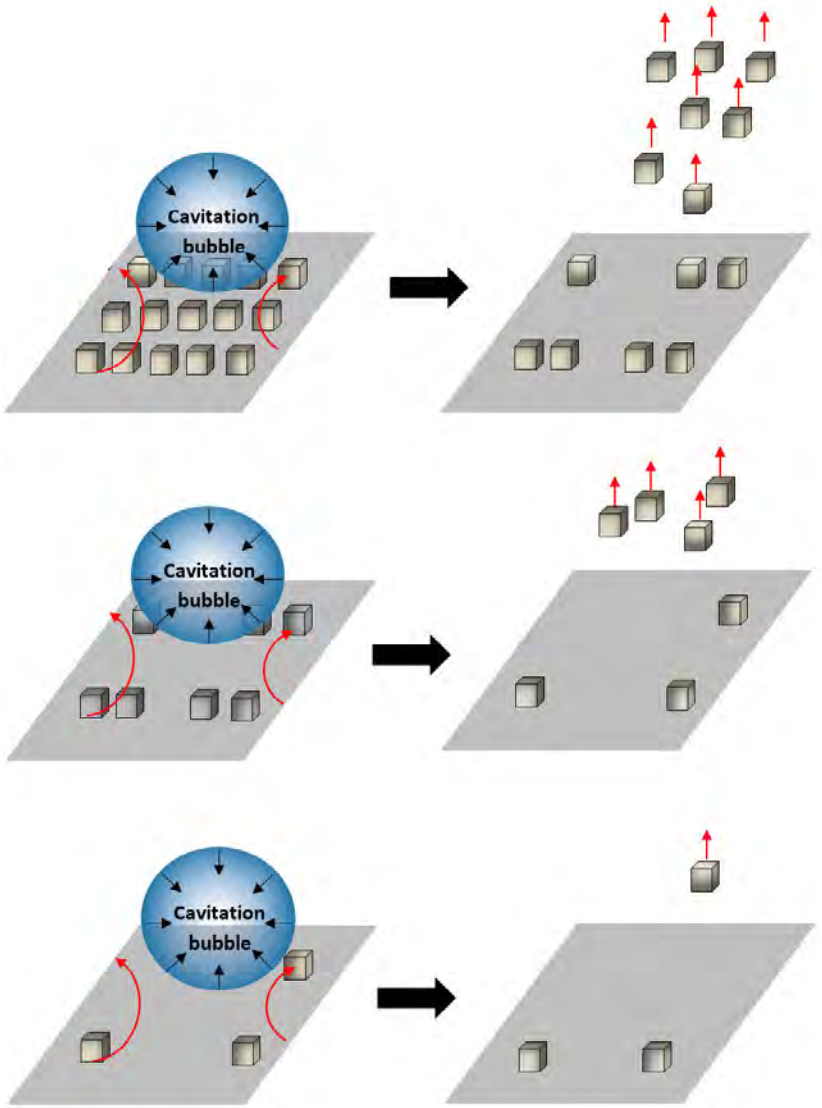

Figure 3.7: Schematic representation of the iron deposit dispersion under ultrasonication with a removed particles flux proportional to the iron quantity remained on the electrode

The difference in the dispersion rate obtained for both vitreous carbon substrates suggests a better adhesion of the iron deposit on the VC1 substrate which confirms results obtained the cyclic voltammetry study (section 3.3.2). This difference in the deposit adhesion has already been highlighted by the study of the substrate influence on the iron electrodeposition (section 2.5, Figure 2.21). Indeed, it has been seen that

the iron electrodeposited on the VC2 substrate appears to be already partially detached during the electrolysis by the rotation speed (SEM pictures of the obtained deposit are presented in the insets of Figure 3.6).

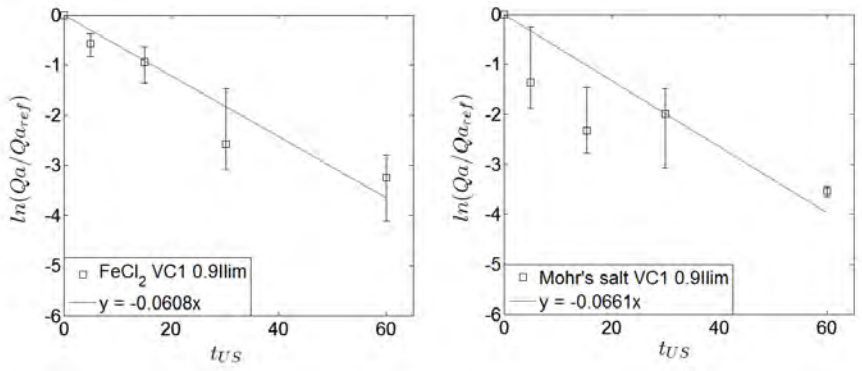

Figure 3.8: $ln(Qa/Qa_{ref})$ versus ultrasonic time t_{US} on VC1 (circles) for a) $FeCl_2$ and b) Mohr's salt, from data of Figure 3.6 a and c. Solid lines correspond to best linear fits

The above-observed differences in iron adhesion on VC1 and VC2 cannot only be explained by the work of adhesion between iron and VC substrates ($W_{Fe/VC2} = 22$ J/m^2 and $W_{Fe/VC1} = 16$ J/m^2). Their surface roughness could be probably another factor, indeed micrometric holes on VC1 (Figure 2.4), that induce a higher roughness (Ra = 35 nm on VC1 and 8 nm on VC2), may act as "anchors" for the electrodeposited iron.

Effect of different polishing level on deposit dispersion

To confirm the effect of the electrode roughness on iron deposit adhesion, three different polishings were applied to the VC2 electrode surface. The substrate was polished with paper grid P800 (electrode VC2 P800), P1200 (electrode VC2 P1200) and with 0.3 mm alumina suspension (electrode VC20.3 mm) as it was explained in the material and method section.

Iron electrodeposits obtained after galvanostatic electrolysis on VC2, polished with P800 and P1200 paper, are presented in the insets of Figure 3.9 a. The effect of the ultrasonication duration on iron dispersion was examined by plotting of the ratio (Qa/Qa_{ref}) as a function of t_{US} (Figure 3.9 a), for the three different polishing levels. As for VC1 (Figure 3.6 a and c, and Figure 3.8), a practically exponential decrease is observed, that

validates the fact that iron electrodeposit dispersion by ultrasonication follows a first order kinetics (Equation 3.1). The lowest dispersion efficiencies are obtained for electrodes that present the highest roughness. For example, after 5 s of ultrasonic duration, the quantity of iron deposit remaining on the VC2 substrate, decreases from $\approx 45\%$ to 15% and $< 5\%$ when polishing was achieved respectively with paper grid P800, P1200 and 0.3 mm alumina suspension. This confirms the effect of the roughness on the dispersion kinetics.

For the VC different substrates (VC2 $0.3\mu m$, VC2 P1200 and VC2 P800), the same quantity of iron was deposited during the electrolyses, but a higher roughness induces a higher surface area of the iron/VC interface, $S_{Fe/VC}$. The roughness of VC2 P800 being higher than those of VC2 P1200 and VC2 $0.3\mu m$ ($Ra_{Fe/VC2P800} > Ra_{Fe/VC2P1200} > Ra_{Fe/VC20.3\mu m}$, see Table 3.2), $S_{Fe/VC}$ is larger for VC2 P800 than for VC2 P1200 and VC2 $0.3\mu m$ ($S_{Fe/VC2P800} > S_{Fe/VC2P1200} > S_{Fe/VC20.3\mu m}$. A higher surface area of the Fe/VC interface induces a higher adhesion energy:

$$E_{adh} = W_{Fe/VC} \times S_{Fe/VC} \tag{3.2}$$

Therefore, the energy required to remove the deposit from the electrode is higher for a rough surface. The ultrasonic power P_{US} being constant, this suggests that the duration t_{US} necessary to disperse the deposit is higher for high electrode roughness: $E = P_{US} \times t_{US}$

As discussed in Chapter II (section 2.5), the morphology of the iron electrodeposited on the rough surface (VC2 P800 and VC2 P1200) is similar to the one obtained on a smooth surface. No influence of the roughness on the deposit morphology has been observed except that on a rough surface, the deposit grows following the topography of the substrate, preferentially at the bottom of the stripes (see inset of Figure 3.9 a) and Figure 3.9 b)). These observations also explain the better adhesion obtained on rough surfaces; indeed, iron deposited onto the stripes is protected against the fluid stream and ultrasonic perturbation that can cause its detachment of the deposit. Indeed, the same quantity of iron is deposited on the rough substrates (VC2 P800 and VC2 P1200) as that on the smooth one, but iron deposited inside the stripes of the rough substrates has an iron/liquid interface less exposed to cavitation bubbles. These results clearly confirm

the major importance of VC electrode surface roughness on the adhesion of iron deposit and demonstrate that the dispersion kinetics effectively slows down as the electrode surface roughness increases.

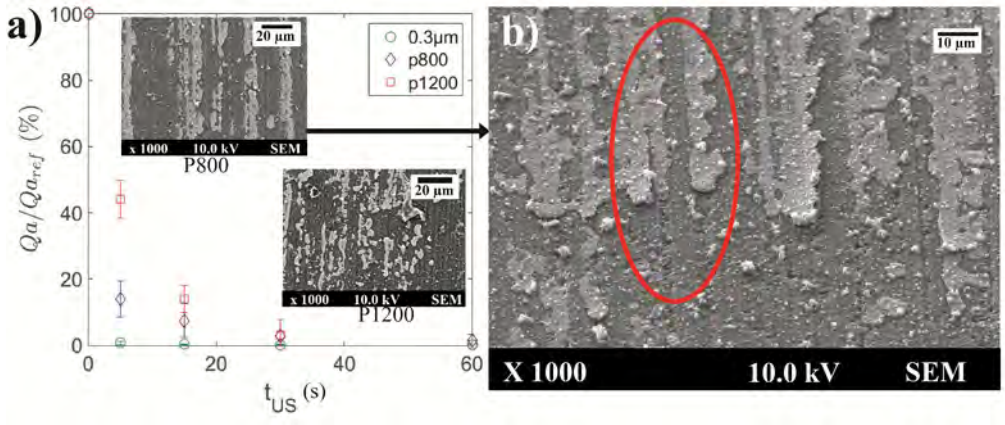

Figure 3.9: Dimensionless iron quantity (Qa/Qa_{ref}) remaining on the electrode as a function of the ultrasonication duration (t_{US}) for VC2 in $FeCl_2$ solution for various polishing levels. Points correspond to the average values Qa/Qa_{ref} measured for at least three experiments; error bars correspond to standard deviations; insets show SEM images of the electrodeposits just after the electrolysis (not exposed to ultrasonication) on VC2 polished with P800 and P1200 paper grids. b) SEM image with 40° tilt, of the iron electrodeposit on VC2 P800; iron deposits located at the stripes bottom are visible in the red ellipse.

To conclude, the influence of the substrate has been demonstrated through the effect of both its surface energy and its roughness. The best substrate for the iron electrodeposit dispersion appears to be a vitreous carbon substrate with a smooth surface, that is why the VC2 electrode polished with an alumina suspension of 0.3 μm will be employed for the rest of this study.

Influence of the iron particles size electrodeposited on the dispersion efficiency

The objective of this section is first to estimate the influence of the particles size on the dispersion process and then to determine the smaller iron particles size removable with our ultrasonic device, indeed, according to Maisonhaute et al. [65], the smaller the particle, the harder the removal from the substrate will be.

The iron particle size is decreased, in a first instance, by reducing the iron quantity deposited during the galvanostatic electrolysis (15.6 mC $\rightarrow$ 7.2 mC $\rightarrow$ 3.4 mC) in order

to obtain iron compact layer of 81 nm, 37 nm and 18 nm thick (estimated from Equation 3.4). To that end, the electrolysis duration (28 s) is kept constant but the concentration of iron salt ($FeCl_2$) is varied from 0.01 M to 0.0025 M (0.01 M $\rightarrow$ 0.005 M $\rightarrow$ 0.0025 M) (see Table 3.4). The current I applied is set to 90% of the corresponding limiting current, I_{lim} and the angular velocity of the RDE is fixed to 1000 RPM.

C (mol/L)	Q_{Fe} (mC)	e (nm)
0.01	15.6	81
0.005	7.2	37
0.0025	3.4	18

Table 3.4: Cathodic charge employed for the three different deposits obtained using three concentrations of $FeCl_2$ and the corresponding compact layer thickness, e, calculated from Equation 3.4. A constant current $I = 90\%I_{lim}$ is applied during 28 s in $FeCl_2$ solution. $\omega = 1000$ RPM. Working electrode = VC2.

SEM pictures of the iron electrodeposits obtained for these different concentrations are shown in Figure 3.10. The deposit obtained in 0.01 M $FeCl_2$ (Figure 3.10, a) has already been described in Chapter II (Figure 2.21 b) section 2.5); it consists of rounded particles and little plates around 5 μm in length (resulting from the coalescence of the rounded particles). As mentioned in Chapter II some of these iron plates are already partially detached at the end of the electrolysis. The deposit obtained in 0.005 M $FeCl_2$ (Figure 3.10, b) is similar to the previous one except that the iron plates are more numerous and smaller (≈ 1 μm). The decrease of the concentration to 0.0025 M (Figure 3.10, c) causes significant changes to the iron deposit which consist of rounded particles of about 1 μm even if some plates are observed. Finally, these electrolyses always lead to the same deposit morphology: starting by the formation of rounded particles which coalesce more or less depending on the amount of charge passed.

The dispersion of these three different deposits is performed by an ultrasonic bath offering the possibility to vary the ultrasound power (see Materials and methods section). Three different ultrasound powers can be applied corresponding to 30 %, 60 % and 100 % of the maximal ultrasound power allowed by its apparatus ($P_{max} = 820$ W). The dispersion process resulting from the three deposits are represented by the Qa/Qa_{ref} value plotted as a function of the ultrasonication duration, t_{US} in the Figure 3.11. Changing the ultrasound power from $0.3P_{max}$ to $1P_{max}$ induces an increase in the acoustic pressure

leading the growth of the population of cavitation bubbles. Therefore, increasing the ultrasound power will allow a faster deposit dispersion.

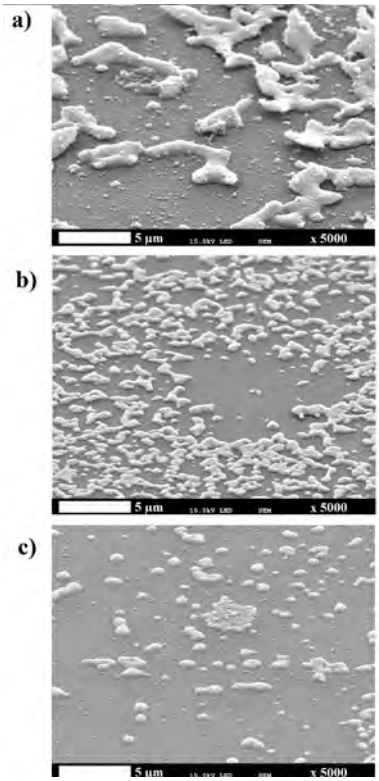

Figure 3.10: SEM images with 40 ° tilt iron electrodeposited on VC2 substrate (polished with a 0.3 μm alumina suspension), with a constant current of 90%I_{lim}, $\omega = 1000$RPM, in $FeCl_2$ with a) 0.01 M, b) 0.005 M and c) 0.0025 M

The Figure 3.11, a) demonstrates that an ultrasound power of 30 % is not high enough to remove any of the three different deposits. Indeed, for each ultrasonication duration, the Qa/Qa_{ref} value remained constant (between 70 and 100 %) indicating a constant iron quantity on the electrode surface and so, no dispersion of the deposit.

Using an intermediate ultrasonic power, 60 % of P_{max}, the dispersion of the deposits becomes appreciable ($0 < Qa/Qa_{ref} < 50\%$) and a certain order is observed between the different deposits. Indeed, the bigger deposit (obtained for the 0.01 M case) is totally dispersed after 15s of ultrasonication while the other two deposits (0.005 M and 0.0025 M) require longer sonification to be "partially" dispersed. After 60 s, around 20 % and 50 % of iron deposit still remained on the electrode for the 0.005 M and 0.0025 M

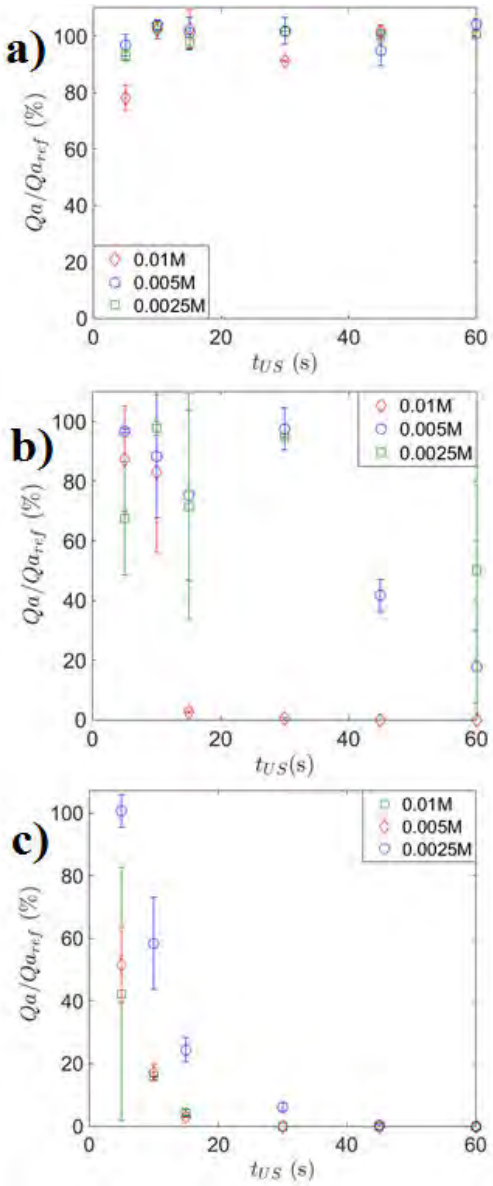

Figure 3.11: Dimensionless iron quantity Qa/Qa_{ref} remaining on the VC2 electrode (polished with a 0.3 μm alumina suspension) as a function of the ultrasonication duration t_{US} in $FeCl_2$ solution for three different iron quantities electrodeposited (15.6 mC $\rightarrow$ 7.2 mC $\rightarrow$ 3.4 mC), a) ultrasound power = 30 %, b) ultrasound power = 60 %, c) ultrasound power = 100 %. $\omega =$ 1000RPM, $I = 90\%I_{lim}$,

deposits respectively. On the other hand, it can be noticed that the Qa/Qa_{ref} evolution for these two deposits does not show the classical exponential decrease discussed above

and the Qa/Qa_{ref} values seem to be more randomly distributed.

Finally, for the last case using an ultrasound power of 100 %, Figure 3.11 c) shows that the deposits are rapidly and totally dispersed. The dispersion appears to be a little bit slower for the 0.0025 M $FeCl_2$ concentration for which 40 s of ultrasonication is required to remove the whole deposit. Here, the classical exponential decrease can be observed for the three cases.

These results confirm that the dispersion appears to be easier for the bigger deposits. Indeed, with ultrasound powers of 30 and 60 %, the deposit obtained with a 0.01 M iron solution is each time the first to be dispersed. Then, the dispersion by an ultrasound power of 100 % has highlighted that the deposit prepared with a 0.005 M solution is also dispersed, more easily than the thinnest deposit (0.0025 M). These results are consistent with the theory proposed by [65] which predicts that the smaller the particles, the harder their removal will be (see Chapter I section 1.1.2).

The exponential decrease of Qa/Qa_{ref} versus t_{US} is observed for the three iron deposits (ultrasound power of 100 %), confirming that the dispersion follows a first order kinetics model (see the discussion section 3.3.3). For the dispersion achieved under an ultrasound power of 60 %, the Qa/Qa_{ref} decrease, appears to be exponential only for the deposit obtained with a 0.01 M $FeCl_2$ solution. For the two other deposits, the dispersion process is too slow to distinguish the exponential decrease (for $t_{US} < 60s$). Therefore, in order to estimate the dispersion rate constant, s, $ln(Qa/Qa_{ref}$ is plotted as a function of t_{US} (see Figure 3.12) for the three deposits and for the three ultrasound power used (in the manner as in section 3.3.3). The obtained dispersion rate constants are presented in Table 3.5.

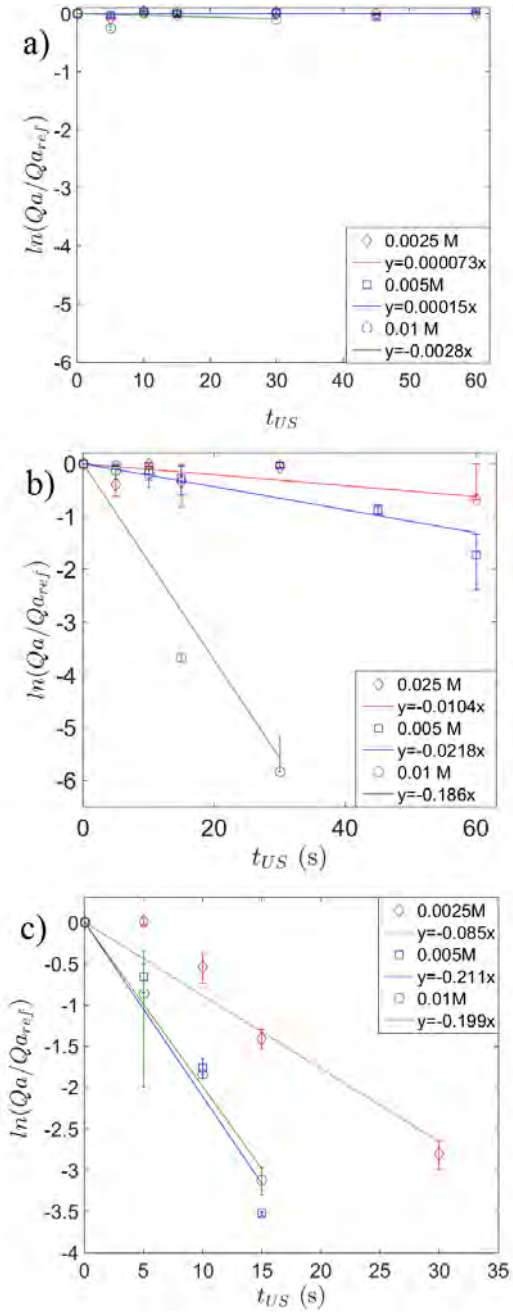

Figure 3.12: $ln(Qa/Qa_{ref})$ versus ultrasonication duration t_{US}, on VC2, for three deposits obtained in three different $FeCl_2$ concentrations (0.01 M, 0.005 M, and 0.0025 M, and three ultrasound powers a) 30 %, b) 60 %, 100 %. Results extracted from Figure 3.11

The value of the dispersion rate constants increases with the precursor concentration and consequently with the size of the iron particles. It also increases with the ultra-

US Power (%) / $[FeCl_2]$ (M)	30	60	100
0.01	2.8×10^{-3}	1.86×10^{-1}	1.99×10^{-1}
0.005	1.5×10^{-4}	2.18×10^{-2}	2.11×10^{-1}
0.0025	7.3×10^{-5}	1.04×10^{-2}	8.85×10^{-2}

Table 3.5: Values of the dispersion rate constants, s (s^{-1}), determined for three iron deposits. Results extracted from Figures 3.11 and 3.12

sound power, for a given deposit. As mentioned in section 3.3.3, the dispersion rate constant depends on the ultrasound power, on the adhesion energy and on the size of the electrodeposited iron particles. In fact, the dispersion rate can be likened to a ratio between the forces acting for the particles removal and forces acting for their adhesion. In [65], Maisonhaute et al. propose a ratio χ to represent the balance between forces acting on a spherical particle in contact with a plate under ultrasonication (see Chapter I section 1.3.2). They conclude that the main forces acting on the particles are the shear forces and the adhesion force resulting from Van der Waals attraction. If the iron deposit obtained in the present study are considered as consisted of spherical particles, the ratio χ, expressed by Equation 1.51 (Chapter I) depends on the particles radius which is consistent with the value of the dispersion rate constants determined previously.

However, the iron deposits do not really consist of spherical particles. Indeed, for experiments achieved with 0.01 M $FeCl_2$, the obtained deposit can be likened to iron plates and in this case the equation of χ becomes:

$$\chi = \frac{F_s}{F_{adh}} = \frac{24\pi d_0^3}{A}\mu \times \frac{dv}{dy} \tag{3.3}$$

With F_s the shear force $F_s = \eta \times \frac{dv}{dy}e^2$ and F_{adh} the adhesion force $F_{adh} = \frac{A_{plate/T/L}e^2}{24\pi {d_0}^3}$, e the length of the iron plates (see Figure 3.13), $A_{plate/T/L}$ the Hamaker constant of the plate in contact with the substrate T, in a liquid L and, d_0 is the separation distance between the deposit and the substrate.

It can be noticed that in this case, the balance between forces acting on the iron plates does not depend on their size. Therefore, it can be concluded that even if the iron deposit does not really consist of spherical particles, the first model (determined for

spherical particles) appears to represent better the mechanism of the deposit removal in our case.

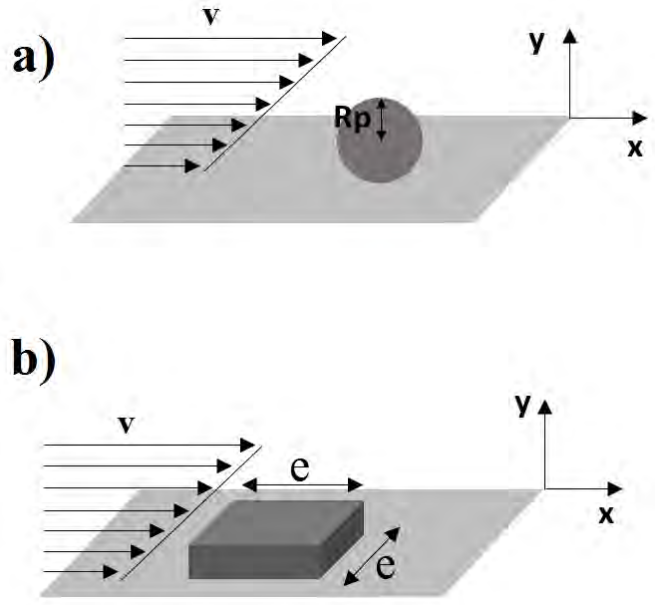

Figure 3.13: Iron deposit subjected to a shear flow. The iron deposit is considered as consisted of a) spherical particles b) iron square plates.

To conclude, these experiments enable to demonstrate the significant effect of the size of the electrodeposited iron particles in their dispersion. It has also been observed that by increasing the ultrasound power, the dispersion rate becomes faster and for a 100 % ultrasound power the dispersion is complete for all the deposits meaning that the 1 μm rounded particles can also be detached from the electrode.

To determine the smallest particle size, that can be removed from the electrode by the ultrasonication, the iron nucleation is achieved by chronoamperometric electrolyses under silent conditions and the iron quantity electrodeposited is decreased (via the amount of charge passed) to 50 μC and 25 μC. SEM picture of the iron electrodeposit, corresponding to a cathodic charge of 25 μC (0.3 s of a chronoamperometric electrolysis) is shown in Figure 3.14. It can be seen in the SEM picture that the deposit consists of iron particles of about 100 nm in diameter.

The ultrasonication of the two deposits corresponding to the cathodic charge of 50 μC, and 25 μC is achieved with an ultrasound power of 100 % to enable the removal of

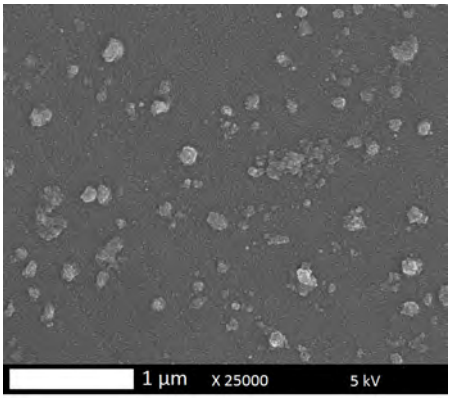

Figure 3.14: SEM picture of an iron deposit obtained by chronoamperometric electrolysis under silent conditions without stirring, for a cathodic charge Qc = 25 μm, in a 0.005 M $FeCl_2$ solution. E = -1360 mV. Working electrode : VC2 polished with an alumina suspension (0.3 μC).

the small particles.

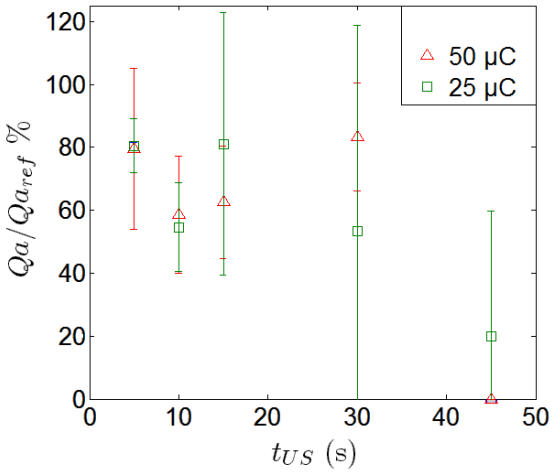

Figure 3.15: Dimensionless iron quantity Qa/Qa_{ref} remaining on the VC2 electrode as a function of the ultrasonication duration t_{US}, in 0.005 M $FeCl_2$ solution, for two different iron quantities electrodeposited (50 μC $\rightarrow$25 μC), $ultrasound\,power = 100\%$, E=-1360 mV.

The resulting Qa/Qa_{ref} values as a function of the ultrasonication duration are presented Figure 3.15, for the two iron deposits (50 μC, 25 μC). The dispersion is almost complete after 45s of ultrasonication for every case, even if for the 25 μC case, 20 % of the iron deposit still remained on the electrode. As already said, the iron particles size

obtained for the lowest iron quantity (25 μC) have a diameter of approximately 100 nm. Therefore, it is possible to remove from the electrode, particles having a diameter around 100 nm.

To conclude, this analysis enables to demonstrate the influence of the size of the electrodeposited iron structures on the dispersion rate. The smaller the electrodeposited particles, the harder the removal is. The dispersion rate constant s appears to depend on the force balance acting on the iron deposit which is (mainly):

- shear forces,
- adhesion force resulting from Van der Waals attraction.

Considering that the iron deposit consists of spherical particles, the ratio between both forces is found to be dependent on the particles radius which is in line with our experimental results. Finally last results show that using the smoothest vitreous carbon electrode (VC2 polished with a 0.3 μm alumina suspension) with an ultrasound power of 820 W (P_{max}), particles about 100 nm in diameter can be removed (for the experimental conditions employed in this study).

3.4 Conclusion

This chapter deals with the effect of ultrasounds on the iron electrodeposits and expect to determine the parameters controlling the deposit dispersion process, the focus is mainly put on the influence of the substrate on the iron deposit dispersion.

As a first step, cyclic voltammetry is performed under ultrasonication and using various substrates (gold, VC1, and VC2) of different surface energy and roughness.

The comparison of cyclic voltammetric scans obtained with and without ultrasounds, enables to observe the effect of ultrasound on the electrochemical process. Thus it has been demonstrated that ultrasounds increase the mass transfer through successive cavitation events. Current fluctuations are also observed, specifically on the diffusion wave of Fe^{II} reduction, confirming that ultrasounds affect the electrochemical process, mainly via the enhancement of the mass transfer and only slightly via the electrode kinetics [25] [30] .

Then the cyclic voltammetry performed under ultrasonication also highlights the effect of ultrasounds on the deposit dispersion. The comparison of cyclic voltammetric scans obtained using different substrates, clearly demonstrates the influence of the substrate material on the dispersion process. Indeed, on the gold electrode, no dispersion is observed while on the VC substrates, the iron deposits are partially or totally dispersed in every case. This is explained by the work of adhesion of the deposit/substrate interface, which is 19 mJ/m^2 for the VC substrate and 149 mJ/m^2 for the gold. In fact, through its surface energy, the choice of the substrate material impacts the adhesion of the deposit on its surface and affects the dispersion process. Results highlight that differences in the dispersion efficiency are also observed between the VC1 and VC2 substrates, suggesting an influence of the roughness. On the VC2, having the smoothest surface (Ra $\approx$ 8 nm), the dispersion appears to be more efficient than on VC1 (Ra $\approx$ 35 nm). Indeed, cyclic scan obtained on VC2 in Mohr's salt shows a complete dispersion of the deposit and, also, the overlapping of the forward and backward curves. This suggests that the deposit is continuously dispersed from the electrode during its formation.

Cyclic scans, performed under ultrasonication, reveal the competition between the enhancement of mass transfer (which induces a higher production of iron) and the removal of the iron deposit, induced by cavitation events.

The dispersion by ultrasounds of electrodeposits produced during galvanostatic electrolysis under silent conditions enables as a second step, to confirm the influence of the electrode roughness on the dispersion efficiency and also to have a better understanding of the deposit removal mechanism. Indeed, the Qa/Qa_{ref} ratio dependence on the ultrasonication duration t_{US} highlights a progressive dispersion of the iron deposit which can be simulated by a simple first order kinetics model: $Qa/Qa_{ref}(t_{US}) = exp(-st_{US})$. The experimental evolution of the Qa/Qa_{ref} as a function of t_{US} demonstrate that increasing the substrate roughness slow down the dispersion process, because the dispersion rate constant s depends on the adhesion energy, the ultrasound power and the size of the particles electrodeposited. Increasing the roughness leads to increase the contact surface between the deposit and the substrate which induces a higher adhesion energy of the deposit.

Finally, the influence of the electrodeposited particles size on the dispersion efficiency is discussed. Estimation of the dispersion rate constant, highlights that decreasing the iron particles size leads to a more difficult removal. Indeed, the dispersion rate constant decreases with the particle size. To explain this behavior, the dispersion rate constant can be likened to the ratio between forces acting for the deposit removal (shear forces) and forces acting for its adhesion (adhesion forces). The balance between these forces is found to be proportional to the radius of the electrodeposited particle (if the deposit is considered as rounded particles). Experiments have shown that the ultrasonic device used in this study enables to remove particles of about 100 nm in diameter.

To conclude, the optimum operating conditions allowing a fast and complete dispersion of the deposit has been determined. It has been shown that using a substrate material of low surface energy enables to minimize the adhesion of the deposit on the substrate and thus enhances the dispersion process. Also, it has been proven that a smooth surface should be preferably used. Therefore, a vitreous carbon substrate polished with the finest alumina suspension (0.3 μm), appears to be a good candidate for the sonoelectrochemical synthesis of iron nanoparticles.

4 Growth and dispersion of an iron deposit inside a Hele-Shaw cell

4.1 Objectives

The purpose of this chapter is to propose a new synthesis way for the production of iron nanoparticles, by the coupling of acoustic vibrations and electrodeposition. The synthesis is performed in a microdevice which consists of a Hele-Shaw cell integrating a piezoelectric diaphragm acting as acoustic waves generator (Figure 4.1). The idea is thus to fragment the electrochemically formed metallic iron branches into fine iron particles via the vibrations induced by the piezoelectric element. The Hele-Shaw cell is an electrochemical reactor of which the electrolytic compartment exhibits specific dimensions: the thickness of the electrolytic compartment (9 mm width and 2.5 cm length) is defined by the thickness of the electrodes (50 μm). This aspect ratio enables a control of the growth and morphology of the deposit. Another advantage of the Hele-Shaw cell is its transparency (thanks to the two glass walls) allowing to observe both the iron growth and its fragmentation. Two fluidic connections enable:

- the supply in the $FeCl_2$ solution
- the rinse off the iron particles for the purpose of their storage
- the recovery of the suspension of particles.

The first part of this chapter aims to study the growth of iron electrodeposits inside the Hele-Shaw cell, to define and optimize the operating parameters of the iron formation. The influence of these parameters on the deposit morphology is also investigated. Thus, several experiments are carried out, under aerated or deaerated conditions by varying both the concentration of the iron salt, and the current density; the resulting deposits morphology and microstructure are analyzed.

The second part of this study consists, in the setting up of the fragmentation step and expects to define the parameters allowing a fast and effective fragmentation of the deposit. Then a deeper analysis is performed to understand the mechanism leading to the break up of the iron branches and thus, to predict the size of the iron particles that could be obtained. Finally, the obtained particles suspension are characterized, and their size, shape, and specific surface are discussed.

4.2 Materials and methods

The experimental device employed in this section to achieve the growth and the dispersion of an iron deposit consists of a Hele-Shaw cell integrating a PZT (see Figure 4.1). The experimental device consists of two iron electrodes of 50 μm (purity $\geq$ 99.5%) width (number 1 and 2 in the Figure 4.1) distant of 9 mm and sandwiched between a glass plate (number 3 in Figure 4.1) and a PZT disk (number 5). The PZT disk (number 5) is a piezoelectric transducer which is used as a vibrating element, expecting to enable the fragmentation of the deposit. More information about the PZT disk are given in the section (4.2.1). The length of the electroactive zone is equal to 2.5 cm (Figure 4.1).

The cell is filled with the ferrous ion solution using a gastight microsyringe (number 11 on the Figure 4.1) via two microtubes (number 10) connected to the cell by fluidic connections (inlet/outlet) (4). Special care is taken to limit the introduction of atmospheric oxygen inside the channel. The fluidic connections are realized by drilling holes in the glass plates and by gluing Nanoport connectors on them.

The face of the glass plate exposed to the channel is entirely covered by a plastic paraffin film (number 6) acting as a gasket to avoid leakages. Also, to protect the PZT disk from the corrosion, an adhesive tape (number 7) is applied to the metallic surface of the PZT in contact with the solution. Finally, the contours of the microchannel are closed by applying an adhesive paste (number 8). Two clamps (number 9), pressing on the glass plate and on the PZT, are used to hold the assembly.

The cell can easily be dismantled to be cleaned before each assembly, the electrodes sides, exposed to the solution, are manually polished using a paper grid (P1200) to operate with reproducible state of the surface of the electrodes.

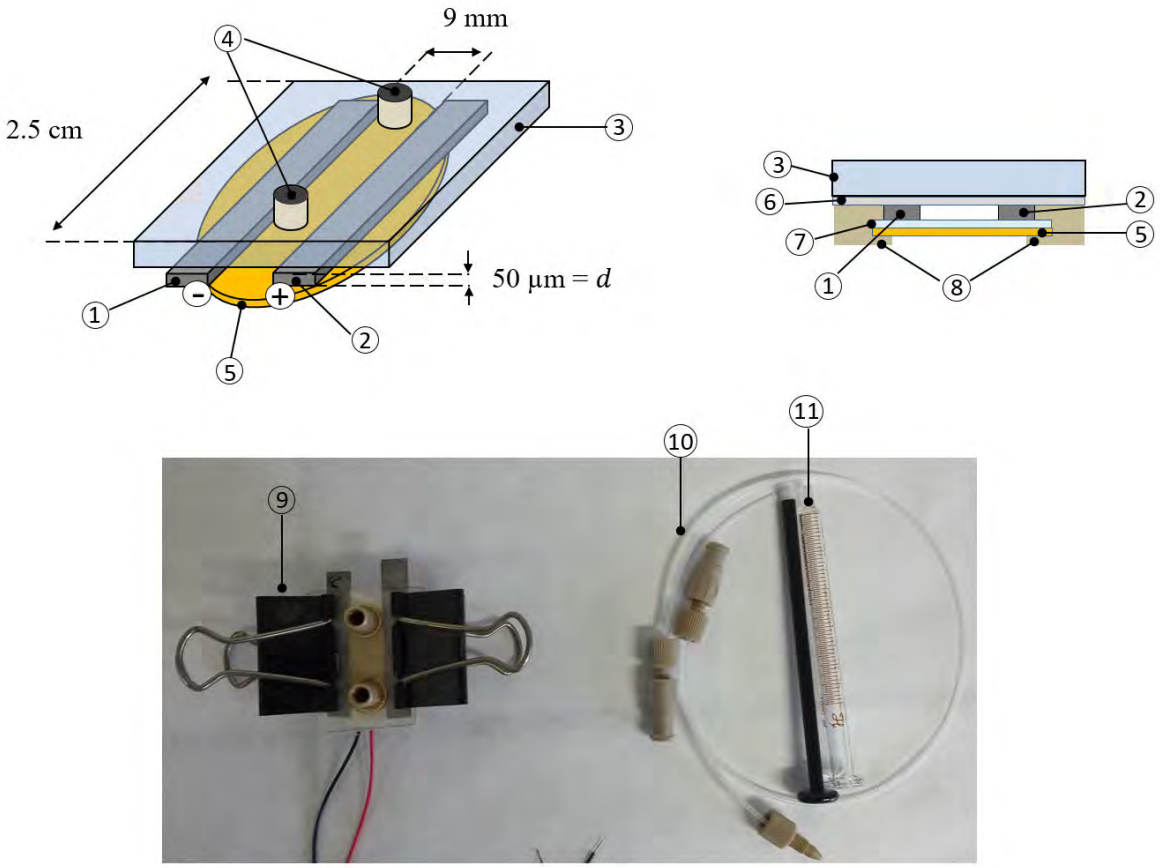

1. **Cathode:** irons trip, 50 µm thick.
2. **Sacrificial anode:** irons trip, 50 µm thick.
3. **Glass plate**
4. **Fluidic connections**
5. **PZT disk:** (lead/zirconate/titanate) buzzer piezo, resonance frequency = 4 kHz
6. **Plastic paraffin film**
7. **Adhesive tape**
8. **Adhesive paste**: (Patafix UHU)
9. **Clamp**
10. **Microtube:** PTFE, diameter interne=0.81 mm
11. **Microsyringe:** Hamilton 1 mL 1001LT

Figure 4.1: Experimental device: Hele-Shaw cell with a PZT integrated.

4.2.1 PZT diaphragm

The PZT disk (or LZT for Lead/Zirconium/titanate), used as a vibrating element in the present experiments, is a piezoelectric diaphragm, composed by a (perovskite made) ceramic plate, sandwiched between two electrodes and attached to a metal plate (see Figure 4.3). The piezoelectric materials have the characteristic either to generate an electrical field in response to applied mechanical stress, or to deform when submitted to an electrical field. This second effect, known as the converse piezoelectric effect, is used here: when the two electrodes are polarized, the piezoelectric ceramic contracts, causing the metal plate to bend (see Figure 4.2 b)), and by reversing the polarization, the PZT ceramic expands and the metal plate bends in the opposite direction (see Figure 4.2 c)). Therefore, when an alternating voltage is applied across the electrode, the PZT diaphragm alternates the bending in the two directions, and thus acts as a vibrating element.

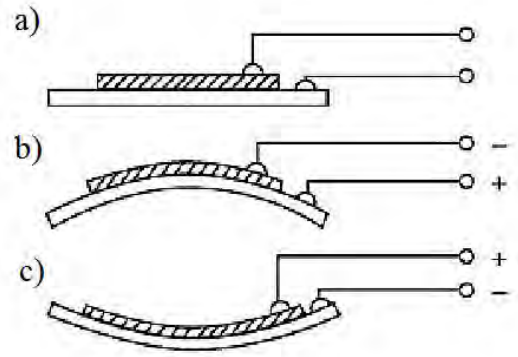

Figure 4.2: Distortions (exaggerated for emphasis) of the PZT disk: a) no polarization, b) and c) bendings of the disk in opposite direction as a function of the direction of the polarization.

The PZT disk used in the present study, operates with a resonance frequency of approximately 4 kHz (maximal frequency: $f_{max} = 4.7kHz$). A low-frequency generator (Figure 4.3, 2) enabling to change the waveform, the voltage amplitude but also the frequency of the signal, is used, and the electrical signal generated is amplified by an amplifier (Figure 4.3, 3).

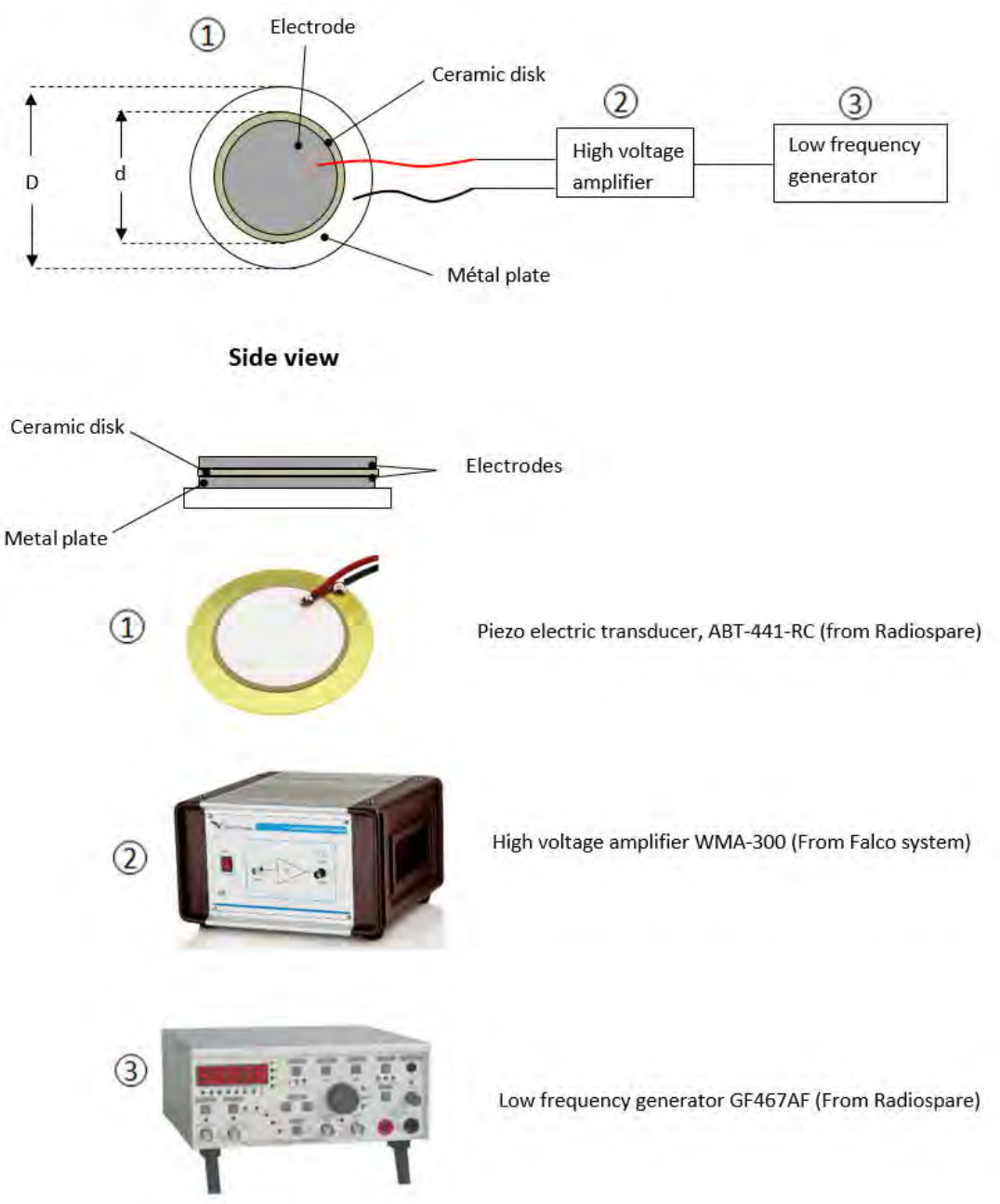

Figure 4.3: Schematic representation of a PZT diaphragm and pictures of the electrical devices used to supply the piezoelectric diaphragm.

4.2.2 Preparation of the ferrous ion solution

All solutions were prepared by dissolving Normapur solid $FeCl_2$ (Purety ≥ 99.0 %) supplied by Sigma aldrich in ultrapure water ($18.2 M\Omega.cm$). To avoid the presence of dissolved O_2 (and so, its co-reduction during the electrodeposition of the metals), these solutions are kept deaereted by N_2 bubbling during at least 15 minutes, before to be collected by the gastight syringe (Figure 4.1). The natural pH of the $FeCl_2$ solutions varies from 3.3 to 3.9 depending on the $FeCl_2$ concentrations used (from 0.1 M to 0.02 M respectively).

4.2.3 Growth, rinse and dispersion procedure

The procedure followed to prepare a suspension of iron particles is a succession of four steps:

- Growth of the iron deposit in the Hele-Shaw cell.
- Rinse of the deposit by ultrapure water.
- Fragmentation of the deposit by activation of the PZT disk.
- Collection of the suspension of iron particles.

The Electrodeposition is driven by applying a constant electrical current between the electrodes using a potentiostat (Autolab PGSTAT302n).

After the formation of the metallic branches, the system is rinsed by a flow of deaerated ultrapure water to decrease the concentration of the metallic salt. This step is necessary to limit the corrosion of the iron branches. Moreover, the presence of salt is undesired for SEM measurements because it induces the formation of crystals when the sample dries which disturb the visualization of the deposit. Thus, the rinse of the cell is performed with a low flow rate of 1 μL/s, to avoid damaging the iron branches, during 10 min (see Figure 4.4); the corresponding injected total volume is equal to approximately 50 times the volume of the microchannel.

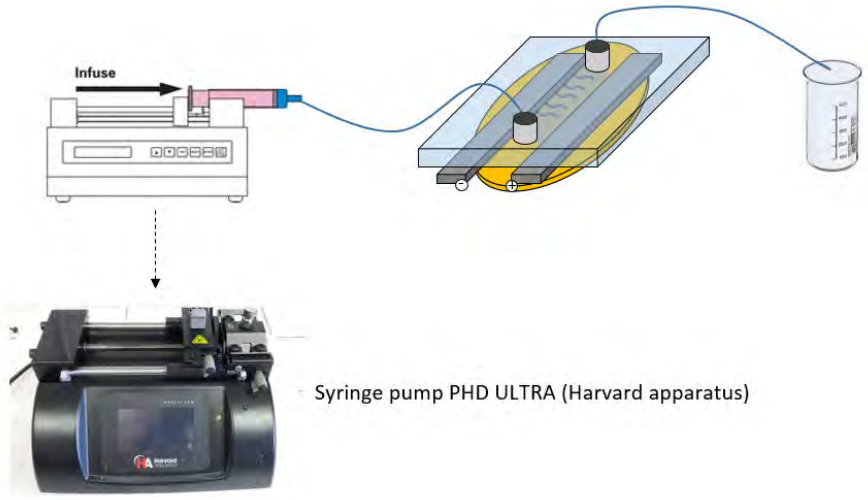

Figure 4.4: schematic representation of the set-up used to rinse of the iron deposit.

To fragment the deposit, an electrical signal is applied to the PZT (as explained above) during about 15s. Then the suspension is collected by drawing out the content of the cell using the microsyringe.

4.2.4 Observation of the growth and the dispersion of the deposit - video equipment

The growth of the iron deposit is observed by a camera PCO pixelfly connected with a 105 mm macro lens. A picture of the deposit is taken every 5 seconds to monitor the evolution of the growth. A led panel is used to adjust the luminosity of the video.

The fragmentation is a fast process. Therefore a high-speed camera (Photron APX/RS 3000) equipped with a 105 mm macro lens is necessary to visualize the fragmentation process. The videos of the fragmentation are taken with a frame rate of 1500 fps (frame per seconds) or 30 000 fps (for a deeper analysis). Since the high-speed camera is less sensitive than the camera PCO pixelfly, a more powerful lighting is used, it is an optical fiber illuminator with two light guides.

To analyze the videos, a specific image processing is applied using Matlab.

4.2.5 SEM observation and preparation of the sample

The iron dendrites, obtained after the electrodeposition step, are observed by scanning electronic microscopy (SEM) with an MEB FEG 7800F Prime-eds.

The recovery of the iron dendrites for the SEM analysis requires special caution. Indeed, the iron electrodeposit is fragile, and the opening of the cell will induce its breakage. Moreover, as mentioned above, it is necessary to rinse the electrodeposit with ultrapure water, to remove the iron salt, which can crystallize, and so disturb the SEM observations. That is why the following procedure is applied:

- Electroformation of the iron deposit, using the Hele-Shaw cell.
- Rinse of the electrodeposit (see Section 4.2.3).
- Cooling of the Hele-Shaw cell during 10 h to solidify the obtained dendrites (T=-10 $^{\circ}C$).
- Dismantling of the cell, trying to keep the deposit intact.
- Recovery of the iron dendrites on a conductive carbon tape.

4.3 Growth of iron electrodeposit inside a Hele-Shaw cell

4.3.1 The stages of iron deposit growth

The polarization of the electrodes induces the growth of the iron deposit through different steps (a, b, b) already detailed in Chapter I Section 1.2.2:

1. Phase a: the depletion phase where the concentration of metal ions at the cathode interface decreases toward zero.
2. Phase b: the destabilization phase which starts when the metal ions concentration reaches zero, at the Sand time Ts [44]. The electrode becomes unstable, and a ramified, and porous deposit starts to grow (detailed in Chapter I Section 1.2.2).

3. Phase c: the growth phase, where the iron branches grow and cross the cell.

This succession of steps can be detected by analyzing the evolution of the cell voltage, measured between the anode and the cathode (see Chapter Section 1.2.2):

1. Phase a: the concentration of metal ions decreases at the cathode surface and increases at the anode (sacrificial anode). However, the ohmic drop due to the resistance of the electrolyte is not modified and thus the voltage measured between the two electrodes stays almost stable.

2. Phase b: the concentration of metal ions reaches zero inducing an increase of the voltage

3. Phase c: the iron branches start to grow inducing the decrease of the resistance between the growth front and the anode: $R = \kappa L/S$ (with L the distance between the growth front and the anode and κ the resistivity). Consequently, the voltage increases.

As the first step, the temporal evolution of the cell voltage during a deposit growth, is compared with the one expected (theory detailed above). The Figure 4.5 shows the cell voltage, measured during an electrolysis achieved with a current of 80 $\mathrm{mA/cm^2}$ with an iron (II) concentration of 0.1 M, in the present study. It can be seen that first, the cell voltage increases from $\approx$ 3.8 V to $\approx$ 4.3 V after 5 s of polarization, which should correspond to the phase b) of the deposit formation: the destabilization phase. Then the voltage decreases from 4.3 V to 4 V after $\approx$ 100 s; this decrease should describe the phase c) corresponding to the growth of the iron branches. Thus, the obtained evolution of the cell voltage is in line with the theory, except that only two (b,c) of the three phases can be detected on this curve (Figure 4.5). To understand why the phase a) is not visible, the Sand time has to be estimated from the following expression [44]:

$$Ts = \left(\frac{FC^{\infty}\sqrt{\bar{D}\pi}}{2 \times |i| \left(1 - t_{+}\right)} \right)^{2} \tag{4.1}$$

where $\bar{D}$ and t_{+} are expressed from Equations 1.37 and 1.48 (Chapter I Section 1.2.2). Using for D_{+} and D_{-} the values of 7.19×10^{-10} and 2.032×10^{-9} $\mathrm{m^2/s}$ [75]

respectively, leads to $Ts = 0.37s$ which is lower than the time step imposed for the cell voltage measurement: 1 s. Thus is why the phase a, for which the cell voltage is approximately constant, is not observed here.

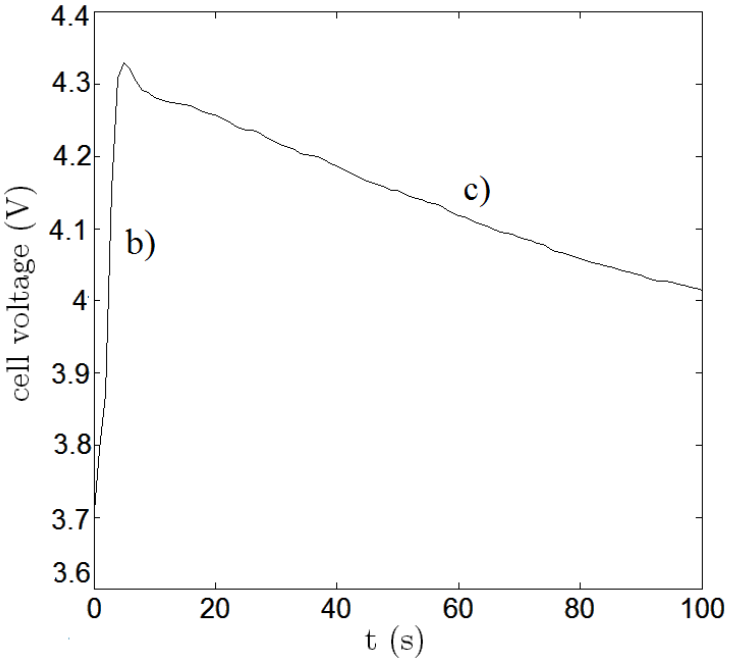

Figure 4.5: Evolution of the cell voltage versus time, during the different stages of the iron electrodeposition (i= 80 mA/cm^2, 0.01 M $FeCl_2$).

4.3.2 Conditions for the growth of the iron deposit

The bibliography shows that the studies on electroformation of metallic deposits in thin layer cells focus mainly on the electrodeposition of zinc, copper, and silver. Few works have been found on the electrodeposition of iron [87] [88], due to the difficulty to produce an iron deposit. Indeed, the reduction of protons requires lower overpotentials (in absolute value) than the reduction of iron(II); thus hydrogen bubbles are produced before or during the growth of iron. In such confined device, the presence of bubbles can hinder or totally inhibit the iron electrodeposition. However, Heresanu [87] shows that in some specific conditions the iron growth becomes possible. He produces iron deposits, using precursors of iron with concentrations ranging between 0.01 M and 1 M, and cell voltage ranging between 5 and 60 V. Wang et al. [88], just mention the hindrance of iron growth by hydrogen bubbles for high voltages.

For now, the operating conditions inducing the generation of hydrogen bubbles and so, the inhibition of the iron growth, are not well understood yet. Heresanu deduces from his results that the influencing parameters are: the concentration of the precursor and the current density applied.

To determine the optimum conditions allowing the growth of the iron, in the Hele-Shaw cell used, various electrolyses are performed in the present study, by varying the concentration of the iron precursor, from 0.02 M to 0.1 M (the natural pH varying from 3.9 to 3.3, see Table 4.1 for an overview of the $FeCl_2$ concentration with the corresponding H^+ concentrations) and the current from 4 to 240 $\mathrm{mA/cm^2}$. The obtained results can be classified into three different groups (see Figure 4.6):

- Only hydrogen bubbles are produced, there is no reduction of Fe^{II} (Figure 4.6 a).
- The main fraction of the current is used for H^+ but some iron ramified branches grow between the bubbles (Figure 4.6 b).
- Ramified iron branches grow and hydrogen bubbles are formed between the branches (same flux of H_2 is produced at constant current applied) (Figure 4.6 c).

It has to be noticed that hydrogen bubbles, are observed for all the experiments conducted (see the zoom in on picture c in Figure 4.6).

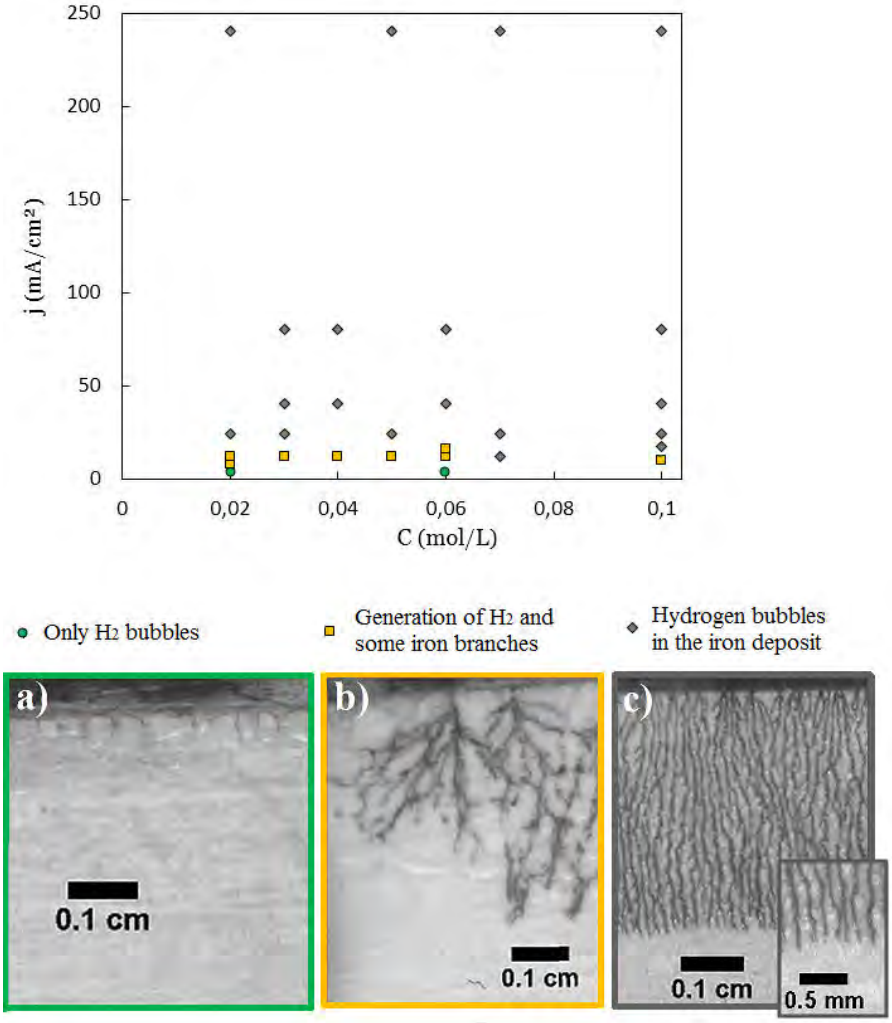

Figure 4.6: Various galvanostatic electrolyses carried out in the present study for various concentrations of the iron precursor ($FeCl_2$) without supporting electrolyte. For each Fe^{II} concentration, different current densities are applied and the phenomena occuring in the Hele-Shaw cell are observed; green circles: only hydrogen bubbles are formed; yellow squares: presence of iron, and generation of hydrogen which hinders the growth; grey diamonds: hydrogen bubbles and ramified iron branches. For each case, an example of the picture of the microchannel obtained after an experiment is shown in a) 0.02 M - 4 mA/cm^2 b) 0.06 M - 12 mA/cm^2 and c) 0.1 M - 80 mA/cm^2.

The Figure 4.6 proposes an overview of all the results obtained during galvanostatic electrolyses, in the examined range of concentrations and current densities applied (0.02

$C_{Fe^{II}}$ **mol/L**	$(C_{H^+} \times 10^4)$ **mol/L**	I_{lim} for H^+
0.02	1.23	8
0.03	1.77	12
0.04	2.23	15
0.06	2.63	17
0.07	3.76	21
0.10	4.57	30

Table 4.1: Summary table of the different concentrations of precursor used with the corresponding theoretical limiting current of H^+ (that would be obtained at the stationary state).

M - 0.1 M and 4 - 240 mA/cm^2). For one concentration of the precursor, various current densities are applied and reported in the graph (3 to 6 experiments).

The results presented in Figure 4.6 reveal that for low current densities (below $\approx$ 8 mA/cm^2), only hydrogen bubbles are produced (green circles in Figure 4.6); meaning that almost 100 % of the cathodic charge passed during the experiment is allotted to the H^+ reduction. For intermediate current densities (8 to 16 mA/cm^2), mainly generation of hydrogen bubbles with some iron ramified branches (yellow squares in Figure 4.6) are observed. In this case, it can be thought that the total cathodic charge is divided between the H^+ and Fe^{II} reduction. For current density higher than 16 mA/cm^2, the third case is obtained: hydrogen bubbles appear between, and on the ramified iron branches (gray diamonds in Figure 4.6). In this case, the current applied is enough to carry out both cathodic reactions, the main part is used to reduce Fe^{II}.

These results highlight that, as mentioned by Heresanu, there is a range of operating conditions (current-precursor concentrations) for which the iron growth is possible. In our case, it seems that for each Fe^{II} concentration, there is a threshold current above which the iron formation is possible.

A representation of the problem could be made regarding the theoretical limiting currents (that would be obtained at the steady state) for the H^+ and Fe^{II} reductions, in order to get a better understanding of the results observed in the Hele-Shaw cell (even if the Fe^{II} reduction is carried out in the transient state and without stirring). Table 4.1 and the corresponding curve, C_{H^+} versus $C_{Fe^{II}}$ (Figure 4.7), demonstrate that the

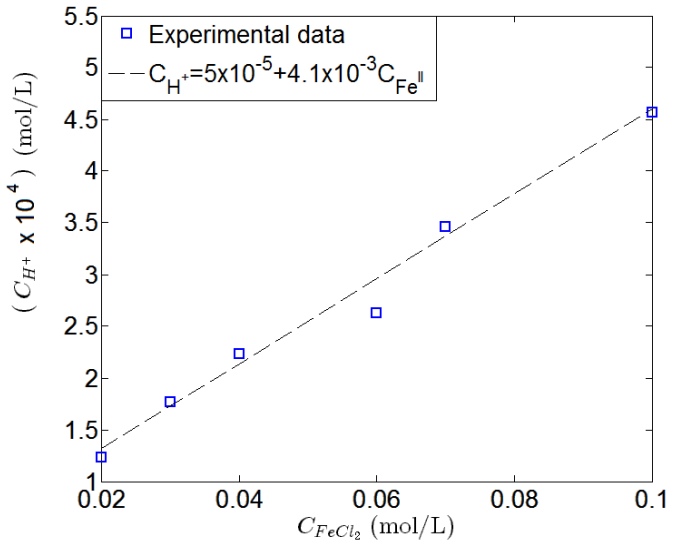

Figure 4.7: Evolution of the proton concentration as a function of the precursor $FeCl_2$ concentration.

concentration of H^+ increases linearly[1] with that of Fe^{II} (at the examined range of precursor concentrations) and consequently the limiting current corresponding to the H^+ reduction increases with the precursor concentration. Thus, for two concentrations of Fe^{II}, $(C_1 > C_2)$, the I/E curves corresponding to the H^+ and Fe^{II} reductions, separately, can be represented as shown in Figure 4.8 (a',b' and a,b respectively) .

Based on this I/E curves representation, it can be seen for each Fe^{II} concentration, that the current applied must be higher than the limiting current of the H^+ reduction, $I_{lim_{H^+}}$ for the Fe^{II} to take place. Considering the increase of the H^+ concentration with the precursor concentration, this threshold current to apply, increases both with the H^+ and Fe^{II} concentrations. Taking for example the case of a 0.02 M Fe^{II} concentration, the formation of iron in this case takes place for $i \geq 8$ mA/cm^2. Thus it can be assumed that this current density corresponds to the limiting current of H^+ for 0.02 M Fe^{II} solution. Based on this limiting current value and using Equation 1.16 (Chapter I Section 1.2.1), the corresponding diffusion thickness is estimated at ≈ 1.4 μm [2]. Assuming that this

[1] Considering the linear evolution of C_{H^+} with $FeCl_2$ concentration, it can be thought that the following reaction (not complete) takes place: $FeCl_2 + H_2O \rightarrow Fe(OH)^+ + H^+ + 2Cl^-$

[2] In fact this value is underestimated since at $i \geq 8$ mA/cm^2, the formation of iron takes place already meaning that 8mA/cm^2 > i_{lim}

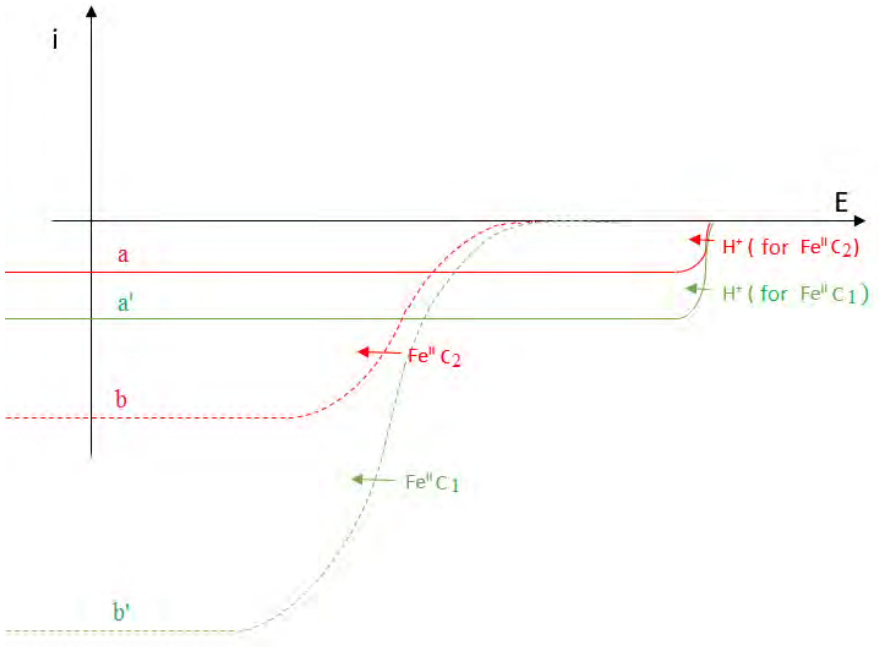

Figure 4.8: Schematic representation of the theoretical I/E curves for the H^+ (solid lines) and Fe^{II} (dashed lines) reductions (at the stationary state) corresponding to two different concentrations of Fe^{II}, $C1$ (red lines) and $C2$ (green lines) for $C1 > C2$ (considering the reduction of H^+ and Fe^{II} alone).

diffusion thickness, δ, is stable for the different Fe^{II} concentrations, a relation can be established between $i_{lim_{H^+}}$ and the precursor concentration, as explained below.

Figure 4.7 shows that C_{H^+} increases linearly with $C_{Fe^{II}}$:

$$C_{H^+} = 5 \times 10^{-5} + 4.1 \times 10^{-3} C_{Fe^{II}} \tag{4.2}$$

and according to the Equation 1.16:

$$i_{lim_{H^+}} = \frac{FD}{\delta}\left(5 \times 10^{-5} + 4.1 \times 10^{-3} C_{Fe^{II}}\right) = 2.5 \times 10^{-3} + 0.2 C_{Fe^{II}} \tag{4.3}$$

Thus, thanks to this equation, the threshold current to apply to allow the formation of the iron deposit could be estimated for any $FeCl_2$ concentration.

According to this reasoning, the threshold current above which the formation of iron is possible, should vary from 8 to 30 mA/cm^2, for Fe^{II} concentrations ranging from

0.02 to 0.1 M (Table 4.1). However, Figure 4.6 shows that even if the threshold current is of the same order of magnitude than those predicted (between 8 and 16 mA/cm^2), no significant effect of the Fe^{II} concentration on this value can be observed. In fact, the problem is more complex and cannot be fully described by the followed reasoning first, because the experiment is carried out at transient state but also due to migration transfer. In addition, for low current values, as mentioned above, the hydrogen bubbles cover the cathode surface progressively (Figure 4.9). Therefore, the active surface of the cathode decreases and so, the area of the cathode uncovered by hydrogen bubbles received increasing current densities. This means that for low current density, i (A/m^2) applied to the system is not stable and cannot be predicted. Figure 4.9 shows a deposit obtained with a 0.02 M Fe^{II} solution, under an applied current density of 8 mA/cm^2 at the first step of its growth. Picture shows that the cathode surface is almost completely covered by hydrogen bubbles, and some iron branches are growing between the bubbles. In this example, the iron branches receive a current density higher than the 8 mA/cm^2 applied, due to the reduction of the electroactive surface.

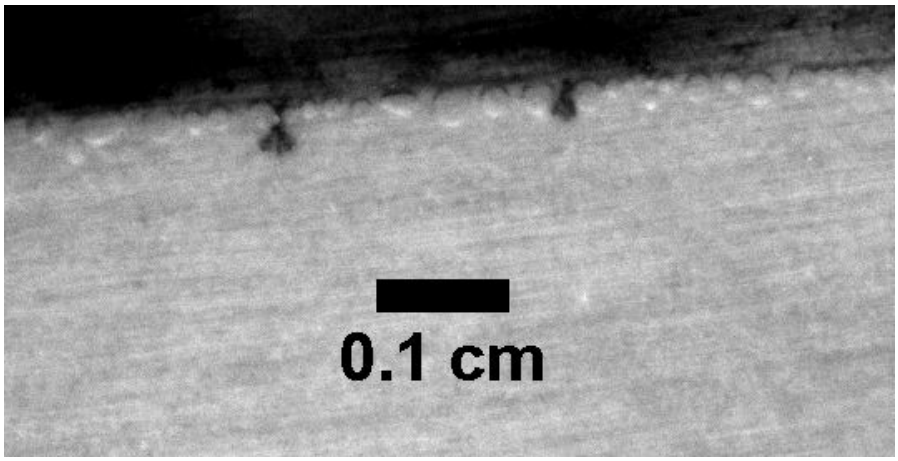

Figure 4.9: Coverage and reduction of the electroactive surface during the iron deposit growth after 80 s: i= 12 mA/cm^2, C=0.06 M.

To conclude even if the reasoning regarding limiting current cannot fully describe the transition between the H_2 bubbles and the iron branches formation, it enables a better understanding of the phenomena observed in the Hele-Shaw cell, for the different operating conditions. For the range of iron precursor concentrations used in this study (0.02

M to 0.1 M) and taking into account the dimensions of the Hele-Shaw cell, the applied current density has to be higher than 16 mA/cm^2 to enable the deposit formation.

4.3.3 Morphology of the iron electrodeposit in the Hele-Shaw cell

When the conditions for the Fe^{II} reduction are respected ($i > 16$ mA/cm^2), the flow of an electrical current through the cell induces the growth of iron branches, which can lead to various distinct morphologies, depending on the operating conditions. As detailed in Chapter I Section 4.6 these morphologies fall into three classes [47] [48] [49]:

- the dendritic morphology,
- the dense branching morphology (DBM),
- the branched and disorderly fractal morphology (DLA).

According to Grier et al. [47], the deposit morphology can vary from a fractal to dendritic growth, by varying the applied voltage and the precursor concentration. To identify the operating conditions favoring each class of morphology, various electrodepositions are performed, for current densities varying from 4 to 240 mA/cm^2 and concentrations precursor ranging between 0.02 M and 0.1 M. The obtained deposits, shown in the Figure 4.10, exhibit two different morphology classes: the DLA morphology and the DBM.

It can be seen on the Figure 4.10 that two different morphology classes are obtained: the DLA morphology and the DBM. No dendritic structures are observed in this range of operating conditions. The DBM structure is obtained mainly for current densities higher than 24 mA/cm^2: increasing i leads to a columnar structure which fills the cell homogeneously. Each iron branch grows with the same velocity, enclosed in a flat envelope. However, regarding the DBM-like deposits, some differences can be observed between the highest current densities (240 mA/cm^2) and the lowest current densities of this class (24 mA/cm^2). It can also be noticed that, the higher the current density, the shorter the distance between two thin branches is, so it can be concluded that the deposits are denser for the highest current densities.

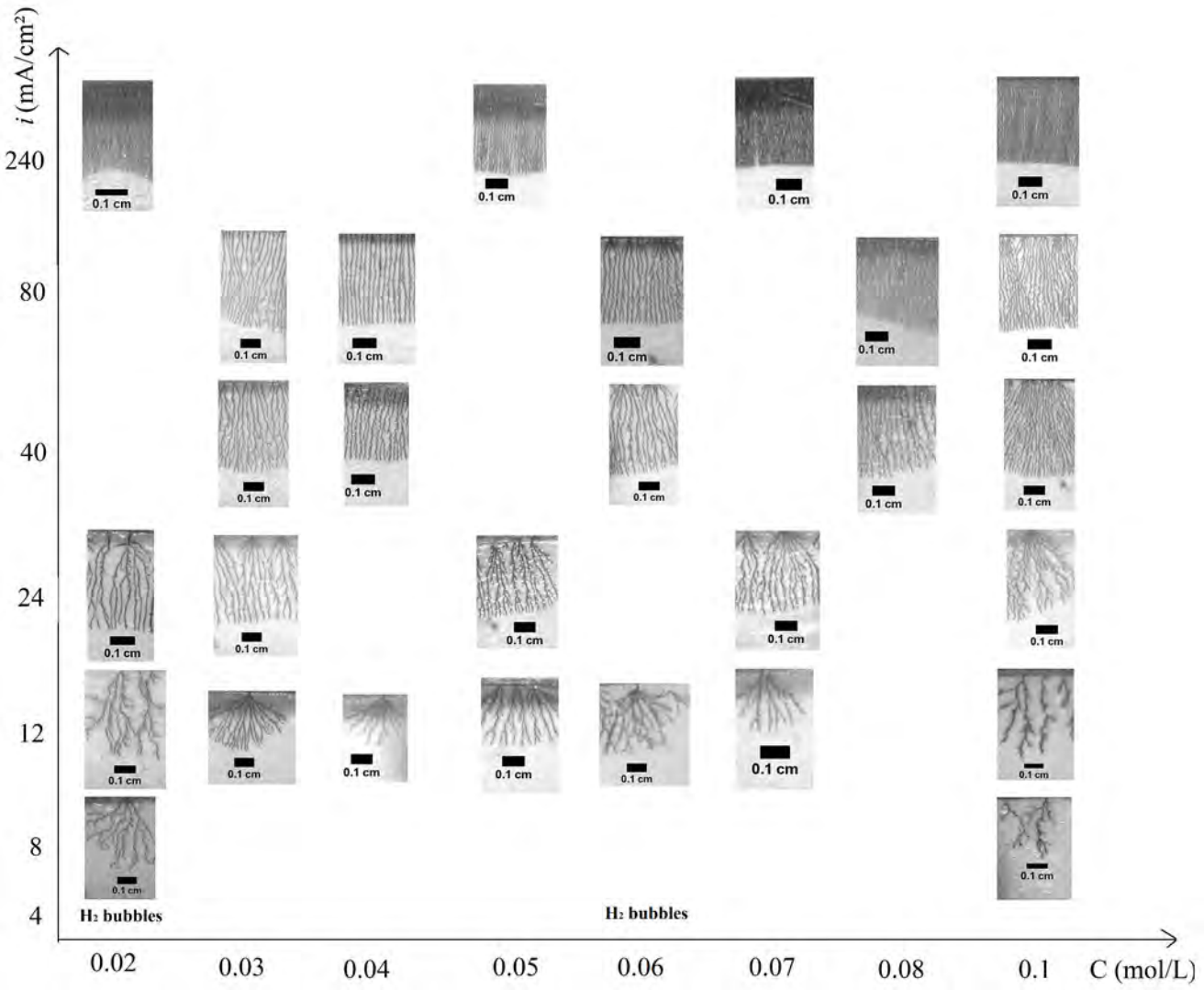

Figure 4.10: Pictures of the different deposit morphologies, obtained in the present study, using a Hele-Shaw cell for the galvanostatic electrolyses indicated in Figure 4.6. $4 \leq i(\mathrm{mA/cm^2}) \leq 240$ and $0.02 \leq FeCl_2(\mathrm{M}) \leq 0.1$.

When the current is decreased below (i<24 mA/cm^2), deposits corresponding to the DLA morphology are obtained, typically at 8 mA/cm^2, the deposits show open structures with fewer branches, and its structure is also less regular to the one obtained for DBM-like deposits.

However the limit between the DLA-like and the DBM-like deposits is not so clear, the deposits obtained at 24 mA/cm^2 and 12 mA/cm^2 appears to be in a transition zone.

These results are consistent with the predominance chart proposed by Grier [48] (see Chapter I, Figure 1.23), which shows that the dense branching morphology is obtained for the higher voltages (and so the higher current densities). As explained in Chapter I Section 2.4.2, it is generally recognized that the deposits obtained under low growth rate have a DLA morphology and conversely, a dense branching morphology is obtained for high growth velocities [44] [47] [52] [53] [54]. Therefore the transition of morphology (DLA to DBM) obtained by varying the operating conditions in the present experiments are consistent with the bibliography.

4.3.4 Small scale morphology of the iron electrodeposits obtained in the Hele-Shaw cell

Bibliography shows several studies focusing on the large-scale structure of the deposits produced in a thin layer. Fleury [57] tries to correlate the "small scale" structure of the deposit, to the branched structure at "large scale." He shows that the branched electrodeposit consist of small grains with almost regular size (see Chapter I, Figure 1.26). Fleury correlates this granular structure to the oscillatory character of the nucleation kinetic (see Chapter I, Section 2.4.2 for more details), and claims that the size of the grains is dictated by the growth speed (and so by the current density): the higher the growth speed, the smaller the grains are.

Among the various deposits obtained in this study (and presented Figure 4.10), five deposits, obtained for current ranging between 8 and 24 mA/cm^2, has been analyzed by SEM. They exhibit, at the large scale, different morphologies going from DBM to DLA. Note that the deposits obtained for $i > 24$ mA/cm^2 (see Figure 4.10) were not analyzed due to their great fragility. The deposits obtained at low current densities appears to be more mechanically resistant.

SEM pictures of these 5 deposits are shown in Figure 4.11 with 3 different magnifications in order to see the large and small scale structures. The three deposits a-b-c) are electrodeposited using a 0.02 M $FeCl_2$ solution under current densities of 24, 12 and 8 mA/cm^2 respectively; and the deposits d-e) are obtained using a 0.1 M $FeCl_2$ solution under current densities of 12 and 8 mA/cm^2 respectively.

Decreasing the current density from 24 to 8 mA/cm^2 (for deposits a-b-c, in Figure 4.11) causes the large-scale morphology to vary from DBM to DLA (the concentration is kept equal to 0.02 M). The small-scale structure of the deposit a (picture in the middle) appears like a carpet of ferns. At the nanometric scale (zoom on the right) the deposit appears to be consisted of several rows of regular grains, with a size about 10 nm, which is in agreement with the observations of Fleury.

The deposit b, Figure 4.11, does not show at large-scale the same columnar structure than the deposit a; however at the small-scale (picture in the middle) the structure of the deposit is similar to the one of the deposit a. At the nanometric scale, the size of the deposit appears slightly different: for the a, grains ranging between 10 and 20 nm are observed while grains lying in the range 50-100 nm constitute the deposit b).

Regarding the apparent growth speed [3] ($v_g \approx 4 \times 10^{-5}$ m/s for the deposit a and $v_g \approx 2 \times 10^{-5}$ m/s for the b), these observations are consistent with the assumption of Fleury [57] who said that a higher growth speed leads to smaller grains size.

The DLA deposit, (c, Figure 4.11), shows a small-scale structure less regular than the deposits a and b; it is constituted by fine branches (fern-like branches), and exhibits big grains ranging between 200 ad 500 nm. This difference of grains size in the same deposit may be explained by its DLA morphology. Indeed, for a DLA-like deposit, the growth speed is not the same for all the branches (contrary to the DBM-like deposit), the growth of some branches can slow down and stop in favor of the growth of other branches. The estimation of the growth speeds of some branches leads to values from 1.2×10^{-5} m/s to 1.9×10^{-5} m/s (see Figure 4.11 c). This variation of growth speed, observed in the formation of a DLA deposit, can explain the various grains sizes observed in the small-scale structure.

[3] The apparent growth speed is estimated by dividing the distance covered by the deposit with the duration of the growth.

The deposits d and e presented in Figure 4.11 are obtained under the same current densities (12 and 8 mA/cm^2) than the ones used for deposits b and c, but using more concentrated solution (0.1 M instead of 0.02 M). At large scale (picture on the right), the deposit d shows thicker branches than the other deposits. This is confirmed by SEM pictures, which show at small scale, really ordered structures. The size of the grains composing the branches ranges between 500 nm and 1 μm, and is consistent with the apparent growth speed estimated for most of the branches of this deposit, $\approx 3.6 \times 10^{-6}$ m/s; this last value is slower ($\approx \div 4$) than the rate observed in the previous case.

Finally, the deposit e shows at large scale a DLA morphology, but it can be noticed that large hydrogen bubbles have been formed during its growth. Regarding the SEM pictures (Figure 4.11 e), it can be observed that the deposit shows a really complex small-scale structure. Some thin branches can be identified, but a wide variety of structure is observed (rough structures, smooth iron blocks...), probably because during its formation, the generation of hydrogen bubbles strongly disturbs its growth. Indeed, the growth of the "first" branches of the deposit, labeled "1" in Figure 4.11, e, has been stopped by the presence of a hydrogen bubble. Considering the branch labeled "2" in Figure 4.11, e, the observations made during the electrolysis, show that, the grow of the right branch is stopped for the benefit of the left branch. Then, the left branch growth is stopped by the presence of a bubble, which reactivates the growth of the right branch. Thus, the growth of one branch is achieved in several steps with different growth speeds.

To conclude, the SEM observations of the deposits have shown that iron branches are composed of small grains, whose size depends on the growth speed. Our results are in agreement with those exposed by Fleury [57], but clearly, demonstrate that the size of the grains composing a deposit, is not always regular. Indeed, for DLA-like deposit, the growth speed of the branches is not uniform inducing changes in the size of the grains composing the deposit. This effect is even more pronounced when hydrogen bubble hinders the deposit growth by stopping the growth of some branches.

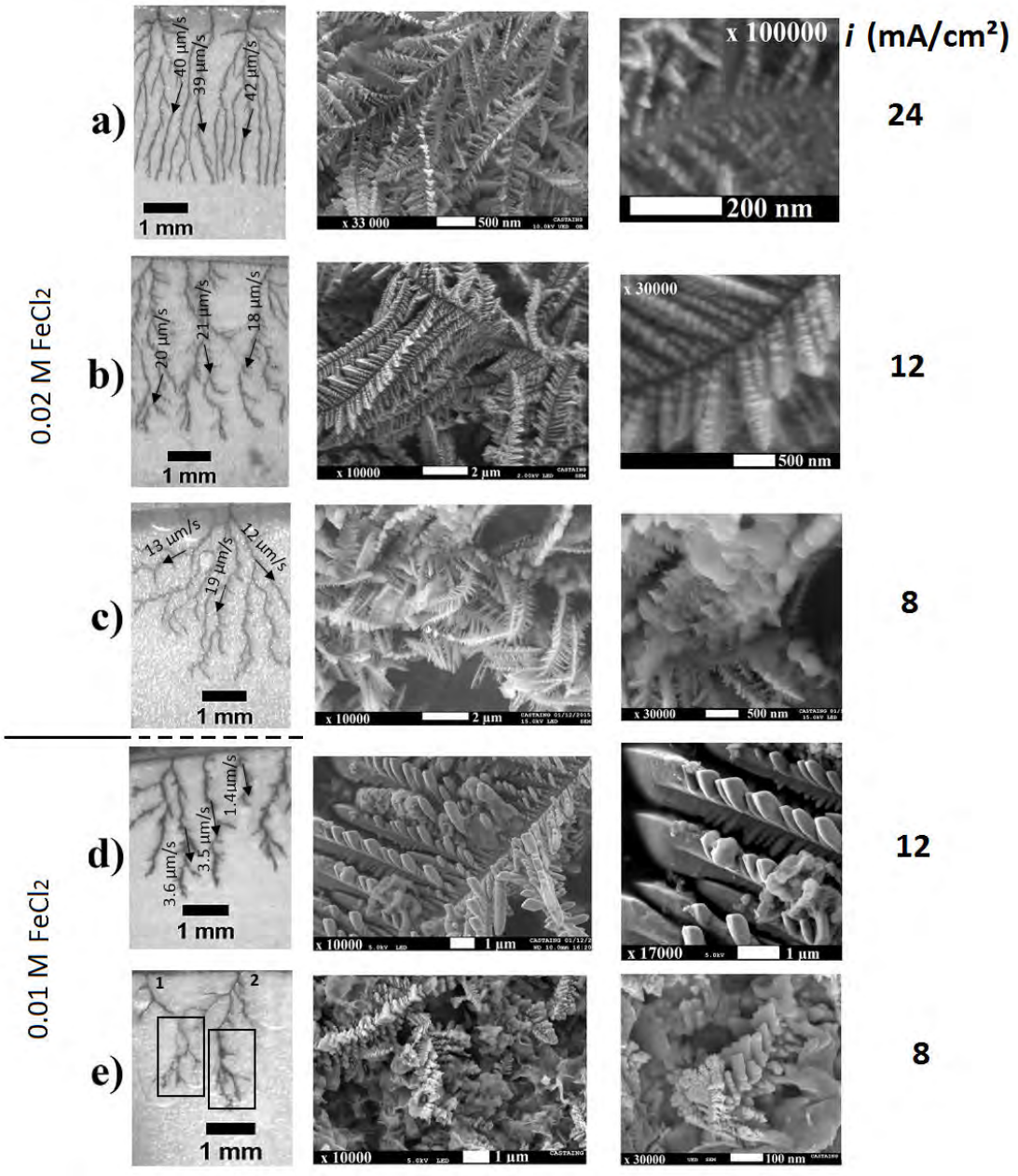

Figure 4.11: SEM pictures of iron electrodeposits obtained in thin cell under various current densities and using various precursor concentrations. a, b, c: 0.02 M $FeCl_2$, and i of 24, 12 and 8 mA/cm^2 respectively; d, e: 0.1 M $FeCl_2$, and i of 12 and 8 mA/cm^2 respectively.

4.3.5 Dense branching morphology

The study of the electrodeposit morphology has highlighted that the deposits produced at high current density have a more regular shape both at large scale and small scale. Indeed, by increasing the current density, the grains composing the branches become smaller but also more homogenous in size. This change in the small scale structure, also induces that the deposit obtained at high current is more fragile than the DLA-like deposit. This point is important here, since the objective is to fragment the deposit in order to obtain a suspension of nanoparticles. Thus, the fragmentation of the DBM-like deposit is expected to be easier than that for the DLA-like deposit. Also, the use of high current densities enables to favor the iron growth against the hydrogen bubbles formation as it was highlighted earlier. For all of these reasons, we will now focus on the electrodeposition of DBM-like deposit.

As it was described previously, the dense branching aggregate consists of a densely ramified deposit which fills uniformly the cell. All branches are growing at the same speed and thus, the DBM-like deposit is bounded by a flat front which shifts the anode with a constant velocity. As detailed in Chapter I in Section 1.2.2, Léger et al [59] and [44] have modeled this velocity (Equation 1.49): $v_g = \frac{i(1-t_+)}{z_+ \upsilon_+ FC}$ (where v_g is the growth velocity, t_+ the transference number, $z_+ = 2$ the valence and $\upsilon_+ = 1$ the stoichiometric coefficient of the cationic species of the precursor, i the current density corresponding to the metal ions reduction.)

Several iron DBM deposits are produced, and their apparent growth speed (distance covered by the deposit divided by the duration of the electrolysis), determined using a camera, is compared with the theoretical one, thanks to the equation (Equation 1.49). To that end, the apparent velocity v_g is plotted as a function of the ratio $\frac{i}{2FC}$. The DBM-like deposit are obtained under current densities ranging between 24 to 240 $\mathrm{mA/cm^2}$ and with concentrations $FeCl_2$ varying from 0.02 M to 0.1 M. It can be assumed that, for this range of current density, the fraction of i allotted to the H^+ can be neglected, therefore the ratio $\frac{i}{2FC}$ is determined from the total current density applied (the H^+ is not taken into account).

The Figure 4.12 shows that the apparent velocity (blue squares) increases linearly with the ratio $\frac{i}{2FC}$. The slope of the curve, which represents the difference $(1 - t_+)$,

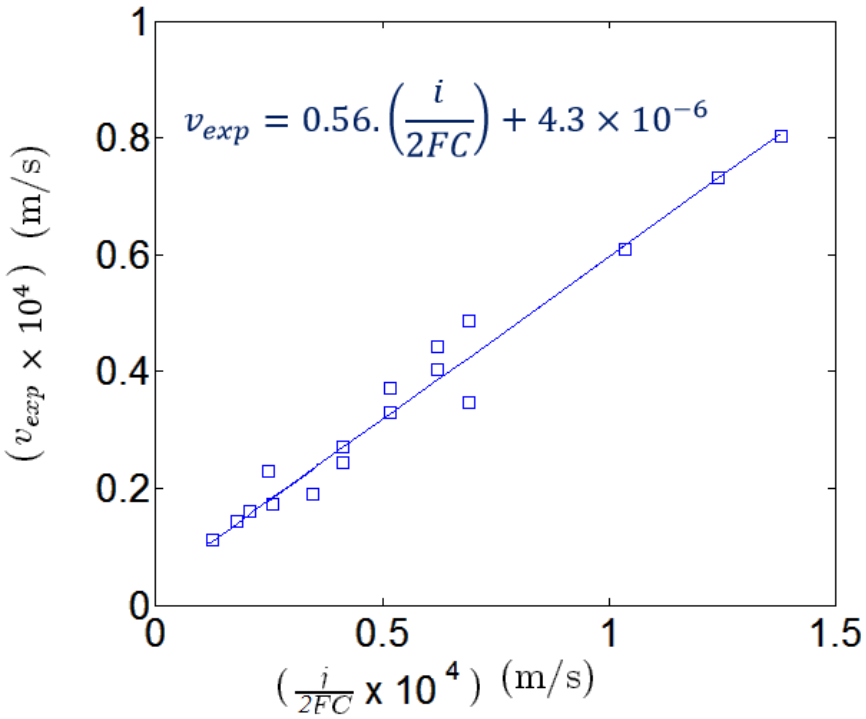

Figure 4.12: Apparent growth speed of DBM-like deposit (determined experimentally in the present study) as function of the ratio $\frac{i}{2FC}$. Blue square: experimental data; blue line: linear regression.

is found to be equal to 0.56. The comparison of the apparent velocity with the one expected from Equation 1.49 can be achieved by the comparison of the theoretical and experimental transference number of the cation t_+, expressed by the equation 1.48: $t_+ = \frac{z_+\mu_+}{z_+\mu_+ - z_-\mu_-}$ [4] [58]. At infinite dilution, the mobility μ of the ions is related to their diffusion coefficient by $\mu = D/RT$, D_+ and D_- are taken to 7.19×10^{-10} [75] and 2.03×10^{-9} m^2/s^{-1} [90]. The equation 1.48 enables to obtain a t_+ value of 0.41 which is close to the t_+ determined with the experimental data: 0.44. These results show that the experimental growth velocity, obtained for the DBM deposits in the present study, can be predicted from Equation 1.49. This suggests that only a small portion of the cathodic current density i is allotted to the H^+ reduction. Even if hydrogen bubbles are generated at the same time that the iron elelectrodeposit, the growth speed of the iron

[4] According to Zhao et al. [89], for low chloride concentration (under 1 mol/kg), the iron ions is uncomplexed.

DBM deposits does not seem to be affected.

4.3.6 Influence of impurities on the deposit growth

It has also been observed in the present study that when the DBM-like deposits reach approximately the half of the distance between the anode and the cathode, changes in its morphology appear (see Figure 4.13), it seems to become denser and darker after crossing a certain distance.

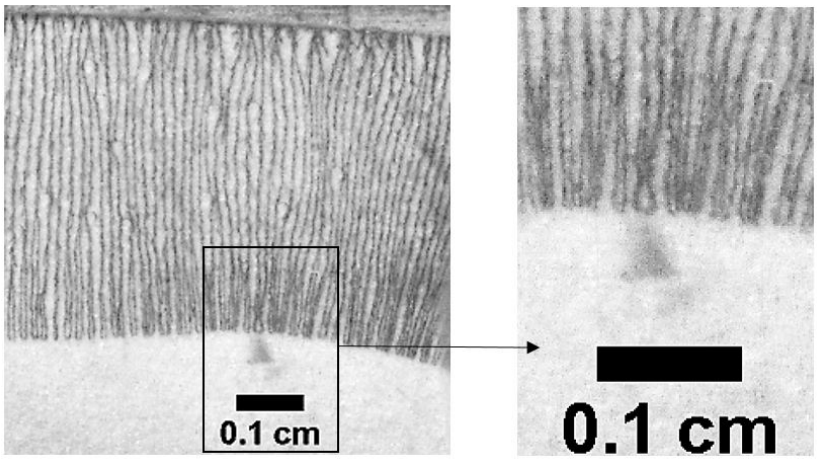

Figure 4.13: DBM-like deposit obtained from a 0.06 M $FeCl_2$ solution under i=80 mA/cm^2.

This effect, known as the Hecker effect, is described in the bibliography by many authors as a sudden change in the deposit morphology, characterized by changes in color, roughness, shape, the number of branches of the deposit, but also by the formation of bubbles which can destroy the deposit [91] [92]. In the present experiments, a change in the number of branches can be observed. In fact, after the transition zone, most of the branches appear to ramify, and consequently the number of branches increases (see the zoom-in Figure 4.13, each branch forms two new branches).

Most of the authors agree that this change in morphology is due to the arrival of an impurity front against the deposit [91] [93] [92] [88]. According to Fleury et al. [91] this could be a flow of cationic species and a flow of protons coming from the opposite electrode. In fact, the position of the transition zone is strictly defined by the transference

number of the cation and anions. In the present study, Fe^{II} moves toward the cathode, and the corresponding depletion front move in the opposite direction. Simultaneously, the Fe^{II} electroformed at the sacrificial anode move toward the cathode. The transition area appears when the depletion front meets the front of the concentrated iron solution coming from the anode.

4.4 Fragmentation of an iron electrodeposit in a Hele-shaw cell

This section focuses on the second step of the studied synthesis process which consists of the fragmentation of the ramified iron deposit in the "vibrating" Hele-Shaw cell.

4.4.1 Parametric study of the fragmentation efficiency

Influence of the hydrogen bubbles on the fragmentation process

Bibliographie reveals that the dimensions of the thin layer do not allow the acoustic field generated by a PZT element to generate a significant effect on the fluid (see chapter I). To induce strong mixing in microfluidic devices, several studies propose to use air bubbles, trapped into the microdevice, as actuators. Indeed, when the surface of the bubble is subjected to acoustic vibration, it starts to vibrate and induces an acoustic streaming around it.

In the current study, the hydrogen bubbles, induced by the reduction of the free proton, are expected to acts as a vibrating element inside the microchannel and to induce an acoustic streaming, able to fragment the iron branches. To verify this assumption, after the electrodeposition of an iron DBM-like deposit (0.1 M, 80 mA/cm^2), the PZT is activated during few seconds (square signal with f = 4 kHz and Vpp = 250 V). To understand the influence of the hydrogen bubbles in the resulting fragmentation, this experiment is compared with the one obtained with a copper deposit (0.1 M, 80 mA/cm^2) where no hydrogen bubbles are formed [5].

[5]The reduction potential of hydrogen in the copper system is more cathodic than electrodeposition potential of copper. Therefore no hydrogen bubble are produced during the growth of the copper deposit

The efficiency of the fragmentation is evaluated, using an image processing on Matlab, which consists of binarizing each picture of the videos and counting the number of black pixels. The binarization threshold is determined by measuring the gray level corresponding to the iron branches. Therefore, after the binarization, the resulting amount of black pixels is representative of the number of unfragmented branches. When the size of an iron fragment becomes lower than the size of one pixel, it can no longer be defined. Consequently, the gray level of the pixel decreases under the binarization threshold. Knowing that a pixel corresponds to ≈ 20 μm, the deposit branches are considered as being fragmented (by the image processing) if their size is lower than 20 μm.

Thus, when the deposit is dispersed, the number of black pixels decreases as a function of time. The lighting equipment can slightly vary from one experiment to the other. Thus, to enable the comparison of the different results, the number of black pixels is normalized by the maximum amount of black pixels measured during the dispersion.

The evolution of the amount of unfragmented branches (AUB) as a function of time is thus represented in the Figure 4.14 for the iron and the copper deposits, e.g., in the presence and in the absence of H_2 bubbles. The idea is to observe the influence of the hydrogen bubbles on the fragmentation efficiency. This graph reveals that for the iron electrodeposit (blue solid line), the AUB decreases of $\approx 90\%$ in one second and stabilizes around 3 %. Three pictures of the fragmentation video, taken at 0, 1 and 2 s confirm the fragmentation of the deposit between 0 and 1 s. It can be noticed that after 2s, only some small (< 200 μm) fragments of branches are still visible. This enables to explain why the AUB does not decrease to zero.

A different evolution of the AUB is observed for the copper case (Figure 4.14 red dotted line). Indeed, in a first instance, the deposit seems to be stable during 0.3 s. Then a perturbation induces the decrease of the AUB to approximately 70-60 in ≈ 0.5 s, then the AUB stays almost stable until the end of the experiment. To understand this evolution, the pictures taken at 0, 0.4 and 2 s are shown. After 0.4 s, the copper deposit appears to be quite similar to the initial deposit, but it can be seen that a bubble, probably trapped under the cathode during the filling of the Hele-Shaw cell, slips from the cathode to the channel under the influence of the PZT vibration. This bubble seems

to induce a vortex, which breaks the branches that are in the vicinity of its surface. However, the presence of this single bubble does not enable to achieve a fragmentation as efficient as for the iron deposit.

To conclude, these experiments highlight that the fragmentation of an iron deposit, in the presence of hydrogen, is possible and fast (almost complete after 2 s). In absence of bubbles, the experiment performed with the copper shows that no fragmentation occurs. Indeed, the AUB is stable during the first 0.4 s of the fragmentation (before the bubble get into the channel) and then remains high $\approx 60\%$ and stable. This experiment also confirms that the bubbles are responsible for the fragmentation, since the decrease of the AUB, in the copper case, is only due to the release of a trapped bubble in the channel which, by creating a vortex under the vibration of the PZT, breaks a part of the deposit. These results confirm the bibliographic statements: the presence of bubbles is essential for the vibration of the PZT to induce strong enough fluid motion to enable the fragmentation of the deposit.

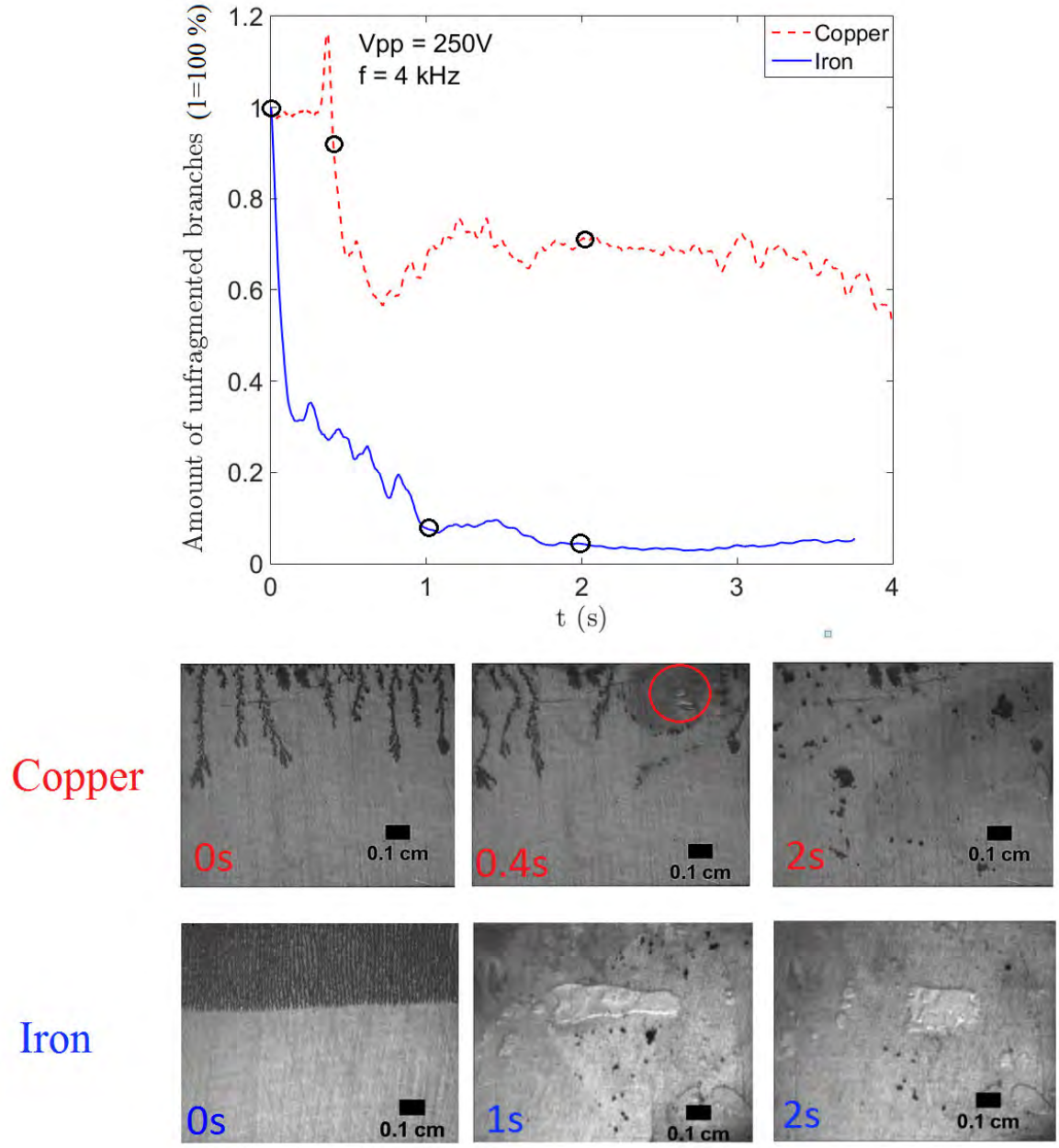

Figure 4.14: Top: Evolution of the amount of unfragmented branches as a function of time, for an iron deposit submitted to acoustic vibrations, in the presence of hydrogen bubbles (blue solid line) and for a copper deposit without bubble (red dotted line). Bottom: Pictures the copper and iron deposit captured at various durations of the fragmentation process, in a Hele-Shaw cell. The PZT is activated with a square signal: f= 4 KHz and Vpp = 250 V (peak to peak voltage).

Influence of the electrical signal parameters applied to the PZT

The electrical signal driving the PZT vibration can be modulated according to the following ways:

- its waveform: triangular, sinusoidal, square.
- the voltage and the frequency applied.

The previous section confirms that the presence of bubbles is a necessary condition to achieve the fragmentation of the deposit. This section is devoted to the influence of the electrical signal properties on the fragmentation efficiency of a DBM deposit (0.1 M, 80 mA/cm^2) by the PZT vibrations, induced for different waveforms, frequencies, and voltages.

As previously, the number of unfragmented branches is represented as a function of time, for sinusoidal, triangular, and square waveforms of the electrical signals (Figure 4.15). Curves show similar results for the sinusoidal and triangle signals; the AUB decreases to 0.5-0.4 after 4 seconds of activation of the PZT. Pictures of the iron deposit, taken at 0, 1 and 4 seconds (Figure 4.15, Bottom), highlight that the activation of the PZT with a sinusoidal signal enables to break the iron branches into blocks of sizes ranging between 100 and 1000 μm. Moreover, the bubbles network, formed during the deposit growth, is not affected by the activation of the PZT. In fact, the PZT induces the vibration of the hydrogen bubbles, leading to the regrouping of the iron branches into small blocks, which are then trapped in the bubbles network. However the deposit is not fragmented (no cloud of fine particles is visible) but compacted[6] and therefore, the surface occupied by the deposit decreases. This leads to a decrease in the number of black pixels on the pictures, and consequently, to the decrease of the AUB, which does not reflect the dispersion of the iron branches. Thus, the small blocks of compacted iron branches are present until the end of the experiment explaining why the AUB does not decrease to zero.

[6]Note that the iron branches are porous and flexible.

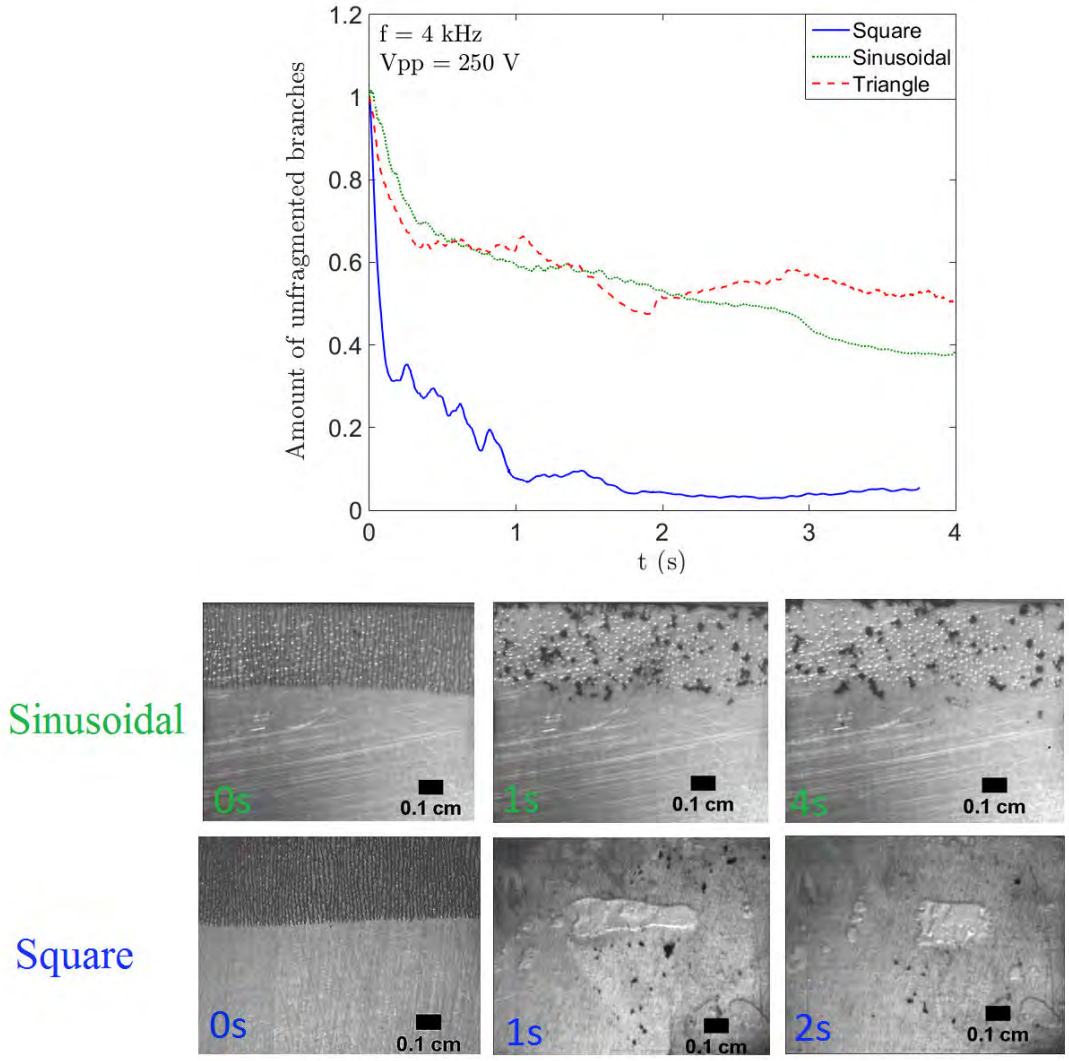

Figure 4.15: Top: Evolution of the AUB obtained during the fragmentation of a DBM-like deposit (0.1 M, 80 mA/cm^2). The PZT diaphragm is driven with an electrical signal of 4 kHz, Vpp = 250 V, and different waveforms : triangular, sinusoidal and square. Bottom: pictures captures during the deposit fragmentation for the sinusoidal and square electrical signals.

In comparison, the AUB obtained with the square signal (blue solid line, Figure 4.15, Top) decreases from 1 to almost zero, in 2 s, as it has been described previously. The picture taken after 2 s only, shows small iron blocks (<200 μm) and a cloud of iron particles hardly distinguishable.

To sum up, only the square signal enables the fragmentation of the deposit into a suspension of fine iron particles. Liu et al. [72] also found that square sound wave leads to a faster mixing than a sinusoidal sound wave but no further explanation was given. According to Murata application manual, a square wave produces higher sound levels than sinusoidal or triangular signals due to the instantaneous rise and fall time of the signal which leads to a more brutal displacement of the PZT disk (further discussed in the following sections). Indeed, under a square electrical signal, the displacement of the PZT interface ε can be represented as in Figure 4.16, a. The resulting theoretical displacement speed of the PZT interface $\frac{d\varepsilon}{dt}$ becomes infinite during the voltage step. Nevertheless, the temporal resolution of the signal generator is a finite value, implying that the displacement speed of the PZT interface is also a finite value (Figure 4.16, b). Therefore, the square wave signal should induce higher displacement speeds of the PZT than sinusoidal or triangular signals. The effect of the PZT displacement speed, on the bubbles oscillations, will be further discussed in the following section enabling to explain the very efficient fragmentation observed using a square electrical signal.

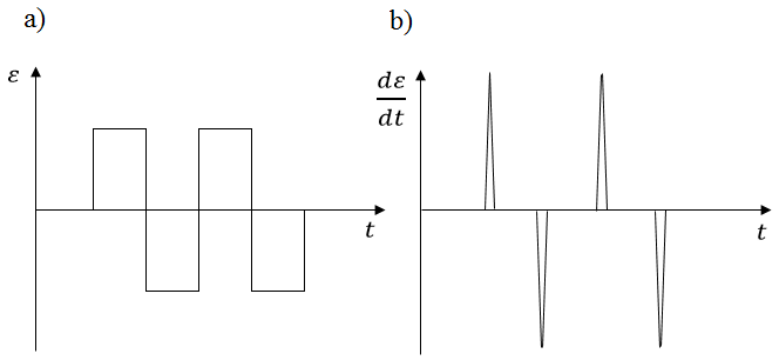

Figure 4.16: Schematic representation of the PZT interface displacements a) and the resulting interface displacement speed, when submitted to a square wave signal.

The temporal evolution of the AUB is determined for four different peak to peak voltages: Vpp = 125, 200, 237, and 250 V (see Figure 4.17, top). The obtained results show that, the higher the voltage of the electrical signal, the faster (and more efficient) the fragmentation is. For a signal of 250 V: the AUB decreases to $\approx$ 30 % after 0.2 s and reaches $\approx$ 5 % after 2 s, while it decreases to $\approx$ 70 % in 1 s and stabilizes at

≈ 45 % when Vpp = 125 V. Pictures showing the evolution of the dispersion for the fastest and the slowest fragmentation (250 and 125 V respectively) are also presented. It appears that applying the lower voltage, the deposit is not fragmented but compacted into several blocks, in the same way as explained previously. Once again, the AUB decreases because the surface occupied by the deposit is reduced, but this does not reflect the efficiency of the fragmentation. For the intermediate voltages (200 and 237 V), the dispersion occurs, but it is slower than for the highest voltage (250 V) and not totally completed after 3s.

The effect of three different frequencies (4 kHz, 1 kHz, and 500 Hz) of a square signal (250 V peak-to-peak voltage) is examined. The temporal evolution of the AUB (Figure 4.18) shows that the higher the frequency of the signal, the faster the fragmentation is. However, the influence of the frequency appears to be low compared to the effect of the voltage or of the waveform of the electrical signal. Indeed, even if the fragmentation is faster at 4 kHz, complete fragmentations are also obtained at 1 kHz and 500 Hz for longer durations of the PZT activation.

Besides, for applied frequencies of 1 kHz and 500 Hz, the evolution of the AUB starts by a sudden and quasi-instantaneous decrease (around 0.034 s), followed by a high increase (around 0.34 s) (squared area, Figure 4.18). This strong variation is not representative of the progress of the fragmentation and can be explained by analyzing both the pictures of the deposit taken at these times, and the corresponding binarized images, resulting from the images processing program (Figure 4.19). The picture taken at 0.034 s shows that the iron branches are regrouped and compacted into numerous iron blocks, and as it was explained previously, this induces a reduction of the surface occupied by the deposit, but does not reflect its fragmentation. The picture taken at 0.34 s shows that, the iron blocks formed are fragmented into a dark cloud of particles, but the suspension of iron particles is not yet well dispersed into the channel. Therefore, some part of the dark cloud formed by the suspension are still above the binarization threshold and are considered as a part of unfragmented branches by the images processing program. This induces the fast increase observed between 0.034 and 0.4 s. Therefore this anomaly in the evolution of the AUB is not relevant.

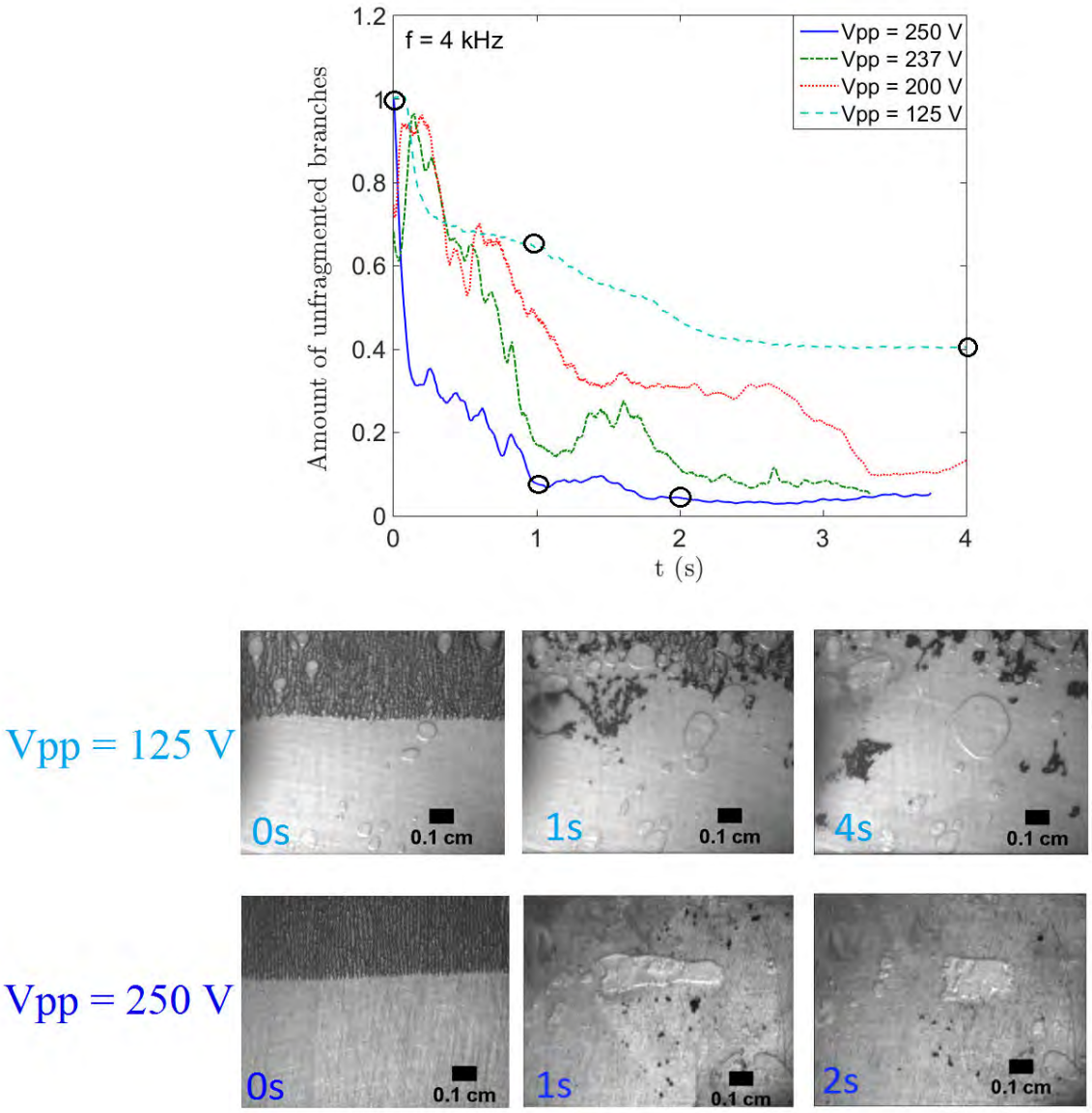

Figure 4.17: Top: evolution of the AUB of a DBM-like deposit (in a Hele Shaw's cell, $FeCl_2$ at 0.1M, 80 mA/cm^2) during the activation of the PZT. The PZT diaphragm is driven with a square electrical signal of 4 kHz with a peak to peak voltages of: 125, 200, 237, and 250 V. Bottom: pictures captures at various times of the deposit fragmentation for the highest and lowest voltage are shown.

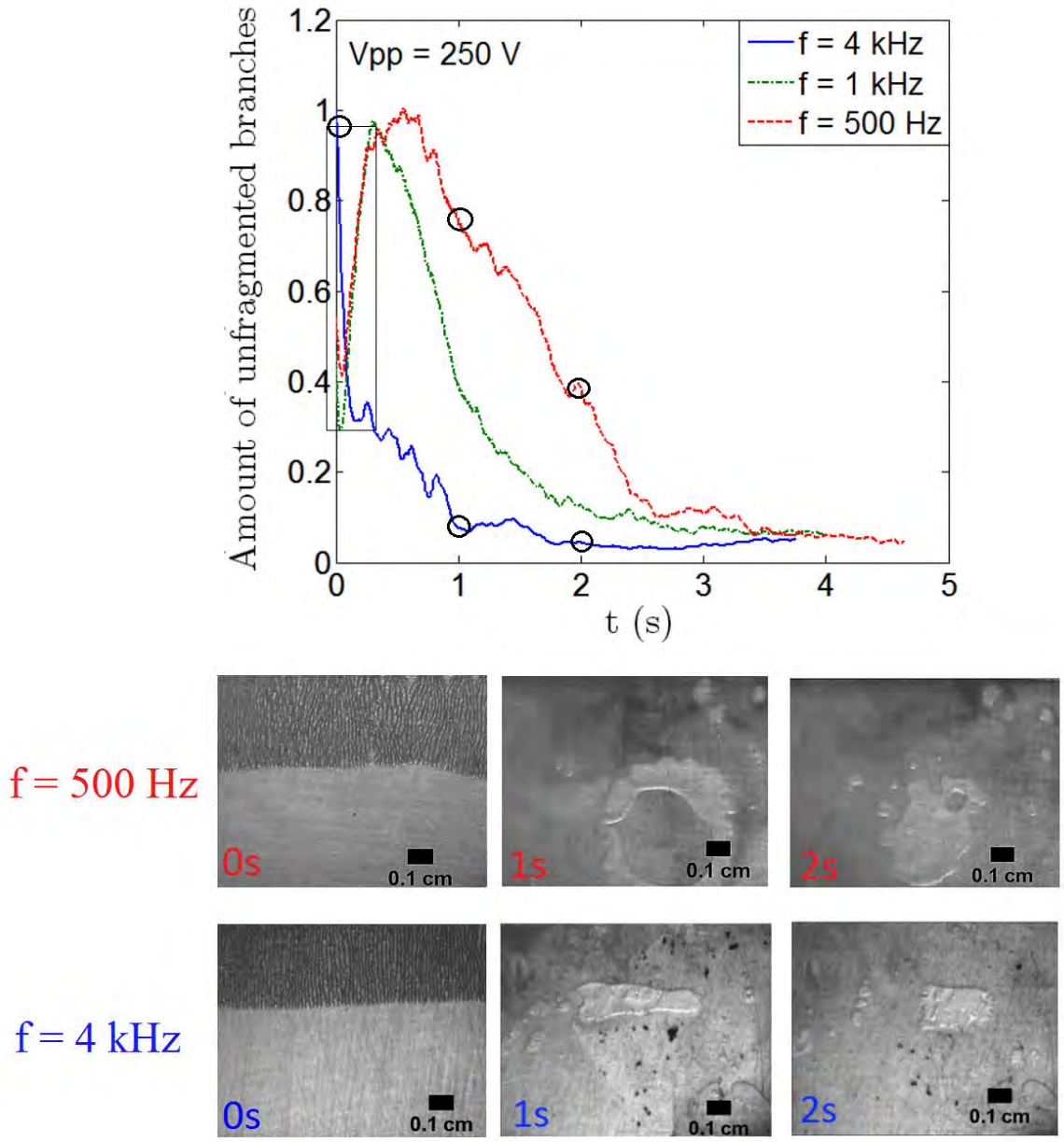

Figure 4.18: Top: evolution of the AUB obtained during the fragmentation of a DBM-like deposit ($FeCl_2$ at 0.1 M - 80 mA/cm^2). The PZT diaphragm is driven with a square electrical signal of 250 V and frequencies of: 4 kHz, 1 kHz and 500 Hz. Bottom: pictures (captured at various times) of the deposit fragmentation for the lowest and highest frequencies.

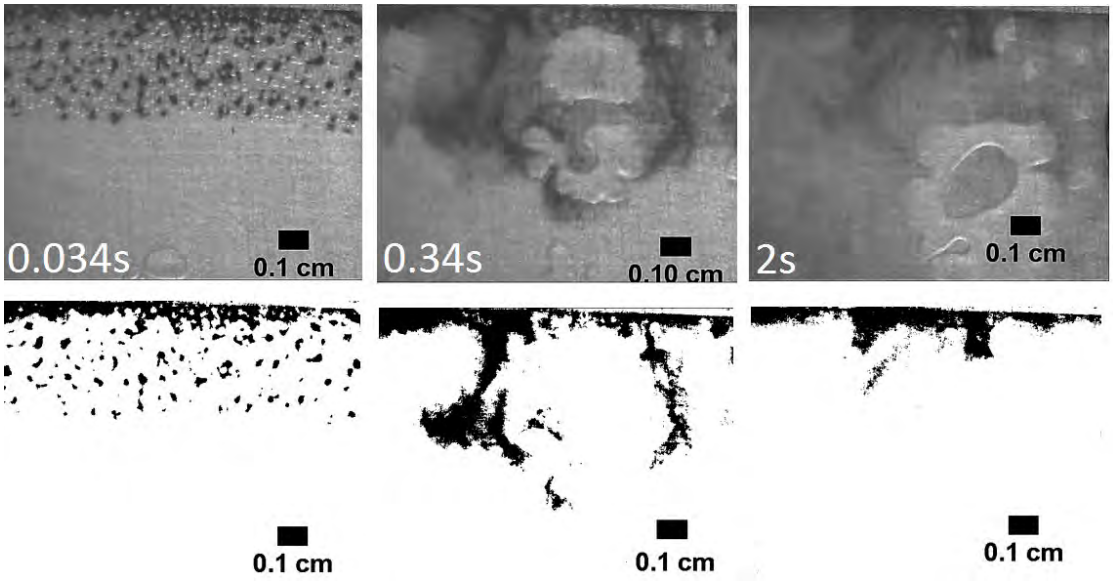

Figure 4.19: Pictures captured at various times of the deposit fragmentation (shown in the Figure 4.18) achieved with a square electrical signal of Vpp = 250 V and f = 500 Hz, and the corresponding binarized pictures obtained after the images processing. Pictures are taken at 0.034, 0.34 and 2 s.

To sum up, on the one hand, this parametric study highlights the importance of the bubbles in the deposit fragmentation. Without bubbles, the vibrations of the PZT induce, by the variation of the microchannel depth, a global fluid motion inside the cell [7]; however, the branches are neither fragmented nor dispersed (copper case). Under the vibrations of the PZT diaphragm, the bubbles induce strong fluid motions which enable the fragmentation of the deposit. On another hand, the efficiency of the fragmentation varies in function of the parameters of the electrical signal driving the PZT. It can be concluded that, the effects induced by the hydrogen bubbles, depend on the applied signal, and are stronger for a square signal with high voltage and frequency (250 V and 4 kHz). Therefore, a deeper analysis of the bubbles behavior as a function of the operating conditions is necessary to understand the effects leading to the break of the iron branches.

[7] Note that one the fluidic connections of the cell is open, allowing the variation of the liquid volume contained by the channel.

4.4.2 Behaviour of the bubbles under the effect of the PZT diaphragm vibrations

The careful observation of all the videos of the deposit fragmentations reveals three different behaviors of the bubbles, when they are subjected to the vibrations of the PZT (see Figure 4.20).

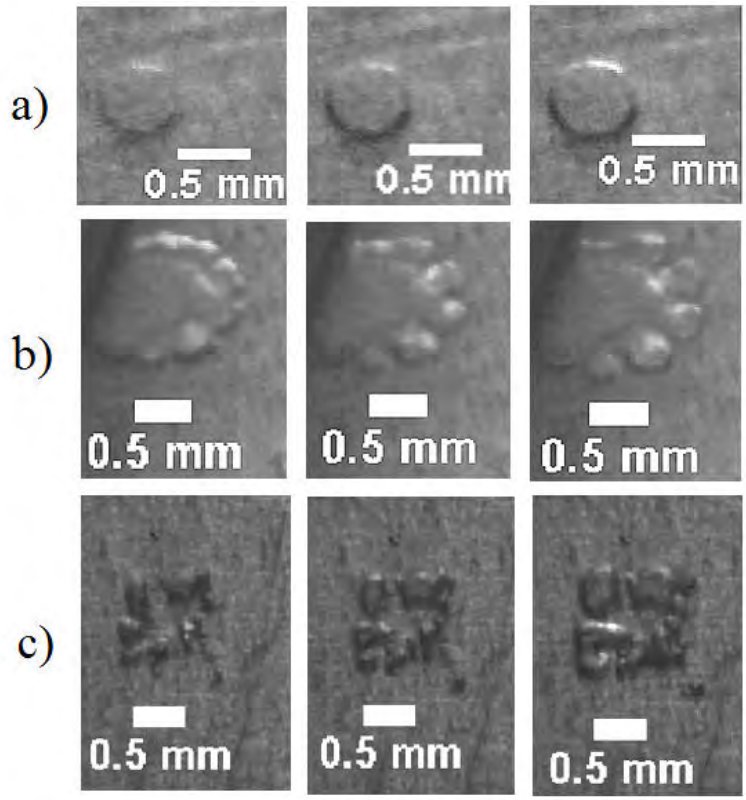

Figure 4.20: Pictures showing behaviours of the hydrogen bubbles (formed during the electroformation of an iron deposit) under the vibration of the PZT diaphragm in a Hele-Shaw cell: a) Breathing mode; b) Shape oscillation mode (SOM); c) splitting mode.

The first "kind" of bubble, oscillates with a radial pulsation, meaning that it expands and contracts radially and periodically, with no transformation of its circular shape (Picture a, Figure 4.20). Bibliography shows that this type of bubble oscillations is known as radial oscillation mode or breathing mode [94] [95] [96].

Another H_2 bubbles population shows a very different behavior, bubbles expand and

contract with deformation of their initial spherical surface. Indeed, Picture b, Figure 4.20 shows that the liquid/gas interface of the bubble is corrugated and shows 6 "fingers" distributed along its interface. This kind of bubble oscillation is known as shape oscillation mode (SOM) [94] [96].

Finally, a last behavior has been observed (see Figure 4.20 c)) for which bubbles oscillate and split into multiple fragments which periodically coalesce and split again.

The analysis of the fragmentation pictures reveals that only the bubbles oscillating with the shape oscillation mode (SOM) or splitting mode induce the fragmentation of the deposit. The fragmentation by SOM bubbles is presented in the Figure 4.21 which shows that some iron branches are brought by microstreaming to the surface of the SOM bubbles (red arrow). When the branches reach the unstable bubble surface, the deposit is fragmented into fine particles which are ejected away (green arrow). It can be noticed that the deposits in the vicinity of the stable bubbles (breathing mode bubbles) do not seem to be affected by the breathing oscillation.

The splitting bubbles induce similar effects than the SOM bubbles. Indeed, the deposit appears to be attracted by the unstable bubbles oscillations and expelled away. The blocks of iron deposit (around 0.5 mm width), brought to the unstable bubble, are totally dissociated into a cloud of particles (Figure 4.21).

These experiments demonstrate that only bubble oscillating with SOM or splitting mode are actually responsible for the fragmentation. Therefore, the following section expects to correlate the parameters of the signal driving the PZT vibration with the behavior of the bubbles.

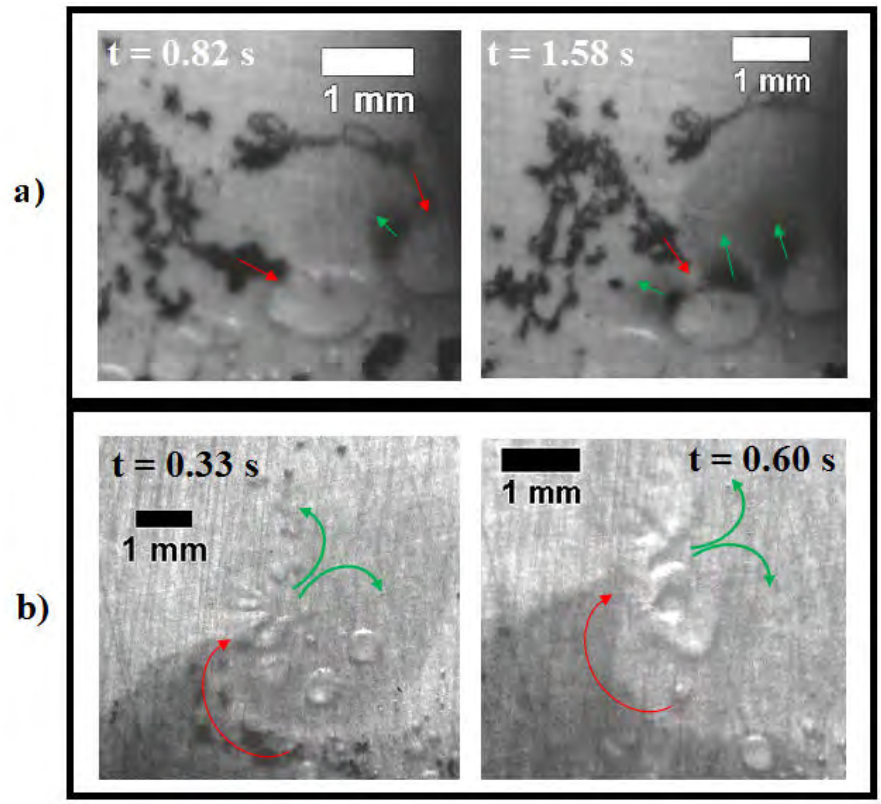

Figure 4.21: Pictures showing the fragmentation of the iron deposits (obtained under i=80 mA/cm^2 and with a 0.01 M $FeCl_2$ solution, in a Hele-Shaw cell), induced by a) SOM bubbles, b) Splitting bubbles. The PZT diaphragm, submitted to a square signal, vibrates under a) f= 4 kHz, Vpp =125 V; b) f= 4 kHz, Vpp = 250 V.

4.4.3 Parameters influencing the behavior of the oscillating bubbles

It has been demonstrated in the Section 4.4 that, the efficiency of the deposit fragmentation varies in function of the parameters of the electrical signal applied to the PZT. To understand the influence of the electrical signal parameters on the bubbles behavior (breathing mode, SOM, splitting mode), various experiments are carried out.

Three H_2 bubbles of similar sizes ($\approx$ 600 μm) have been subjected to the PZT vibration for different values of the electrical signal voltage (Figure 4.22). The videos of the bubbles oscillation show that, by increasing the voltage, the oscillation mode of the bubbles changes from the breathing mode to the shape oscillation mode. Indeed, at low voltages (72-96 V) each of the three bubbles shows a rounded shape, whereas

surface waves appear for Vpp > 216 V. However, the threshold voltage enabling surface deformation is different for each bubble. For the first and second cases the surface deformations appear around 140-168 V and 168-192 V respectively. For the third case, surface deformations only appear above 192 V. This difference can be explained by the position of the bubbles into the Hele-Shaw cell. Indeed, as explained in the section Materials and methods, the PZT disk bends alternately (see Figure 4.2) in a concave and convex position; therefore, its displacement is more important at the center of the disk than at the edges, meaning that the vibrations inside the channel are not homogeneous.

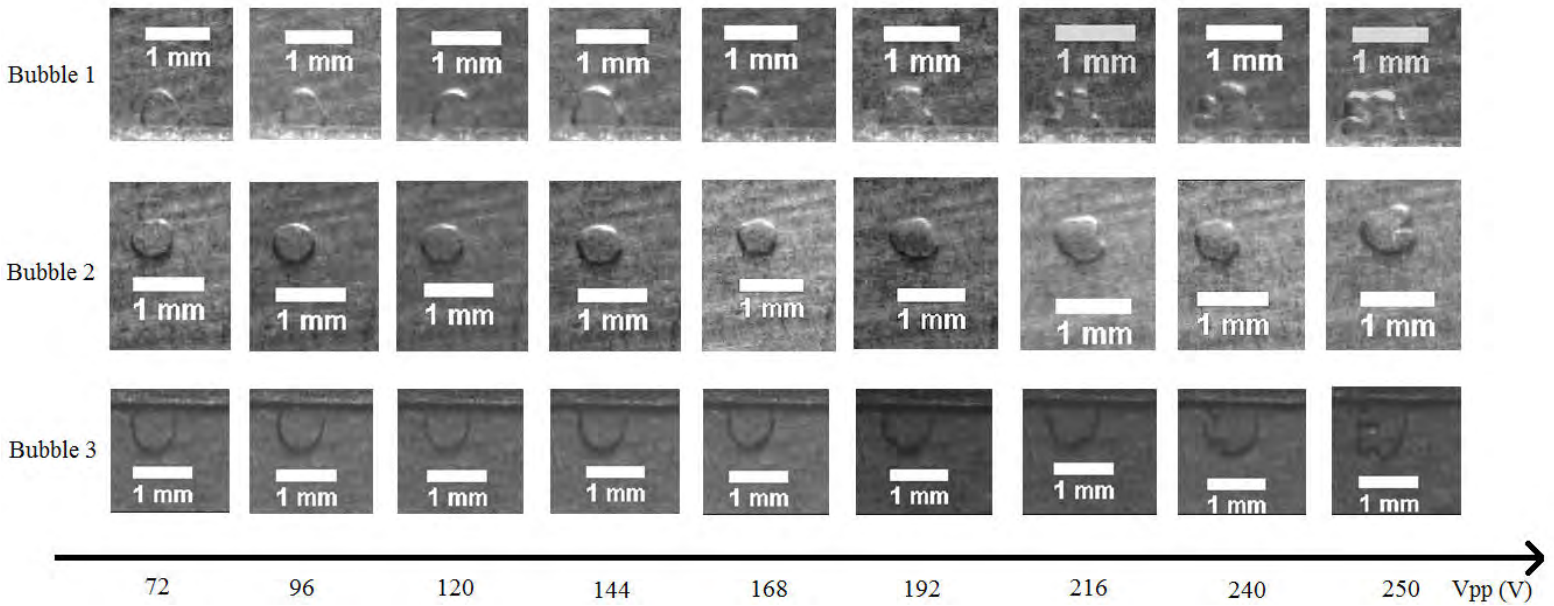

Figure 4.22: Pictures showing the behaviour of three H_2 bubbles trapped in a Hele-Shaw cell, as a function of the voltage of the electrical signal applied to the PZT (f= 4 kHz , Vpp varying from 72 to 250 V.

The behavior of three bubbles (having almost the same size), submitted to various frequencies (at constant voltage Vpp= 250 V), are examined, and show that shape oscillations occur for sufficiently high frequencies values. It can indeed be observed on the Figure 4.23, that a frequency of 100 Hz is not high enough to induce surface deformations on bubbles of $\approx$ 1 mm diameter.

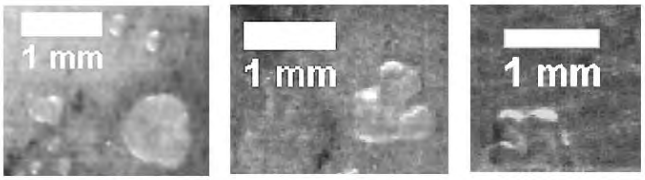

Figure 4.23: Pictures showing three different hydrogen bubbles, trapped in a Hele-Shaw cell, and submitted to vibrations of a PZT driven by an electrical signal of various frequencies (Vpp= 250 V; f varying from 100 Hz to 4 kHz).

In summary, the surface deformations of the bubbles, which are responsible for the fragmentation of the iron deposit, are induced when threshold values of peak to peak voltage and frequency are reached. This conclusion is in line with the parametric study of the fragmentation efficiency, which reveals that the fragmentation process is faster when increasing the voltage and the frequency.

The size of the bubbles also impacts their oscillating behavior (Figure 4.24). It appears that large bubbles are more easily deformed by shape oscillations, than small bubbles and that explains for example, why the fragmentation is still efficient with low frequencies (500 Hz for example).

Indeed, the analysis of the video of the deposit fragmentation carried out with a square signal of 500 Hz frequency and 250 V (Figure 4.25), shows that during the early stage of the process, the bubbles are too small to undergo surface deformations. However, the vibrations generated by the PZT induce the coalescence of the bubbles which become larger: e.g., after 0.258 s bubbles diameter reach $\approx$ 3 mm for the largest, instead of $\approx$ 1 mm at the beginning (Figure 4.25, c). After 0.353 s, only the largest bubbles (1.5-2 mm of diameter) undergo surface deformations (Figure 4.25, d). Finally, at the end of the fragmentation process (Figure 4.25, e), almost all the bubbles have

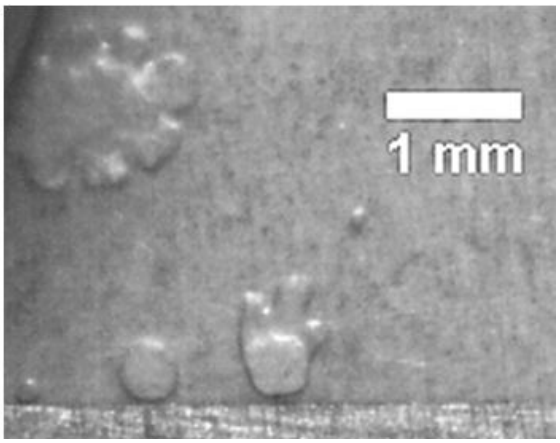

Figure 4.24: Picture of three hydrogen bubbles of different sizes, trapped in a Hele-Shaw cell and subjected to acoustic vibration of a PZT (f= 4 kHz, Vpp= 200 V). The picture reveal the influence of the bubble size on its oscillation mode

coalesced and formed a single big bubble oscillating with a SOM.

In comparison, applying to the PZT a square signal of 4 kHz and 250 V (Figure 4.26), enables the rapid coalescence of bubbles: after 0.082 s it can be seen that some bubbles (on both sides of the cell) have already coalesced forming bigger bubbles of $\approx$ 1 mm diameter which oscillate with SOM. This demonstrates that, by increasing the frequency, the size of the bubbles showing surface deformations decreases. Therefore, the fragmentation is faster (see the section 4.4) for higher frequencies signals both because shape oscillations appear for smaller bubbles and because coalescence of the bubbles is faster. After 0.25 s, most of the bubbles have coalesced, and at the end of the fragmentation (1.62 s) one single bubble, oscillating with SOM, is present in the cell. In fact, the process is quite similar than for lowest frequencies except that at 4 kHz, the unstable bubbles appears quicker.

To simplify the following discussion, the SOM bubbles and the splitting bubbles will be qualified as unstable bubbles and the bubbles oscillating with breathing mode will be named stable bubbles.

To get a better understanding of the joint effects of the voltage, the frequency, and the size of the bubbles, on the efficiency of the fragmentation, the proportion of stable and unstable bubbles has been determined as a function of their size and for the different

operating conditions [8] (Figure 4.27 and Figure 4.28).

As explained above, due to the coalescence process, inducing the increase of the bubble size, there are more unstable bubbles at the end of the fragmentation than initially. Furthermore, due to the coalescence process, the number of small stable bubbles initially present into the cell, is higher than the number of big unstable bubbles obtained at the end (see Figure 4.25 and Figure 4.26). Therefore, the stable and unstable bubbles are counted on the basis of several pictures taken at different moments of the fragmentation; the idea here is not to compare the number of stable and unstable bubbles but to determine a critical size above which bubbles become unstable.

Regarding the obtained histograms (Figures 4.27 4.28), it appears that, for almost every operating condition applied, the ratio "unstable bubbles/stable bubbles" is higher than 1 for the large size, and, lower than 1 for small bubbles. This confirms the assumption made above. Moreover, for almost every case, there is a critical bubble size above which only unstable bubbles are found.

For example for Vpp = 120 V (Square signal with f = 4 kHz) the critical size is about 1380 μm, above this value, the bubbles become unstable (Figure 4.27). Furthermore, increasing the peak to peak voltage causes the critical size to decrease. Typical values are 786, 982 and 393 μm for voltages of 168, 228 and 250 V respectively. Therefore, increasing the voltage causes more hydrogen bubbles to exhibit surface deformation, thus, enabling the fragmentation of the deposit. Also, as it was explained for the influence of the frequency, increasing the voltage also leads to a faster coalescence of the bubbles and thus to increase the number of unstable bubbles.

In the same way as for the effect of the voltage, increasing the frequency of the electrical signal also leads to decrease the critical size of bubbles, above which surface deformations appear (Figure 4.28). Indeed, for frequencies of 100 Hz and 500 Hz (square signal and Vpp = 250 V), no critical size is found. For the first case (100 Hz) only few unstable bubbles are found even at the end of the fragmentation. It can also be noticed that few big bubbles are found. This suggests that the PZT vibrations are not strong enough to allow the coalescence of the bubbles, which consequently, can not reach the critical size required to become unstable. For an applied frequency of 500 Hz,

[8] The procedure followed to count the stable and unstable bubble is detailed in the Annexe 1.

even if no critical value is found, the majority of the bubbles are unstable above 982 μm. Finally, for higher frequency (4 kHz), the critical size decreases to 393 μm.

To conclude about the parameters influencing the bubbles deformation (and consequently the deposit fragmentation), it has been demonstrated that only unstable bubbles induce the dispersion of the deposit. To become unstable, the bubble must reach a critical size which depends on the parameters of the electrical signal driving the PZT vibration. Increasing the voltage and the frequency leads to a decrease of the critical size (for f= 4 kHz, Vpp= 250 V: critical size $\approx$ 400 μm). The hydrogen bubbles produced during the DBM deposit growth are too small to exhibit surface deformation $\approx$ 50 μm. That is why the coalescence of the bubbles is also a key phenomenon conditioning the fragmentation of the deposit. Indeed, if the PZT vibrations are strong enough (high voltage and frequency), they allow the coalescence of the initial bubbles which can, thus, exhibit surface deformations. The higher the voltage and the frequency, the faster the coalescence is (for f= 4 kHz, Vpp= 250 V, all the bubbles have coalesced in one single bubble after 1.62 s Figure 4.26). Therefore, increasing the voltage and the frequency enables both to decrease the critical size above which a bubble become unstable and to make the coalescence of the bubbles faster. Thus, more hydrogen bubbles are unstable, and the fragmentation becomes faster than for lower voltages and frequencies.

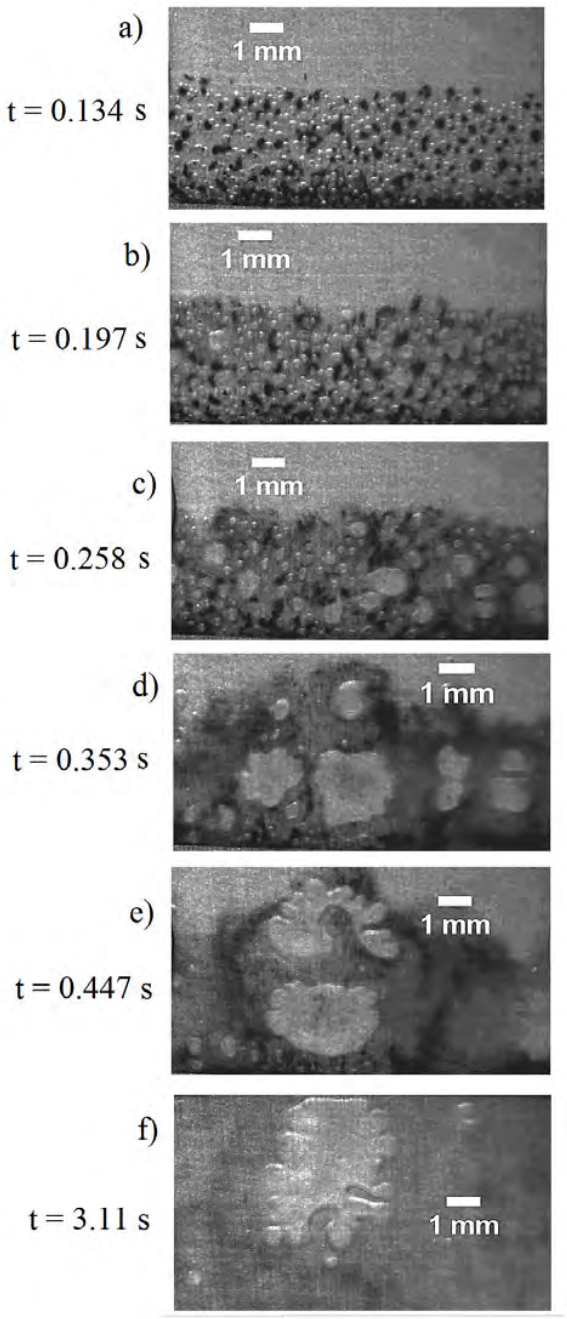

Figure 4.25: Pictures showing the coalescence of the hydrogen bubbles (formed during the growth of DBM deposit i= 80 mA/cm^2, in a 0.1 M $FeCl_2$ solution) trapped in a Hele-Shaw cell and submitted to acoustic vibrations by a PZT diaphragm: Square signal, f = 500 Hz, Vpp = 250 V

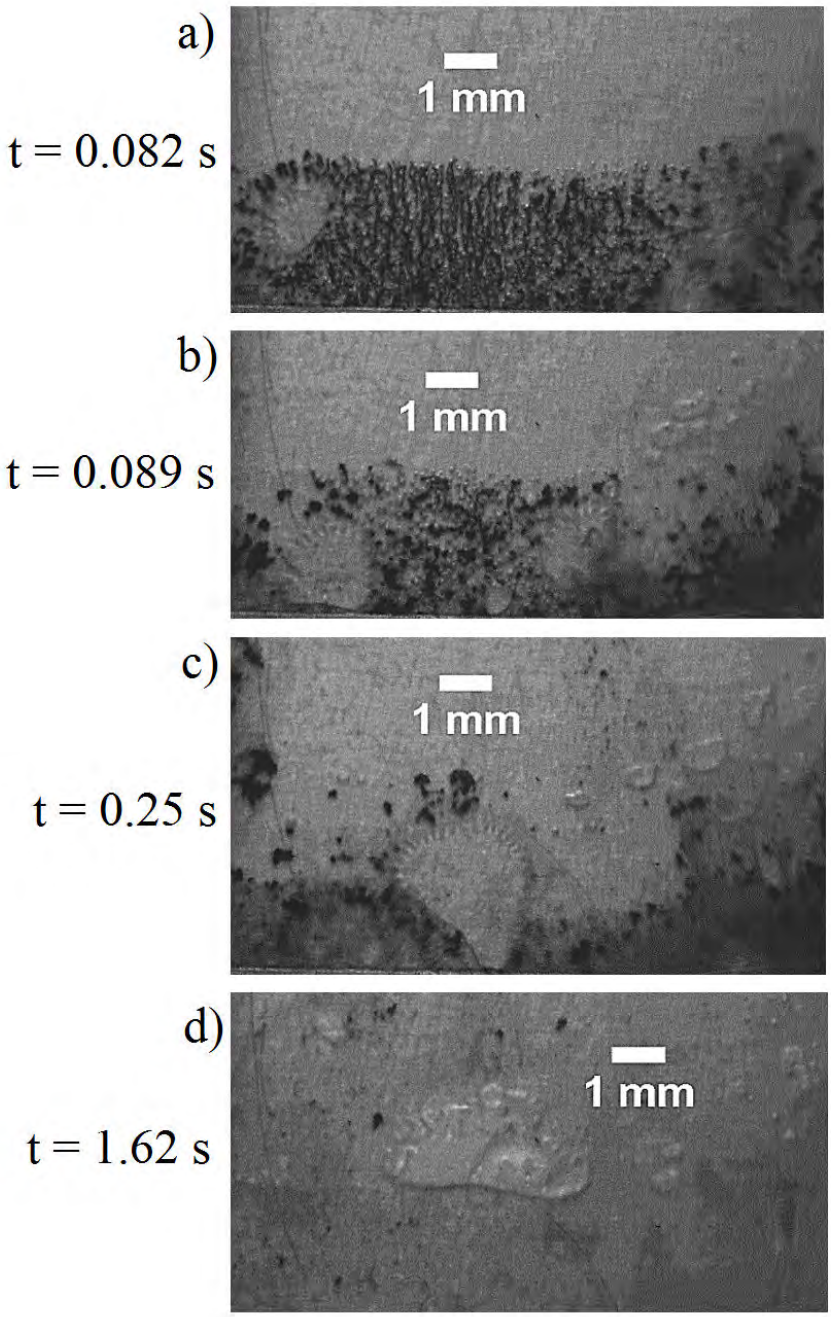

Figure 4.26: Pictures showing the coalescence of the hydrogen bubbles (formed during the growth of DBM deposit, i= 80 mA/cm^2, in a 0.1 M $FeCl_2$ solution), trapped in a Hele-Shaw cell, and submitted to acoustic vibrations by a PZT diaphragm: Square signal, f = 4 kHz, V = 250 V

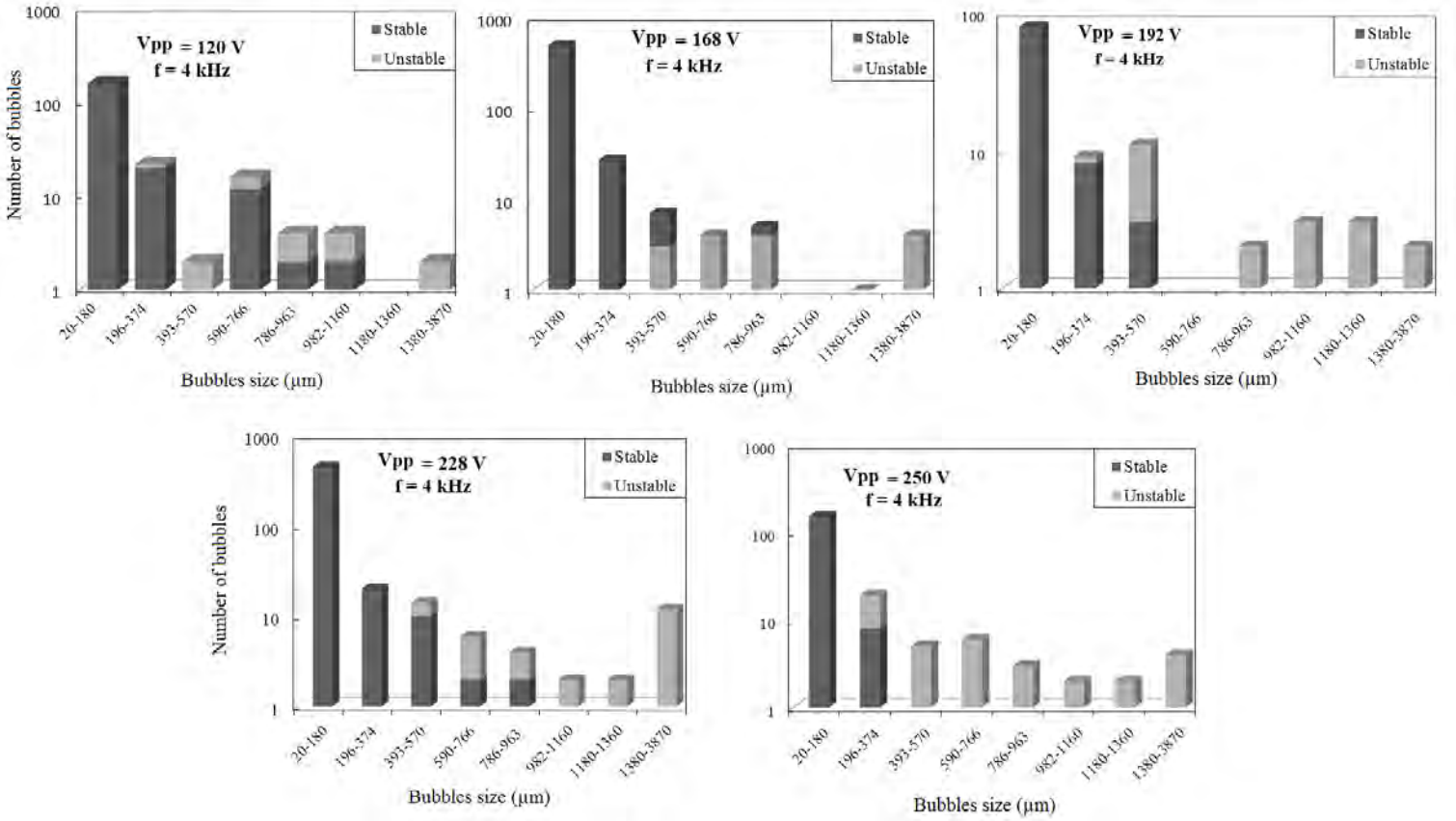

Figure 4.27: Histograms providing the number of bubbles obtained as a function of their size (classified in size domains) for various voltages and frequencies of the electrical signal applied to the PZT. The histograms indicate the fraction of stable and unstable bubbles as a function of the applied voltage.

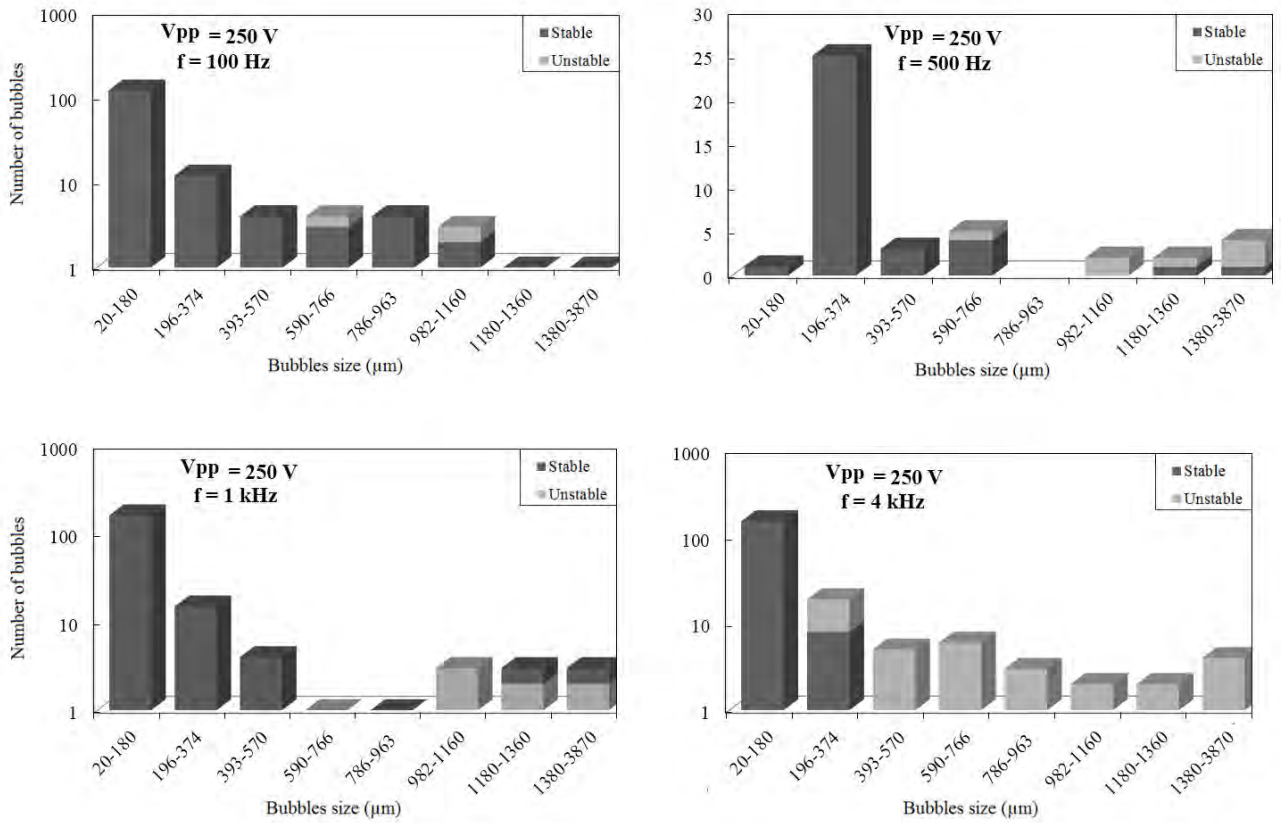

Figure 4.28: Histograms providing the number of bubbles obtained as a function of their size (classified in size domains) for various voltage and frequencies of the electrical signal applied to the PZT. The histograms indicate the fraction of stable and unstable bubbles as a function of the applied frequency.

4.4.4 Origin of the bubbles surface deformation

This section focuses on the reasons for the generation of surface oscillations, at the bubble surfaces. The change from volume oscillation to shape oscillations has already been the subject of several studies [95] [97] [98]. According to Franscecutto et al. [95], the bubbles keep their spherical shape surface for small amplitude pulsations, but when this amplitude becomes too large, the spherical surface becomes unstable and small disturbances lead to its deformations. Thus, Franscecutto et al. predicted the amplitude threshold of bubble pulsation (above which the bubble becomes unstable) as a function of the bubbles radius for a given frequency. Unfortunately, this study deals with the oscillation of free bubbles in water (the bubbles are not in contact with any surface), and cannot be directly applied to determine the amplitude threshold for the experiments performed in the present study (where the bubbles are confined in a microchannel). Nevertheless, the work of Franscecutto can serve as a basis for the following discussions.

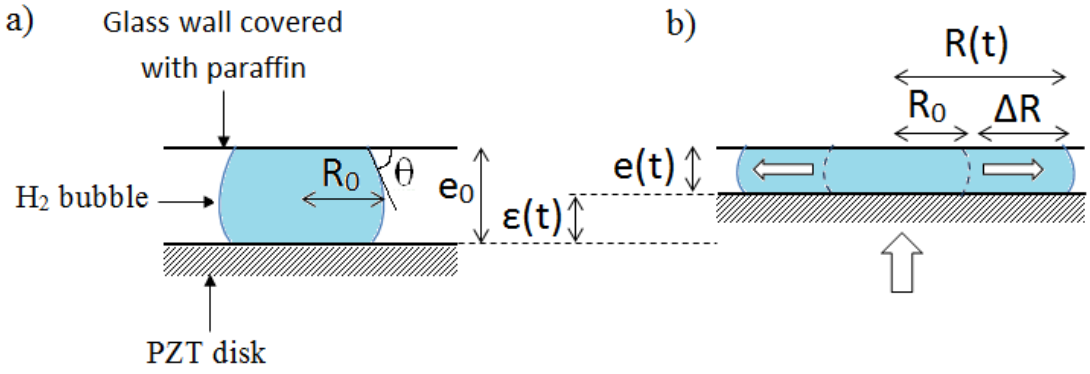

Figure 4.29: Schematic representation of a Hele-Shaw cell including a PZT disk and a bubble into the microchannel. a) initial state of the bubble in the microchannel; b) contraction of a bubble after the bending of the PZT disk.

For the experiments achieved here, the bubbles contract and expand under the PZT disk vibration, which bends alternatively in a concave and convex position, leading to the variations of the channel depth, e [9]. The amplitude of the bubble pulsation ΔR,

[9]Note that one of the microfluidic connections is opened allowing the variation of the liquid volume

therefore, depends on both its volume and the PZT displacement (Figure 4.29). Assuming the bubble incompressible and having a cylindrical shape[10], its volume can be considered as constant and expressed as follows:

$$V = \pi {R_0}^2 e_0 = \pi R(t)^2 e(t) \tag{4.4}$$

With, R_0 and e_0, the initial bubble radius and cell thickness respectively (PZT not activated). $R(t)$ and $e(t)$, the radius and cell thickness when the PZT is activated.

The radius of the bubble during the vibrations of the PZT can be expressed as follows:

$$R(t) = R_0 \sqrt{\frac{e_0}{e(t)}} \tag{4.5}$$

And the velocity of the bubble interface is:

$$v(t) = \frac{dR}{dt} = -\frac{1}{2} R_0 . \sqrt{e_0} . e(t)^{-3/2} \frac{de}{dt} \tag{4.6}$$

where $e(t) = e_0 - \varepsilon(t)$, and $\varepsilon(t)$ is the amplitude of vibration of the PZT.

Therefore:

$$v(t) = \frac{1}{2} R_0 . \sqrt{e_0} . e(t)^{-3/2} \frac{d\varepsilon}{dt} \tag{4.7}$$

Assuming that $\varepsilon(t) << e_0$: $e(t) \approx e_0$.

Thus the velocity of the bubble interface can be expressed as:

$$v(t) = \frac{R_0}{2e_0} . \frac{d\varepsilon}{dt} \tag{4.8}$$

The term $\frac{d\varepsilon}{dt}$ of Equation 4.8 represents the displacement speed of the PZT interface; it is assumed that $\frac{d\varepsilon}{dt}$ depends linearly on Vpp. For a sinusoidal signal it also depends on the frequency and can thus be expressed as follow:

$$\frac{d\varepsilon}{dt} = \psi(t) . Vpp . f \tag{4.9}$$

inside the microchannel.

[10] In the present experiments, the surfaces of the microchannel are covered with adhesive tape and plastic paraffin film showing low wettability. Therefore, the angle θ formed by the liquid on the channel surfaces $\approx 90°$, and the bubbles are considered as cylindrical.

$\psi(t)$ being a function which incorporates properties of the PZT as well as the properties of the signal generator (temporal resolution) and the amplifier (see the discussion about the efficiency of the square electrical signal in Section 4.4.1) The maximal displacement speed of the PZT interface can be written:

$$\left.\frac{d\varepsilon}{dt}\right|_{max} = \psi_{max}.Vpp.f \tag{4.10}$$

And finally, the maximal displacement speed of the bubble interface is:

$$v_{max} = \frac{R_0}{2e_0}\psi_{max}.Vpp.f \tag{4.11}$$

e_0 being a constant in the present study (50 μm), v_{max} can also be expressed:

$$v_{max} = a.R_0.Vpp.f \tag{4.12}$$

In addition, the experiments are carried out with a square signal, thus the frequency is not expected to affect the displacement speed of the PZT interface $\frac{d\varepsilon}{dt}$, which means that v_{max} is:

$$v_{max} = a'.R_0.Vpp \tag{4.13}$$

In order to have a better description of the coefficient a', the displacement speed of the bubble interface as a function of the applied voltage, is determined experimentally [11], for a given frequency (f = 4 kHz) and for the three bubbles presented in Figure 4.22 ($\approx$ 600 μm diameter).

[11] The method used to determine the displacement speed of the bubble interface is detailed in the Annexe 2

An overview of the maximal displacement speed (average of the maximal speed determined for both bubble expansion and contraction) obtained for the three bubbles is given Figure 4.30. For low voltages (under 200 V), the displacement speed of the bubbles interface increases linearly with the voltage, with a slope, p, equals to $5.95 \times 10^{-3}\ \frac{m/s}{V}$. Therefore, for this range of voltages, the coefficient a' can be expressed as follows:

$$a' = \frac{p}{R_0} \tag{4.14}$$

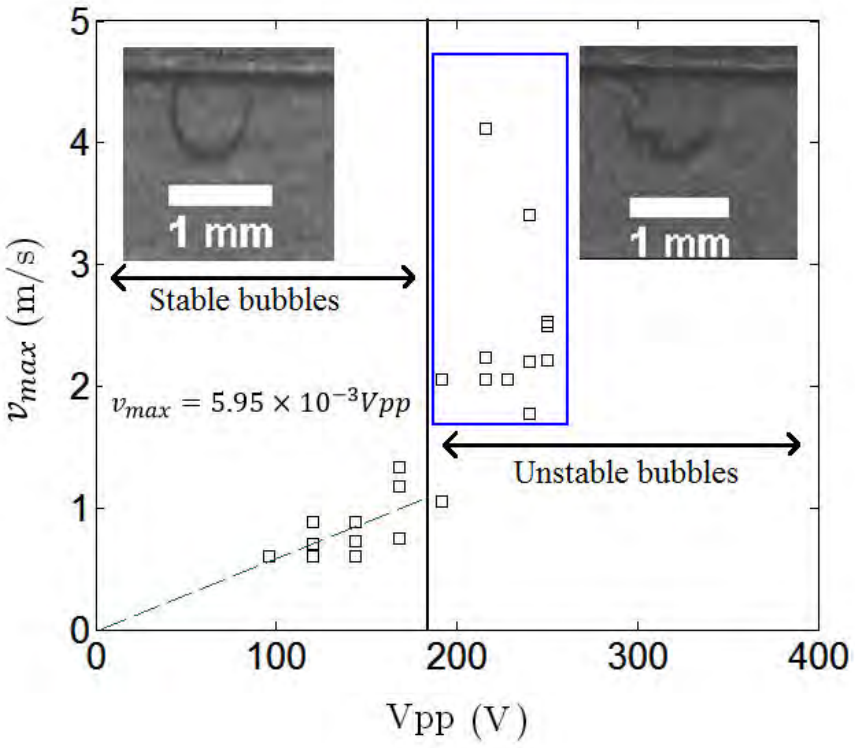

Figure 4.30: Maximal displacement speed of bubbles interface as a function of the applied voltage. The electrical signal is a square signal with f = 4 kHz, the bubble diameter is about 600 μm.

As mentioned already, for this range of voltages (0-200 V), the bubbles oscillate with breathing mode oscillations and no deformation of the surface is observed. For higher voltages ($Vpp > 200V$), the bubbles show surface oscillations; the resulting dis-

placement speed of the bubbles interface increases strongly and a non-linear dependence of the applied voltage is observed. It can, therefore, be concluded that above a certain displacement speed, the interface of the bubble oscillates too fast to keep its rounded shape.

As it was mentioned by Francescutto [95], the spherical shape of the bubble (rounded shape in this work) is maintained at low-amplitude pulsations, because of the surface tension. Therefore, the destabilization of the bubble shape occurs when external forces overcome the surface tension of the bubbles. The surface tension force of a bubble being stronger for small bubble sizes [99], it explains that smaller bubbles are more hardly destabilized than larger bubbles. To characterize the destabilization of the bubble shape we propose, to use the Weber number, We, which describes the ratio between the liquid inertia force and the surface tension of the bubble:

$$We = \frac{\Delta P_{Dynamic}}{\Delta P_{capillarity}} = \frac{\rho v^2}{\frac{\gamma}{R_0}} \tag{4.15}$$

Where, $\Delta P_{Dynamic} = \rho v^2$ is the dynamic pressure, and $\Delta P_{capillarity}$ is the capillary pressure, assumed to be $\frac{\gamma}{R_0}$, ρ and γ are the density (1000 kg/m^3) and the surface tension of water (71.97 $\times 10^{-3}$ N/m) respectively at T= 20 °C.

In fact, for a non spherical bubble, the capillary pressure $\Delta P_{capillarity}$ takes into consideration the two radii of curvature and is expressed as follows:

$$\Delta P_{capillarity} = \gamma \left[\frac{1}{R_0} + \frac{1}{R'} \right] \tag{4.16}$$

where R' is the second radius of curvature, expressed as $\frac{1}{R'} = \frac{2cos\theta}{e_0}$, θ being the contact angle formed by the liquid on the surfaces of the microchannel. As mentionned before, in the present experiments, the surfaces of the microchannel are covered with adhesive tape and plastic paraffin film showing low wettability. Therefore, $\theta \approx 90°$, which means that $\frac{1}{R_0} >> \frac{1}{R'}$ and $\Delta P_{capillarity} \approx \frac{\gamma}{R_0}$.

Using Equation 4.15, the obtained values of the Weber number range between 1.5 and 7.5 for Vpp $<$ 200 V (linear part of the curve $V_{max} = f(Vpp)$, Figure 4.30); and after the transition zone (Vpp>200 V), the Weber number increases and reaches values between 35 and 141. This demonstrates that, the liquid inertia force becomes higher

than the surface tension of the bubble, for low voltages. The maximal Weber number reached, just before the destabilization of the bubbles surface, can be defined as a critical Weber number, We_c; here $We_c = 7.5$. This critical Weber number describes the change from volume oscillation mode to SOM, for bubbles of 600 μm diameter; under this value, the surface tension is sufficiently high, compared to the inertia forces, to keep the bubble rounded; above this value, the surface of the bubble becomes unstable and show shape oscillations. Applying the critical Weber number to our experimental results, enables the determination of the critical bubble radius as a function of the applied voltage. Combining equations 4.12 and 4.15, the critical Weber number can be expressed:

$$We_c = \frac{\rho a'^2 {R_c}^3 V pp^2}{\gamma} \tag{4.17}$$

Thus:

$$R_c = \sqrt[3]{\frac{We_c \gamma}{\rho a'^2 V pp^2}} \tag{4.18}$$

The coefficient a' is determined using data obtained with bubbles of $R_0 = 600$ μm, as explained above (Figure 4.30).

The evolution of the obtained critical bubble radius (determined from the critical Weber number) as a function of the voltage is compared to the experimental data obtained from the histograms of Figure 4.27, and the results has been reported on the graph, Figure 4.31. Each range of size of the histograms (we choose the average of the size range) is represented on the graph by a colored squares:

- blue, if only stable bubbles are observed for this size range.
- violet, if both stable and unstable bubbles have been reported.
- red, if all the bubbles of this size range are unstable.

Figure 4.31 shows that the values of the critical radius determined from the critical Weber number are in satisfactory agreement with the experimental data. Indeed, below the critical radius, experiments show that most of the bubbles are stable; when the size of the bubble slightly overcomes the critical radius value, a portion of the bubbles becomes

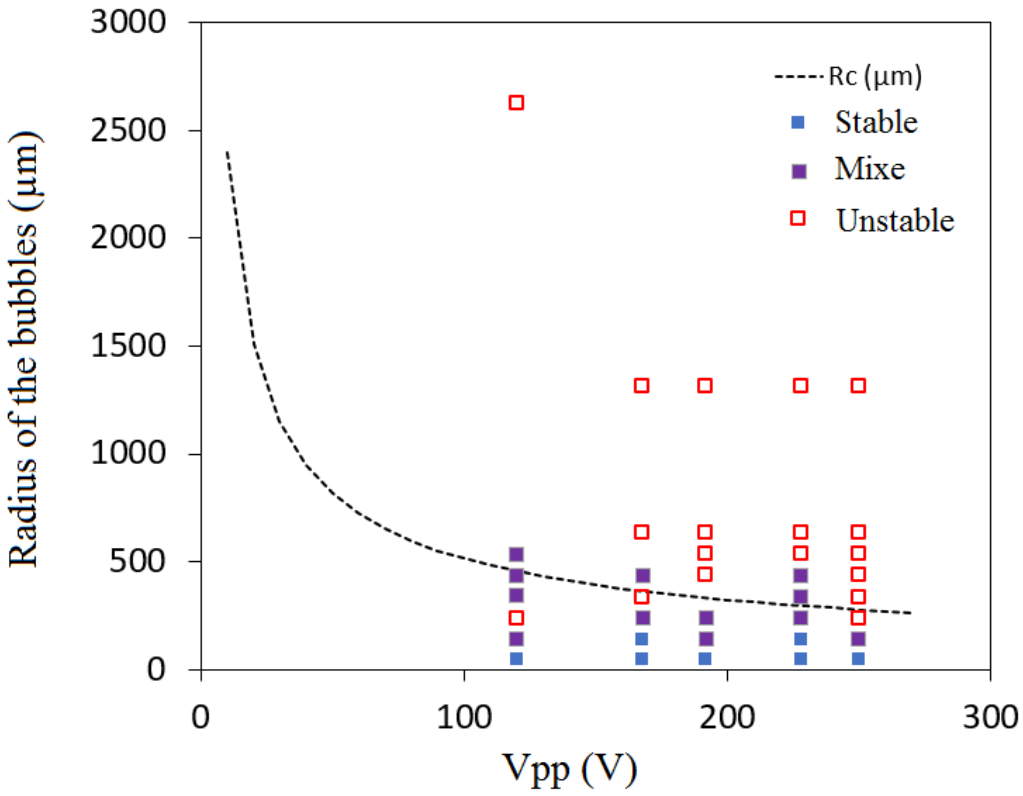

Figure 4.31: Critical radius of bubbles (determined from the critical Weber number) evolution against the peak to peak voltage (dashed line). Squares correspond to the experimental data extracted from Figure 4.27.

unstable, and finally, for radius significantly higher than the critical radius, only unstable bubbles are reported.

It has to be noticed that this interpretation of the results based on the critical Weber number does not take into account the effect of the frequency since it should not affect the bubbles interface speed for a square signal. However, as described before, the histogram showed in Figure 4.28 highlights that increasing the frequency leads to decrease the critical radius above which the bubbles are unstable. Thus, this suggests that the frequency also influence the bubbles oscillation. This can be explained by the fact that, when a bubble is submitted to a PZT pulse (square signal), the bubble contract or expand as mentioned before, but the position of the bubble interface is not immediately stable after the PZT pulse. In fact, there is a relaxation time during which the bubble keeps

showing slight volume oscillations until the bubble radius stabilizes. Thus, by increasing the frequency of the PZT pulse, the time separating two pulses will become lower than the relaxation time, which could lead to the destabilization of the bubble interface.

The splitting of the bubbles requires stronger destabilization of their interface. Indeed, visualizations of a bubble oscillations at the early stage of the PZT activation (see Figure 4.32) shows that bubbles exhibit surface shape oscillations, before to break up into several smaller bubbles. This is in agreement with Movassat et al. results [99], which show that bubbles splitting occurs at higher amplitude and frequency oscillations, than for SOM. The break up of the bubble is due to a further increase of the liquid inertia. In fact, the transition from SOM to splitting mode may be characterized by a second critical Weber number, higher than the one described above.

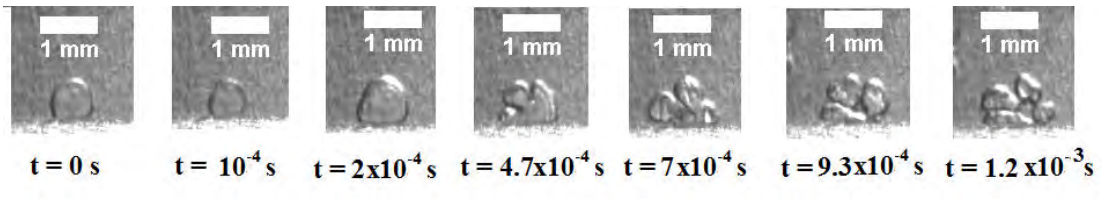

Figure 4.32: Pictures showing the splitting of an oscillating hydrogen bubble, at the early stage of the PZT activation. The PZT is driven with square signal, f = 4 kHz and Vpp = 250 V

The chaotic behavior of the splitting bubbles, does not enable the determination of the resulting surface displacement speed. It is likely that this displacement speed (reached by the splitting bubbles) is higher than the ones determined previously for the SOM bubbles ($\approx$ 4 m/s).

4.4.5 Characterization of the obtained iron particles suspension

The suspensions of iron particles obtained after the fragmentation, are analyzed by a morphological optical analyzer, which reveals a size distribution (in number) varying from 200 nm to several micrometers (Figure 4.33). The morphological optical analyzer does not allow to determine particle sizes under 200 nm, that is why the size distribution seems to be cut off. However, this analysis enables to demonstrate that a significant

proportion of submicrometric particles are obtained, even if large particles still remained unfragmented.

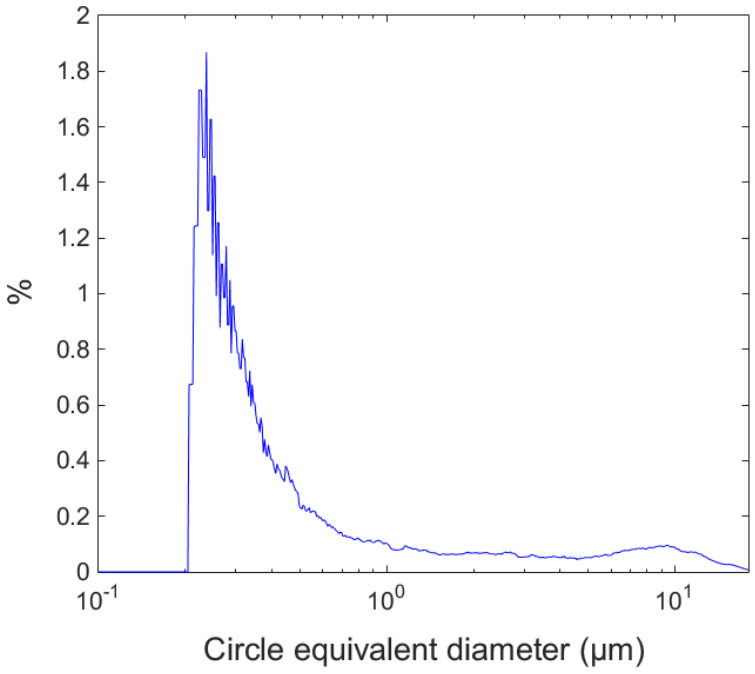

Figure 4.33: Size distribution (in number) determined by analyzing the suspension of iron particles obtained after the fragmentation, using a morphological optical analyzer.

The iron particles are also analyzed by TEM (transmission electronic microscopy), enabling the size and the shape of iron particles to be determined. The TEM analysis reveals that iron particles consist of fragmented dendrites of various sizes, from several micrometers (Picture a, b, c of Figure 4.34) to hundreds of nanometers (Picture e, f of Figure 4.34). Pictures a, b, c show fragments of dendrites which are secondary arms of bigger iron branches, which have been cut off at their root. In picture a and b the micrometric fragments of dendrite, seem to be unaffected by the fragmentation process while on Picture c, the secondary arm seems to have been peeled off on its right side. This suggests that smaller fragments (around 200 nm) are broken by the stress induced. It can be seen on picture d, a pile of dendrites along with a group of smaller entities. They consist of needle-like fragments which appear to be the small branches of the secondary branches.

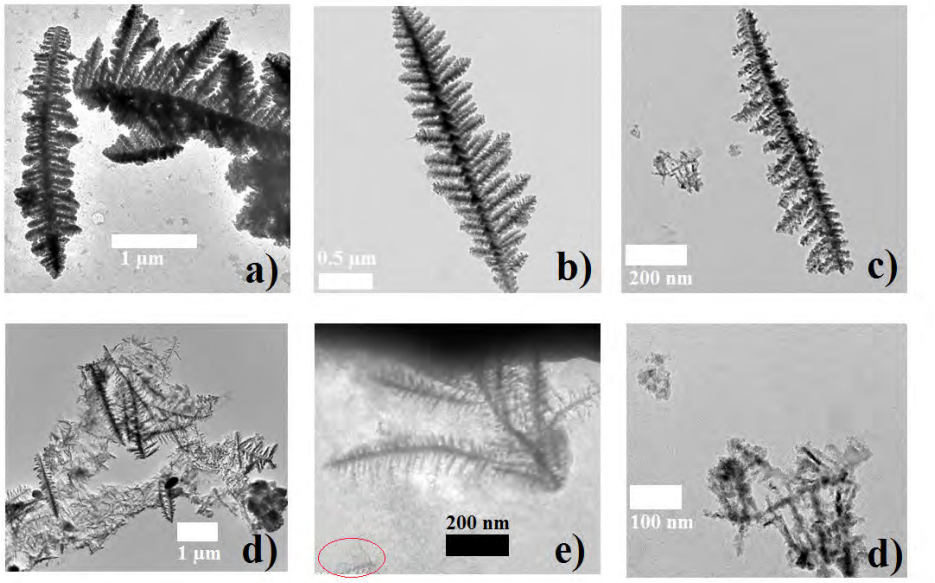

Figure 4.34: TEM pictures of fragments of iron dendrites obtained after the fragmentation of DBM-like deposits (i = 80 mA/cm^2, 0.1 M $FeCl_2$ solution) under acoustic vibrations of a PZT (f=4 kHz, Vpp = 250 V).

It can be concluded from these analyses that, the coupling "electrodeposition" and "fragmentation" of ramified deposit in a "vibrating" Hele-Shaw cell, enables to obtain a suspension of micro and submicroparticles exhibiting sizes varying from hundreds of nanometers to few micrometers. This process has not enabled to synthesize a suspension of monodispersed iron nanoparticles. However, the interest of using nanoparticles is due to their high specific surface and even if the fragments of dendrites obtained are about 1 μm their dendritic shape gives them a high surface to volume ratio.

To compare the specific surface of the dendrite fragments with the one of the nanoparticles, the fragment showed in picture b, Figure 4.34, is analyzed via an image processing software which enables to determine the surface and the contours (perimeter) of the dendrite (see Figure 4.35). Thus, a perimeter to surface ratio P/S, of $7.7 \times 10^7\ m^{-1}$ is obtained which corresponds to the P/S of nanoparticles of approximately 30 nm in diameter. Therefore, the catalytic properties of the suspension of iron dendrites obtained from our experiments should be comparable to that obtained with a suspension of nanoparticles.

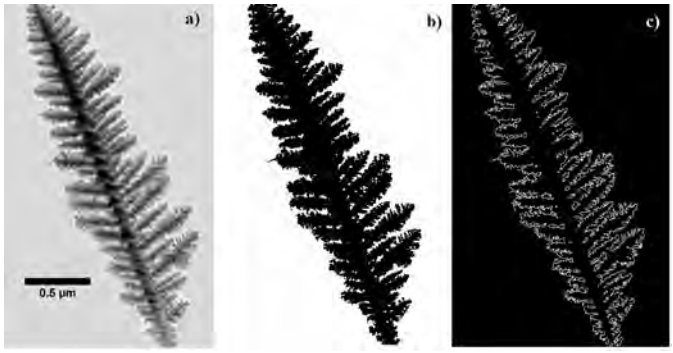

Figure 4.35: Image processing of the picture of a dendrite fragment : a) initial TEM picture of the dendrite; b) estimation of the perimeter, c) estimation of the surface.

4.4.6 Fragmentation of the iron dendrites by oscillating bubbles

This section aims to understand why the fragmentation of the iron branches is possible with the SOM bubbles (maximal displacement of the interface $\approx$ 4 m/s) and not with the bubbles undergoing breathing mode (maximal displacement of the interface $\approx$ 1 m/s, Figure 4.30).

To fragment electrodeposits (dendrites), it is required to induce mechanical stress within the triphasic mixture. This stress can be induced by the motion of the fluid or/and by the bubbles oscillations/splitting. The aim of this section is to examine if the stress resulting from the bubble displacement (e.g., the values of the displacement speed) is strong enough to fragment the dendrite and, if so, which size of dendrite fragments can be obtained. The results will be based on the TEM pictures of the particles suspension presented above.

Shu et al. [100] use a model enabling to estimate the instantaneous stress, resulting from a convective flow, acting on a dendrite "attached" to a wall, and perform this calculation to estimate the stress induced by a cavitation bubble on a dendrite, to compare it with the strength of the material (failure stress [12]).

In the present work, the dendrites are not attached to a wall, they are in suspension in the liquid, and submitted to a vigorous oscillatory flow, close to the bubbles surface (the local flow velocity oscillates between $\approx +4$ m/s and ≈ -4 m/s, when bubbles are

[12]Maximal tensile, compressive or shearing stress that a given unit of area of a material can bear without failing.

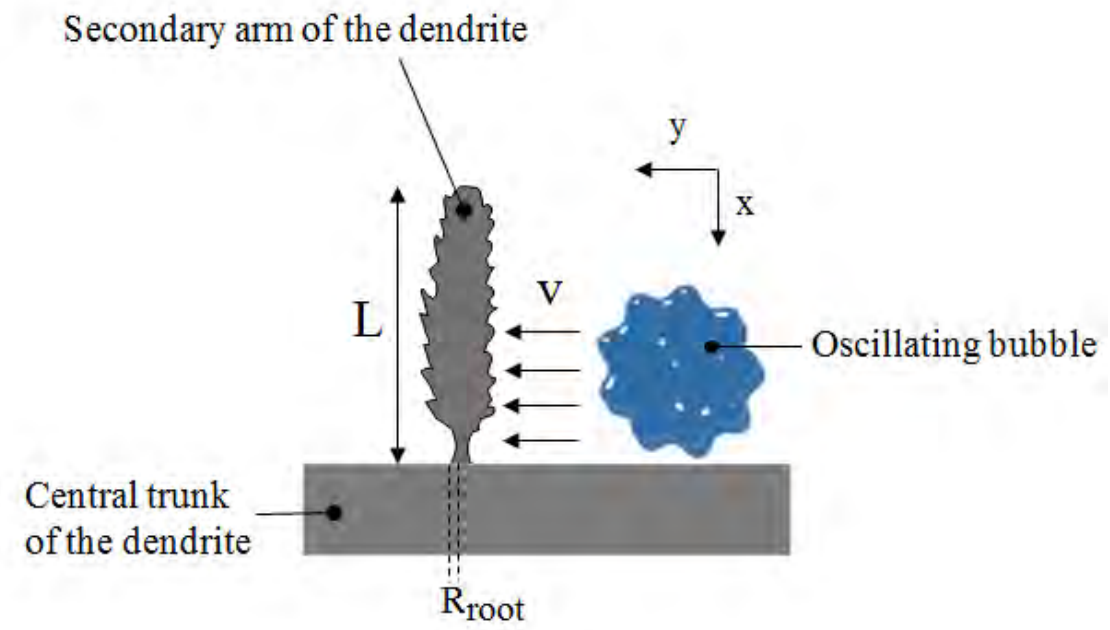

Figure 4.36: Scheme of a secondary arm of a dendrite (attached to the central trunk of the dendrite by its root) in interaction with an oscillating bubble which induces a flow velocity perpendicular to the dendrite

unstable). The use of the Shu model here implies that, the still unfragmented branches, arriving at the bubbles surface, are considered as immobile compared to the vigorous oscillatory flow close to the bubbles surface. Such a situation occurs, if the unfragmented branches piles are so heavy that, the time required for matching their displacement velocity with the oscillatory flow velocity, is well higher than the characteristic time of the oscillatory flow ($\approx$ 1/4000 s). The estimation of this time is possible but complicated, mainly because the mass of the arriving branches piles is undetermined (the piles of branches could be more or less compressed during their transport by microstreaming that renders difficult the estimation of their density as well as their thickness inside the channel). However, this assumption is made here to enable, in a first order approximation, the estimation of the mechanical stress acting on the dendrites. Thus, the same approach as used by D. Shu is applied here to determine if the oscillating bubbles can

theoretically fragment the deposit branches.

As seen in the Section 4.3.4 Figure 4.11, most of the iron branches are constituted of a central trunk and secondary arms. The stress acting on a secondary arm (connected to the central trunk) by a fluid flow of velocity v (Figure 4.36) can be estimated by the following expression:

$$\sigma(x) = \frac{-M(x)R(x)}{I(r(x))} \tag{4.19}$$

With M (N.m) the bending moment, I (m^4) the moment of inertia of the secondary arm section and $R(x)$ is the radius of the secondary arm section (the coordinate axis "x" being parallel to the dendrite):

$$M(x) = \frac{-Fx^2}{2} \tag{4.20}$$

$$I(R(x)) = \frac{\pi(R(x))^4}{4} \tag{4.21}$$

and F is the force per unit length acting perpendicularly on the secondary arm:

$$F = 3\pi\mu v \tag{4.22}$$

with μ the viscosity of the liquid. Considering a secondary arm of length (L) showing a root of radius (R_{root}), the stress induced by a fluid velocity (v) can be expressed as follows:

$$\sigma(L) = \frac{6\mu v L^2}{{R_{root}}^3} \tag{4.23}$$

The ultimate failure stress of iron is σ_f = 350 MPa [101]; if the stress acting on the secondary arm is higher than this value ($\sigma > 350$ MPa), the secondary arm will be dissociated from the trunk of the dendrite.

Section 4.4.5 has revealed that micrometric fragments of dendrites (probably secondary arms of bigger iron branches) have been obtained. Considering the fragment of dendrite shown in Figure 4.34, b, the stress induced by fluid flows of 1 m/s (corresponding to the breathing mode bubbles) and 4 m/s (for the SOM bubbles) on a secondary arm

of similar dimensions (L = 2.88 μm and R_{root} = 56 nm) can be estimated. The obtained results show that, if v = 1 m/s, $\sigma = 283$ MPa, while, if v = 4 m/s, $\sigma = 1100$ MPa which is five times higher. This demonstrates that the stress induced by a SOM bubbles on secondary arms is strongly higher than the one induced by breathing mode bubbles.

To conclude this simple model enables to understand why, for the breathing mode, the displacement speed of the bubbles interfaces does not allow the fragmentation of the deposit: a displacement speed of 1 m/s induces a stress ($\sigma = 283$ MPa) lower than the failure stress of iron (σ_f = 350 MPa). Conversely, for a SOM bubbles, the displacement speed of the bubbles interfaces (v= 4 m/s) induces a stress ($\sigma = 1100$ MPa) higher than the failure stress of iron (σ_f = 350 MPa), allowing the deposit fragmentation.

4.5 Conclusion

In this chapter, a new process using the coupling of the electrodeposition and acoustic waves for the synthesis of iron nanoparticles is proposed and studied. The electrodeposition of ramified electrodeposits and their fragmentation are carried out in a high aspect ratio device consisting of a Hele-Shaw cell (50 μm depth, 2.5 cm length) integrating a piezoelectric element. Parameters for both the iron growth and its fragmentation are studied and optimized.

It has been found that, due to the early reduction of the free proton, ($E^0_{H^+/H_2} =$ 0 V/SHE $E^0_{Fe^{II}/Fe} = -0.44$ V/SHE), the growth of an iron deposit requires to use a current density, higher than the one attributed to the H^+ reduction (this latter being function of the Fe^{II} precursor concentration). Electrodeposition experiments performed with various operating conditions show that the iron growth is not affected by hydrogen bubbles, for current densities higher than 16 mA/cm^2. Furthermore, the current density also controls the morphology of the iron electrodeposit. High current densities (above 24 mA/cm^2) favor the formation of dense branching deposits, while at low current densities (under 12 mA/cm^2) DLA-like deposits are obtained.

The focus is then put on the growth of DBM-like deposits. This kind of deposit is of particular interest, because of its regular shape and its well-controlled growth velocity. Also, experiments show that, this type of deposit is more fragile than the DBM-like

deposits and thus, more easily breakable and dispersible, which is interesting for the expected catalytic applications. Comparison of the obtained experimental data of the growth velocity of DBM-like deposit with the theoretical predictions from [44], leads to a good agreement. This confirms that the co-production of hydrogen during the Fe^{II} reduction does not disrupt the growth of the deposit. However, other impurities like cationic species (Hecker's effect) can affect the deposit morphology.

The second part of this chapter present the study of the deposit fragmentation. As a first step, the optimum operating conditions for the complete fragmentation of the deposit are determined. Results show that the presence of hydrogen bubbles is a sine qua non condition for the deposit fragmentation (for the applied electrical signals). Then the study of the parameters applied to the PZT shows that:

- a square electrical signal is more efficient (final AUB $\approx$ 3 %) than a triangular (final AUB $\approx$ 50 %) and a sinusoidal signal (final AUB $\approx$ 40 %);
- the higher the frequency, the more efficient the fragmentation is (AUB < 10 % in 1s for f= 4 kHz, in 3s for f= 1 kHz, in 4s for f= 0.5 kHz);
- the higher the voltage, the more efficient the fragmentation is (final AUB $\approx$ 3 % for Vpp = 250 V, 10 % for Vpp = 200 V and 40 % for Vpp = 125 V.

A better understanding of the fragmentation process is then gained by the analysis of the bubbles behavior by high-speed camera visualizations. Experiments reveal that under the PZT vibration, the bubbles undergo different oscillating modes: breathing, shape oscillation or splitting modes. However, only SOM and splitting bubbles are found to induce the fragmentation of the deposit. Study of the bubbles behavior reveals that the control parameters are:

- the frequency of the electrical signal,
- the voltage,
- the size of the vibrating bubbles.

It has been demonstrated that there is a critical radius, depending on the frequency and the voltage (200 < R_c<500 μm for f= 4 kHz and 100 < Vpp < 300 V), above which

the bubbles oscillation changes, from the breathing mode to the surface shape mode (splitting mode is reached for even higher frequencies and voltages). This critical radius decreases by increasing the frequency and the voltage of the electrical signal. This explains why the fragmentation of the iron deposit is more efficient for high frequencies and voltages. This destabilization from the breathing mode to the surface shape mode is due to high displacement speeds of the bubble interface which changes the ratio between the surface tension of the bubble (that keeps the bubble rounded) and the inertia force of the liquid. Indeed, the Weber number ranges between 1.5 and 7.5 when the bubbles surface is stable, and reaches values ranging between 17 and 48 for destabilized bubbles.

The displacement speed of the interface reaches a value of ≈ 4 m/s, which is high enough to enable the fragmentation of iron branches into particles ranging from hundreds of nanometers to few micrometers. TEM characterization of these particles shows that they consist of small fragments of iron dendrites of various size. Estimation of their specific surface reveals that despite their micrometer sizes, the specific surface is comparable to one of the nanoparticles of 30 nm diameter (the ratio perimeter/surface is about $7.7 \times 10^7\ m^{-1}$). Therefore, one can expect that, due to their high specific surface, the obtained suspension of iron particles shows interesting catalytic properties. It would be interesting to test the reductive properties of this suspension of iron particles for the decontamination of pollutants (like organic compounds or heavy metals) and to compare it with the suspension of iron nanoparticles obtained by the chemical reduction of Fe^{II} by $NaBH_4$.

Finally, this microdevice offers interesting outlook since it offers the possibility to apply a flow of iron precursor solution and an in situ magnetic separation. Therefore the optimization of this process could lead to a new way for the electrochemical synthesis of micro/nanoparticles in microchannels.

Conclusion

The zero valent iron nanoparticles (nZVI) have been increasingly investigated in the last 20 years, particularly for their use as reducing agent in the treatment of contaminated soil and water. They are also of great interest for the medical field due to their magnetic properties. Among the various synthesis ways explored to produce nZVI, the sonoelectrochemical aqueous synthesis appears to be a promising, ecological, economic and safe aqueous technique, specifically because it does not require any reagent. Its principle is based on the electrochemical formation of zero valent iron on a conductive substrate; the ultrasonication is then used to remove the deposit from the substrate, and disperse it into the liquid, as a suspension of particles. The cavitation phenomenon, induced by ultrasound, is expected to induce a sufficient shear stress to overpass the adhesion of the deposit. This specific phase of the synthesis (the removal of the electrodeposited iron) implies the control of the balance between the forces acting on the electrodeposit adhesion and those acting on its removal. Various studies have investigated the influence of some parameters, such as the ultrasound power, the duration of the ultrasonication, the current density and the size of the electrodeposited particles, on the deposit dispersion as well as on the size of the nanoparticles in the resulting suspension. However, few considerations has been given to the effect of the substrate on the deposit dispersion process. For these reasons, the first objective of this thesis was to study the influence of the substrate on the global sonoelectrochemical synthesis, e.g. , on the iron electrodeposition and on its dispersion under ultrasonication.

The electrochemical formation of iron has been studied under various operating conditions: the electrodeposition was achieved by steady-state voltammetry and galvanostatic electrolyses, using two different precursors ($FeCl_2$ and Mohr's salt), at different pH. Results highlight:

- the early reduction of the proton H^+, ($E^0_{H^+/H_2} = 0$ V/SHE and, $E^0_{Fe^{2+}/Fe} = -0.44$ V/SHE)
- the spontaneous chemical corrosion of iron by H^+, H_2O, eventually O_2.
- the formation of iron hydroxides.

The early reduction of the proton H^+ affects the overall process on various points (decrease of the Faradaic yield, formation of hydrogen bubbles, basification of the interfacial solution...). In addition, the proton concentration also induces the iron corrosion:

$$Fe + 2H^+ \rightarrow Fe^{2+} + H_2 \tag{4.24}$$

Corrosion rates, ranging between 2.9×10^{-12} and 7.4×10^{-11} mol/s have been estimated for pH varying from 3.0 to 5.3. Higher pH solutions (pH$\geq$ 5.0) were used to decrease the corrosion rate, however, voltammetric analyses reveal the formation of iron hydroxides on/within the iron electrodeposit. The voltammetric study also highlights the importance of choosing the appropriate potential for iron electrodeposition: electrolyses at low potentials (E< -1.4 V/SCE) also lead to the formation of iron hydroxides.

The electrodeposition of iron was performed on two substrate materials, gold and vitreous carbon, exhibiting different surface energies ($\gamma_{Au} = 27$ mJ/m^2 and γ_{VC} = 31.5 mJ/m^2) and different roughnesses (Ra varying between 8 and 345 nm, for the VC substrates). Results reveal that the substrate material, by affecting the deposit/substrate interfacial energy, controls both the energy required for the iron deposit formation as well as its morphology. Indeed, voltammetric study shows that a lower overpotential ($\approx$ 100 mV lower) is needed for Fe^{II} reduction on gold than on VC substrates; in parallel SEM analyses clearly show that iron forms a 2D layer on gold, while a 3D growth is obtained on the VC substrates. No significant effect was observed concerning the influence of the roughness, except that the deposit grows following the topography of the substrate surface.

The second part of this study focused on the electrodeposit dispersion process. A steady-state cyclic voltammetry has been performed under ultrasonication, using substrates (Gold and VC) of different surface energies and roughnesses. Two effects of

ultrasonication have been highlighted: the increase of the mass transfer and the dispersion of the iron electrodeposit induced by successive cavitation events. The crucial role of the substrate on the dispersion efficiency was clearly established. Comparison of the cathodic and anodic charges passed during the cyclic scans was used as tool to quantify the dispersion of the deposit. Typically, on the VC substrates, Qc/Qa varies in the range 1.6-240 when ultrasounds were applied, against 1.14-1.4 under silent conditions. Conversely, no dispersion was observed on the gold substrate: the same ratios were obtained under silent conditions or by applying ultrasounds, $1.08 \leq \frac{Qc}{Qa} \leq 1.31$. These results were correlated to the work of adhesion of the deposit/substrate interface, which is 19 mJ/m^2 for VC and 149 mJ/m^2 for gold substrates. In fact, through its surface energy, the substrate material controls the adhesion of the deposit on its surface and consequently affects the dispersion process.

The dispersion of the iron electrodeposited by galvanostatic electrolyses performed under silent conditions, has been also studied. A simple first order kinetic model $Qa/Qa_{ref}(t_{US}) = exp(-s.t_{US})$ was proposed to simulate the dispersion of the electrodeposits which appears to be a progressive process. These results also demonstrate a significant influence of the substrate roughness on the deposit dispersion: after 5 s of ultrasonication, 50 % of the deposit was dispersed on a rough VC substrate (Ra = 345 nm), while dispersion of the deposit was complete from a smooth VC substrate (Ra = 8 nm). In fact, increasing the roughness leads to increase the contact surface between the deposit and the substrate, which induces a higher adhesion energy of the deposit.

To conclude, this first part of the thesis highlights the influence of the substrate on both, the growth of the iron electrodeposit and its dispersion by ultrasonication. It has been shown, among other, that using a substrate material of low surface energy enables to minimize the adhesion of the deposit on the substrate and consequently enhances the dispersion process. Thus, the best operating conditions to obtain a fast and complete dispersion has been determined allowing the application of the sonoelectrochemical synthesis at the large scale under satisfactory energy consumption.

This thesis also proposes a new approach for the synthesis of nZVI, using the coupling of the iron electrodeposition with acoustic vibrations induced by a PZT. Instead of removing electrodeposited iron particles (as it is the case in a typical sonoelectro-

chemical synthesis), the idea is to form an electrochemically ramified electrodeposit, by longer growth duration and then, to fragment it by acoustic vibrations. In this case, the substrate has no major effect, neither on the growth nor on the fragmentation. This acoustofluidic synthesis, performed in a high aspect ratio microchannel (Hele-Shaw cell) enables to carried out both steps (growth and fragmentation) in a confined space, and under controlled conditions.

The study of the iron growth in the Hele-Shaw cell has been investigated by varying the current density and the precursor concentration. It has been highlighted that, due to the early reduction of the proton, the growth of the iron deposit is only possible above a certain current density (16 $\mathrm{mA/cm^2}$, for 3.3 <pH< 3.9 and $0.02M < C_{Fe^{II}} < 0.1M$) corresponding to the one required by the H^+ reduction. Hydrogen bubbles are produced in all cases, but below this threshold only hydrogen bubbles are observed. Besides, increasing the current density leads to change the iron morphology from DLA to DBM. SEM analysis reveals that, at small-scale, the granular structure of the iron branches is also affected by the current density. More precisely, the size of the nanometric grains composing the iron branches decreases by increasing the growth speed (and consequently the current density), typically: from 500 nm to 1 μm for a growth speed of $\approx 3.6 \times 10^{-6}$ m/s, and from 10 to 20 nm for a growth speed of $\approx 4 \times 10^{-5}$ m/s. The velocity of the iron branches being homogeneous for DBM deposits, they show a regular structure.

Consequently, DBM deposits were prepared to study the fragmentation process because of their:

- well controlled shape and growth velocity
- regular structure
- fragility.

Analysis of the deposit fragmentation clearly highlights that the hydrogen bubbles produced by the side reaction during the iron growth, is a condition sine qua non for the deposit fragmentation. Indeed, under the vibrations of the PZT, bubbles undergo different oscillations modes: breathing mode, surface oscillation mode (SOM), splitting mode, depending on the frequency and the voltage of the electrical signal but also on

the size of the bubbles. SOM and splitting modes enable to reach high velocities of the bubbles interface ($\approx$ 4 m/s), inducing the fragmentation of the iron branches into a cloud of fine particles. The parameters of the electrical signal enabling a fast fragmentation are resumed in the following tables:

Waveform of the electrical signal	Square	Triangular	Sinusoidal
Final AUB [13](%)	3	50	40

Vpp (V)	250	200	125
Final AUB (%)	3	10	40

Frequency (kHz)	4	1	0.5
Duration of the fragmentation to reach AUB < 10 % (s)	3	10	40

Suspensions of dendrite fragments of sizes ranging between the hundred of nanometers to few micrometers, were obtained. Higher voltage and fragmentation durations could enable to reach nanosized. The dendrite fragments obtained here, show a high specific surface: 7.7×10^7 m^{-1}, which is comparable to the one of nanoparticles of 30 nm diameter.

Future prospects

- The stability and the catalytic properties of the obtained iron suspension requires further investigation. Typically, their ability to reduce pollutants (TCE, CCl3-CCl3, ...) could be another field to study.

- The addition of a stabilizer to the solution used for the rinse of the iron deposit, before its fragmentation, would enable to limit the aggregation and sedimentation of the submicrometric dendrites fragments without affecting the iron growth. However, a stabilizer could also affect the efficiency of the deposit fragmentation by changing the viscosity of the precursor solution or the surface tension of the bubbles. Thus, it can modify the critical size above which the bubbles undergo SOM under acoustic vibrations.

- Investigating the possibility to apply a flow of iron precursor and an in situ magnetic separation, would allow achieving a continuous production of iron particles and could lead to the proposal of a new continuous electrochemical synthesis of micro/nanoparticles in microchannels.

Bibliography

[1] R.A. Crane and T.B. Scott. Nanoscale zero-valent iron: Future prospects for an emerging water treatment technology. *Journal of Hazardous Materials*, 211-212:112–125, 2012.

[2] X. Li, D.W. Elliott, and W. Zhang. Zero-Valent iron nanoparticles for abatement of environmental pollutants: Materials and engineering aspects. *Critical Reviews in Solid State and Materials Sciences*, 31(4):111–122, 2006.

[3] D.L. Huber. Synthesis, properties, and applications of iron nanoparticles. *Small*, 1(5):482–501, 2005.

[4] C.G. Hadjipanayis, M.J. Bonder, S. Balakrishnan, X. Wang, H. Mao, and G.C. Hadjipanayis. Metallic iron nanoparticles for MRI contrast enhancement and local hyperthermia. *Small*, 4(11):1925–1929, 2008.

[5] Y.J. Wang, S.M. Hussain, and G P Krestin. Superparamagnetic iron oxide contrast agents: Physicochemical characteristics and applications in MR imaging. *European Radiology*, 11(11):2319–2331, 2001.

[6] A. Ito, M. Shinkai, H. Honda, and T. Kobayashi. Medical application of functionalized magnetic nanoparticles. *Journal of Bioscience and Bioengineering*, 100(1):1–11, 2005.

[7] A. Jordan, R. Scholz, P. Wust, H. Fähling, and R. Felix. Magnetic fluid hyperthermia (MFH): Cancer treatment with AC magnetic field induced excitation of biocompatible superparamagnetic nanoparticles. *Journal of Magnetism and Magnetic Materials*, 201:413–419, 1999.

[8] J.E. Martin, A. Herzing, W. Yan, X. Li, B.E. Koel, C.J. Kiely, and W. Zhang. Determination of the oxide layer thickness in core-shell zerovalent iron nanoparticles. *Langmuir*, 24(8):4329–4334, 2008.

[9] B.D. Yirsaw, M. Megharaj, Z. Chen, and R. Naidu. Environmental application and ecogicaoll significance of nano-zero valent iron. *Journal of environmental sciences*, 44:88–98, 2015.

[10] W. Yan, H.L. Lien, B.E. Koel, and W. Zhang. Iron nanoparticles for environmental clean-up: recent developments and future outlook. *Environmental Science: Processes & Impacts*, 15(1):63, 2013.

[11] X. Li and W. Zhang. Sequestration of metal cations with zerovalent iron nanoparticles - A study with high resolution X-ray photoelectron spectroscopy (HR-XPS). *Journal of Physical Chemistry C*, 111(19):6939–6946, 2007.

[12] J.T. Nurmi, P.G. Tratnyek, V. Sarathy, D.R. Baer, J.E. Amonette, K. Pecher, C. Wang, J.C. Linehan, D.W. Matson, R. Lee Penn, and M.D. Driessen. Characterization and properties of metallic iron nanoparticles: Spectroscopy, electrochemistry, and kinetics. *Environmental Science and Technology*, 39(5):1221–1230, 2005.

[13] W. Yan, A.A. Herzing, C.J. Kiely, and W.X. Zhang. Nanoscale zero-valent iron (nZVI): Aspects of the core-shell structure and reactions with inorganic species in water. *Journal of Contaminant Hydrology*, 118(3-4):96–104, 2010.

[14] F. Fu, D.D. Dionysiou, and H. Liu. The use of zero-valent iron for groundwater remediation and wastewater treatment: A review. *Journal of Hazardous Materials*, 267:194–205, 2014.

[15] Y. Liu and G.V. Lowry. Effect of particle age (Fe0 content) and solution pH on NZVI reactivity: H2 evolution and TCE dechlorination. *Environmental science and technology*, pages 1–9, 2006.

[16] A. Amir and W. Lee. Enhanced reductive dechlorination of tetrachloroethene by nano-sized zero valent iron with vitamin B12. *Chemical Engineering Journal*, 170(2-3):492–497, 2011.

[17] G. Zanaroli, A. Negroni, M. Vignola, A. Nuzzo, H.Y. Shu, and F. Fava. Enhancement of microbial reductive dechlorination of polychlorinated biphenyls (PCBs) in a marine sediment by nanoscale zerovalent iron (NZVI) particles. *Journal of Chemical Technology and Biotechnology*, 87(9):1246–1253, 2012.

[18] S. Kang, S. Liu, H. Wang, and W. Cai. Enhanced degradation performances of plate-like micro/nanostructured zero valent iron to DDT. *Journal of Hazardous Materials*, 307:145–153, 2016.

[19] N. Groza, R. Radulescu, E. Panturu, A. Filcenco-Olteanu, and R.I. Panturu. Zerovalent iron used for radioactive waste water treatment. *Scientific Bulletin of the Politehnica University of Timisoara*, 54(68):21–25, 2009.

[20] V. Smuleac, R. Varma, S. Sikdar, and D. Bhattacharyya. Green synthesis of Fe and Fe/Pd bimetallic nanoparticles in membranes for reductive degradation of chlorinated organics. *Journal of Membrane Science*, 379(1-2):131–137, 2011.

[21] J.E. Muñoz, J. Cervantes, R. Esparza, and G. Rosas. Iron nanoparticles produced by high-energy ball milling. *Journal of Nanoparticle Research*, 9(5):945–950, 2007.

[22] F.E. Kruis, H. Fissan, and A. Peled. Synthesis of nanoparticles in the gas phase for electronic, optical and magnetic applications - A review. *Journal of Aerosol Science*, 29(5-6):511–535, 1998.

[23] C. Wang and W. Zhang. Synthesizing nanoscale iron particles for rapid and complete dechlorination of TCE and PCBs. *Environmental Science & Technology*, 31(7):2154–2156, 1997.

[24] G. Zhang, Y. Liao, and I. Baker. Surface engineering of core/shell iron/iron oxide nanoparticles from microemulsions for hyperthermia. *Materials Science and Engineering: C*, 30(1):92–97, 2010.

[25] M.E. Hyde and R.G. Compton. How ultrasound influences the electrodeposition of metals. *Journal of Electroanalytical Chemistry*, 531(1):19–24, 2002.

[26] J. Delplancke, J. Dille, J. Reisse, G.J. Long, A. Mohan, and F. Grandjean. Magnetic nanopowders: Ultrasound-assisted electrochemical preparation and properties. *Chemistry of Materials*, 12(4):946–955, 2000.

[27] C.N.R. Rao, A. Müller, and A.K. Cheetham. *The chemistry of nanomaterials: synthesis, properties and applications Vol2*. John Wiley & Sons, 2006.

[28] J. Klima, C. Bernard, and C. Degrand. Sonoelectrochemistry: transient cavitation in acetonitrile in the neighbourhood of a polarized electrode. *Journal of Electroanalytical Chemistry*, 399(1-2):147–155, 1995.

[29] R.G. Compton, J.C. Eklund, and F. Marken. Sonoelectrochemical processes: A review. *Electroanalysis*, 9(7):509–522, 1997.

[30] D.J. Walton, S.S. Phull, A. Chyla, J.P. Lorimer, T.J. Mason, L.D. Burke, M. Murphy, R.G. Compton, J.C. Eklund, and S.D. Page. Sonovoltammetry at platinum electrodes: surface phenomena and mass transport processes. *Journal of Applied Electrochemistry*, 25(12), 1995.

[31] S.S. Chen, H.D. Hsu, and C.W. Li. A new method to produce nanoscale iron for nitrate removal. *Journal of Nanoparticle Research*, 6(6):639–647, 2004.

[32] R.G. Compton, J.C. Eklund, F. Marken, T.O. Rebbitt, R.P. Akkermans, and D.N. Waller. Dual activation: coupling ultrasound to electrochemistry-an overview. *Electrochimica Acta*, 42(19):2919–2927, 1997.

[33] A. Khachatryan, R. Sarkissyan, L. Hassratyan, and V. Khachatryan. Influence of ultrasound on nanostructural iron formed by electrochemical reduction. *Ultrasonics Sonochemistry*, 11(6):405–408, 2004.

[34] V. Sáez and T.J. Mason. Sonoelectrochemical synthesis of nanoparticles. *Molecules*, 14(10):4284–4299, 2009.

[35] A.J. Bard and L.R. Faulkner. *Electrochemical methods: fundamentals and applications*, volume 2. Wiley New York, 1980.

[36] J.A.V. Butler. Studies in heterogeneous equilibria. *Transaction of the Faraday society*, 19:659–665, 1923.

[37] E. Budevski, G. Staikov, and W.J. Lorenz. *Electrochemical phase fomation and growth: An introduction to the initial stages of metal deposition*. VCH Publishers, 1996.

[38] P. Milan and S. Mordechay. *Fundamentals of electrochamical deposition*. John Wiley & Sons, the electr edition, 2006.

[39] B. Scharifker and G. Hills. Theoretical and experimental studies of multiple nucleation. *Electrochimica Acta*, 28(7):879–889, 1983.

[40] D. Grujicic and B. Pesic. Electrodeposition of copper: The nucleation mechanisms. *Electrochimica Acta*, 47(18):2901–2912, 2002.

[41] A.M. Rashidi and A. Amadeh. The effect of current density on the grain size of electrodeposited nanocrystalline nickel coatings. *Surface and Coatings Technology*, 202(16):3772–3776, 2008.

[42] J.L. Trompette and H. Vergnes. Influence of base electrolytes on the electrodeposition of iron onto a silicon surface. *Journal of Physical Chemistry B*, 110(30):14779–14786, 2006.

[43] D. Grujicic and B. Pesic. Iron nucleation mechanisms on vitreous carbon during electrodeposition from sulfate and chloride solutions. *Electrochimica Acta*, 50(22):4405–4418, 2005.

[44] C. Léger. *L'électrodeposition en cellule mince sous l'œil d'un interférometre : une étude expérimentale et théorique de processus limités par la diffusion.* PhD thesis, Université de Bordeaux I, 1999.

[45] J.N. Chazalviel. Electrochemical aspects of the generation of ramified metallic electrodeposits. *Physical Review A*, 42(12):7355–7367, 1990.

[46] L.G. Sundström and F.H. Bark. On morphological instability during electrodeposition with a stagnant binary electrolyte. *Electrochimica Acta*, 40(5):599–614, 1995.

[47] D. Grier, E. Ben-Jacob, R. Clarke, and L.M. Sander. Morphology and microstructure in electrochemical deposition of zinc. *Physical Review Letters*, 56(12):1264–1267, 1986.

[48] D.G. Grier, D.A. Kessler, and L.M. Sander. Stability of the dense radial morphology in diffusive pattern formation. *Physical Review Letters*, 59(20):2315–2318, 1987.

[49] Y. Sawada, A. Dougherty, and J.P. Gollub. Dendritic and fractal patterns in electrolytic metal deposits. *Physical Review Letters*, 56(12):1260–1263, 1986.

[50] T.A. Witten and L.M. Sander. Diffusion-limited aggregation. *Physical review B*, 27(9):5686–5697, 1982.

[51] F. Argoul, A. Arneodo, and G. Grasseau. Self-Similarity of Diffusion-Limited Aggregates and Electrodeposition Ousters. *Physical Review Letters*, 61(22):2558–2561, 1998.

[52] I.B. Hibbert and J.R. Melrose. Copper electrodeposits in paper support. *Physical Review A*, 38(2):1036–1048, 1987.

[53] V. Fleury, J.H. Kaufman, and D.B. Hibbert. Mechanism of a morphology transition in ramified electrochemical growth. *Nature*, 367:435–438, 1994.

[54] M. Wang, J.P. Willem, N. Ming, and P. Bennema. Formation of a mesh-like electrodeposit induced by electroconvection. *Nature*, 367:438–441, 1994.

[55] R.L. Smith and S.D. Collins. Generalized model for the diffusion-limited aggregation and Eden models of cluster growth. *Physical Review A*, 39(10), 1989.

[56] R.W. Bower and S.D. Collins. Fractal transitions in diffusion-limited cluster formation. *Physical Review A*, 43(6):3165–3167, 1991.

[57] V. Fleury. Branched fractal patterns in non-equilibrium electrochemical deposition from oscillatory nucleation and growth. *Nature*, 390(6656):145–148, 1997.

[58] J. Newman and K.E. Thomas-Alyea. *Electrochemical Systems Third Edition*. John Wiley & Sons, 2004.

[59] C. Léger, J. Elezgaray, and F. Argoul. Internal structure of dense electrodeposits. *Physical Review E - Statistical Physics, Plasmas, Fluids, and Related Interdisciplinary Topics*, 61(5 B):5452–5463, 2000.

[60] V. Fleury, J. Kaufman, and B. Hibbert. Evolution of the space-charge layer during electrochemical deposition with convection. *Physical Review E*, 48(5):3831–3840, 1993.

[61] C. E. Brennen. *Cavitation and Bubble Dynamics*. Oxford University press, 1995.

[62] C. Pétrier, N. Gondrexon, and P. Boldo. Ultrasons et sonochimie. *Techniques de l'ingénieur*, 33(0):0–15, 2008.

[63] F. Priego Capote and M.D. Luque De Castro. *Analytical applications of ultrasound*. Elservier, 2007.

[64] J. Klima. Application of ultrasound in electrochemistry. An overview of mechanisms and design of experimental arrangement. *Ultrasonics*, 51(2):202–209, 2011.

[65] E. Maisonhaute, C. Prado, P.C. White, and R.G. Compton. Surface acoustic cavitation understood via nanosecond electrochemistry. Part III: Shear stress in ultrasonic cleaning. *Ultrasonics Sonochemistry*, 9(6):297–303, 2002.

[66] O. Wess. Physikalische Grundlagen der extrakorporalen Stoßwellentherapie. *Journal für Mineralsstoffwechsel*, 11(4):7–18, 2004.

[67] G.W. Gale and A.A. Busnaina. Roles of cavitation and acoustic streaming in megasonic cleaning. *Particulate Science and Technology*, 17(3):229–238, 1999.

[68] F. Zhang, A.A. Busnaina, M.A. Fury, and S.Q. Wang. The removal of deformed submicron particles from silicon wafers by spin rinse and megasonics. *Journal of Electronic Materials*, 29(2):199–204, 2000.

[69] J. Israelachvili. *Intermolecular and surface forces*. Budevski1996, 2nd edition, 1999.

[70] S.S. Wang, Z.J. Jiao, X.Y. Huang, C. Yang, and N.T. Nguyen. Acoustically induced bubbles in a microfluidic channel for mixing enhancement. *Microfluidics and Nanofluidics*, 6(6):847–852, 2009.

[71] D. Ahmed, X. Mao, J. Shi, B.K. Juluri, and T.J. Huang. A millisecond micromixer via single-bubble-based acoustic streaming. *Lab on a chip*, 9(18):2738–2741, 2009.

[72] R.H. Liu, J. Yang, M.Z. Pindera, M. Athavale, and P. Grodzinski. Bubble-induced acoustic micromixing. *Lab on a chip*, 2(3):151–7, 2002.

[73] D.K. Owens and R.C. Wendt. Estimation of the surface free energy of polymers. *Journal of Applied Polymer Science*, 13(8):1741–1747, 1969.

[74] E.L. Cussler. *Diffusion mass transfer in fluid systems*. Cambridge University Press, 3rd edition, 2009.

[75] Y. Li and S. Gregory. Diffusion of ions in sea water and in deep sea sediments. *Geochimica et Cosmochimica Acta, 1974*, 38(2):703–714, 1973.

[76] C. Chern. *Principles and applications of emulsion polymerization*. John Wiley & Sons, 2008.

[77] T.X. Phuoc. A comparative study of the photon pressure force, the photophoretic force, and the adhesion van der Waals force. *Optics Communications*, 245(1-6):27–35, 2005.

[78] L.A. Girifalco and R.J. Good. A theory for the estimation of surface and interfacial energies. I. Derivation and application to interfacial tension. *The Journal of Physical Chemistry*, 61(7):904–909, 1957.

[79] G.M. Jenkins and K. Kawamura. Structure of glassy carbon. *Nature*, 231(5):16–17, 1971.

[80] M.J. Siegfried and K.S. Choi. Elucidating the effect of additives on the growth and stability of Cu2O surfaces via shape transformation of pre-grown crystals. *Journal of the American Chemical Society*, 128:2–4, 2006.

[81] N. Ibl and K. Schadegg. Surface roughness effects in the electrodeposition of copper in the limiting current range. *Journal of The Electrochemical Society*, 114(1):54–58, 1967.

[82] G. Orhan and G. Hapçi. Effect of electrolysis parameters on the morphologies of copper powder obtained in a rotating cylinder electrode cell. *Powder Technology*, 201(1):57–63, 2010.

[83] N. Ibl, P. Javet, and F. Stahel. Note on the electrodeposits obtained at the limiting current. *Electrochimica Acta*, 17(4):733–739, 1972.

[84] R.G. Compton, J.C. Eklund, S.D. Page, T.J. Mason, and D.J. Walton. Voltammetry in the presence of ultrasound: mass transport effects. *Journal of Applied Electrochemistry*, 26(35):775–784, 1996.

[85] W.R. Tyson and W.A. Miller. Surface free energies of solid metals estimation from liquid surface tension measurements. *Surface science*, 62:267–276, 1977.

[86] S. Floate, M. Hyde, and R.G. Compton. Electrochemical and AFM studies of the electrodeposition of cobalt on glassy carbon: an analysis of the effect of ultrasound. *Journal of Electroanalytical Chemistry*, 523(1):49–63, 2002.

[87] V. Heresanu. *Electrodéposition sous champ magétique de zinc et de fer. Propriétés magnétiques des arborescences de fer*. PhD thesis, Université Joseph Fourier-Grenoble I, 2003.

[88] M. Wang and N. Ming. Alternating morphology transitions in electrochemical deposition. *Physical Review Letters*, 71(1):113–116, 1993.

[89] R.H. Zhao and P.J. Pan. A spectrophotometric study of Fe(II)-Chloride complexes in aqueous solutions from 10 to 100 ^{o}C. *Canadian Journal of Chemistry*, 79(2):131–144, 2001.

[90] E. Samson, J. Marchand, and K.A. Snyder. Calculation of ionic diffusion coefficients on the basis of migration test results. *Materials and Structures/Materiaux et Constructions*, 36(36):156–165, 2003.

[91] V. Fleury, M. Rosso, and J.N. Chazalviel. Geometrical aspect of electrodeposition: The Hecker effect. *Physical Review A*, 43(12):6908–6916, 1991.

[92] A. Kuhn and F. Argoul. Spatiotemporal morphological transitions in thin-layer electrodeposition: The Hecker effect. *Physical Review E*, 49(5):4298–4305, 1994.

[93] O. Younes, L. Zeiri, and S. Efrima. Two- to three-dimensional Hecker transitions in the interfacial electrodeposition of silver. *Langmuir*, 13(6):1767–1772, 1997.

[94] P. Tho, R. Manasseh, and A. Ooi. Cavitation microstreaming patterns in single and multiple bubble systems. *Journal of Fluid Mechanics*, 576(5):191–233, 2007.

[95] A. Francescutto and R. Nabergoj. Pulsation amplitude threshold for surface waves on oscillating bubbles. *Acustica*, 41(3):215–220, 1978.

[96] M. Versluis, S.M. van der Meer, D. Lohse, P. Palanchon, D. Goertz, C.T. Chin, and N. de Jong. Microbubble surface modes. In *Ultrasonics Symposium, 2004 IEEE*, volume 1, pages 207–209, 2004.

[97] M. Movassat. *Bubble dynamics, oscillations and breakup under force vibration*. PhD thesis, University of Toronto, 2012.

[98] A.I. Eller and L.A. Crum. Instability of the motion of a pulsating bubble in a sound field. *The Journal of the Acoustical Society of America*, 47(3B):762–767, 1970.

[99] M. Movassat, N. Ashgriz, and M. Bussmann. Oscillation and breakup of a bubble under forced vibration. *International Journal of Heat and Fluid Flow*, 54:211–219, 2015.

[100] D. Shu, B. Sun, J. Mi, and P.S. Grant. A high-speed imaging and modeling study of dendrite fragmentation caused by ultrasonic cavitation. *Metallurgical and Materials Transactions A*, 43(10):3755–3766, 2012.

[101] A.M. Howatson, P.G. Lund, and J.D. Todd. *Engineering Tables and Data*. Springer Netherlands, 1972.

Appendix

Appendix 1

Procedure followed to count the number of stable and unstable bubbles as a function of their size

The procedure followed to construct the histograms shown in Figure 4.27, and 4.28, Chapter 4, is described below.

- For each operating condition (f = 4 kHz - 120V<Vpp<250V or Vpp = 250 V - 100Hz<f<4kHz), six pictures of the fragmentation video, representative of the whole process, are selected as it was shown in Figure 4.25, Chapter 4 (picture shown below as reminder)

- For each picture, the number of stable and unstable bubbles are counted, and their size determined. If the bubbles do not show a rounded shape, their maximal and minimal diameter are measured, and, the average of these two values is used.

- For each operating condition, the portion of stable and unstable bubbles are classified by their size domains.

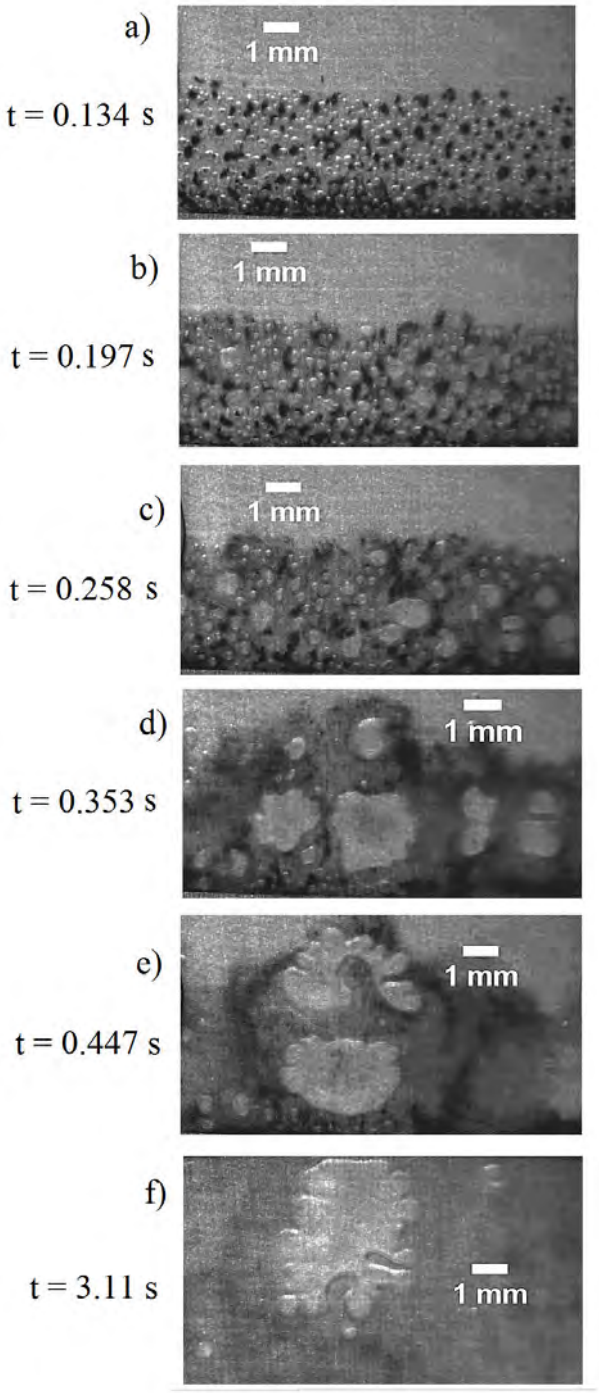

Figure 37: Six pictures representative of the fragmentation process of a DBM deposit ($i = 80$ mA/cm^2, 0.1 M $FeCl_2$), induced by the PZT vibrations (f = 500 Hz, Vpp = 250 V, Square signal).

Appendix 2

Estimation of the maximal displacement speed of the bubble interface

The displacement speed of a bubble interface is determined by an image processing using the grey level of the bubble pictures throughout the oscillation.

1. An axis, from the middle of the bubble and crossing the bubble interface is set (Figure 38, 1).

2. The evolution of the grey level along this axis enables to determine the position of the bubble interface, $R(t)$: it corresponds to the minimal value (Figure 38, 2).

3. Thus, the position of this minimal value is recorded and plotted as a function of time (Figure 38, 3).

4. The displacement speed is determined plotting $\frac{dR(t)}{dt}$ as a function of time (Figure 38, 4); the maximal displacement speeds correspond to the maximal values of this curve: $max\left(\frac{dR(t)}{dt}\right) = v_{max}$

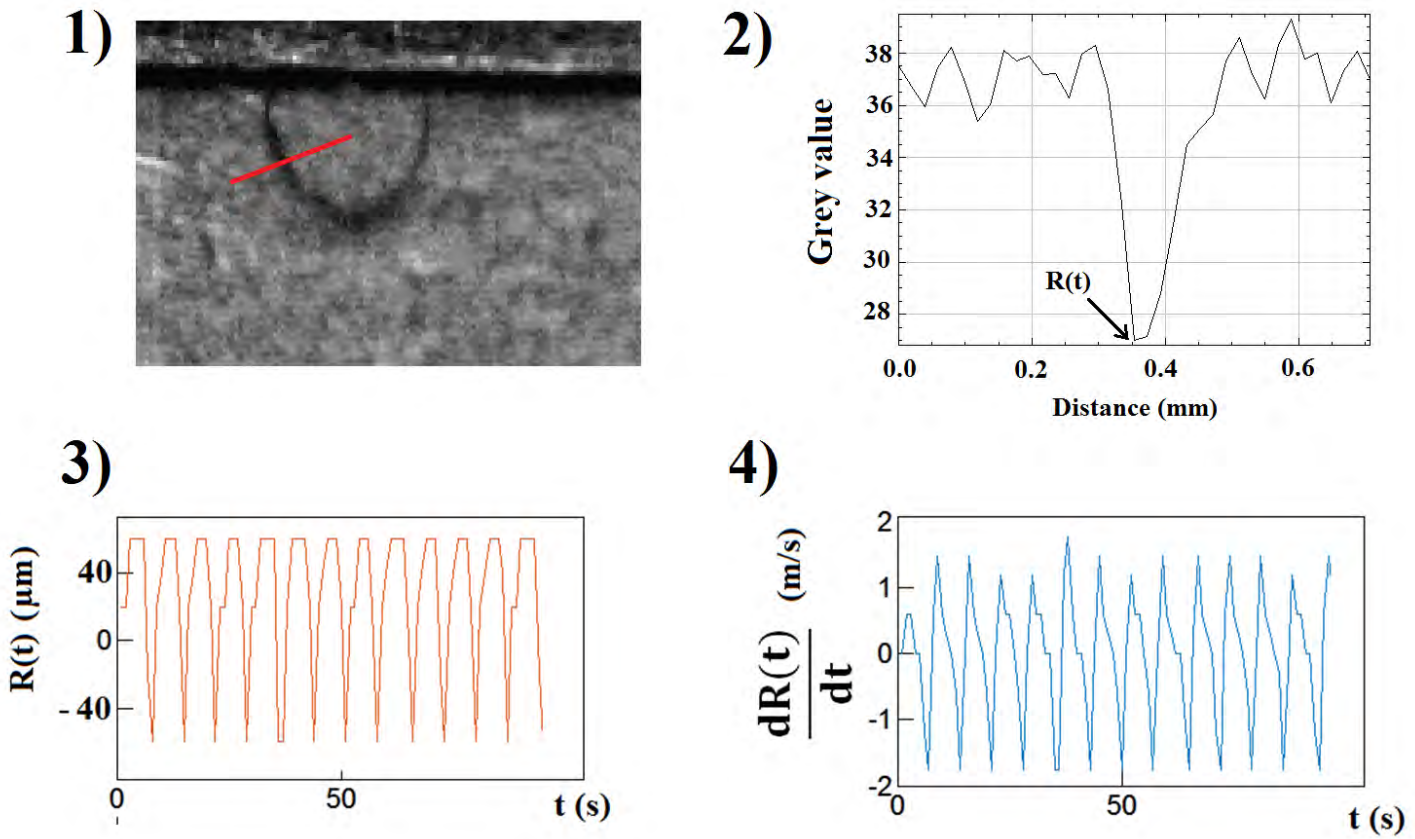

Figure 38: Process to determinate the displacement speed of the bubble interface during its oscillation: 1) picture of a bubble trapped in the Hele-Shaw cell and, in red, the axis along which the bubble interface displacement is measured, 2) grey level measured along the red axis allowing to determine the bubble interface position (minimal value), 3) position of the bubble interface along the axis as a function of time, 4) Displacement speed of the bubble interface as a function a time.

Electrosynthèse assistée par ultrasons de nanoparticules de fer zéro-valent : étude de la croissance de dépôts et de leur dispersion par ondes acoustiques

La synthèse de nanoparticules de fer zéro-valent, par le couplage des procédés d'ultrasonication et d'électrodéposition, est étudiée selon deux approches. La première partie de l'étude s'intéresse à l'influence du substrat, utilisé pour l'électrodéposition, sur la croissance des dépôts de fer et sur leur dispersion par ultrasonication. L'énergie interfaciale ainsi que l'énergie d'adhésion du dépôt sur le substrat ($\gamma_{Fe/substrat}$ et $W_{Fe/substrat}$ respectivement) étant reliées à l'énergie de surface et à la rugosité du substrat, un intérêt particulier a été porté à ces deux propriétés. Ainsi, deux matériaux présentant des énergies de surface différentes, l'or (Au) et le carbone vitreux (VC), ainsi que des rugosités différentes ont été testés. Un développement théorique basé sur les interactions de Van der Waals a permis de démontrer que $\gamma_{Fe/VC} > \gamma_{Fe/Au}$ ce qui suggère une meilleure affinité du dépôt de fer avec l'or qu'avec le VC. Cette différence influence la morphologie (croissance 2D sur or et 3D sur le VC) mais aussi l'adhésion des dépôts. En effet, les expériences réalisées pour étudier l'effet des ultrasons sur le dépôt de fer révèlent une dispersion du dépôt progressive et complète pour le cas du VC alors qu'aucun détachement du dépôt n'est obtenu en utilisant l'or. La seconde partie de l'étude est consacrée à la synthèse de nanoparticules de fer par une nouvelle approche : l'électrodéposition de dépôts de fer ramifiés est étudiée dans une cellule de Hele-Shaw intégrant un élément vibrant (diaphragme piézoélectrique) permettant à la fois la formation de dépôts de fer et leur fragmentation. Les expériences menées révèlent que les bulles d'hydrogène, formées lors de la co-réduction des protons libres durant l'électrodéposition du fer, influencent fortement le processus de fragmentation. En utilisant des hautes fréquences et amplitudes de vibration du PZT, les bulles d'hydrogène oscillent avec des déformations de surface. Celles-ci génèrent des vitesses d'interface suffisamment hautes (≈ 4 m/s) pour permettre aux bulles de fragmenter des dépôts ramifiés en particules de fer, de tailles comprises entre 1 µm et 100 nm, et présentant une grande surface spécifique due à leur morphologie dendritique. Cette deuxième partie de l'étude permet d'ouvrir la voie à une nouvelle technologie de fabrication des nanoparticules.

Mots clés: nanoparticules de fer zéro-valent, sonoélectrochimie, énergie interfaciale, croissance ramifiée, oscillations de bulles

Ultrasounds assisted electrosynthesis of zero valence iron nanoparticles: study of the deposit growth and dispersion by acoustic waves

This study concerns the coupling of the ultrasounds with the electrodeposition process for the synthesis of zero-valent iron nanoparticles; it is structured in two sections. The first focuses on the electrode substrate used for the iron electrodeposition and aims to determine its influence on both the deposit growth and its dispersion by ultrasonication. The interfacial and the adhesion energies of the deposit on the substrate ($\gamma_{Fe/substrate}$ and $W_{Fe/substrate}$ respectively) being related to the surface energy and the roughness of the substrate, a particular focus is put on the influence of these two properties. Thus, two materials of different surface energies, gold (Au) and vitreous carbon (VC), as well as various roughnesses, are tested. Considering only the Van der Waals interactions, a theoretical development has enabled to determine that $\gamma_{Fe/VC} > \gamma_{Fe/Au}$ which suggests a better affinity of the iron deposit with the gold than with the VC substrate. This difference impacts the deposit morphology (2D growth on the gold and 3D growth on the VC substrate) but also the deposit adhesion. Indeed, experiments performed to study the effect of ultrasounds on the iron electrodeposit reveal its progressive and complete dispersion for the vitreous carbon case while no dispersion (no removal of the deposit from the electrode) is obtained with the gold substrate. The second section of the present study deals with the synthesis of iron nanoparticles; to this end, the electrodeposition of branched deposits has been investigated in a Hele-Shaw cell integrating a vibrating element (piezoelectric diaphragm), expected to allow both the deposit formation and its fragmentation. Experiments reveal that the hydrogen bubbles, formed by the co-reduction of free protons during the iron electrodeposition, strongly influence the fragmentation process. Using high vibration frequencies and high amplitudes, the bubbles oscillate with surface deformations, inducing interface velocity sufficiently high (≈ 4 m/s) to allow the fragmentation of the deposit into particles of sizes ranging between 1 µm and 100 nm and showing a high specific surface due to their dendritic morphology. Thus this work opens the way for a new particles manufacturing technology.

Keywords: Zero-valent iron nanoparticles, sonoelectrochemistry, interfacial energy, ramified growth, bubbles oscillations